RAPID SOLIDIFICATION PROCESSING AND OXIDATION OF FINE GRAINED Fe-Cr-Al ALLOYS

by

MICHAEL MALONEY

B.S., University of Illinois
(1983)

M.S., University of Illinois
(1984)

Submitted in Partial Fulfillment of the
Requirements for the Degree of

Doctor of Philosophy

at the

MASSACHUSETTS INSTITUTE OF TEGHNOLOGY

June 1989

Signature of Author_____
Department of Material Science and Engineering
May 8,1989

Certified by_____
Gregory J. Yurek
Thesis Supervisor

Accepted by_____
Samuel M. Allen
Chairman, Departmental Committee on Graduate Students

RAPID SOLIDIFICATION PROCESSING AND OXIDATION OF FINE GRAINED Fe - Cr - Al ALLOYS

by

MICHAEL MALONEY

Submitted to the Department of Materials Science and Engineering on 25 May, 1989 in partial fulfillment of the requirements for the Degree of Doctor of Philosophy in Metallurgy

ABSTRACT

A small-scale inert gas atomization system was developed to produce oxidation resistant, fine-grained, rapidly solidified Fe-Cr-Al alloys by spray-forming and powder processing techniques. The use of alloy processing to control microstructure and to obtain an improvement in oxidation resistance as an alternative to changing alloy content was demonstrated. The results indicate that in certain applications where highly alloyed stainless steels are presently used, the substitution of rapidly solidified, low-alloy steels can result in increased component life and a reduction of the consumption of expensive and/or strategic elements.

Alloys of the compositions Fe-2.5Cr-2.5Al-1Ti-0.6B and Fe-4Cr-4Al-1Ti-0.6B were processed to obtain grain sizes down to 1μm by a spray-forming process. The alloys contained a fine dispersion of 0.05μm TiB_2 particles that did not coarsen and that prevented normal grain growth at temperatures up to 1000 °C. An Fe-2.5Cr-2.5Al-1Ti-0.6B alloy that was atomized to produce powder contained an interdendritic amorphous phase. During consolidation of the powder, the amorphous phase crystallized to form a TiB_2 network that effectively prevented grain boundary migration. The dispersion of TIB_2 was ineffective in preventing abnormal grain growth in alloys that contained a high dislocation density.

Compared to a conventionally processed Fe-2.5Cr-2.5Al alloy, the rapidly solidified Fe-2.5Cr-2.5Al-1Ti-0.6B alloy had a greatly reduced rate of oxidation and formed much less iron oxides at 600 and 700 °C. The improvement in oxidation resistance of these alloys can be directly attributed to short circuit diffusion along alloy grain boundaries that results in the formation of a more protective aluminum-rich oxide scale on the surface of the alloy. The spray-formed Fe-4Cr-4Al-1Ti-0.6B alloy was found to have good oxidation resistance from 400 to 1000 °C and greatly improved oxide scale adhesion at 900 and 1000 °C compared to a conventionally processed Fe-4Cr-4Al alloy. It was demonstrated that titanium improves adhesion of alumina scales. The dispersion of fine titanium diboride particles in the rapidly solidified alloy act as reservoirs for this element, thereby providing an effective way to take advantage of the improvements in alumina scale adhesion provided by titanium.

Thesis Supervisor: Dr. Gregory Yurek
Title : Professor of Metallurgy

TABLE OF CONTENTS

LIST OF AND FIGURES

Figure Page Number

LIST OF TABLES

ACKNOWLEDGEMENTS

I would like to thank my thesis advisor, Professor Gregory Yurek, for the years of guidance and support he has given to me. I also express my sincere thanks to Professors John Elliott and John Vander Sande for reviewing the thesis and serving on the examining committee. I thank Dr. John Stringer at the Electric Power Research Institute for Financial Support.

The skillful microscopy work performed by Mike Frongillo and Tony Garratt-Reed in support of this research is greatly appreciated. I especially thank Daniel Eppelsheimer for his friendship and the extensive use of his photographic equipment and knowledge. The assistance of Gunter Ardnt and Dr. Wang was of great help in the processing of alloys and I greatly enjoyed the experience of working with them.

I thank the many friends that I made during my stay at MIT; Alex Otto, Allison Warren, Bob Frank, Bruce Pint, Don Bolger, Cathy Cottel, Basu, Katy Barmak, Young Kil Kim, Tom Moffat, and many more.

I am very grateful to my parents for the financial support to allow the purchase of computer equipment. I am also very thankful to my wife, Mary Lou, for raising three children in a very small apartment during my course of study.

1. INTRODUCTION

The useful life of metallic components employed at high temperatures is determined by mechanical properties, such as yield and creep strength, or by resistance to oxidation. Excessive consumption of material by high temperature oxidation is detrimental because it reduces load bearing capacity and can alter the shape of a component. The majority of high temperature alloys consist chiefly of a base metal such as Fe, Ni, or Co, plus additional elements intended to improve mechanical and oxidation properties.

Resistance to oxidation is achieved by the use of an alloying element in the alloy that reacts with oxygen in the environment and form a protective oxide scale on the alloy surface. Protective oxide scales are those that grow at a slow rate, remain adherent to the base alloy, and do not form volatile reaction products. Oxides of aluminum, chromium and silicon are the slowest growing and, if the oxide remains adherent to the alloy, are the most effective in providing oxidation resistance.

Usually, oxidation resistance is improved by increasing the concentration of elements in the alloy that form a protective oxide. This promotes the initial formation of a protective oxide and the reformation of the oxide when the scale is lost by spallation or abrasion. This approach has the disadvantage that it increases the cost of alloys, consumes strategic and/or critical elements and may, as in the use of high concentrations of aluminum in iron alloys, adversely affect mechanical properties. An alternate approach to improving oxidation resistance is by control of alloy microstructure through materials processing. Microstructural features such as a dispersion of fine particles and alloy grain size can influence oxide scale formation[1,2]. Increased oxidation resistance resulting from a refinement in alloy grain size has been well documented and has been attributed to increased transport of reactive elements in the alloy by short circuit, grain

boundary diffusion.

Rapid solidification processing provides a convenient means of controlling alloy microstructure. This processing method has been used widely to produce alloys that have grain sizes much finer than could be produced by conventional processing methods. In addition, rapid solidification processing can be used to produce a dispersion of fine, second-phase particles, which may be effective in stabilizing a fine grain size at high temperatures and may provide a reservoir of elements that are useful in improving oxidation resistance.

This research program was undertaken to study the rapid solidification processing and oxidation behavior of fine-grained, low alloy steels. The work was divided into two parts. The first part consisted of the design and development of a laboratory scale rapid solidification processing apparatus and the processing of rapidly solidified alloys by spray-forming and powder processing techniques. Both of these processing techniques are currently used successfully on an industrial basis. The second part of the work consisted of investigating the isothermal and cyclic oxidation behavior of rapidly solidified and conventionally processed alloys.

Two series of alloys were chosen for this study from the Fe-Cr-Al system, alloys containing 2.5 wt.% chromium and aluminum and alloys containing 4 wt. % chromium and aluminum. Steels that are alloyed in this concentration range generally have very poor resistance to oxidation at temperatures above a few hundred degrees centigrade and readily form iron oxides. The development of oxidation resistant low-alloy Fe-Cr-Al steels by means of rapid solidification processing could result in potential benefits including low cost, the use of lower concentrations of strategic and/or critical elements, and the formation of a very protective aluminum oxide scale.

2. LITERATURE SURVEY

This chapter is divided into one section on alloy processing and one on alloy oxidation. The first section includes a discussion of rapid solidification processing methods and the evolution and stability of rapidly solidified alloy microstructures. In the second section, the high temperature oxidation of conventionally processed and rapidly solidified alloys is reviewed. The focus of this section is on alloys in the Fe-Cr-Al system.

2.1. Alloy Processing

2.1.1. Rapid Solidification Processing

Rapid solidification processing can be defined as cooling an alloy through its freezing range at a rate of 10^5°C/s or greater.[3] Rapid solidification processing has been used extensively over the past two decades to obtain microstructural refinement and produce unique microstructures in many types of alloy systems. Advantages attributed to this process include reduced grain size or dendrite arm spacing, reduced chemical segregation, extended solute solubility, and metastable phase formation.[4] Property improvements made possible by this control over alloy microstructure have been far reaching and have established rapid solidification processing as a viable commercial process.

Several techniques have been developed to produce rapidly solidified alloys in a variety of forms, but the most widely used and most practicle method for producing large amounts of alloy is inert gas atomization.[5] This process uses high velocity jets of an inert gas such as argon or helium that are directed onto a stream of molten metal. The metal stream is accelerated by the gas jets and broken up into small droplets that are typically less than 200μm in size. The small particle size increases the rate at which heat can be transferred from the particle to the atomization gas. The atomization process is carried out in a chamber, usually under an inert atmosphere in order to prevent oxidation of the particle surface. Gas

atomization is being used to produce rapidly solidified products in two forms. If the atomized droplets are allowed to fully solidify in flight, the rapidly solidified product is a fine powder, which can then be consolidated into a useful form. Alternately, in a process termed spray forming, the atomization and the consolidation processes are combined. In this method, a substrate is place in the path of the atomized droplets at some point before the droplets have completely solidified. Typically, the alloy is sprayed vertically downward in the enclosed atomization camber onto a stationary substrate. The droplets impact upon the substrate and solidify to form a built-up deposit of material.

In the case of gas atomization and the production of powder particles less that 200μm in size, the solidification rate of individual particles is determined by heat transfer across the particle/gas interface.[6] Cooling rates on the order 10^4 to 10^5°C/s have been estimated by measurements of secondary dendrite arm spacings and are typical for this process.[7,8,9] Decreasing particle size, which increases the surface to volume ratio of the particles, is the most practical way to increase solidification rate.[10] An increase in solidification rate can also be obtained by use of an atomization gas with a high thermal conductivity and heat capacity such as helium.[11] The primary disadvantage to the production of rapidly solidified powders is that the material must be further processed into a useful form by a consolidation step. The conventional means of consolidation is hot isostatic pressing or hot extrusion.[12] Since these consolidation processes take place at high temperatures and for an extended periods of time (>900°C for approximately 3h for hot isostatic pressing of ferrous alloys) changes to the rapidly solidified microstructure can occur.

The spray forming process combines atomization and consolidation in one step and eliminates the problem of microstructural changes that can take place when rapidly solidified powders are consolidated. A few closely related versions of

this process include Liquid Dynamic Compaction (LDC)[13] and the Osprey Process.[14] Following atomization, particles that are completely or partially in the liquid state impact and solidify onto a substrate that is placed in the flight path of the particles. Ideally, the particles should contain a enough liquid phase so that upon impact with previously deposited material the particles have sufficient fluidity to readily deform and spread to a thin disk shape and solidify before another droplet arrives at that location on the deposit surface. Alloy microsructure is more difficult to control with spray-forming than atomization. During spray-forming the microstructure of the deposit is much more sensitive to changes to processing parameters such as melt superheat, substrate location and atomization gas pressure than during the production of rapidly solidified alloy powder.

The temperature and degree of solidification of the atomized spray at the time of impact with the substrate is critical in determining the the microstructure of the deposit. After atomization, the fraction of solid phase in the atomized spray of particles increases in a manner that depends on supercooling effects, the solidification range of the alloy, and the rate of heat transfer from the droplets. Solidification behavior during gas atomization has been modeled for nickel-[15,16] and aluminum-base[17] alloys. Figure 2.1 shows the calculated droplet temperature and fraction of solid phase that forms in a nickel-base alloy after atomization as a function of flight distance.[16] Effects of recalecence have been neglected. If the substrate is placed close to the point of atomization a large amount of liquid phase is deposited resulting in build up of heat and a slowly cooled deposit. As the substrate position is lowered, particles are cooled to a greater extent before being deposited and, at impact, the particle temperature is lower and volume fraction solid is greater. The deposit remains at a lower temperature and acts as a more efficient heat sink so that particles are solidified at a higher rate upon impact. If the deposit is placed too far from the point of atomization, many of the atomized

particles will have solidified to a large extent before contact with the deposit. Particles that contain appreciable solid phase can not readily spread and fill in irregularities on the deposit surface. The result is a porous deposit with poor interparticle bonding. The substrate is usually placed in the atomization spray at a position that will maximize the particle cooling rate and minimize the deposit porosity.

2.1.2. Formation of Dispersoids

Several processing methods are used to produce alloys that contain a dispersion of fine particles. These include precipitation hardening, internal oxidation, mechanical alloying, and rapid solidification. Precipitation hardening is used mainly for aluminum alloys and some steels. It is limited to alloys that can be solutionized and is typically used only for low temperature strengthening because overaging can occur at elevated temperatures.[18] Internal oxidation of an alloy to form a homogeneous dispersion of oxide particles has been used successfully for cobalt[19] and nickel-base[20] alloys. This processing method is limited to systems that consist of a relatively noble base metal and a reactive alloying element present at low concentrations. The alloy, after being atomized to produce a powder, is ball milled to produce platelets that are approximately 30μm in thickness. The platelets are oxidized to form internal oxide particles of the reactive element and an external oxide film of the base metal. The base metal oxide is reduced by annealing the flakes in a hydrogen atmosphere before consolidation into a bulk form. Alloys produced by this method are costly and it is difficult to control particle size and obtain a uniform particle distribution.

Mechanical alloying is a successful commercial process that is used to produce iron and nickle base alloys that contain oxide particles.[21] Alloy powder and oxide powder are blended in a high energy ball mill, often with an organic liquid. The oxide particles become reduced in size and incorporated into the alloy

by a process of repeated fragmentation and cold welding of the alloy particles. After extensive milling (typically over 20hrs), the oxide eventually becomes uniformly distributed into the alloy at which point the particles are removed from the mill, dried and then consolidated. Some disadvantages to the mechanical alloying process include difficulty in obtaining the proper fracturing and welding action, low alloy yields, and contamination of the alloy due to wear of the milling ball and vessel materials.

Rapid solidification processing has been used to produce dispersions of particles in iron- [22], nickel- [18,23], titanium-[18,24,25], and aluminum-base[26] alloys. The processing of these alloys was similar in that precipitates were formed that are soluble in the liquid alloy but have limited solubility in the solid. Particles are formed by precipitation from the melt at some point during the solidification process or by solid-state precipitation from the supersaturated solid after solidification.

Factors such as the rate of heat extraction during solidification which influences liquid/solid interface morphology and the nucleation rate of the primary phase from the melt which influences solidification distances, determines the degree of solute segregation and the precipitate size obtained in the solid. At very rapid rates of solidification, high liquid/solid interfacial velocities can trap solutes and produce segregationless or massive solidification.[27] If cooling after solidification is sufficiently rapid, a supersaturated, single phase solid may be retained to room temperature that can be annealed to form precipitates in the same way as a precipitation hardenable alloy.[28] Cases where massive solidification have been observed are restricted to situations where the heat extraction and cooling rate is very large (> 10^6°C/s), such as in the formation of very small particles by gas atomization[29] and solidification involving rapid heat transfer to a substrate.[30,31]

Usually solute segregation takes place to some extent during rapid solidification. At lower rates of heat extraction and therefore lower liquid/solid interface velocities, solute diffuses ahead of the liquid/solid interface and become segregated in the liquid. The liquid/solid interface morphology can be cellular or dendritic and trap enriched pockets of liquid in intercellular or interdendritic regions.[32] Figure 2.2 shows qualitatively how the solidification morphology depends on temperature gradient and solidification velocity. The size, number and distribution of precipitates retained in the solid will be determined by the liquid/solid interface morphology and cell or dentrite arm spacing obtained during solidification. A cellular or dendritic interface morphology becomes finer at higher solidification rates, resulting in the formation of a large number of small liquid pockets from which precipitates form. Since a planar interface morphology does not entrap pockets of liquid, fine precipitates will not form if solute segregation occurs.

2.1.3. Processing of Alloys Containing an Oxide Dispersion

The processing method used to produce alloys containing a dispersion of fine particles that was discussed in the previous section was limited to the formation of particles that were completely soluble in the liquid alloy. Particles, such as many oxides, that are very stable in the solid alloy also have a low insolubility in liquid. A processing method to produce alloys containing these insoluble particles that is more direct than mechanical alloying and internal oxidation techniques is to disperse the oxide particles particles into the liquid alloy and retain the dispersion during solidification. Hasegawa and Takeshita[33] reported on a process where they sprayed Al_2O_3 and ZrO_2 particles into a liquid stream of an 18Cr-8Ni austenitic stainless steel alloy and obtained an oxide dispersion in the liquid. They successfully cast the alloy to obtain a dispersion of particles in the solid. Hasegawa and Osawa[34] used the same method to produce a

HASTELLOY X alloy (HASTELLOY is a regestered trademark of the Cabot Co., Kokomo, IN) alloy containing as dispersion of ZrO_2 particles. Details of the processing method were not published.

Dispersing oxide particles in a molten alloy is made dificult by surface energy effects and density differences between the oxide and metal. The characteristic high surface energies between oxides and liquid metals promote the agglomeration of oxide particles in the melt and the trapping of oxide particles at interfaces such as crucible walls and the melt surface.[35] Particle agglomeration is a result of the recession of metal and the formation of a vacuum meniscus at the piont of contract between two oxide particles.[36] High interfacial energies between oxide and liquid metal lead to the formation of a large meniscus and strong attractive forces between the oxide particles. Surface tension forces which lead to the formation of a vacuum meniscus can be illustrated by the sessile drop configuration as shown in figure 2.3. The degree of wetting is indicated by the angle of contact angle θ between the liquid/solid and liquid/gas interfaces. The degree of wetting is determined by the relative values of the three surface tensions shown in figure 2.3. For contact angles that are less than 90°, the liquid is considered to wet the substrate. Oxide particles that are not wet by an alloy tend to agglomerate into clusters.[37] System having an oxide/gas surface tension greater than the oxide/liquid surface tension form a contact angle of less than 90° and in these systems a meniscus between particles is not stable and agglomeration is not observed to take place.[38]

Buoyancy forces resulting from density differences between the metal and the oxide can cause floatation of oxide particles out of the melt. Floatation rates can be calculated by Stoke's Law which equates bouyancy and drag forces on a particle in a melt and gives the terminal rising velocity of the particle. Figure 2.4 shows the rising velocity of a sperical, nonporous alumina particle in stagnant

liquid iron as a function of particle diameter.[39] For oxide particles in a melt that are the size that would be used for processing a dispersion containing alloy(< 0.5 μm in diameter), the floatation velocity is insignificant compared convective currents in the melt. Floatation will only be important if particle agglomeration occurs and the effective particle size becomes large.[40]

If particles can be successfully dispersed in a melt, the question exist as to whether the dispersion can be retained during solidification. Rapid solidification processing would be an excellent means to solidify an alloy if an oxide dispersion can be obtained in the liquid. In conventional castings, oxide particles are observed to segregate to the lower central portion of an ingot during soilidification. The fast liquid/solid interfacial velocities that are obtained with rapid solidification processing can trap oxide and prevent segregation in the melt.[41] There is also the potential to form a very fine grained alloy if the oxide particles in the melt serve as heterogeneous nucleation sites for the solid phase.

2.1.4. Microstuctural Stability

A fine alloy grain size is retained at elevated temperatures by preventing grain boundary migration. Particles, pores, solute segregation, and free surfaces can inhibit grain boundary motion.[42] Zener was the first to show that particles dispersed in an alloy can slow down the progress of a migrating grain boundary in metals and that grain growth eventually ceases when the restraining force on grain boundaries due to particle pinning becomes equal to the driving force for grain growth.[43] He developed a simple model for the limiting grain size by equating these two forces, which yields the relationship,

$$d = \frac{4r}{3f} \qquad (1)$$

where d is the limiting grain size according to Zener, r is the mean particle radius and f is the particle volume fraction. Refinements to Zener's model by Gladman[44] and by Haroun and Budworth[45] take into account more realistic grain shapes than those used by Zener and predict grain sizes that are about an order of magnitude smaller than those predicted by Zener's model. Measured grain sizes have been observed to fall between the values predicted by the models. Both the theoretical treatments lead to the conclusion that the ultimate grain size is directly proportional to the term r/f. For a fixed volume fraction of second phase, the grain size is directly proportional to the particle size.

Ashby reviewed the possible interactions between a migrating grain boundary and a dispersion of particles.[46] Boundary migration is controlled by Zener-type pinning only if the particle size is stable and the particles are immobile. Dragging of particles by a migrating boundary has been documented by Ashby and Centamore[47] and mechanism maps have been constructed illustrating the rate controlling processes.[48] Particle dragging has been observed only when the particle volume fraction and radius were very small. As particles coarsen, their number decreases and they become less effective in pinning grain boundaries. Particle coarsening may occur homogeneously throughout the alloy in which case particle growth is controlled by lattice diffusion. Particle coarsening may also occur preferentially on alloy grain boundaries in which case particle growth is controlled by grain boundary diffusion.

In the case of a uniform dispersion, the lattice-diffusion controlled coarsening of particles is given by

$$r^{-3} - r_o^{-3} = \frac{8\,DC}{9\,RT}\,\sigma V_p^2\,t, \qquad (2)$$

where r_o is the initial particle radius, D and C are the diffusivity and concentration of the rate controlling species, R is the gas constant, T is the absolute temperature, σ is the particle/alloy interfacial energy, V_p is the molar volume of the particle and t is the time interval during which the coarsening is measured.[49] The chemical species with the smallest value of the product DC controls the rate of growth of the particles. A combination of equations (1) and (2) predicts a $t^{1/3}$ dependence of grain growth when boundary migration is controlled by a uniform dispersion of particles. At low temperatures particle coarsening may take place predominantly at alloy grain boundaries.[50] As long as the volume fraction of particles on the boundary is constant, the value of r/f in equation 1 increases to a point at which the grain boundary can break away. The boundary then migrates until repinned, followed by further coarsening and a repeating cycle.

2.2. Alloy Oxidation

2.2.1. Oxide Scale Formation

Iron-, nickel- and cobalt-base alloys used at elevated temperatures depend on the selective oxidation of certain elements in the alloy that are able to form external, slow-growing oxide scales and protect the base metal from oxidation.[51] Protective oxide scales are those that form quickly on the alloy, remain adherent to the alloy surface, and have low growth rates. The rate of thickening of compact oxide scales is determined by diffusion of reacting species through the scale layer and can be described by a parabolic rate law, i.e.,

$$\Delta x^2 = 2\,k_p\,t \qquad (3)$$

where Δx is the instantaneous scale thickness, t is the reaction time and k_p is the parabolic rate constant. The oxidation rate may be measured using a thermogravimertric apparatus (TGA) to determine the weight change of an alloy as a function of reacton time. This method is useful if an adherent, uniform scale forms on the specimen and the thickness of the scale can be directly related to a specimen weight gain. This assumes that volatilization of the reaction does not occur. Figure 2.5 shows order of magnitude parabolic rate constants for the oxides of Fe, Ni, Co, Cr, Si, and Al.[52] Iron, nickel and cobalt, which are elements commonly used as the basis for alloys, form oxides with the highest growth rates. Alloys using these elements as a base typically contain large concentrations of chromium, aluminum and sometimes silicon to permit to formation of an external layer of one of these slow growing oxides.

Figure 2.6 shows schematically three stages of oxidation typically observed for alloys that form a protective scale.[53] The first stage (I) is characterized by rapid oxidation of the alloy. After a period of time, the oxidation rate slows and eventually becomes nearly constant. During this stage (II) the scale morphology does not change and the alloy experiences steady-state oxidation. The oxidation rate during this period is given by the parabolic rate constant of the protective oxide. Eventually the scale formed in stage II may breakdown resulting in rapid oxidation of the alloy (stage III). The duration and oxidation rate of the three stages is variable and depends on alloy composition and oxidizing environment.

Stage I represents a transient period that occurs when the alloy is initially exposed to the oxidizing environment. During this period, oxides of all the reactive elements in the alloy form in an amount approximatelly proportional to the concentration of the elements in the alloy.[54] Oxide nuclei with high growth rates, such as iron, nickel, and cobalt oxides, grow rapidly over the nuclei of the slower

growing oxides, such as Cr_2O_3 and Al_2O_3. The rapid growth of the base metal oxides causes the relatively large weight gain that takes place during this period. Concurrent with the growth of the fast growing oxides, the slower growing, more stable oxides spread laterally over the alloy surface.[55] These oxides may link up and form a continuous layer, isolating the alloy from the fast growing oxide, or may remain isolated and be incorporated into the fast growing oxide as the alloy is consumed. The rapid establishment of a continuous layer of slow growing oxide is a requirement for oxidation resistant alloys.

Eventually, a steady-state period, stage II, is reached when the oxide morphology is essentially constant. During this stage the oxide growth rate is determined by transport of a reacting species through a single oxide layer. The oxidation reaction rate can be controlled by metal cation diffusion to the scale/gas interface or by oxygen anion diffusion to the scale/metal interfaced, depending on the defect nature of the oxide. Since the oxidation is controlled by solid-state diffusion through a thickening oxide layer, the oxidation kinetics during this period obey a parabolic rate law. An oxidation resistant alloy is designed to attain quickly the steady-state, stage II condition and to maintain this condition throughout the service life of the alloy.

Selective oxidation requires removal of one of the alloy components from the alloy, so the alloy becomes progressively depleted in this element. A point can be reached where a mechanical disruption of the scale, such as by spallation or abrasion, cannot be rehealed. The exposed base metal, being depleted of the protective oxide forming element, is unable to reform the scale characteristic of the steady state condition. At this point the third stage of oxidation occurs, the base metal oxides form resulting in an increase in the rate of oxidation.

Figure 2.7 shows schematically two scale morphologies that can form during the oxidation of a binary A-B alloy. The oxides of both elements are

thermodynamically stable with the oxide BO having the lower free energy of formation and the slower growth rate. Figure 2.7a illustrates the case where a continuous external layer of BO is unable to form. A relatively thick layer of AO forms on the alloy surface with an internally oxidized region penetrating into the alloy that consists of particles of BO in a matrix of essentially pure A. The oxygen activity at the AO/metal interface is set by the equilibrium between the oxide AO and the element A. The oxygen activity at the interface is greater than that required for the oxidation of B to BO, so oxygen diffusion into the alloy results in the internal formation of BO particles. Although BO may be a slow growing oxide, its formation as isolated particles makes it ineffective as a diffusion barrier and therefore ineffective in retarding oxidation. The A-B alloy in figure 2.7b has a larger concentration of B and this element is supplied to the alloy surface in suffficient quantity to form a continous layer of the external oxide BO.

Wagner described the factors that determine whether or not selective oxidation of an alloying element will lead to the formation of an external scale.[56] According to Wagner, a critical volume fraction of the oxide BO must from at the surface region of the alloy in order to for BO to form a continuous oxide. The formation of an external scale is promoted by the use of high concentrations of the selectively oxidized element, by a high diffusion rate of the selectively oxidized element in the alloy, and low a diffusion rate of oxygen in the alloy.

2.2.2. Fe-Al Alloys

The oxidation behavior of Fe-Cr-Al alloys is most easily understood by first discussing the behavior of binary Fe-Al alloys. Although the significant improvement in oxidation resistance obtained by alloying iron with aluminum is well documented[57,58,59], most of the work has concentrated on investigating oxidation at temperature above 800°C. The first systematic study at lower temperatures was carried out by Saeguse and Lee.[60] They oxidized Fe-1Al and

Fe-5Al alloys at temperatures between 500 and 1000°C and found that the oxidation behavior depended on both aluminum concentration and the temperature of oxidation. Figure 2.8 shows their parabolic rate constants plotted as a function of the reciprocal the of oxidation temperature. For comparison they included the parabolic rate constants for the oxidation of pure iron. At all temperatures, the oxidation rate decreaced with an increase in aluminum concentration in the alloy. The variation in parabolic rate constant with temperature for a given alloy could be related to the oxide scale that formed on the alloy. For both Fe-Al alloys, the scale that formed at oxidation temperatures of 500, 600, and 700°C was reported to be essentially iron oxide with a thin aluminum oxide layer at the scale/metal interface. It was suggested that the aluminum oxide layer acted as a diffusion barrier for iron ions and lowered the rate of oxidation. The activation energy of 27 kcal/mole for the oxidation process calculated from their work is in good agreement with the value of 27.6 kcal/mole for diffusion of iron in Al_2O_3. The oxide phases that formed were not identified. The break in the in the curve for the Fe-1Al and Fe-5Al alloys at 700°C was due to the formation of a layer of hercynite, $FeAl_3O_4$, along the scale/metal interface which also was supposed to act as a diffusion barrier to the transport of iron cations. At 1000°C, the oxidation rate of the alloy containing 1wt%Al increased sharply while the oxidation rate of the alloy containing 5wt%Al decreased. The increase in oxidation rate of the alloy containing 1wt%Al was attributed to a rapidly growing Fe_2O_3 oxide scale. The Fe-5Al alloy formed a thin external Al_2O_3 oxide layer which greatly lowered the rate of oxidation.

Boggs studied the oxidation of binary Fe-Al alloys that ranged in aluminum content from 0.003 to 8wt% at temperatures between 450 and 900°C[61]. The kinetic results were in general agreement with Saeguse and Lee's work, but Boggs more clearly identified oxide the phases that formed on the alloys. Figure 2.9 shows the

effect of aluminum concentration on the oxidation kinetics of Fe-Al alloys at 500°C. The oxide scale formed on alloys containing less than 0.092wt%Al consisted of two layers, an inner layer of magnitite, Fe_3O_4, and an outer layer of hemitite, α–Fe_2O_3. It was suggested that the increase in oxidation rate with aluminum concentration up to 0.092wt% was due to a doping effect; i.e., Al^{+++} substitutes for Fe^{++} in Fe_3O_4 causing an increase in the cation vacancy concentration and the diffusion rate iron ions through the magnetite layer. Alloys containing between 0.5 and 8.03wt%Al formed three oxide layers, an outer layer of α–Fe_2O_3, a middle layer of Fe_3O_4 and a layer of hercynite, $FeAl_3O_4$, at the metal surface. Boggs came to the same conclusion as Saeguse and Lee, that the formation of the hercynite layer decreaced diffusion of iron ions through the oxide scale and resulted in the decrease in oxidation rate in alloys containing more than 0.092wt%Al.

Figure 2.10 shows the effect of temperature on the oxidation kinetics of an Fe-4.94Al alloy. The oxidation rate increased as the oxidation temperature was raised from 450 to about 570°C. In this temperature range, a three layer scale formed consisting of $FeAl_3O_4$ along the alloy surface, a middle layer of Fe_3O_4, and an outter layer of α–Fe_2O_3. Boggs suggested that the increase in oxidation rate in this temperature range was due to the temperature dependent diffusion of iron through the hercynite layer. Above 570°C, the oxidation rate decreased sharply and an aluminum-rich oxide layer formed along the alloy surface repacing the $FeAl_2O_4$ layer. At 600°C, only two oxide layers formed, an outer layer of α–Fe_2O_3 and a mixed inner layer of consisting of $FeAl_2O_4$ and γ–Al_2O_3. Above 600°C two phases of aluminum oxide were formed, the cubic γ–Al_2O_3 and the hexagonal α–Al_2O_3. The metastable γ–Al_2O_3 apparently formed initially in epitaxial relationship with the alloy substrate and partially recrystallized to α–Al_2O_3. Above 800°C the oxide scale consisted almost entirely of a slow-growing aluminum oxide, although some large iron rich oxide nodules formed on the alloy surface. The nodules were

randomly located on the alloy surface and consisted of layered iron oxides similar to the scales formed at the lower temperatures. The decrease in oxidation rate and the formation of an external Al_2O_3 scale at high temperatures was attributed to increased mobility of aluminum atoms in the alloy; i.e., at higher temperatures, aluminum was supplied to the alloy surface in a sufficient amount to form a continuous, external Al_2O_3 scale.

2.2.3. Fe-Cr-Al Alloys

Investigations of the oxidation behavior Fe-Cr-Al alloys has concentrated mostly on alloys containing high concentrations of chromium and aluminum, such as iron-base superalloys or Kanthal alloys, at temperature above 900°C where these alloys readily form an external α–Al_2O_3 scale.[62] Only a few studies have been carried out on alloys that contain low concentrations of chromium and aluminum and form oxide scales that are marginally protective.[63] Tomaszewicz and Wallwork examined the oxidation behavior of a series of low alloy content Fe-Cr-Al alloys at 800°C. They classified the oxidation behavior of the alloys into four categories according to the type of oxide scale that formed. Figure 2.11 shows an oxide map they constructed that indicates composition of the oxide scale that formed as a function of alloy composition. Alloys with compositions within region I contained less than 2.4wt% aluminum and less than 13wt% chromium. These alloys formed a complex oxide consisting of an outer layer of Fe_2O_3, an inner layer of $Fe(Cr, Al)_2O_4$, and precipitates of Al_2O_3 in the alloy near the scale/metal interface. The inner spinel layer had a higher concentration of aluminum at the spinel/metal interface than at the spinel/hemitite interface. Alloys in region II formed an external scale of Cr_2O_3 with internal precipitates of Al_2O_3.

Alloys with compositions within region III formed external oxide scales of Al_2O_3 in addition to iron-rich oxide nodules. The size and number of oxide nodules varied with aluminum and chromium concentration. Close to the boundary

between regions I and III lateral growth of the oxide nodules was extensive. Many of the nodules impinged upon each other and eventually covered most of the alloy surface. Alloys that contained higher concentrations of aluminum and chromium formed smaller nodules that are fewer in number. The morphology of the nodules that formed on these ternary Fe-Cr-Al alloys were similar to those that formed on the binary Fe-Al alloys as reported by Boggs. The nodules consisted of essentially two oxide layers, an outer layer of α–Fe_2O_3 and an inner spinel layer. In the case of the binary alloy that Boggs studied, the spinel layer was $FeAl_2O_4$, for the ternary alloy in Bogg's work the spinel phase was identified as $Fe(Cr,Al)_2O_4$. The spinel became richer in aluminum as the alloy aluminum concentration increased. For alloys with high concentrations of aluminum within region III, an aluminum-rich oxide layer formed at the base of the nodules and halted nodule growth into the alloy. Alloys having composition within region IV contained sufficiently high concentrations of chromium and aluminum to completely prevent the formation of any iron oxides and the scale consisted entirely of an external layer of aluminum oxide. Whether the external aluminum oxide that formed at the higher alloy content was γ–Al_2O_3 or α–Al_2O_3 was not reported.

Figure 2.12 shows the effect of alloy content on the extent of oxidation for alloys with compositions along the Fe-Al binary in figure 2.11. The weight gain per unit surface area is plotted as a function of aluminum concentration after oxidation at 800°C for 20 hours. As the aluminum concentration is increased above 2 wt% aluminum, an external later of Al_2O_3 forms in some areas on the alloy surface and the oxidation rate drops off. At progressively higher concentrations of aluminum, the amount of surface area covered by iron oxide nodules decreases until at 7 wt% aluminum only Al_2O_3 forms and the alloy gains very little weight.

According to Tomaszewicz and Wallwork's results, the concentration of aluminum required to prevent the formation of iron oxides on Fe-Cr-Al alloys is

dependent on the chromium concentration in the alloy. The boundary between regions I and IV indicate the compositions. Chromium has the effect of decreasing the aluminum concentration that is required to form an external, continuous aluminum oxide scale. As shown in figures 2.11 and 2.12, a binary Fe-Al alloy must contain at least 7.5wt% aluminum in order to prevent the formation of iron oxide nodules, but only 3wt% aluminum is required to give the same oxidation resistance if the alloy contains 5wt% chromium. The beneficial effect that chromium has on the oxidation behavior of Fe-Cr-Al alloys has been explained by Wagner.[64] According to Wagner's model, the addition of a third element to an Fe-Al alloy that has an affinity for oxygen between that of iron and aluminum lowers the concentration aluminum required to form an external aluminum oxide scale and prevent the formation of iron oxides. During the initial stages of oxidation of Fe-Cr-Al alloys the oxides of aluminum, chromium and iron form on the alloy surface. Chromium, being more noble than aluminum and more reactive than iron, acts as a secondary getter for oxygen near the alloy surface and limits oxygen diffusion into the alloy. This inhibits the internal formation of Al_2O_3 particles and allows time for aluminum diffusion to the alloy surface region where it is able to react with chromium oxide and oxygen and form aluminum oxide in sufficient volume to produce a continuous Al_2O_3 layer.

2.2.4. Grain Size Effect on Alloy Oxidation

Whether a selectively oxidized element in an alloy forms an external oxide scale or internal oxide particles depends on the rate at which oxygen penetrates the alloy relative to the rate at which the selectively oxidized element can be supplied to the alloy surface. Increasing the diffusivity of the reactive element in an alloy promotes transport to the alloy surface and helps insure formation of an external scale. Diffusion through an alloy takes place through the crystal lattice and along line and planar defects such as dislocations, grain boundaries and

phase boundaries. The effective or apparent alloy diffusivity is dependent on the magnitude of the diffusivity along each path and the volume fraction of the path in the solid. Figure 2.13 shows order of magnitude values for diffusion on a free surface, along a grain boundary, and through the crystal lattice[65]. Grain boundary diffusion can be several orders of magnitude greater than lattice diffusion, especially at temperatures that are less than half the alloy melting point. The activation energy for diffusion along grain boundaries is roughly 0.4-0.6 times that for diffusion through the lattice.[66] The importance of grain boundary diffusion has been recognized in phenomena such as Coble creep, sintering and cellular precipitation. Balluffi[67], Peterson[68] and Gupta[69] have reviewed the subject of grain boundary diffusion and Martin and Perraillon[70] have compiled grain boundary diffusion data. The difference in the diffusivity and activation energy for diffusion along different paths is attributed to the varying degrees of constraint placed upon atomic mobility.[71] A grain boundary can be thought of as a more open structure than the perfect crystal lattice, which means that it offers less resistance to atomic motion.

The contribution of grain boundary and lattice diffusion to the effective or observed alloy diffusivity can be expressed by the Hart equation[72]; i.e.,

$$D_{eff} = f D_{gb} + (1 - f) D_l \qquad (4)$$

where D_{eff} , D_{gb} and D_l are the effective, grain boundary and lattice diffusion coefficients respectively and f is the volume fraction of the alloy that consists of grain boundary. Grain boundary volume is defined as the product of grain boundary area and grain boundary thickness. For metals, grain boundary thickness is taken as the region of poor atomic fit, which is usually taken to be about 5Å.[73]

Giggens and Pettit were among the first to report the effect of inhanced diffusion along alloy grain boundaries on the formation of oxide scales.[74] They oxidized conventionally processed Ni-Cr alloys that contained 5 to 30 weight percent Cr at temperatures between 800 and 1200°C. The alloys contained insufficient chromium to form an external scale of Cr_2O_3 and instead formed a thick scale of NiO and internal precipitates of Cr_2O_3. They found that the nickel oxide scale that formed at regions where alloy grain boundaries intersected the alloy surface was much thinner than in areas over the grain interiors and that less of the alloy was consumed in this region. Over the alloy grain boundaries an external scale of Cr_2O_3 formed which grew laterally, protecting the alloy from oxidation in this region. They reasoned that during the initial period of oxidation, chromium depleation was less in the grain boundary regions and a sufficient amount of chromium was oxidized to form an external Cr_2O_3 scale. Chromium was belived to be supplied preferentially to this region by short-circuit diffusion along grain boundaries from the alloy interior.

After their initial findings, Giggens and Pettit carried out careful experiments to determine if the overall oxidation resistance of Ni-Cr alloys could be improved by a reduction in alloy grain size.[75] They compared the oxidation resistance of a Ni-10Cr alloy with a grain size between 40μm and 140μm to that of an alloy of the same composition that had a grain size of 10μm. The fine-grained alloy was processed by first grit blasting the surface of the conventionally processed alloy to obtain a cold worked surface layer and then annealing the alloy to recrystallize the deformed region. The recystallized grains had a diameter of about 10μm and the fine grained region extended only about 15μm into the alloy. When oxidized at 900°C, the fine-grained alloy formed a scale that was composed entirely of a thin, external layer of Cr_2O_3. The large grained alloy formed an external NiO scale and internal particles of Cr_2O_3. The reduction in grain size decreased the parabolic

rate constant at 900°C by more than three orders of magnitude and gave the fine grained alloy with 10wt%Cr the same oxidation resistance as a large grained alloy containing 30wt%Cr. The fine grain size of the alloy was believed to result in an increase in the selective oxidation of chromium at the alloy surface and the formation of a large enough volume fraction of Cr_2O_3 to form a continuous external chromium oxide layer.

Chattopadhyay and Wood studied the early stages of oxidation of Fe-Cr and Fe-Al alloys that contained 5, 10, 15, and 30%Cr, at 600°C.[76] They found that for dilute Fe-Cr (<10wt%Cr) and very dilute Ni-Cr alloys (<5wt%Al), a thicker oxide formed over grain and subgrain boundaries than over grain interiors on the alloy surface. This was presumably due to the grain boundaries acting as efficient cation vacancy sinks or to the existence of local diffusional paths in the oxide above the grain boundaries and subgrain boundaries. At higher chromium concentrations, a thin oxide healing layer formed over alloy grain boundaries for both the Fe-Cr and Ni-Cr alloys. Although not identified, the thin oxide layer was assumed to be Cr_2O_3.

Hossain studied the oxidation of a series of binary Fe-10Cr alloys with grain sizes of 3, 60, 120 and 400μm.[77] The alloys were processed by first cold rolling to a 94% reduction in cross-sectional area followed by annealing at specific temperatures between 700 and 900°C in order to obtain a variety of grain sizes. Alloys having a grain size greater than 60μm formed a nonprotective scale consisting of an external α–Fe_2O_3 layer over a thinner layer of $(Fe, Cr)_3O_4$. The alloy having a 3μm grain size oxidized at a much lower rate than the larger grained alloys, as shown in figure 2.14, and formed a scale that was richer in chromium. The chromium-rich oxide phase that formed on the fine grained alloy was not identified.

2.2.5. Oxidation of Rapidly Solidified Alloys

Rapid solidification processing has been successfully used to produce fine-grained alloys that show better resistance to oxidation than conventionally processed, large-grained alloys. Wade et al. used a laser glazing technique to produce fine grained regions on the surface of 304 and 430 stainless steels.[78] The alloys were cyclicly oxidized at 900 and 1000°C to determine if the treated and untreated surface areas oxidized differentlly. The fine grained, laser glazed regions formed a slow-growing Cr_2O_3 scale with SiO_2 intrusions that had grown from the scale into the alloy along grain boundaries. Areas on the alloy surface that were not laser glazed and had a large grain size formed a non-protective, stratified scale consisting of αFe_2O_3 and $(Fe, Cr)_3O_4$.

Yurek et al.[79,80] studied the oxidation resistance of a rapidly solidified AISI 303 stainless steel that was produced by a centrifugal atomization process.[81] The alloy had a 5.6μm grain size that was stabilized at elevated temperatures by a dispersion of MnS particles. The rapidly solidified alloy had better resistance to isothermal oxidation at temperatures between 800 and 1100°C and resisted scale spallation during cyclic oxidation better than a conventionally processed alloy of similar composition. The improvement in oxidation resistance was attributed mainly to enhanced transport of chromium in the alloy resulting from the fine grain size. Silica intrusions, similar to those observed by Wade et al., extended from the underside of the chromia scale into the alloy along grain boundaries. The improvement in cyclic oxidation resistance was attributed to the SiO_2 intrusuions that supposedly anchored the oxide to the alloy surface.

Guruswamy et al. investigated the formation of Al_2O_3 scales on rapidly solidified ferritc steels.[82] A series of Fe-Si-Al alloys that contained between 0 and 5wt% silicon and between 0 and 8wt% aluminum were oxidized at temperatures between 900 and 1100°C. The alloys were solidified rapidly by the centrifugal

atomization process and consolidated by hot isostatic pressing or hot extrusion. After consolidation, the alloys had a grain size less than 1μm. The fine grain size was stabilized at oxidation temperatures up to 1000°C by a dispersion of fine TiB_2 particles. Their oxidation study showed that at 900 and 1000°C the rapidly solidified alloy quickly formed an adherent Al_2O_3 scale that had a very slow growth rate. The convoluted, detached Al_2O_3 scale that typically forms on conventionally processed Fe-Si-Al alloys at these temperatures was not observed on the rapidly solidified alloys. At 1100°C grain growth occurred in the alloys that resulted in loss of adherence of the alumina scale and the formation of rapidly growing iron oxides. The rapid formation of Al_2O_3 on the fine-grained alloy was attributed to a high density of Al_2O_3 nucleation sites at alloy grain boundaries and the rapid diffusion of aluminum along grain boundaries in the alloy. The improvement in oxide scale adhesion at 900 and 1000°C was explained as being likely due to oxide intrusions growing into the alloy along grain boundaries that mechanically keyed the scale to the alloy, although no intrusions were observed.

Noble oxidized a series of conventionally processed and rapidly solidified Fe-Al alloy at temperatures between 800 and 1000°C.[83] The rapidly solidified alloys were produced with a twin-roller quenching technique and consolidated by hot extrusion. The alloys contained a fine dispersion of MnS particles in the alloy that effectively stabilized a grain size that was between 7 and 10 μm. A fine-grained, Fe-6Al alloy formed a protective Al_2O_3 scale when oxidized at 800°C compared to a conventional Fe-6Al alloy that formed iron-rich nodules over 50% of the surface of the alloy. At 900 and 1000°C, both the rapidly solidified and conventionally processed alloys formed non-adherent Al_2O_3 scales with iron-rich nodules located randomly over the alloy surface. It was suggested that the large amount of grain boundary area and the fine dispersion of MnS particles increased

the nucleation of Al_2O_3 on the alloy surface and promoted the rapid transport of Al to the alloy surface.

Barmak[84] produced a series of rapidly solidified Fe-18Cr-8Ni alloys that contained 0, 0.6, and 1.5wt%Si. The alloys were processed by an atomization/twin roller quenching technique that produced alloy flakes that were approximately 15μm in thickness and 150μm in diameter. After consolidation of the flakes and thermo-mechanical processing, the alloy had a grain size of about 10μm. The rapidly solidified alloy that contained 1.5wt% Si showed improved resistance to cyclic oxidation at 900°C compared to a conventionally processed alloy of similar composition. The improvement in oxidation resistance was attributed to the formation of a continuous amorphous silicon oxide layer along the alloy surface that was covered by an external chromium oxide layer. A conventionally processed, large-grained alloy that contained the same concentration of silicon did not form a silica layer and suffered severe scale spallation during thermal cycling. The rapidly solidified alloy that contained 0.6wt% Si did not form a continuous silica layer and demonstrated no better resistance to scale spallation than a conventionally processed alloy of the same composition. The fine-grained, rapidly solidified Fe-18Cr-8Ni alloy that contained no silicon, also showed no improvement in oxidation resistance compared to a conventionally processed alloy of similar composition.

3. OUTLINE OF WORK

This research program consists of two sections; alloy processing and alloy oxidation. The goals of the processing section were:

i) Design and development of a small-scale inert gas atomization system.

ii) Production of fine-grained (grain size <10μm) Fe-Cr-Al alloys containing a dispersion of TiB_2 and α- Al_2O_3 particles.

iii) Production of the dispersion containing alloys by two rapid solidification processing techniques, spray-forming and powder processing.

The inert gas atomization system was constructed to produce the rapidly solidified alloys for this program. The apparatus was designed to simplify operation and cleaning to allow for the efficient production of contamination free, rapidly solidified alloy products.

Initially, the primary objective was to produce Fe-Cr-Al alloys containing a dispersion of fine α-Al_2O_3 particles. Due to the difficulties in processing an a-Al_2O_3 containing alloy and the possibility of not obtaining the desired dispersion of alumina particles, it was decided to process, in parallel, alloys containing a TiB_2 particle dispersion. From an experimental point of view, the alloy containing an alumina dispersion is desirable because the alloy chemically is simpler.

Industrially, the bulk of the rapidly solidified alloys that are produced, are produced by powder processing or spray-forming techniques. It was felt that the alloy for this program should be produced by these two methods so that the processing and oxidation results could be carried over to an industrial scale.

The goals of the of the alloy oxidation section were:

i) Determine the oxidation behavior of conventionally processed Fe-4Cr-4Al and Fe-2.5Cr-2.5Al alloys at temperatures between 400 and 1000°C.

ii) Oxidize rapidly solidified alloys based on Fe-4Cr-4Al and Fe-2.5Cr-2.5Al

compositions at selected temperatures and determine the effect of microstructure on the resistance to oxidation.

The oxidation of the two conventionally processed alloys was intended to establish a base against which the oxidation of the rapidly solidified alloys could be compared. The oxidation of Fe-Cr-Al alloys at temperatures below 800°C has not been reported previously. Initially, the Fe-4Cr-4Al alloy composition was chosen to produce a series of alloys on the basis of Walwork's results for the oxidation of Fe-Cr-Al alloys at 800°C. The Fe-4Cr-4Al alloy composition just barely lies in the region of α-Al_2O_3 scale formation (Figure 2.11) and it is expected that at lower temperatures iron oxides would form on this alloy. The conventionally processed Fe-4Cr-4Al alloy showed better resistance to oxidation than anticipated originally so further work was concentrated on conventionally processed and rapidly solidified alloys based on the Fe-2.5Cr-2.5Al alloy.

4. EXPERIMENTAL PROCEDURE

This section is divided into four sections: (1) the design and operation of an inert gas atomization system, (2) the processing of rapidly solidified and conventionally cast alloys, (3) the high temperature oxidation of alloys, and (4) the characterization of alloy microstructures and oxide scales.

4.1. Atomization System

4.1.1. System Design

Figure 4.1 shows a photograph and schematic diagram of the atomization system that was constructed to produce the rapidly solidified alloys. The system was designed to produce both rapidly solidified alloy powders and spray-formed deposits. The chamber consists of a 0.51m (20in) diameter ISO (International Standardization Organization) vacuum vessel with vacuum feedthroughs installed for induction power supply, thermocouple, stopper rod, atomization gas supply, cooling gas supply, and á connection to a mechanical vacuum pump. An induction coil/crucible assembly, where the alloy was melted and atomized, was located in the upper portion of the chamber. Atomization was carried out using an ultrasonic gas atomization nozzle (USGA) that was located below the crucible. This design of atomization nozzle is capable of delivering pulsations of gas at ultrasonic frequencies and at velocities in exess of Mach 2.[85] An access port for loading the crucible and a site port to enable viewing of the atomization process were installed in the front of the chamber. To prevent overpressurization of the chamber in the event that a high pressure gas line should fail, or if cooling water should come into contact with liquid metal inside the vessel, a spring loaded pressure relief valve was installed into the chamber cover plate that vented the camber at a gage pressure of 55kPa (8psi).

For the production of spray-formed deposits, a 6.4mm (0.25in) steel substrate was placed below the induction coil/crucible assembly to collect the

spray of atomized particles. If alloy powder was produced, the substrate was removed and the atomized particles were allowed to solidify in flight. The powder particles were carried in suspension by the atomization gas out of the bottom of the chamber and through a 50.8mm (2in) diameter transfer pipe to a cyclone. The powder was separated from the atomization gas by the cyclone and dropped into a collection vessel.

Figure 4.2 is a schematic diagram of the induction coil/crucible assembly. The assembly was mounted on a stainless steel stage that was supported by brackets from the chamber walls. A crucible contained the moten metal prior to atomization. The bottom of the crucible was fitted with a melt pour tube which was inserted into the atomization nozzle. The crucible was supported by a 3mm thick flange that prevented direct contact betwen the crucible and atomization nozzle. The atomization nozzle was cooled during heating of the alloy by flowing argon gas through a copper cooling line that was brazed to the nozzle base. Alloys were melted by induction heating using a 10kHz, 20kW induction power supply. If the mass of the alloy charge to be atomized was greater than about 0.8g (1.76lb), a fibrous alumina insulating material (Zircar Products, Inc., Florida, NY) that was preformed into the shape of a cylinder was placed between the crucible and the induction coils. In this case, the induction field coupled directly with the alloy charge for heating. Charges that were less than about 0.8kg (1.76lb) did not couple efficiently with the induction field and a 5mm (0.20in) thick graphite cylinder had to be installed between the crucible and insulating material to act as a susceptor in order to heat the crucible. A type B thermocouple (Pt-30%Rh vs. Pt-6%Rh) sheathed in an alumina protection tube was connected to a digital thermometer to monitor melt temperature. The accuracy of the thermocouple/thermometer was checked by measuring the melting point of pure iron and was found to be accurate within 10°C. The thermocouple was inserted

into the melt to a depth of at least 51mm (2in). A 9.53mm (0.375in) diameter alumina rod was used as a stopper to prevent the flow of liquid metal into the pour tube prior to atomization. The stopper rod was connected to a stainless steel rod that passed through a linear-motion vacuum feedthrough in the chamber cover plate and could be raised from outside the chamber to start the flow of metal from the crucible.

Atomization gas was supplied to the USGA nozzle by a battery of eight compressed gas cylinders with an a total internal volume of $0.39m^3$ ($13.84 ft^3$). Eight gas cylinders were used in order to have a large enough gas reservoir to lessen pressure loss during atomization. Gas flow was initiated by opening a solenoid valve located at the inlet to the atomization nozzle, and gas delivery pressure was controlled by a high gas flow rate pressure regulator (Tescom Corp., Elk River, MN, model 44-1316-2081). The atomization gas pressure was measured by a pressure transducer and displayed on a digital pressure meter.

4.1.2. Pour Tube Design

The design and operation of the melt pour tube was found to be the most critical factor in the operation of the gas atomization system. The pour tube served three functions; i.e., in conjunction with the stopper rod it acts as a valve to start the flow of metal and begin the atomization process, it delivers liquid metal from the crucible to the atomization gas jets and, with the USGA nozzle, it deflects the atomization gas jets to control gas pressure at the pour tube opening. Figure 4.3 shows a schematic diagram of the two pour tube designs that were used for alloy atomization. The designs shown in Figures 4.3a and 4.3b are designated as noninsulating and insulating type pour tubes. The noninsulating type consists of three parts, a boron nitride insert that fits into a hole in the bottom of the crucible, a steel sheath that mates to the BN insert and crucible bottom, and an alumina tube that is inserted inside the steel sheath. With the exception of the BN insert, this

design is essentially the same as that has been used by the research group of Professor N.J. Grant at MIT. The insulating type pour tube was developed during the course of this work and was found to give more consistent results than the noninsulating type. This design consists of two parts; i.e., a BN insert that extends the full length of the pour tube, and a steel sheath with a wall thickness reduced to 0.25mm (0.01in).

In both pour tube designs, an alumina stopper rod was fitted into a 1cm (0.39in) deep recess that was drilled into the BN insert and prevented liquid alloy from entering the pour tube until the rod was raised. The only problem encountered with this configuration was occasional binding of the stopper rod in the BN insert as the charge was heated. This was caused by the greater thermal expansion of alumina compared to boron nitride ($\alpha_{Al_2O_3} = 10^4 \alpha_{BN}$), where α is the coeffiicient of thermal expansion) and was avoided by machining a 0.05mm (0.02in) clearance between the stopper rod and the insert. The molten alloys that have been melted until the present time did not appear to wet alumina or boron nitride, and thus surface tension forces effectively prevented the liquid alloy from entering the gap before the stopper rod was raised.

During atomization, the pour tube was heated by the passage of molten metal through it, and it was cooled by direct contact with the atomization nozzle. Typically, alloys were heated to 300°C above their liquidus temperature in order to adequately heat the pour tube and keep the pour tube temperature above the freezing range of the alloy. The insulating type pour tube was designed to replace the noninsulating type and better insulate the melt from the atomization nozzle, and to retain melt superheat. The difference in the design of this pour tube is that the BN insert was extended from the crucible, were it was in contact with the melt, along the entire length of the pour tube. Also, the outer diameter of the BN insert was reduced in the region where it was in close contact with the atomization

nozzle. This was done to form an air gap that insulates the heated BN tube and from the cooled nozzle during atomization.

Boron nitride has several characteristics that make it an ideal material for the pour tube. Because of a very low thermal expansion coefficient, BN has excellent resistance to thermal shock, which is important when the stopper rod is raised and metal first enters the tube. Boron nitride also has a high thermal conductivity. With the nozzle design shown in figure 4.3b heat is transferred readily from the melt through the BN and preheats the pour tube prior to pouring. Boron nitride resists attack by most iron base alloys and it is easily machined into complex shapes. The primary disadvantage, is the low tensile and bending strengths of BN. This made necessary the use of the steel sheath shown in figure 4.3b that strengthened the pour tube for easy insertion into the atomization nozzle.

The extension of the gas jets of the USGA nozzle form an inverted cone with an included angle of 45°. Under certain conditions during atomization, a portion of the atomization gas can be deflected upward causing a back pressure at the pour tube opening that can prevent the flow of metal out of the pour tube and even cause a reverse flow and eject metal from the top of the crucible. To prevent a back pressure at the pour tube opening, the pour tube was positioned carefully with respect to the atomization nozzle to ensure deflection of the gas jets downward. This not only eliminated a back pressure at the pour tube opening, but yielded aspiration of the melt from the crucible. Figure 4.4 is a schematic diagram illustrating qualitatively the gas flows from a USGA nozzle for the pressurization and aspiration conditions. In figure 4.4a, a short pour tube is installed in the atomization nozzle that does not interfere with the gas jets and a portion of the gas is deflected upward through the pour tube opening. In figure 4.4b, a longer pour tube is installed that deflects the gas jets downward slightly and draws gas from the crucible through the pour tube.

Since the pressurization condition must be avoided in order to drain the crucible during atomization, the pour tube opening pressure was measured as a function of pour tube length for atomization pressures of 0.69, 1.38, 4.14 and 5.52 MPa (100, 200, 600, and 800psi). The pour tube reference position is shown in Figure 4.5. The zero point is the position where the pour tube contacts the extension of the jet orifice. This position was obtained by inserting a drill bit into the atomization jet orifice and lowering a pour tube into the atomization nozzle until contact was made between the pour tube and drill bit. Pour tube pressure was measured by attaching a Bourdon tube pressure gauge to a tube that had the same dimensions of the pour tube. The tube height was adjusted by using shims. The results are shown in Figure 4.6. Negative pressure values indicate a vacuum and positive values indicate a pressure. At the higher atomization pressures the pour tube pressure is very sensitive to small changes in pour tube length. Variations in length of fractions of a mm can generate pressures that easily overcome the metallostatic head in the crucible. The large readings of both vacuum and back pressure at the high atomization pressures is due to the increased velocity of the gas jets. At atomization pressures of 0.69 and 1.38 MPa (100 and 200psi), a back pressure does not develop at the pour tube opening regardless of pour tube length. In practice, the pour tube is lengthened only far enough to produce a slight vacuum at the pour tube opening. If the pour tube is lengthened too far into the jet stream, cooling by the gas jets will result in solidification of metal in the pour tube and closing off of the pour tube opening.

An important function of the the pour tube is to deflect the atomization gas jets, and thus, it is important that the shape of the pour tube tip does not change during the atomization process. With the noninsulating type pour tube, the outer edge on which the gas jets impacts is plain carbon steel as shown in figure 4.5a. It was found that during atomization, the pour tube edge was melted by direct contact

with the molten alloy, which changed the gas jet deflection angle. The pour tube became effectively shorter causing the pressure at the pour tube opening to increase. This resulted either in a decrease in the metal flow rate or a comptete halt to the flow of metal. The BN edge of the insulating type pour tube was found to resist erosion by the atomization gas jets and be stable in contact with the liquid alloy, thereby avoiding a change in the angle of deflection of the gas jets during an atomization run.

4.1.3 Operating Procedure

The pour tube components were prepared by machining a 15.8mm (0.625in) diameter BN (Standard Oil Engineered Materials, Niagra Falls, NY) rod to form the insert and a 25.4mm (1in) diameter plain carbon steel bar to form the sheath. A 15.8mm (0.625in) diameter hole was drilled using a diamond core drill into the bottom of the alumina crucible to accept the insert. The pour tube components and crucible were cemented together and cured according to specifications of the manufacturer (Aremco Products, Inc., Ossing, NY). After curing, the crucible was placed inside the induction coil and the pour tube was inserted into the atomization nozzle. The pour tube pressure was checked by fitting a pressure gauge to the BN insert inside the crucible and allowing the atomization gas to flow through the nozzle at the pressure to be used for atomization. The pour tube was initially machined slightly longer than necessary and was reduced in length until the desired pour tube pressure was obtained. The pour tube length was adjusted to obtain a vacuum of approximately 13.8kPa (2 psi) at the pour tube opening. Once the crucible was in place, the chamber was sealed with the exception of the access port. The stopper rod was inserted into the recess in the BN insert and connected to the stainless steel vacuum feedthrough rod. The thermocouple and protection tube were lowered into the crucible to a position a few millimeters off the crucible bottom. The charge was then placed into the crucible, fitted around the stopper rod

and thermocouple, and the access port closed up. The atomization system was evaluated using a mechanical vacuum pump to a pressure of 150μm Hg (19.7Pa).

Power was supplied to the induction coil to heat the alloy charge at a rate of 10°C/min. During the heat-up period, the chamber pressure rose to about 1000μm Hg (131Pa) due to outgassing. After the alloy melted, the chamber was back filled with an inert gas until the chamber reached a vacuum of 2in Hg (6752Pa). A slight vacuum in the chamber was necessary in order to keep the exhaust valve at the outlet of the cyclone sealed tightly until it was forced open by the flow of atomization gas. When the alloy reached the desired temperature for atomization, the stopper rod was raised from outside the chamber to start the flow of metal. After the metal flowed through the pour tube for approximately two seconds, the solenoid valve was opened to supply atomization gas to the atomization nozzle. It was necessary to flow metal before the atomization gas to heat the pour tube. After the crucible was drained, the flow of atomization gas was continued for about 30 seconds. If the run was made to produce powder, the gas flow flushed powder from the chamber for collection in the cyclone. If a spray deposit was produced, the blast from the atomization nozzle helped cool.

4.2. Alloy Processing

Table 4.1 lists the ten alloys that were processed. The alloys are divided into two groups, those containing 2.5 wt. %Cr and 2.5 wt. % Al and those containing 4 wt. %Cr and wt. % 4Al. The 2.5Cr-2.5Al group includes one conventionally processed alloy with a nominal composition of Fe-2.5Cr-2.5Al, and five rapidly solidified alloys with a nominal composition of Fe-2.5Cr-2.5Al-1Ti-0.6B. One of the rapidly solidified alloys in this group was processed by a powder processing route and the remaining four were produced by spray forming using different substrate positions. Of the three alloys in the 4Cr-4Al group, two alloys with a composition of Fe-4Cr-4Al and Fe-4Cr-4Al-1.5Ti were conventionally

processed and a single alloy with a composition of Fe-4Cr-4Al-1Ti-0.6B was processed by spray forming. Table 4.2 lists the suppliers and purity of the elements that were used to process the alloys and table 4.3 lists the chemical compositions of the alloys.

4.2.1. Conventionally Processed Alloys

The conventionally processed alloys were made by melting the metals in a vacuum induction melter. Electrolytic iron was first melted in an alumina crucible (79% dense, Al_2O_3 content > 99.5%, Norton Refractories, Worcester, MA) under a vacuum of 0.1μmHg. A graphite susceptor was not used. Once the iron was completely melted, electrolytic chromium was added to the melt followed by aluminum. Aluminum was added last because it was found that the addition of aluminum caused a dross to form over the melt surface making further additions to the melt difficult. If the alloy was to contain titanium, this element was added to the melt at the same time as the chromium. After addition of all the elements, induction power was supplied for 10 minutes to insure complete mixing of the melt. The alloys were not cast but allowed to solidify in the crucible to eliminate possible contamination by mold material. The ingot, which was 7cm (2.76in) in diameter and approximately 9cm (3.54in) high, was sectioned using a silicon carbide abrasive wheel into slabs about 0.8cm (0.38in) thick by 1.0cm (0.39in) wide. The slabs were hot rolled at 900°C in repeated passes to a final thickness of about 0.4cm (0.16in) which gave a 50% reduction in cross-sectional area. The rolled alloys were annealed at 900 or 1000°C for 50 hours in order to stabilize the microstructure before oxidation experiments. The 900°C anneal was carried out on alloys that were to be oxidized at temperatures of 900°C or below and the 1000°C anneal was carried out on alloys were to be oxidized at 1000°C.

4.2.2. Rapidly Solidified Alloys

The alloys to be atomized were made by melting the elements in a vacuum induction melter in the same manner as was the case with the conventionally processed alloy. The only difference was that these alloys contained boron and this element was mixed with the electrolytic iron in the crucible prior to melting. Boron could not be added directly to the melt in the same manner as the chromium and aluminum because upon contacting the melt surface, boron pieces shattered explosively. This was evidently due to the strongly exothermic reaction of mixing. After the ingot solidified and was removed from the crucible, the alloy was sectioned into pieces that could be fitted into the crucible in the atomization system. The pieces had to be fairly small to fit around the stopper rod and thermocouple protection tube. For the production of powder, the maximum amount of charge was placed in the crucible which was about 1.2 kg (2.62lb). The charge for producing the spray-formed alloys was reduced to about 0.6kg (1.32lb). This was done to produce a fairly thin deposit that remained at a low temperature during the spray forming process.

All atomization runs were carried out at a melt temperature of 1625°C. The liquidus temperature of both alloy compositions, Fe-2.5Cr-2.5Al-1Ti-0.6B and Fe-4Cr-4Al-1Ti-0.6B, was estimated from inflections in the heating curves during melting to be approximately 1475°C. This gave a superheat of about 150°C for atomization. Argon gas (99.996%) was used for both backfilling the atomization chamber after the alloy was melted and atomization of the molten alloy. An atomization gas pressure of 690kPa (100psi) was used for producing a spray-formed deposit, and a pressure of 5.7 MPa (800psi) was used for producing powder.

The atomized spray of particles becomes wider as the atomization gas pressure is decreased. A low atomization pressure was therefore used for spray

forming to obtain a deposit with a large diameter. In the production of powder, a higher atomization pressure was used to minimize particle size and maximize the solidification rate. It was found that if the atomization gas pressure was increase above 5.7MPa (800 psi), a deposit formed on the conical section at the bottom of the chamber. At these high pressures, particles were accelerated at such a high rate that a large fraction was still partially in the liquid state when the chamber bottom was reached. It was therefore impractical to increase the atomization gas pressure above 5.7MPa (800 psi) without increasing the length of the atomization chamber.

The average gas flow rates at 690kPa and 5.7MPa (100 and 800 psi) atomization pressures were 630l/min (22ft^3/min) and 2770l/min (98ft^3/min) respectively. The gas flow rate was calculated by determining the difference in the amount of argon in the gas reservoir before and after an atomization run of known duration. The mass of argon in the gas reservoir was calculated by using the volume of the reservoir with tabulated values of the density of argon as a function of gas pressure.[86] The calculated gas flow rates are in good agreement with the values reported by other investigators as shown in Figure 4.7.[87]

The average metal flow rate during atomization was approximately 2kg/min (4.41lb/min). The flow rate of metal from the crucible was calculated using the inner diameter of the pour tube and the pressure at the pour tube opening. For all atomization runs the pour tube inner diameter was 2.8mm (0.11in) and the pour tube length was adjusted to obtain a vacuum reading of 2in Hg at the pour tube opening.

The spray-formed Fe-4Cr-4Al-1Ti-0.6B alloy was produced using a substrate distance of 0.23m (9in). Because of difficulties encountered in processing this alloy using the noninsulating type tube, the four spray-formed and single powder-processed Fe-2.5Cr-2.5Al-1Ti-0.6B alloys were made using the

insulating type pour tube. The Fe-2.5Cr-2.5Al-1Ti-0.6B alloys were spray-formed at substrate positions of 0.23, 0.28, 0.48 and 0.64m (9, 11, 19, and 25in). The spray-formed deposits were sectioned into rectangular slabs, hot rolled, and annealed in exactly the same manner as the conventionally processed alloys.

The steel substrate was removed from the atomization chamber for the processing of the rapidly solidified Fe-2.5Cr-2.5Al-1Ti-0.6B alloy powder. Figure 4.8 shows the efficiency of the cyclone to collect iron powder from air flowing at a rate of 1130l/min ($40ft^3$/min).[88] Since the flow rate of argon gas during the production of the powder was 2770l/min ($98ft^3$/min) this curve can be used as a lower limit on the collection efficiency. After atomization, the collected powder was passed through a 125μm mesh sieve to remove coarses particles. More than 98% of the atomized alloy powder was less than 125μm in size. During handling no precautions were made to protect the powder from contact with air.

Consolidation of the powder was carried out by hot isostatic pressing at IMT Corp., Andover MA. The powder was loaded into a 3.18cm (1.25mm) diameter steel tube and heated at 400°C for 2 hrs under a vacuum of 20μm before being sealed. The alloys were hot isostatically pressed at a pressure of 300MPa (30ksi) and a temperature of 1000°C for 2.5 hours. The consolidation cycle is shown in Figure 4.9. The diameter of the stainless steel tube was reduced from 3.18mm (1.25in) to 23.36mm (0.92in) during consolidation. Slabs were machined from the consolidated bar and hot rolled to process the powder-processed alloy in exactly the same manner as was employed with the spray-formed alloy. However, it was found that internal stresses generated during rolling caused the strip to fracture along weak prior particle boundaries. The consolidated powder was, therefore, only annealed at 900 and 1000°C and did not undergo deformation processing.

4.2.3. Wettability Experiments

To determine the feasibility of producing Fe-Cr-Al alloys containing an Al_2O_3 dispersion by rapid solidification, the wetting characteristics of alumina by an Fe-4Cr-4Al alloy was determined by performing sessile drop experiments. Three additional sessile drop experiments were carried out with alloys of composition Fe-4Cr-4Al-1Ti, Fe-4Cr-4Al-1.5Ti, and Fe-4Cr-4Al-2Ti. Titanium was chosen as a wetting agent because it has been found to promote the wetting of ceramics by various metals.[89]

Figure 4.10 shows a schematic diagram of the sessile drop apparatus that was used to carry out the wettability experiments. A sample of the alloy with dimensions of approximately 7 X 7 X 7mm was place on a high purity alumina substrate (99.98% Al_2O_3, Coors Refractories, Golden, CO). For the alloys that contained titanium, a small hole was drilled into a sample the Fe-4Cr-4Al alloy and sufficient titanium placed in the hole to give the desired concentration of titanium when the alloy melted. After the titanium was placed into the hole the opening was peened shut. The alloy and substrate were placed into an alumina tube that was enclosed by a graphite susceptor. The entire assembly was contained in a standard vacuum induction melting furnace that had the induction coils positioned horizontally. The sessile drop was photographed through a quartz site port in the furnace door using a 35mm camera with a 300mm telephoto lense and a 250mm lense extension tube. The alloy temperature was measured, also through the site port, using a two color optical pyrometer (Ircon Corp., Skokie, IL). The pyrometer measured the melting point of pure iron to within ±15°C. The alloy specimen was heated under a vacuum of 10^{-5}torr and brought from room temperature to 1600°C in about 15min. After the alloy was brought to 1600°C, the induction power was regulated manually to keep the temperature reading within 20°C of 1600°C. Metal vapors from the sample began coating the site port after melting so that the sessile drop could be photographed for only about 10 minutes.

4.3. Alloy Oxidation

Table 4.4 shows a matrix of the isothermal oxidation experiments that were carried out. A complete series of isothermal oxidation experiments were carried out on the conventionally processed Fe-2.5Cr-2.5Al and Fe-4Cr-4Al alloys at temperatures between 400 and 1000°C. These experiments form the basis against which the oxidation of the rapidly solidified alloys were compared.

Three rapidly solidified alloys with a composition of Fe-2.5Cr-2.5Al-1Ti-0.6B were oxidized at 600 and 700°C. One of the alloys was processed from powder and the remaining two were processed by spray forming. Two different processing techniques were used in order to demonstrate any resulting variation microstructure on oxidation. The two spray-formed alloys in this group were processed at 0.23 and 0.64m (9 and 25in) substrate positions. These alloys were oxidized to determine the effect of the difference in their microstructures on oxidation.

A spray-formed Fe-4Cr-4Al-1Ti-0.6B was oxidized under isothermal conditions at temperatures of 400 to 1000°C (Table 4.4). An additional conventionally processed alloy with a composition of Fe-4Cr-4Al-1Ti was oxidized at 900, and also at 1000°C to determine the effect of titanium on oxidation at these temperatures. These alloys were studied in some detail to follow the work carried out by Guruswany et al.[90] with rapidly solidified Fe-Al-Ti-B alloys at 900 and 1000°C . Cyclic oxidation experiments were carried with the conventionally processed Fe-4Cr-4Al, Fe-4Cr-4Al-1Ti and the spray deposited Fe-4Cr-4Al-1Ti-0.6B alloys at 1000° in order to determine the oxidation resistance of these alloys under more severe environmental conditions than experienced during isothermal oxidation.

4.3.1 Preparation of Specimens for Oxidation

The spray-formed and conventionally processed alloys were in the form of strips 3mm (0.118in) in thickness and 15mm (0.59) in width following thermo-mechanical processing. A 1mm (0.039in) layer was removed from each of the sides of the strip by machining to remove any effects of surface oxidation that occurred during annealing. Square coupons, 1cm X 1cm (0.394in X 0.394in), were then cut from the alloy strip for oxidation tests. The hipped rod of the Fe-2.5Cr-2.5Al-1Ti-0.6B alloy was machined to remove all of the canning material, which yielded a 14 X 14mm (0.55 X 0.55in) square bar. Oxidation coupons 1 mm (0.039in) thick were sliced from the bar using a low speed diamond saw. All oxidation coupons were abraded using silicon carbide abrasive paper and given a final polish using 0.3μm alumina polishing compound. A 0.6mm (0.025in) hole was drilled through each coupon for attachment of a suspension wire. Coupon dimensions were measured with a micrometer. Immediately before the oxidation test, each coupon was ultrasonically cleaned in a detergent/water solution, degreased with methanol, and weighed to within ± 0.1mg.

4.3.2. Isothermal Oxidation

Figure 4.11 is a schematic diagram of the thermogravimetric apparatus that was constructed to carry out the isothermal oxidation experiments. The apparatus consists of a Cahn 1000 microbalance that measures the weight of the oxidation coupon and records it continuously on a strip chart recorder. Oxidation coupons were suspended from one beam of the balance by a quartz fiber into a 40mm (1.57in) diameter quartz reaction tube. The furnace which was wound noninductively with Kanthal (Zircar Products, Inc., Florida, NY) wire and could be raised to bring the specimen up to the reaction temperature and lowered to cool the specimen to room temperature. The furnace temperature was controlled by a proportional/integral/derivative temperature controller (Eurotherm Corp., Reston,

VA, model 919), which held the temperature to within ±1°C of the set value. The temperature gradient in the hot zone of the furnace was less than 2°C over a length of 3 cm. The specimen temperature was measured using a type S thermocouple (Pt -10%Rh vs Pt) that was sheathed in a quartz protection tube and located in the reaction tube within 1cm (0.39in) of the oxidation coupon. The thermocouple was found to be accurate to within ±5°C when compared against an NBS calibration thermocouple (Leeds and Northrop Instruments). A correction was not applied to compensate for the error of the thermocouple. Oxygen gas (99.95% pure) was passed first through Ascarite (sodium hydroxide) to remove carbon dioxide and then through Drierite (calcium sulfate) and phosphorous pentoxide to remove water vapor. The oxygen was preheated in the furnace before entering the bottom of the reaction tube. The volumetric gas flow rate was 21cm^3/min (1.28in^3/min), which gave a linear flow rate in the reaction tube of 1.7cm/min (0.66in/min).

After the oxidation coupon was cleaned and weighed, it was attached to the quartz hangdown fiber with a platinum wire tie and inserted into the reaction tube. The reaction tube was sealed and flushed with oxygen for at least one hour. The furnace was heated to the reaction temperature in the lowered position and was then raised to bring the oxidation specimen up to temperature. The specimen reached the reaction temperature within 5 minutes. The displacement of the sepecimen weight reading due to the difference in the buoyancy force of the specimen at room temperature and at the reaction temperature was taken into account by subtracting the difference in the forces from the recorded weight reading. Once the specimen reached a constant temperature, the specimen mass could be determined to within ±0.02mg. The primary cause of uncertainty in the weight measurement was due to noise caused by natural convection of oxygen gas in the open volume of the reaction tube. Specimen weight change was divided by the initial area of the specimen and plotted as a function of reaction time.

4.3.3. Cyclic Oxidation

Cyclic oxidation experiments were carried out in a furnace and reaction tube of the same design as that used for the isothermal experiments. A quartz specimen tree that could hold five oxidation specimens was suspended by a platinum wire from a magnet enclosed in a Teflon case. The magnet was levitated from outside the reaction tube by a D.C. solenoid which in turn was raised and lowered at selected time intervals by a screw gear driven by a motor. The oxidation specimens were lowered into the furnace for 55 minutes and raised out of the furnace to be cooled for 5 minutes. It took approximately 25 seconds for the specimens to travel from the hot zone of the furnace to the cool zone above the furnace. After a period of 50 cycles, the specimens were removed from the reaction tube, weighed, and then returned to the reaction tube for another 50 cycles. The mass change of the cyclic oxidation specimens was divided by the original specimen surface area and plotted as a function of the number of thermal cycles.

4.4. Alloy and Oxide Scale Characterization

The microstructure of the alloys was characterized using reflected light microscopy, transmission electron microscopy (TEM) using a JEOL 200CX transmission electron microscope, and scanning transmission electron microscopy (STEM) and convergent beam electron diffraction (CBED) using a V.G. HB5 scanning electron microscope . All metallographic specimens were mounted in Bakelite and polished to a 0.3μm surface finish with alumina polishing compound. Reflected light microscopy was used to determine alloy grain sizes that were greater than 1μm. Grain size was determined by the lineal intercept method as described in ATSM Standard E112-85. Alloys were etched with ASTM etchant #89 (30ml nitric acid, 20ml acitic acid, 20ml hydrochloric acid, and three drops of glycerol) to reveal alloy grain boundaries[91]. TEM and STEM were used to determine grain sizes that were less than 1μm in diameter and to determine

precipitate size and distribution. TEM specimens were prepared by grinding 3mm (0.12in) diameter disks of the alloys to 0.07mm (0.003in) thickness followed by electropolishing with a methanol-10% perchloric acid solution. TEM specimens of the powdered alloys were prepared by a technique that was described by Kelly et al.[92], in which the alloy powder was encapsulated in a nickel matrix by electroplating. The nickel matrix effectively retained the powder particles during thinning so that electron transparent specimens of the powder could be prepared. The precipitate particles in the rapidly solidified alloys were identified by selected area and convergent beam electron diffraction.

Oxide scale were characterized by scanning electron microscopy (SEM) using an AMRAY 1000A scanning electron microscope, electron microprobe analysis (EMPA) using a Jeol 733 microprobe, x-ray diffraction (XRD) using a Phillips difractometer, and reflected high energy diffraction (RHEED) using a Phillips 300 transmission electron microscope. SEM was used to examine oxide scale surface morphology. A thin coating of gold was evaporated onto the oxide surface to make the surface conductive and prevent charging in the SEM. Oxidation specimens for cross-sectional examination were prepared by electroplating a layer of nickel onto the specimen surface that was approximately 0.25mm (0.009in) in thickness. Prior to electroplating, the oxidation specimens were gold coated to form a conductive surface. The electroplated specimens were mounted in Bakelite, sectioned, and polished to 0.3μm surface finish with alumina polishing compound. EMPA was used to determine the distribution of elements in the oxide scale. XRD and RHEED were used for oxide phase identification. XRD was used for thick oxide scales (>1μm in thickness) while RHEED was used for oxide scales that were too thin to be identified by conventional XRD.

5. RESULTS

In this section, the results of the alloy processing and oxidation experiments are presented. The microstructures of the conventionally processed and rapidly solidified alloys are described in Section 5.1. The processing of alloys that contained Al_2O_3 particles was not successful; however, wettability experiments that were carried out in this phase of the program are presented. Results of the isothermal and cyclic oxidation experiments are presented in Section 5.2.

5.1. Alloy Processing

5.1.1. Conventionally Processed Alloys

The microstructures of the conventionally processed Fe-2.5Cr-2.5Al, Fe-4Cr-4Al and Fe-4Cr-4Al-1Ti alloys were similar. Figure 5.1 shows the microstructure of the Fe-2.5Cr-2.5Al alloy after thermo-mechanical processing. The alloy grains were equiaxed, and the size ranged from 150μm to several millimeters. Alloys that were oxidized at 1000°C and were annealed at 1000°C before oxidation showed no observable difference in grain size compared to the alloys annealed at 900°C.

5.1.2. Rapidly Solidified Alloys

5.1.2.1. Spray-Formed Fe-4Cr-4Al-1Ti-0.6B Alloy

A photograph of the spray deposition process is shown in Figure 5.2. Liquid metal was atomized at the point of exit from the pour tube and accelerated to be deposited onto a substrate. A typical spray deposit is shown in Figure 5.3. The deposit was approximately 0.15m (5.9in) in diameter and 0.01m (0.39in) thick at the center. The deposit thickness decreased toward the edges because the density of particles was greatest along the central axis of the atomization cone.

Figure 5.4 shows a cross-section through the spray deposited Fe-4Cr-4Al-1Ti-0.6B alloy that was processed at a substrate distance of 0.23m (9in) using the noninsulating type pour tube. Porosity was uniformly distributed through the deposit thickness and was calculated to be approximately 5% as measured by

ASTM Standard B328-73 . An optical micrograph of the microstructure of the deposit is shown in Figure 5.5. Boundaries that separate individually deposited particles are clearly seen. Particles that had, to some extent, solidified in flight before becoming incorporated into the deposit are indicated by arrow heads. The larger particle had not completely solidified before contacting the deposit and had deformed upon impact. It is apparent that the alloy microstructure is not uniform. A cellular type microstructure can be clealy resolved in the large, entrapped particles and some of the thicker splats while the microstructure of much of the surrounding material cannot be clearly resolved and appears to have a much finer microstructure. Pores in the deposit were generally observed to be associated with entrapped, presolidified or partially solidified droplets. Figure 5.6 shows a region where several solidified droplets were deposited and evidently were not fluid enough to fill in irregularities on the deposit during the spray forming process. Hot rolling the spray-formed alloys to a 50% reduction in area effectivelly closed up the pores in the deposit and reduced the porosity in this alloy to less than 1%. The porosity in the alloy was not interconnected, so that internal oxidation of the alloy did not occur during hot rolling.

The level of porosity in the spray-formed alloy prevented successful preparation of electron transparent specimens for TEM observation by jet electropolishing because of exessive metal removal around pores. Only after the spray deposited material was hot rolled and the porosity reduced could the alloy be successfully thinned. Figure 5.7 shows a TEM micrograph of the spray deposited material after rolling to 50% reduction in area and annealing at 900°C for 100h. Approximatelly a dozen foil samples were prepared and the alloy grain size was found to be less than 0.5μm. (One note will be added here. Some confusion exists over the use of the use of the terms cells and grains. In this work no difference will be made between low and high angle grain boundaries and all celular structures

will be refered to as grains.) Fine particles were observed dispersed through out the alloy matrix. Figure 5.8 is a higher magnification TEM micrograph of the area shown in Figure 5.7 and more clearly reveals the microstructure. The grains are equiaxed and fine particles appear to lie preferentially on alloy grain boundaries. Figures 5.9 a and b show an STEM image of the alloy and an X-ray intensity map for titanium that indicates that the particles are rich in titanium. The particles did not appear to contain iron, chromium, or aluminum. The presence of boron could not be confirmed because the X-ray detector used was not sensitive to this element. A convergent beam electron diffraction image of the particle indicated by an arrow in Figure 5.9a is shown in Figure 5.9c. The pattern is indexed to the [100] zone axis of titanium diboride in Figure 5.9d. In some regions of the alloy very large particles were observed such as those shown in Figure 5.10.

Abnormal grain growth was observed to occur in the spray-formed and hot-rolledFe-4Cr-4Al-1Ti-0.6B allloy that was annealed at 1000°C for 100h. To determine the sensitivity of the alloy to abnormal grain growth, addition samples of the hot-rolledalloy were annealed at 900 and 1000°C for 300h. Also, an alloy sample that was not rolled but retained in the as-sprayed condition that was annealed at 1000°C for 300h. The abnormal grain growth was found to occur preferentially at the alloy surface and was more extensive at longer annealing times and at higher temperatures. Figure 5.11 shows an optical micrograph of the surface region of the spray-deposited and hot-rolledalloy after annealing at 900°C for 100h. Recrystallization and grain growth occurred to a depth of about 0.5mm (0.02in) into the alloy from the alloy surface. Figures 5.12 and 5.13 are TEM micrographs of the alloy shown in Figure 5.11. The micrograph shows the interface between the fine grain region and a large grain growing into that region. Boride particles that had previously decorated alloy grain boundaries were left behind in the large grain as the fine grained region was recrystallized. In Figure 5.13 the fine

grained region appears to contain a high density of dislocations while the region in the large grain is dislocation free. An optical micrograph of the alloy after annealing at 100°C for 100h is shown in Figure 5.14. This micrograph shows the center of the rolled strip with grain growth occurring from both surfaces and only a small area at the center of the strip remaining fine grained. The spray-deposited and hot-rolled alloy was entirely recrystallized after annealing at 1000°C for 300h while the spray deposited alloy that was not hot rolled showed no evidence of grain growth when annealed under the same conditions.

5.1.2.2. Spray-Formed Fe-2.5Cr-2.5Al-1Ti-0.6B Alloy

Initially, the Fe-2.5Cr-2.5Al-1Ti-0.6B alloy was spray-formed using the same processing parameters as used for the Fe-4Cr-4Al-1Ti-0.6B alloy with the exception that the insulating type pour tube was used . The change in pour tube design alleviated the problems of pour tube freezing and the stoppage of metal flow due to pressurization at the pour tube opening that occured during the spray forming of the Fe-4Cr-4Al-1Ti-0.6B alloy. A photograph of the surface of the deposit that was spray-formed using the noninsulating pour tube at a substrate distance of 0.23in (9in) is shown in Figure 5.15. The top surface of the deposit is rippled and gives evidence of the formation of a liquid pool in the deposit. The blast of gas from the atomization nozzle pushed down on the deposit and deformed the surface during the spray forming process. Figure 15.16 shows optical micrographs of the deposit microstructure. The microstructure is coarser than that of the Fe-4Cr-4Al-1Ti-0.6B alloy processed with the noninsulating pour tube and using the same processing parameters. The alloy grains are equiaxed with an average grain size of 8.6μm. Figure 15.16b shows coarser precipitates than those formed in the Fe-4Cr-4Al-1Ti-0.6B spray-formed alloy. X-ray diffraction of the alloy generated diffraction peaks for α-Fe and a small peak for TiB_2.

Since it appeared that appreciable liquid collected in the deposit formed at a substrate position of 0.23m (9in) during processing, a series of alloys of this composition were processed at substrate positions of 0.27, 0.38, 0.48 and 0.63m (11, 15, 19 and 25in). The objective of this was to produce a spray-formed Fe-2.5Cr-2.5Al-1Ti-0.6B alloy with the same microstructure as was obtained at a 0.23m (9in) substrate position with the spray-formed Fe-4Cr-4Al-1Ti-0.6B alloy. The alloys that were spray-formed at positions of 0.28 and 0.38m (11 and 15in) had nearly identical microstructure to the alloy processed at a substrate position of 0.23m (9in), and these microstructures are shown in Figure 15.17. The grain size was 8.8 and 9.0μm and TiB_2 particles with a size on the order of 1μm were distributed throughout the alloy. The alloy spray-formed at a 0.48m (19in) substrate position showed no significant change in alloy grain size or particle size, but many spherical particles were observed in the alloy. Four of these particles are indicated by arrows in Figure 15.18a. Most of the particles observed in this alloy showed evidence of being partially melted, as shown in Figure 5.18b, which suggests that they were in contact with liquid metal in the deposit. The alloy spray-formed at a 0.63m (25in) substrate position had a much different microstructure than the alloys that were spray-formed at shorter distance. An optical micrograph of this alloy is shown in Figure 15.19, which shows that the microstructure is similar to that of the Fe-4Cr-4Al-1-Ti-0.6B alloy that was spray-formed at a 0.23m (9in) substrate position. Both entrapped powder particles and splat boundaries are visible. Also porosity resulting from incomplete filling in around a powder particle is shown. There is obvious variability in the refinement of the microstructure. As with the spray-deposited, Fe-4Cr-4Al-1-Ti-0.6B alloy, foils of this alloy could not be prepared until after the alloy was hot rolled and the porosity reduced. Figure 15.20 shows TEM micrographs of the alloy after hot rolling to a 50% reduction in cross-sectional area and anealling at 900°C for 100h. The grain size was generally less

than 1μm, although in some foils the grains were a few microns in size. Particles were distributed throughout the alloy but tended to be clustered in some regions. Many of the grain interiors and grain boundaries lacked any particles. Figure 5.21 shows a TEM micrograph of a region in the alloy were the precipitates were clustered and a selected area diffraction pattern of the the same area. The concentration of particles in the region was not great enough to produce, athough partial rings could be indexed to TiB_2. Because of the extensive abnormal grain growth that occured in the Fe-4Cr-4Al-1-Ti-0.6B alloy at 1000°C, annealing was only carried out at 900°C for 100h. After this annealing period grain growth in the alloy was not observed. Figure 5.22 is a plot of the alloy porosity and grain size as a function of substrate position for the spray-formed Fe-2.5Cr-2.5Al-1Ti-0.6B alloys. The alloy grain size and porosity were not very sensitive to substrate placement between positions of 0.23 and 0.48m (9 and 19in). At the 0.64m (25in) position the grain size decreased from about 9μm to 1μm and the pososity increased from a value that was between 1 and 2 % to 5.8 %.

5.1.2.3. Powder-Processed Fe-2.5Cr-2.5Al-1Ti-0.6B Alloy

Figure 5.23 shows SEM micrographs of the gas atomized Fe-2.5Cr-2.5Al-1Ti-0.6B alloy. The powder was generally spherical in shape although some particles were somewhat elongated and there was evidence of particle collisions and joining during atomization. The particle size distribution of the atomized powder is shown in Figure 5.24. Since the cyclone collects 100% of the powder at the lower end of this curve (see Figure 4.8), this plot gives a valid representation of the particle sizes produced by the atomiztion process. Optical micrographs of cross-sections through the powder are shown in Figure 5.25. It is evident that the alloy microstructure becomes much finer as the particle size decreases. The large particle shown in 5.25a has columnar grains that had grown inward from the particle surface during solidification and the center of the particle consists of

randomly oriented dendrites. The smaller powder particles shown in Figure 5.25b lack the columnar grains at the powder surface and consist entirely of randomly oriented grains that are much finer in size than those in the interior of the particle shown in Figure 5.25a. A STEM micrograph of a foil prepared from the powder is shown in Figure 5.26. Figure 5.26a shows the thinned powder particles contained by the nickel matrix that had been electroplated onto the powder. Figure 5.26b is a higher magnification image of the powder particle at the edge of the thinned hole. An interconnected second phase is present throughout the powder particle. Convergent beam diffraction patterns taken of the interconnected phase and the adjoining alloy is shown in Figure 5.27. The common crystallographic orientation of the regions on either side of the interconnected phase indicates that the regions are arms of the same dendrite. The intredendritic phase generates a diffuse diffraction pattern indicating an amorphous structure. Figure 5.28 shows concentration profiles taken across the interdendritic amorphous phase. Titanium and chromium are segregated to this phase while aluminum is depleted.

An optical micrograph of the hot isostatically pressed powder is shown in Figure 5.29. Prior particle boundaries are clearly evident in this etched microstructure and grains that are several microns in size are visible. Figure 5.30 shows TEM micrographs of the hipped alloy. There is no evidence of the interdendritic amorphous phase that had existed in the powder prior to consolidation, but there is now a network of particles distributed throughout the alloy matrix. The allloy grain sizes range from 0.5 to 2μm. The boride particles, as shown in Figure 5.30a are strongly clustered in some regions and not present in grain interiors. Fugure 5.30b shows linear arrays of boride particle that delineate prior particle boundaries. Figure 5.31 shows a TEM micrograph of a region in the alloy were the precipitates were clustered and a selected area diffraction pattern of the the same area. Partial rings in the were indexed to TiB_2.

The steel can that was used for hot isostatic pressing of the powders was crimped closed at the ends and sealed by welding. In these regions grain growth occurred in the consolidated powder during hot isostatic pressing. Figure 5.32 shows a cross-section through the can and the consolidated alloy powder close to the crimped end. The alloy recrystalized in bands that formed two circular regions. Two tubes of this alloy were consolidated, and similar grain groth took place at all four ends. The recrystallized bands are shown more clearly at higher magnifications in Figure 5.33. At regions away from the can ends recrystallization and grain growth did occur during consolidation.

5.1.3. Oxide Wetting

Figure 5.34 shows photographs of the sessile drop experiments for five alloy compositions; pure iron, Fe-4Cr-4Al, Fe-4Cr-4Al-1Ti, Fe-4Cr-4Al-1.5Ti, and Fe-4Cr-4Al-2Ti alloys. Vibration from the mechanical vacuum pump that was used to evacuate the sessile drop apparatus caused blurring of some of the images. Although the contact angles could not be measured with great precision, the objective of these experiments were to determine the general extent of wetting and this information could be adequately determined with these experiments. The contact angle for pure iron is approximately 135° which agrees well with the published value of 141°.[93] An Fe-4Cr-4Al alloy did not significantly wet the alumina substrate to any greater extent than pure iron. The addition of 1 weight percent titanium to the Fe-4Cr-4Al alloy increases wetting of the substrate and the contact angle decreased to a value that is close to 90°. Increasing the titanium concentration up to 2 weight percent did not result in increased wetting of the alumina substrate by the alloy over that obtained by adding 1wt%Ti.

5.2 **Alloy Oxidation**

5.2.1. Fe-4Cr-4Al Alloy Series

Figure 5.35 shows the weight change per unit surface area of the conventionally processed Fe-4Cr-4Al and spray-formed Fe-4Cr-4Al-1Ti-0.6B alloys after 50h of isothermal oxidation. The alloys were oxidized at 100°C increments at temperatures between 400 and 1000°C. All oxidation experiments were carried out twice; however, room temperature fluctuations caused the base-line reading of the balance to drift during some of the experiments. Weight gain results from these experiments were discarded so that only one data point is shown at temperatures where this occurred. Where two data points were obtained, the average value of the weight gain is used to place the connecting line. In the temperature range of 400 to 800°C, both the conventionally processed and rapidly solidified alloys showed very little weight gain and the scatter in the values is not much greater than the 0.025mg/cm^2 noise band produced by the microbalance. The weight of both alloys increased when the oxidation temperature was increased above 800°C, with the rate of increase greater for the conventionally processed Fe-4Cr-4Al alloy.

Figure 5.36 shows the thermogravimetric results for the oxidation at 900°C of conventionally processed Fe-4Cr-4Al and Fe-4Cr-4Al-1Ti alloys and a spray-formed Fe-4Cr-4Al-1Ti-0.6B alloy. The two conventionally processed alloys gained more weight initially than the spray-formed alloy and were undergoing oxidation at a greater rate at the end of the 50h experiment. Figure 5.37 shows thermogravimetric results for the oxidation of the same set of alloys at 1000°C. Two curves are shown for the conventionally processed Fe-4Cr-4Al-1Ti alloy and spray-formed Fe-4Cr-4Al-1Ti-0.6B alloy. One spray-formed alloy coupon gained about three times more weight than the other. The weight gain occurred almost entirely in the first several hours of the experiment. After about 10h both specimens showed very little weight gain. The conventionally processed Fe-4Cr-4Al and Fe-

4Cr-4Al-1Ti-0.6B alloys oxidized at a greater rate than the spray-formed alloy. Although the two conventionally processed Fe-4Cr-4Al-1Ti alloy coupons gained different total amounts of weight during the 50h oxidation period, they had similar oxidation rates at the end of the experiment.

5.2.1.1 Conventionally Processed Fe-4Cr-4Al Alloy

Figure 5.38 shows the surface and cross-section of the scale formed on a conventionally processed Fe-4Cr-4Al alloy that was oxidized at 400°C for 50h. (In Figure 5.38(b) and all subsequent micrographs that show a scale cross-section, the alloy with overlying scale is shown in the lower portion of the microgragh and a nickle layer that was plated onto the scale to prevent rounding of the edges of the specimen during metallographic preparation is shown in the upper portion of the micrograph.) The scale appears as a dark band in the backscattered imaging mode of the microprobe. The scale covering the alloy surface was uniform in appearance and less than 200nm in thickness. The scale was too thin for phase determination by conventional X-ray diffraction. Figure 5.39 shows a reflected high energy diffraction pattern taken from the specimen surface and an index of the pattern. A photograph of the diffraction pattern is shown with arrows indicating the rings that were measured and represented in Figure 5.39(b). The position of the measured rings are compared to those that should be generated by electron diffraction from α-Al_2O_3. The match between the sets of rings is good. Bright spots in the diffraction pattern correspond to α-iron.

Figure 5.40 shows the scale that formed on the conventionally processed Fe-4Cr-4Al alloy oxidized at 500°C for 50h. Unlike the alloy oxidized at 400°C, the scale formed at this temperature was not uniform. Patches of scale of variable thickness formed on the alloy surface and it is apparent that the patches formed at different rates over individual grains in the alloy. Figure 5.40(b) shows the oxide that formed at the the junction of three grain boundaries in the alloy. On the grain

to the right in Figure 5.40(b) a thick oxide layer formed, while over the other two the oxide is apparently much thinner. Of the two grains that are covered with the thinner oxide, one is covered with a higher density of a white-looking particles. Figure 5.41 shows a cross-section through an oxide mound that formed on the alloy shown in Figure 5.40. In figure 5.41 (a) the mound appears to consist of two layers and the scale on either side of the thick oxide mound is about the same thickness as the oxide that had formed on the same alloy when oxidized at 400°C. The optical micrograph in Figure 5.41 (b) shows that the mound actually consists of three layers.

A cross-section through the oxide mound is shown at higher magnification along with elemental X-ray intensity maps for iron, chromium, and aluminum in Figure 5.42. The nickle plating did not adhere well to the oxide so a thin gap exists between the nickle layer at the top of the micrograph and the oxide. The gap appears as a black line in Figure 5.42(a). There is no difference in contrast between the upper two layers in the EPMA images shown in Figure 5.41 (a) and 5.42 (a). The elemental maps show that, of the three elements, only iron is detected in the outer two oxide layers. The inner oxide layer contains iron, chromium and aluminum. X-ray diffraction of the alloy surface generated diffraction peaks for hematite (α-Fe_2O_3), magnetite (Fe_3O_4), aluminium chromite $Fe(Al, Cr)_2O_4$ and the base alloy, α-iron. Aluminum detected along the top of the scale layer is the result of alumina polishing compound that entered the gap during metallographic polishing. The alumina contamination could not be eliminated even with extended ultra-sonic cleaning of the metallographic specimen. The thin scale that is shown on either side of the oxide mound in Figure 5.41 and covered most of the alloy surface was probably α-Al_20_3 and was to thin to be detected by X-ray diffraction. The X-ray diffraction and metallographic results suggest the mounds consist of an outer layer of Fe_2O_3, an middle layer of Fe_3O_4, and an inner layer is

$Fe(Cr,Al)_2O_4$. The intensity of the signal that is used to generate the EPMA backscattered electron image is related to the atomic number of the material imaged. The poor contrast between the Fe_2O_3 and Fe_3O_4 layer in Figure 5.42(a) is a result of both oxides containing similar amounts of iron and no other metals.

Figure 5.43 shows the scale formed on the conventionally processed Fe-4Cr-4Al alloy that was oxidized at 600°C for 50h. Patches of thick scale formed preferentially over some of the alloy grains. The thick scale that formed at this temperature was covered with whiskers that gave the patches a whitish appearance at low magnification in the SEM. The thicker oxide on this alloy consisted of a three-layered oxide similar to the patches formed on the alloy oxidized at 600°C. An X-ray diffraction pattern indicated the presence of Fe_2O_3, Fe_3O_4, and $Fe(Cr,Al)_2O_4$. A reflected high energy electron diffraction pattern was taken from the alloy surface in an attempt to identify the thin scale. Figure 5.44 shows the Rheed diffraction pattern and three faint lines that could be indexed to α-Al_2O_3.

Figure 5.45 shows the scale that formed on a conventionally processed Fe-4Cr-4Al alloy oxidized at 700°C for 50h. The growth of thick oxide mounds over individual alloy grains was not observed. Large oxide nodules formed preferentially along the edges of the oxidation coupon, as shown in Figure 5.45(a). Except for the large nodules, most of the alloy surface was covered by a uniform scale, the surface of which is shown at high magnification in Figure 5.45(b). Figure 5.45(b) shows that the oxide layer was covered by small particles or mounds. A cross-section of the uniform portion of the scale and elemental X-ray maps for iron, chromium, and aluminium are shown in Figure 5.46. The scale was less than 1μm thick and was enriched in aluminum, as is shown in Figure 5.46(d). A cross-section through an oxide nodule that had formed on the edge of the specimen is shown in Figure 5.47. The nodule had penetrated a distance of about 40μm into the alloy

and consists of two distinct layers . The outer layer appears porous and contains mostly iron, while the inner layer appears more dense and contains iron, chromium, and aluminum. The apparent porosity of the outer layer could have originated from pull-out during metallographic polishing. The aluminum enriched regions in the outer layer shown in figure 5.47(d) originated from alumina polishing compound that was deposited in the pores during sample preparation. The inner oxide layer appears to be richer in aluminum and chromium closer to the scale/metal interface. Examination with optical microscopy showed the iron-rich outer layer consisted of a single phase that had the same reflectivity as the outer layer found on the three-layered scale.

The Fe-5Cr-5Al alloy when oxidized at 800°C for 50h did not form iron oxides either as patches or nodules. The scale surface was homogeneous and was covered with very small white mound as shown in figure 5.48. A cross-section through the scale and X-ray intensity maps for iron, chromium, and aluminium are shown in Figure 5.49. One of the bumps on the scale surface is shown in Figure 5.49(a) along with the scale covering the alloy which appears to be about 0.1μm thick. As shown in Figure 5.49(d) the scale covering the alloy and the small mound on the surface is rich in aluminum. X-ray diffraction of the scale surface generated diffraction peaks only for α-iron. Figure 5.50 shows a Rheed pattern taken from the alloy surface and an index of the pattern to α–Al_2O_3.

Figures 5.51 and 5.52 show the scale that formed on the conventionally processed Fe-4Cr-4Al alloy when oxidized at 900 and 1000°C. Both scales are extremely convoluted with the oxide that formed at 1000°C having large folds. The oxides formed on both alloys were generally non-adherent to the alloy surface and had the consistency of a very thin, easily removed ash layer when lightly abraded. X-ray diffraction of the alloy surface showed diffraction peaks for α-Al_2O_3 and α-iron. The presence of iron oxides was not detected. The non-adherence

prevented successful nickle plating and metallographic examination of the scale cross-section. From fractures that occurred at folds in the scale, the scale thickness was found to be less than 1μm.

5.2.1.2. Spray-formed Fe-4Cr-4Al-1Ti-0.6B Alloy

The spray-formed Fe-4Cr-4Al-1Ti-0.6B alloys that were oxidized for 50h at temperatures between 400 and 800°C did not form iron oxide patches or iron oxide nodules such as those that formed on the conventionally processed Fe-4Cr-4Al alloys that had been oxidized in this temperature range. The topographies of the scales formed on these alloys are shown in Figures 5.53 through 5.55. The growth rates of the scales that formed on these alloys were low, and the scale thicknesses were no more 1μm. Reflected high energy electron diffraction of the surface of the alloy oxidized at 400°C did not produce complete diffraction rings but several diffraction spots were generated that correspond to α-Al_2O_3. The alloy that was oxidized at 600°C, formed localized clusters of oxide that were shown to be rich in iron when analyzed by energy dispersive X-ray analysis (EDA) using a scanning electron microscope. The oxide clusters that formed on this alloy are shown in Figure 5.54. Also apparent is preferred scale growth along prior particle boundaries in the alloy. Boundaries between individually deposited droplets of alloy are outlined by small oxide ridges. Small oxide surface particles also formed on the alloy oxidized at 700°C, as shown in Figure 5.55(a). The alloy oxidized at 800°C formed a scale that did not appear to contain any iron oxides and was featureless except when viewed at very high magnification as shown in Figure 5.55(b).

In contrast to the conventionally processed Fe-4Cr-4Al alloys oxidized at 900 and 1000°C, the spray-formed Fe-4Cr-4Al-1Ti-0.6B alloys formed an adherent, non-convoluted oxide scale when oxidized at these temperatures. Figure 5.56 shows the surface of the oxide formed on the spray-formed alloy that was oxidized

at 900°C. The oxide shows no evidence of the folds that had formed on the conventionally processed alloy. Figure 5.57 shows a cross-section and elemental X-ray intensity of the scale. The scale is less than 1μm in thickness, adherent to the alloy surface and, as shown in figure 5.57(d), enriched in aluminum. X-ray diffraction of the alloy surface produced peaks for α-iron and very small diffraction peaks for α-Al_2O_3. Figure 5.58 shows the surface of the scale that formed on the spray-formed Fe-4Cr-4Al-1Ti-0.6B alloy oxidized at 1000°C. This oxide also lacks the folds characteristic of the conventionally processed alloy. The surface of the scale formed at this temperature appears more porous than the scale formed at 900°C, and is covered with small, white particles that were rich in titanium when analyzed by energy dispersive X-ray analyses with a scanning electron microscope. Figure 5.59 shows an EPMA image and X-ray intensity maps of a cross-section through the scale. The scale is adherent to the alloy surface and is approximately three times thicker than the scale that formed on this alloy at 900°C. The scale is enriched in aluminum as shown in Figure 5.59(b). A small mound that is indicated by an arrow in Figure 5.59(a) is shown to be enriched in titanium in Figure 5.59(e). X-ray diffraction of the alloy surface generated diffraction peaks for α-Al_2O_3 and α-iron .

5.2.1.3. Conventionally Processed Fe-4Cr-4Al-1Ti Alloy

Figure 5.60 shows the surface of the scale that formed on a conventionally processed Fe-4Cr-4Al-1Ti alloy that was oxidized at 900°C for 50h. The oxide scale completely lacks the folds that formed on the conventionally processed Fe-4Cr-4Al alloy and is covered with nodules that vary size. Large nodules, that were up to 50μm in diameter, were randomly distributed over the alloy surface and smaller nodules, on the order of a micron in size, were closely spaced and uniformly covered the surface. Figure 5.61 shows an EPMA image and X-ray intensity maps of a cross-section through the scale shown in Figure 5.60. The

nodule consists of an outer cap that appears light grey in Figure 5.61(a) and an inner base that has penetrated into the alloy. The base of the nodule appears to contain both a light and dark colored oxidation product. The elemental maps indicate only titanium in the outer layer of the nodule. The lighter oxide in the base contains both chromium, Figure 5.61(c), and titanium, Figure 5.61(e). The dark-colored oxide in the nodule base is aluminum-rich. The scale that formed on the alloy surface can be seen on either side of the large nodule and is less than 1μm thick. The scale is adherent to the alloy and is aluminum-rich, as shown in Figure 5.61(d).

The scale formed on the conventionally processed Fe-4Cr-4Al-1Ti alloy oxidized at 1000°C had similar appearance to that which formed on the alloy at 900°C. Figure 5.62 shows that the scale surface is covered by both large and small nodules having the same morphology as those shown in Figure 5.60. Figure 5.63 shows an EPMA image and X-ray intensity maps of a cross-section through scale shown in Figure 5.62. The nodule shown also consists of a lighter colored outer cap that contains exclusively titanium, Figure 5.63(e). The base of the nodule consists of a mixture of the lighter-colored, titanium-rich oxide and the darker-colored, aluminum-rich oxide. Chromium and iron do not appear strongly concentrated in the nodule. The oxide scale that covers the alloy and is shown on either side of the nodule is about 1μm thick and adherent to the alloy. As shown in Figure 5.63(d) the scale covering the alloy surface is rich in aluminum. X-ray diffraction from the scale surface of the alloy oxidized at both 900 and 1000°C generated diffraction peaks for α-iron, α-Al_2O_3, and TiO_2. This suggests that the adherent, alumina-rich scale covering the alloy surface is α-Al_2O_3 and the nodules consist of a cap of TiO_2 and a base of mixed oxides containing aluminum, titanium and some chromium.

5.2.1.4. Cyclic Oxidation

Figure 5.64 shows the result of the cyclic oxidation tests that were carried out on the conventionally processed Fe-4Cr-4Al and Fe-4Cr-4Al-1Ti alloys and spray-formed Fe-4Cr-4Al-1Ti-0.6B alloy at 1000°C. The alloys were held at 1000°C for 55min and then removed from the hot zone and allowed to cool to room temperature for 5min. Weight changes were measured and recorded after every 25 cycles. The conventionally processed Fe-4Cr-4Al alloy showed little weight change until approximately 150 cycles when the oxidation coupon began to decrease in weight. The specimen continued to decrease in weight until 200 cycles and then began to gain weight rapidly. The rate of weight gain continued to increase until the end of the experiment. The conventionally processed Fe-4Cr-4Al-1Ti and spray-formed Fe-4Cr-4Al-1Ti-0.6B alloys underwent very little change in weight during the 425 cycles. The Fe-4Cr-4Al-1Ti alloy gained slightly more weight than the spray-formed alloy during the first 75 cycles.

Figure 5.65 shows the surface and a cross-section of the scale formed on the conventionally processed Fe-4Cr-4Al alloy after 425 oxidation cycles. The scale surface has the same convoluted type of morphology as the α–Al_2O_3 scale that had been formed on the this alloy when isothermally oxidized at 1000°C. This scale, however, has been repeatedly spalled and rehealed during the cyclic oxidation process and has formed non-adherent patches of oxide on the alloy surface. The corners and edges of the specimen have been extensively oxidized. Figure 5.65(b) shows a cross-section through the oxidation specimen and shows the extensive oxidation of the specimen edge and the formation of iron oxide. Figure 5.66 shows low and high magnification images of a cross-section through the scale that formed closer to the center of the alloy surface. Figure 5.66(a) shows that multiple layers of scale had formed, which is indicative of spallation and reformation of the aluminum oxide. Deformation of the alloy surface caused by the

convoluted growth of the oxide can be seen in Figure 5.66(a) and at higher magnification in Figure 5.66(b).

Figure 5.67 shows the surface and a cross-section through the oxide formed on the spray-formed Fe-4Cr-4Al-1Ti-0.6B alloy after 425 oxidation cycles. The scale is similar to that which had formed on the same alloy when oxidized isothermally at 1000°C for 50h, with the exception that a few titanium rich particles formed on the surface. The scale formed on this alloy during cyclic oxidation is only about 50% thicker than that formed on the same alloy when oxidized isothermally for 50h.

Figure 5.68 shows the surface and a cross-section through the oxide formed on a conventionally processed Fe-4Cr-4Al-1Ti alloy after 425 thermal oxidation cycles. The scale was completely adherent to the alloy and showed no sign of convolutions such as those formed on the conventionally processed Fe-4Cr-4Al alloy. The oxide surface was more densely covered with small titanium rich oxide particles, but the larger nodules were no larger in dimension than those that formed on this alloy after 50h of isothermal oxidation at 1000°C. Figure 5.68(c) shows that the scale formed on this alloy during cyclic oxidation for 425 cycles is only slightly thicker than that which formed during 50h of isothermal oxidation at 1000°C and is approximately the same thickness as that which formed on the spray-formed alloy during the same cyclic oxidation test.

5.2.2. Fe-2.5Cr-2.5Al Alloy Series

Figure 5.69 shows the weight gain per unit surface area of the Fe-2.5Cr-2.5Al series of alloys after 50h of oxidation as a function oxidation temperature. Results are shown for the conventionally processed Fe-2.5Cr-2.5Al alloy that was oxidized at 100°C increments from 400 to 1000°C and three different Fe-2.5Cr-2.5Al-1Ti-0.6B rapidly solidified alloys that were oxidized at 600 and 700°C. The rapidly solidified alloys consisted of spray-formed alloys processed at 0.23m (9in)

and 0.64m (25in) substrate positions that had grain sizes of approximately 9 and 1μm respectively and a powder processed alloy with a grain size of approximately 1μm.

The Fe-2.5Cr-2.5Al alloy gained very little weight when oxidized at 400°C. The rate of oxidation increased slightly at 500°C and then to a much greater extent at 600°C. The weight change decreased at 700°C and reached a local minimum value at 800°C. The extent of oxidation was then increased by raising the oxidation temperature to 900 and 1000°C. At 1000°C, the weight change values for two specimens differed by more than a factor of two.

The three rapidly solidified alloys in this series were oxidized at only 600° and 700°C. At both temperatures, two weight change values are shown for each of the spray-formed alloys and a single value is shown for the powder processed alloy. The extent of oxidation of the rapidly solidified alloys at these two temperatures was much less than that for the conventionally processed Fe-2.5Cr-2.5Al alloy and the results showed good reproducibility. The oxidation rate of the rapidly solidified alloys was slightly greater rate at 700 than at 600°C.

Figure 5.70 shows the thermogravimetric results for the Fe-2.5Cr-2.5Al series of alloys oxidized at 600°C. Two curves are shown for each of the spray-formed alloys and the single curve is shown for the powder processed alloy. The rapidly solidified alloys gained very little weight and at the resolution that the measurements were made the curves could not be differentiated. The conventionally processed Fe-2.5Cr-2.5Al alloy coupons oxidized at a much greater rate than the rapidly solidified alloys throughout the oxidation experiment.

Figure 5.71 shows the thermogravimetric results for the Fe-2.5Cr-2.5Al series of alloys oxidized at 700°C. Again, there was a large difference between the rate of oxidation of the rapidly solidified alloys and the conventionally processed alloy. The total weight gained by the two conventionally processed alloy coupons

differed by about 30%, although the rate of oxidation of both specimens at the end of the experiment was nearly the same . The rate of oxidation of the conventionally processed alloy was greater during the first several hours of the oxidation experiment at 700°C than at 600°C. At the end of the 50h experiment, the oxidation rate of the conventionally processed alloys oxidized at 700°C dropped to a rate below that of the same alloy oxidized at 600°C.

5.2.2.1. Conventionally Processed Fe-2.5Cr-2.5Al Alloy

Figure 5.72 shows the surface and cross-section of the scale formed on a conventionally processed Fe-2.5Cr-2.5Al alloy that was oxidized for 50h at 400°C. The scale was uniform and less than 0.2μm thick. Figure 5.73 shows a RHEED pattern taken from the scale surface. The measured diffraction diffraction lines are indexed to α-Al_2O_3. This is the same result obtained for the conventionally processed Fe-4Cr-4Al alloy oxidized at the same temperature.

Figure 5.74 shows the surface of the scale formed on a conventionally processed Fe-2.5Cr-2.5Al alloy that was oxidized for 50h at 500°C. The scale surface is covered with pits and linear depressions. An EPMA image and elemental X-ray intensity maps of a cross-section through the scale is shown in Figure 5.75. The scale is about 6μm thick and, based on light microscopy, consists of three layers. The two outer layers contain iron; the presence of chromium or aluminum in this layer was not detected. The 1μm thick inner layer contains iron, chromium, and aluminum and the iron content of the inner layer is less than that of the outer two layers. X-ray diffraction from the scale surface generated diffraction peaks corresponding to Fe_2O_3, Fe_2O_3, and $Fe(Cr,Al)_2O_4$. As with the iron oxide patches formed on the conventionally processed Fe-4Cr-4Al alloy that was oxidized at this temperature, this scale probably consists of an outer layer of α-Fe_2O_3, a middle layer of Fe_3O_4, and an inner layer of $Fe(Cr,Al)_2O_4$.

Figure 5.76 shows the scale surface of a conventionally processed Fe-2.5Cr-2.5Al alloy that was oxidized at 600°C for 50h. The scale was uniform and the surface appeared porous with some whisker growth. An EPMA and elemental X-ray intensity images of a cross-section through the scale is shown in Figure 5.77. The entire scale is approximately 25μm thick and consists of three layers. In Figure 5.77 (a) the interfaces between the three oxide layers are indicated by arrows. The outer two layers contain only iron. The inner scale layer is about 10μm thick and contains cracks that run parallel to the alloy surface. The inner scale layer contains iron, chromium, and aluminum. X-ray diffraction of the scale surface generated diffraction peaks for Fe_2O_3, Fe_3O_4 and $Fe(Cr,Al)_2O_4$, which in conjunction with the elemental intensity maps suggests that these three compounds comprise the top, middle, and bottom layer, respectively. The oxide scale was not very adherent to the alloy surface and separated in the $Fe(Cr,Al)_2O_4$ layer.

Figure 5.78 shows the surface of the scale formed on a conventionally processed alloy oxidized at 700°C for 50h. Linear depressions are seen on the scale surface and correspond to grain boundaries in the underlying alloy. Figure 5.78(b) shows the oxide scale that had formed over two grain boundary triple points in the alloy. The scale on this alloy was non-adherent and Figure 5.79(c) shows a region of the oxidation coupon where a large section of scale had spalled during cooling. The scale that formed on this alloy had two different morphologies in cross-section when oxidized at 700°C. Figure 5.79 shows an EPMA image and elemental X-ray intensity maps of a cross-section through the scale showing one of the two morphologies that were found. This scale contains three layers and is similar to the scale that formed on the alloy when it was oxidized at 600°C. Figure 5.80 shows an EPMA image and elemental X-ray intensity maps of a cross-section through the second type of scale that formed. The scale consists of an external double layer of iron-rich oxide and an internal oxidation zone in the alloy that is

located along the scale/metal interface. The external scale consist of an outer layer of Fe_2O_3 and a very thin inner layer of Fe_3O_4. From the elemental maps, the internal precipitates appear rich in chromium and aluminum. It is difficult to differentiate if the internal precipitates are Al_2O_3 and Cr_2O_3 or $Fe(Cr,Al)_2O_4$. The external scale was non-adherent to the alloy in this region and a gap has formed between the external scale and the alloy. Figure 5.81 shows an EPMA image and elemental X-ray intensity maps of a cross-section through the scale shown in Figure 5.78 at a point where a grain boundary intersects the alloy surface. The external oxide scale is reduced in thickness at the region where the grain boundary meets the surface. This effect is shown in a view of the scale surface in Figure 5.78(b). Also, the formation of internal oxide precipitates is prevented in this region and a continuous oxide layer formed in the alloy branching out from this point.

Figure 5.82 shows the surface of the scale formed on the conventionally processed Fe-2.5Cr-2.5Al alloy that was oxidized at 800°C for 50h. A thin oxide covered a major portion of the specimen surface and a thick oxide growth formed over an extensive area along the specimen edges. Oxide nodules were also apparent at random locations on the alloy surface. Figure 5.83 shows an EPMA image and elemental X-ray intensity images of a cross-section through a nodule. The morphology of the nodule is similar to that of the nodule formed on the conventionally processed Fe-4Cr-4Al alloy that was oxidized at 700°C and is shown in Figure 5.45. The nodule consists of two layers, an outer layer of Fe_2O_3 and an inner layer of $Fe(Cr,Al)_2O_4$. In the elemental intensity map for aluminum shown in Figure 5.83(a), a concentration of aluminum can be seen along the nodule base and along the thin oxide on the alloy surface. Reflected high energy electron diffraction of a region of the thin oxide generated diffraction spots corresponding to α-Al_2O_3.

Figure 5.84 and 5.85 show the surface of the scale that formed on the conventionally processed Fe-2.5Cr-2.5Al alloy oxidized at 900 and 1000°C respectively. Large nodules formed at the edges of the alloy during oxidation at both temperatures and the alloys formed convoluted scales similar to those formed on the conventionally processed Fe-4Cr-4Al alloys oxidized at 900 and 1000°C.

5.2.2.2. Spray-formed Fe-2.5Cr-2.5Al-1Ti-0.6B Alloys

Figure 5.86 shows the surface and a cross-section through the scale formed on a spray-formed Fe-2.5Cr-2.5Al-1Ti-0.6B alloy that was oxidized at 600°C for 50h. This alloy was spray-formed at a 0.23m (9in) substrate distance and had a grain size of approximately 9μm. At high magnification, the scale does not appear homogeneous and consists of patches that are slightly thicker than some of the surrounding oxidation product. The cross-section shown in Figure 5.86(b) shows that the oxide is less than 1μm thick and some thickness variation does exists between an oxide patch and the thinner surrounding oxide. By contrast, the oxide scale that was formed on the conventionally processed Fe-2.5Cr-2.5Al alloys at this temperature was 25μm thick after 50h. The dark spots shown in Figure 5.86(b) are the coarse titanium diboride particles in the alloy that were shown in Figure 5.16.

Figure 5.87 shows low and high magnification images of the scale formed on the spray-formed Fe-2.5Cr-2.5Al-1Ti-0.6B alloy that has a 9μm grain size after oxidation at 700°C for 50h. At low magnification, the oxide appears homogeneous. At high magnification, it is seen that the scale consists of thick mounds that are separated by a thin oxide. By comparing the oxide surface shown in Figure 5.87(b) with an optical micrograph of the alloy that is shown in Figure 5.16, it is apparent that the thinning of the scale occurs over alloy grain boundaries. The thick islands of scale form over grain interiors away from the point where grain boundaries intersect the alloy surface. An EPMA image and elemental X-ray intensity maps of a cross-section through the scale are shown in Figure 5.88. The scale islands are

less than 5μm thick and are separated by a thin oxide that is appears to be much less than 1μm thick. In the central portion of Figure 5.88(a), an internal oxidation zone is apparent beneath an oxide mound. Indicated by arrows are TiB_2 particles becoming incorporated into the external scale. The upper portion of the scale mounds contain iron with no indication of the presence of chromium, aluminum, or titanium. At the base of the islands a dark band of scale is present that contains iron, chromium, aluminum, and some titanium. X-ray diffraction of the scale surface generated peaks for Fe_2O_3, $Fe(Cr,Al)_2O_4$, and α-iron.

Figures 5.89 and 5.90 show the morphology of the scale formed on a spray-formed Fe-2.5Cr-2.5Al-1Ti-0.6B alloy that has a 1μm grain size after oxidation at 600 and 700°C respectively. Figure 5.89 shows the surface and cross-section of the scale that formed on the alloy when oxidized at 600°C for 50h. The scale was found to be very thin and to contain a few scattered oxide patches of the type formed on the coarser grained, spray-formed alloy that was oxidized at 600°C. X-ray diffraction of the surface of the thin scale region generated small peaks for Fe_2O_3 and $Fe(Cr,Al)_2O_4$ along with α-iron.

Figure 5.90 shows the surface of the scale formed on the spray-formed alloy oxidized at 700°C for 50h. As compared to the scale formed on the coarser-grained, spray-formed alloy that was oxidized at 700°C, there are much fewer of the scale mounds present. Figure 5.91 shows an EPMA image and elemental X-ray intensity maps of a cross-section through the scale shown in Figure 5.90. The scale has the same general morphology as that formed on the coarser-grained, spray-formed alloy that was oxidized at 700°C. The islands consists of an outer iron-rich later and an inner layer composed of iron, chromium, and aluminum. An internal oxidation zone is present beneath some of the surface oxide. Titanium does not appear to be concentrated in the scale to any substantial extent.

5.2.2.3. Powder Processed Fe-2.5Cr-2.5Al-1Ti-0.6B Alloy

Figure 5.92 shows the surface and cross-section of the scale formed on the powder processed Fe-2.5Cr-2.5Al-1Ti-0.6B alloy that had a grain size of about 1μm after oxidation at 600°C for 50h. The oxide was very similar to that formed on the fine-grained, spray-formed alloy oxidized at this temperature, which is shown in Figure 5.89(a). The scale was uniform and less than 1μm thick. X-ray diffraction of the scale surface produced minor peaks for Fe_2O_3, $Fe(Cr,Al)_2O_4$, and major peaks corresponding to α-iron.

Figure 5.93 shows the surface of the scale formed on the powder processed alloy oxidized at 700°C for 50h. In Figure 5.93(a), it is shown that certain powder particles contained in the alloy have oxidized to produce scales of slightly different thickness. Figure 5.93(b) shows that the scale is similar to that which formed on the coarse-grained, spray-formed alloy except that the scale islands are of a smaller size. Unlike with the coarse-grained alloy, the islands do not correspond with the alloy grain size of this alloy, which is about 1μm. Figure 5.94 shows an EPMA image and elemental X-ray intensity maps of a cross-section through the scale shown in Figure 5.93. The scale has a similar morphology to that formed on the spray-formed alloys oxidized at 700°C, consisting of an iron-rich outer layer and an inner layer containing iron, chromium, and aluminum. Also present is an internal oxidation zone that is located beneath an oxide mound.

Figure 5.95 shows the surface and cross-section through the scale formed on the powder processed alloy in a region where abnormal grain growth had occurred during consolidation. The microstructure of this region of the alloy is shown in Figure 5.33. The scale that formed over the large grained area of the alloy is noticeably thicker than that which has formed over the unrecrystallized, fine-grained region. In Figure 5.95(b) the edge of the thick oxide mound is scalloped. This shows the interface between fine-grained powder particles and the

recrystallized region. Figure 5.95(c) shows an EPMA image of a cross-section through a thick oxide region. The prior boundaries of unrecrystallized powder particles can be seen in the alloy. Over the large-grained region, a three-layered scale that is approximately 8μm thick has formed. The scale thins to less than 1μm over the fine grained alloy.

6. DISSCUSION

The discussion section is divided into two parts, alloy processing and alloy oxidation. In the processing section, the microstructural evolution and stability of the spray-formed and powder-processed alloys are discussed. An analysis of grain boundary stability is presented. In the oxidation section, the oxidation of the conventionally processed alloys is compared to that of the rapidly solidified alloys. An analysis of the oxidation of conventionally processed and rapidly solidified alloys is presented.

6.1 Alloy Processing

6.1.1. Atomization System Design Considerations

A major portion of this program of research and the necessary first step in its successful completion was the development of a laboratory scale, inert gas atomization system. A few comments will be made on the outcome of this part of the work. The atomization system proved to be capable of producing both rapidly solidified powdered alloys and spray-formed alloys that are comparable with those produced with much larger units. Problems with alloy contamination, expense, and long scheduling and turn around times were eliminated by the construction of an in-house facility for the production of rapidly solidified alloys.

The main design flaw in the system was an inadequate chamber length. At the time of construction, the most reliable estimate of the particle solidification distance was on the order 0.46m (l.5ft).[94] The atomization system was designed so that the distance from the atomization nozzle to the chamber bottom was twice this value. It was found that for atomization pressures greater than approximately 5.52Mpa (800psi), molten droplets were accelerated in the atomization chamber to such an extent that they were molten or partially molten when striking the bottom. Since refinement in microstructure is dependent on particle size and particle size is most conveniently decreased by increasing atomization pressure, the present

chamber length can be a serious processing limitation. The chamber was constructed from standard vacuum components in anticipation of such problems and a section can easily be installed to lengthen the chamber for future work that requires the use of atomization pressures in excess of 5.52Mpa (800psi).

A second design consideration concerns the atomization nozzle. A great deal of difficulty arose from the requirement that the melt pour tube act as a deflector for the atomization jets in order to obtain aspiration at the pour tube opening. An improvement in the design would consist of redesigning the atomization nozzle to decrease the included angle of the gas jets to obtain an aspirating condition without the necessity of a pour tube being present. This would have two major advantages. First, the pour tube length could be shortened to alleviate cooling by the atomization gas jets. This would allow a reduction in the melt superheat necessary to prevent freezing of the pour tube and possibly allow some control of melt temperature at the point of atomization. A second advantage is that the efficiency of the atomization process could be improved. The use of a shorter pour tube would allow the atomization gas jets to contact molten metal flowing from the pour tube directly and increase the kinetic energy transfer from the gas to the liquid metal.

6.1.2. Microstructural Evolution of Powder Processed Alloy

The powder particle that is shown in Figure 5.25(a) shows a solidification microstructure that has a morphology similar to that which is often observed in a slowly cooled casting.[95] The columnar grain region indicates that grains had nucleated initially at the particle surface and advanced into the liquid toward the center of the particle. This suggests that a temperature gradient had existed in the powder particle, at least during the initial stages of solidification, and cooling had not been Newtonian as is often assumed during atomization.[96,97,98,99] Before the columnar grains had reached the center of the powder particle, random nucleation

of iron occurred in the remaining liquid and formed the equiaxed microstructure shown in the interior of the powder particle. As discussed by Mehrabian and coworkers,[100] the condition for Newtonian cooling of droplets is that the Biot Number, hR/κ, be less than 0.1. Here h is the interface heat transfer coefficient, R is the droplet radius and κ is the thermal conductivity of the alloy. According to Mehrabian, interfacial heat transfer coefficients on the order of 40kJ/m^{2}s are obtained for convectively cooled droplets and Newtonian cooling applies for droplets less than 100μm in diameter. Wood and Honeycomb[101] came to the same conclusion and stated that only in a situation were the molten alloy was in intimate contact with a substrate, such as with laser glazing, would a high enough interfacial heat transfer coefficients be obtained to produce a departure from Newtonian cooling. However, Cantor[102] reviewed the rapid solidification of iron-base alloys and pointed out that direct experimental evidence shows that Newtonian cooling does not always occur. Cantor measured the cooling rate of splat quenched iron alloys of varying thickness and used the results to calculate interfacial heat transfer coefficients and Biot numbers that were in the range of 0.1 to 1.30. Since the alloys were cooled by a substrate, it is not surprising that the Biot numbers are slightly larger than those predicted by Mehrabian for convective cooling. With the atomized Fe-2.5Cr-2.5Al-1Ti-0.6B alloy powder, columnar grain growth was observed only in powder particles with a diameter greater than about 30μm. Smaller particles completely lacked the columnar growth and consisted entirely of a very fine equiaxed structure. Since the Biot number varies directly with particle size, this observation is consistent with a transition from non-Newtonian to Newtonian cooling at a particle size of about 30μm.

The presence of the amorphous phase that formed during atomization of the Fe-2.5Cr-2.5Al-1Ti-0.6B alloy was an unexpected result. Slaughter[103] had atomized Fe-Al intermetallic alloys that contained titanium and boron and reported

the presence of a TiB_2 dispersion in the alloy after consolidation of the powder. Powell et al.[104] characterized the microstructure of rapidly solidified Fe-Cr-Si alloys that also contained titanium and boron. The TiB_2 was found as a fine dispersion throughout the alloy. In both cases, the powder product was not characterized by transmission electron microscopy prior to consolidation and it was evidently assumed that the TiB_2 particles observed in the consolidated, alloy were formed by solidification from the melt.

The amorphous phase that formed in the atomized Fe-2.5Cr-2.5Al-1Ti-0.6B alloy is just barely resolved in the optical micrograph shown in Figure 5.25. The phase is seen as a thin film between the columnar and equiaxed grains and between the poorly formed, stubby dendrite arms of some of the grains. The composition profile across a band of the amorphous phase shows a high concentration of chromium and titanium in the amorphous phase relative to the matrix. The amorphous phase also contains an appreciable amount of iron. The presence of boron and its distribution in the solidification microstructure could not be determined because of the poor sensitivity of the X-ray detector to this element. Boron has a solubility in α-iron that is less than 50ppm[105] and a partition coefficient that is about 0.05.[106] These factors indicate that that boron is strongly partitioned during conventional solidification and might be strongly partitioned during during rapid solidification. Since there was no indication of the formation of boride particles in the α-iron matrix after long term anneals at temperatures up to 1000°C, it is reasonable to assume that boron was not supersaturated in the α-iron matrix and nearly complete partitioning of this element occurred during solidification. It appears that after nucleation and growth of primary α-iron grains in the atomized droplets, the interdendritic, iron-rich, liquid became enriched in titanium, chromium, and boron to a level where the liquid transformed to an amorphous solid. Boron-transition metal alloy systems are well known to be easy

glass formers because of the low eutectic temperatures that are commonly found in these systems. Shastry et al[107] has demonstrated that an Fe-13 at %Ti-20 at % B alloy could be solidified to form an amorphous solid by melt spinning.

Kelly et al.[108],[109] observed the same type of solidification behavior in a rapidly solidify high-phosphorous content austenitic steel. In this alloy, chromium and phosphorous were partitioned to the interdendritic liquid during solidification, resulting in the formation of what was termed an intercellular amorphous phase. The powdered alloy was consolidated by hot extrusion at 950°C which resulted in complete recrystallization of the amorphous phase. The recrystallization temperature of the amorphous phase to γ-iron was found to be about 500°C. Precipitates had formed in the alloy during consolidation and were identified as chromium carbides.

At the time the powdered Fe-2.5Cr-2.5Al-1Ti-0.6B alloy was hot isostatically processed, TEM specimens of the powder had not been prepared successfully and the existence of the amorphous phase was not known. Special annealing precautions, prior to or during consolidation, were not considered in order to crystallize the the amorphous phase to produce an optimum dispersion of fine particles. Fortunately, the hot isostatic pressing cycle that was used for consolidation, which is shown in Figure 4.9, resulted in crystallization of the amorphous phase and formation of the desired dispersion of TiB_2. As shown in Figure 5.30, the dispersion of TiB_2 particles is not uniform but the particles are clustered in interconnecting regions. Only a small number of particles were observed in grain interiors. The clusters are most likely positioned in regions were the interconnected amorphous phase had been present. Figure 5.30(b) shows a region in the alloy that is close to the point where four powder particles meet. There is a high density of TiB_2 along the prior particle boundaries which indicates

that the powder surface may have been covered by the amorphous phase prior to consolidation.

It is important to note that all the particles identified in the alloy were titanium borides. Atomized alloy powder generally contains appreciable amounts of oxides which are evident on prior particle boundaries in the consolidated alloy. For the rapidly solidified Fe-Cr-Al-Ti-B alloys, the presence of the glassy phase coating the powder particles may have prevented or hindered oxidation of the particle surfaces during atomization.

A key difference between the development of an amorphous phase in this alloy and the high-phosphorous austentic steel studied by Kelly, is that in the case of the high-phosphorous steel, the amorphous phase crystallized to austenite during high temperature consolidation and the precipitates in the alloy were formed by the combination of chromium with residual carbon in the alloy. In this work, the precipitate forming elements, titanium and boron, are both concentrated to the interdendritic region and are the precipitate forming elements. The importance of this is that consolidation of the powder and crystallization of the amorphous Fe-Cr-Ti-B phase results in the formation of precipitates lying preferentially along alloy grain boundaries. Grain boundary pinning, in this case, is more efficient for a given volume fraction of precipitates than if the distribution were uniform.

The presence of the amorphous phase presents a further possibility for developing alloy microstrucure. It should be possible to control crystallization of the amorphous phase by heat treatment of the powder prior to consolidation. By annealing the powder at certain temperatures (probably below the temperature at which the present material was hot isostatically pressed), it should be possible to increase the number of TiB_2 nuclei and obtain a finer dispersion that is more effective in stabilizing the grain size.

6.1.3. Microstructural Evolution of Spray-Formed Alloys

It was found that the insulating properties of the melt pour tube and the substrate position were interrelated and had a great bearing on the microstructure of the spray deposit. The difference in the grain size and particle size of the spray-formed Fe-2.5Cr-2.5Al-1Ti-0.6B alloys that were processed at a 0.23m (9in) and 0.64m (25in) substrate distance can be attributed to the difference in the temperature of the alloy at the point of atomization. The Fe-4Cr-4Al-1Ti-0.6B alloy was processed first using the non-insulating type pour tube shown in Figure 4.3(a). With this pour tube design, cooling of the melt during transfer through the tube was sufficient to often cause freezing and plugging of the pour tube opening. When the Fe-4Cr-4Al-1Ti-0.6B alloy was successfully atomized, the melt temperature was probably only slightly above the freezing range of the alloy. After atomization, a flight distance of only 0.23m (9in) was required to cool the droplets to the extent that the microstructure shown in Figure 5.5 was produced upon deposition. When the insulation type pour tube was used for the processing of the Fe-2.5Cr-2.5Al-1Ti-0.6B alloy, a flight distance of 0.64m (25in) was required to obtain the same microstructure as shown in Figure 5.19. This is an indication that the volume fraction of solid in the spray and the temperature of the spray was about the same at the point of contact with the substrate in the two cases.

Another indication of cooling of the melt during transfer in the non-insulation type pour tube was the presence of large boride particles in the spray deposited Fe-4Cr-4Al-1Ti-0.6B alloy as shown in Figure 5.10. These particles were clearly visible even by optical microscopy. Particles of this size were not observed in the spray-formed Fe-2.5Cr-2.5Al-1Ti-0.6B alloy that was processed using the insulating pour tube with a substrate distance of 0.64m (25in). It is possible that the large TiB_2 particles precipitated from the cooling melt during transfer in the non-insulating pour tube prior to atomization. The Fe-2.5Cr-2.5Al-1Ti-0.6B alloy that

was processed using the insulating pour tube had a higher melt temperature at the point of atomization and TiB_2 had not yet precipitated from the melt. The question that then arises is at what temperature does TiB_2 precipitate from the melt. Using the available thermodynamic information that is shown in Appendix 1[110,111], the free energy change for the reaction:

$$Ti_{(wt\%)} + 2B_{(wt\%)} = TiB_{2(s)} \qquad (4)$$

was calculated as a function of melt temperature from 1600°C to the temperature where α-iron began to crystallize, ~1580°C. For the calculation, the assumption was made that the interaction coefficients did not vary with temperature. It was found that at 1580°C the free energy change for the formation of TiB_2 is -8.6 kcal, indicating that TiB_2 would be formed as a secondary inclusion after the formation of primary ferrite, and should not form as large blocky precipitates in the melt.

The spray-formed Fe-4Cr-4Al-1Ti-0.6B alloy processed at a 0.23m (9in) substrate distance and the Fe-2.5Cr-2.5Al-1Ti-0.6B alloy processed at a 0.64m (25in) substrate distance had similar microstructures, a grain size on the order of 1μm and a dispersion of TiB_2 particles that had dimentions generally less than 200nm. It is not known whether an amorphous phase formed in these alloys during spray-deposition. The spray-formed alloy was cooled during solidification not by convection, as was the powdered alloy, but by conduction; i.e., by heat transfer through the previously deposited material. It is generally the case that cooling by heat conduction to a substrate occurs at a greater rate and results in finer microstructures than cooling by convection. In the case of spray forming, solidification does not occur on a cooled substrate but on previously deposited material that may be at a fairly high, although undetermined, temperature. Judging from the brightness of the deposit during spray forming, the deposit temperature

was well above 1000°C. The fine-grained, spray-formed alloys and the powder processed alloy after consolidation had a grain size that was between 0.5 and 1μm in size which suggests that the cooling rate was on the same order for both cases. Furthermore, the TiB_2 particles in the two fine-grained, spray-formed alloys were located in interconnected, clustered regions in the same manner as the consolidated powdered alloy. If an amorphous phase was formed in these two spray-formed alloys, crystallization of TiB_2 could have taken place while the deposit was at a high temperature, during or immediately after the spray-forming operation. Alternately, recrystallization could have occurred during the anneal after hot rolling. Since the as spray-formed material could not be thinned successfully for TEM observation due to porosity in the deposit, direct evidence supporting crystallization having taken place either during the spray-forming operation or during subsequent thermo-mechanical processing was not obtained. However, dislocation pile-ups were evident around TiB_2 particles in the rolled alloy after annealing. This indicates that the particles were present before the rolling operation and that they had, therefore, formed during the spray-forming process while the deposit was at a high temperature.

The spray-formed Fe-2.5Cr-2.5Al-1Ti-0.6B alloys that were processed at 0.23, 0.28, 0.38, and 0.48m (9,11,15, and 19in) substrate distances showed evidence that liquid metal had collected on the deposit surface during the spray forming process. The alloys had nearly identical microstructures and the same density, which indicates that solidification occurred in a similar fashion for each deposit. The alloy in this group that was spray-formed at the longest substrate distance, 8m (19in), contained powder particles that had been partially remelted. This indicates that some of the smaller powder particles that had solidified in flight by the time the substrate was reached were subsequently immersed in the molten pool on the deposit surface. At the shorter substrate positions, the atomized spray

was cooled less at the point of deposition and any small, presolidified powder particles had completely remelted upon contact with the molten metal in the deposit.

It was surprising that the spray-formed Fe-2.5Cr-2.5Al-1Ti-0.6B alloys that were processed at the shorter substrate positions had such a fine grain size even though the alloys had solidified from a liquid pool. Previous work with an alloy of similar composition and processed in the same manner formed a very different microstructure. A spray-formed Fe-10Cr-8Al-1.5Mn-0.6S alloy formed a liquid pool during processing became too short a substrate distance had been used.[112] The core of the deposit had solidified to form very large columnar grains. The formation of very fine grains in the Fe-2.5Cr-2.5Al-1Ti-0.6B alloy can be attributed to the presence of titanium and boron. Titanium diboride is used as a grain refining agent in aluminum castings[113] and to a lesser extent in steel castings.[114] In aluminum castings, TiB_2 particles are believed to act as potent heterogeneous nucleation sites for the formation of primary aluminum crystals. In steel castings, the mechanism that produces the fine grained casting is more complex. Titanium diboride is dissolved into the melt and upon cooling titanium combines with carbon in the melt to form titanium carbide. Titanium carbide, rather than TiB_2 provides the nucleation site for α-iron grains. Boron is believed to prevent grain growth during solidification by being rejected ahead of the advancing liquid/solid interface and results in the formation of a low-melting point liquid that surrounds and slows the growth of the α-iron grains. The slowing of grain growth into the melt, in turn, allows more nucleation events to occur. The carbon content of the spray-formed alloy shown in Figure 5.16 was less than 0.040 wt% so it is likely, in this case, that TiB_2 played a part in increasing the nucleation rate of the iron crystals.

For the Fe-2.5Cr-2.5Al series of alloys, the possibility exists that the alloy could go through a phase transformation upon cooling. Figure 6.1 shows the

phase diagram and the gamma region in the iron-rich corner of the iron-chromium-aluminum phase diagram.[115] The ternary Fe-2.5Cr-2.5Al composition appears from the phase diagram to be very close to the α-iron/(α-iron+γ-iron) surface at 900°C, but the conventionally processed Fe-2.5Cr-2.5Al alloy was found to retain a columnar grained microstructure, typical of castings, after solidification and cooling of the ingot to room temperature. This indicates that the ternary composition does not pass through the γ-iron phase field. Titanium is a very strong ferrite stabilizer.[116] Boron appears to have little effect on expanding or contracting the austenite phase field.[117] Thus, the net effect of the addition of titanium and boron to the ternary alloy should be to reduce the size of the austenite phase field. It is probable, therefore, that the spray-formed and powder processed Fe-2.5Cr-2.5Al-1Ti-0.6B alloy did not pass through the austenite phase field during solidification or thermo-mechanical processing.

6.1.4. Particle Stability

Titanium diboride was the only precipitate identified in the rapidly solidified alloys. Figure 6.2 shows the standard free energy of formation of the various boride particles that can form in the Fe-Cr-Al-Ti system. Titanium diboride is by far the most stable boride. The TiB_2 particles in the rapidly solidified alloys did not appear to coarsen after annealing at temperatures up to 1000°C for times up to 300h. The only coarse TiB_2 particles observed were those in the spray deposited Fe-4Cr-4Al-1Ti-0.6B alloy that most likely formed in the melt prior to atomization. In general, fine TiB_2 particles in iron-base alloys have been found to resist coarsening at elevated temperatures. Michal et al.[118] found that TiB_2 particles in a melt spun austenitic steel coarsened from a size of 0.01μm to 0.2μm after annealing at 1000°C for 3h. Bourdeau[119] produced rapidly solidified Fe_3Al intermetallic alloys containing a TiB_2 dispersion and found that the particles did not

coarsen to a size greater than 0.18μm when held at a temperature of 1093°C for 3h.

As discussed previously, the rate of coarsening of the TiB_2 particles in the rapidly solidified alloys should be determined by the product $D_{Ti}C_{Ti}$ or D_BC_B, , depending on which product is lower. According to Olsen et al[120] there are two advantages in adjusting the concentrations of the elements in the alloy that form the precipitate to the stochiometric ratio, as was done in this work. First, the volume fraction of precipitate in the alloy will be maximized for a given composition product, $(C_{Ti})(C_B)^2$ and secondly, the concentration of both elements in the alloy matrix is minimized and coarsening of the particles will be controlled by the slower diffusing of the two elements. Using the diffusivities of titanium[121] and boron[122] in α-iron, and the Lifshitz-Slyozov-Wagner equation which is

$$\bar{r}^{-3} - \bar{r}_o^{-3} = \frac{8\,DC}{9\,RT}\,\sigma V_p^2\,t, \qquad (2)$$

an estimate can be made of the coarsening resistance of TiB_2 in α-iron. The variables in Equation 2 were defined previously in section 2.1.4. The diffusion coefficient of titanium and boron are plotted as a function of temperature in Figure 6.3. The maximum temperature that the rapidly solidified alloys were annealed at was 1000°C, so at this temperature the coarsening resistance will be estimated. As shown in Figure 6.3, titanium has a diffusivity that is almost four orders of magnitude less than that of boron at 1000°C. Because the concentrations of titanium and boron in the alloy are on the same order, it is expected that the transport of titanium in the alloy controls the coarsening rate of the TiB_2 particles. The solubility product of TiB_2 in iron is not known , and thus, limiting values for the concentration of titanium were used to obtain an estimate of the maximun coarsening rate. With the exception of the powder processed alloy, all the rapidly

solidified alloys had titanium concentrations that were slightly greater than the stochiometric value. If all the boron in the alloys combined with titanium, there would be 0.33 wt. % of excess titanium in the alloy matrix. This will be used as the worst case and it will be assumed that the concentration of titanium in the alloy is 0.33 wt. % ($C = 1.5 \times 10^{-3}$ moles/cm^3). This concentration of titanium is below the maximum solubility of titanium in pure iron, which has been determined to be 2.5 wt. % at 600°C and 6.3 wt. % at 1350°C.[123] The TiB_2/ α-iron surface energy is taken as a relatively high value of 2500 mJ/m^2 which gives a high value to the coarsening rate,[124] The molar volume of TiB_2 is 15.35cm^3/mole. Using these values in Equation 2, it is found that a particle initially 0.1μm in diameter increases in size to 0.3μm after annealing at 1000° for 100h. The TiB_2 particles were not observed to coarsen to this extent. It is possible that the excess titanium in the alloy lowered the boron concentration to a value where the transport of boron and not titanium controlled the coarsening rate of the TiB2 particles.

6.1.5. Grain Size Stability

Although the rapidly solidified alloys completely resisted normal grain growth, both the spray-formed and powder processed alloys were shown to be susceptible to abnormal grain growth. The abnormal grain growth tendency was clearly related to strain which had occurred in the alloys during thermo-mechanical processing. The spray deposited alloy had been hot rolled and showed a tendency for abnormal grain growth to occur initially at the surfaces of the rolled strip. At higher temperatures and at longer times, the extent of abnormal grain growth toward the center of the strip increased. The abnormal grain growth in the rolled strip is a result of inhomogeneous strain that had occurred during the rolling operation. As described by Schey,[125] sticking friction between the work piece and the roll results in an extrusion effect, causing a backward flow of originally vertical planes in the entry zone of the rolls, and a forward curvature in the exit zone. This

effect is termed redundant work and leads to a strain gradient in the through thickness direction of the rolled strip. The center of the strip receives the minimum amount of strain and the edges the greatest amount of strain. For the spray-formed alloy, the greatest driving force for abnormal grain growth existed at the strip surface where the stored work and dislocation density was the greatest.

The unusual shape of the recrystallized regions in the hot isostatically pressed Fe-2.5Cr-2.5Al-1Ti-0.6B alloy powder was a result of significant strain that occurred in the end regions of the can during consolidation. Abnormal grain growth occurred only in the regions at the ends of the can that was used for encapsulating the alloy powder. In regions away from the ends of the can, the powdered alloy was subjected to an isostatic pressure and had undergone plastic deformation only to the extent that was necessary to fill in the space between the powder particles. At the can ends, the crimped and welded seam constrained deformation of the can so that force on the alloy powder was not isostatic. The powdered alloy flowed in the can in response to the force and the recrystallized bands shown in Figure 5.33 represent the regions in the alloy that had been strained during consolidation.

The usefulness of fine-grained, rapidly solidified alloys as oxidation resistant materials depends on the ability of the alloys to be processed in a manner that will prevent the occurrence of abnormal grain growth and the loss of oxidation resistance. It is necessary, therefore, to analyze the abnormal grain growth characteristics and establish microstructural and processing requirements that stabilize a fine grain size. According to Zener's model, a distribution of particles with a diameter of 0.1μm and a volume fraction of 0.03 yields a limiting alloy grain size of 4μm. This relationship assumes a homogeneous distribution of particles throughout the alloy matrix and does not consider the presence of strain energy in

the alloy matrix. In the present case, the particle distribution is not uniform and strain energy in the alloy plays a major role in grain size stability.

An analysis can be carried out by calculating the forces generated on a boundary that ispinned by an array of particles and that is subjected to driving pressures that originate from a reduction in both grain boundary area and stored strain energy. A schematic diagram of the particles, boundary, and relevant forces is shown in Figure 6.4. The particles are assumed to lie preferentially on a grain boundary that separates a recrystallized region from strained region.

In this analysis, the experimentally determined particle size and spacing of the rapidly solidified alloys is first used to determine the critical dislocation density above which boundary detachment and abnormal grain growth occurs. Using this result a diagram can be constructed that indicates the necessary combination of particle size, spacing, and volume fraction of particles required to stabilize grain boundaries in an alloy that contain a certain dislocation density.

The driving pressure that results in grain boundary migration can arise from a reduction in grain boundary energy, a reduction in plastic strain energy, and a phase transformation. Phase transformations can provide the largest driving forces for boundary migration; however, the Fe-Cr-Al alloys processed in this work remained in the α-iron phase field during processing so phase transformation will not be considered. Following a similar analysis that was carried out by Ashby,[125] the driving pressure due to grain coarsening is given by

$$P \approx \frac{\gamma}{d} \qquad (5)$$

where γ is the boundary energy and d is the grain size. Plastic deformation generally leads to higher driving pressures and is given by the relation

$$P \approx \frac{1}{2} G b^2 \rho \qquad (6)$$

where G is the shear modulus, b is the Burger's vector and r is the dislocation density. The total pressure is taken as the sum of the terms on the right hand side of Equations 5 and 6.

As illustrated in Figure 6.4, a boundary pinned by a particle exerts a force on a particle

$$F_p = A_p P \qquad (7)$$

where A_p is the average area of boundary per particle. In this analysis the particles are assumed to lie in a square array on the boundary and A_p is then equal to the square of the particle spacing. The maximum force that the particle can exert on the boundary is obtained by multiplying three terms; the boundary area that is blanked off by the particle (πr^2), the boundary surface energy (γ), and the inverse of the distance the boundary moves in pulling away from the particle (1/r); i.e.,

$$F_{max} = \pi r \gamma \qquad (8)$$

For a uniform distribution of particles, Ashby[126] has given the average area per particle as

$$A_p = \frac{2}{3} \frac{\pi r_0^2}{f} , \qquad (9)$$

where f is the volume fraction of particles. Combining Equations 7, 8, and 9, yields the pressure at which grain migration occurs;

$$P \geq P_{max} = \frac{3}{2}\frac{f\gamma}{r_0}. \qquad (10)$$

For the rapidly solidified alloys processed in this work, the particles were distributed on grain boundaries and the area per particle is given by

$$A_p = X^2, \qquad (11)$$

instead of Equation 9, where X is the interparticle spacing. The force per particle is now given by

$$F_p = X^2 P, \qquad (12)$$

and detachment of the grain boundary occurs when

$$P \geq P_{max} = \frac{\pi \gamma r_0}{X^2} \qquad (13)$$

Assuming that grain boundary migration occurs only from a reduction in the grain boundary area and plastic strain energy, the driving pressure is given by

$$P \approx \frac{\gamma}{d} + \frac{1}{2} G b^2 \rho \qquad (14)$$

Finally, for an alloy that does not undergo normal grain growth, detachment occurs when the dislocation density exceeds a critical level defined by

$$\frac{\pi \gamma r_0}{x^2} = \frac{\gamma}{d} + \frac{1}{2} G b^2 \rho^* \qquad (15)$$

where ρ^* is the critical dislocation density required to cause detachment of the grain boundary from the particle array.

To calculate the critical dislocation density for the fine grained rapidly solidified alloys processed in this work, the following values were used in Equation 15; a grain boundary energy of 1J/m2, a shear modulus of 79GPa, a Burger's vector of 0.248nm, a particle radius of 0.05μm, and a particle spacing of 0.2μm. The calculated critical dislocation density is to $1.2X10^{15}m^{-2}$. Assuming a uniform distribution of the same size and volume fraction of particles yields a dislocation density of $3.70X10^{14}m^{-2}$. This indicates that by having the particles preferentially on the grain boundaries, the dislocation density can be increased by about a factor of three without causing boundary migation. A well annealed polycrystalline alloy typically has a dislocation density on the order of 10^9 to $10^{12}m^{-2}$ while a heavily worked alloy can have a dislocation density up to $10^{16}m^{-2}$.[127] It is therefore, reasonable to expect these rapidly solidified alloys to undergo abnormal grain growth if highly strained. It would be useful to know to what extent the rapidly solidified powder and spray-formed deposit could be worked during processing and still have a dislocation density below the critical value. This would require that a relationship between strain and dislocation generation for the alloy be known. This relationship is generally material and process dependent and must be determined experimentally. For instance such factors as alloy grain size, the

presence of a dispersed second phase, and working temperature greatly affect dislocation multiplication during deformation processing.

The critical dislocation density was also calculated for the case of the large-grained, spray-formed alloy. A grain size of 10μm with a particle radius of 1μm was used for the calculation. It was found that a dislocation density of $3.22X10^{16}m^{-2}$ is required for abnormal grain growth in the alloy. This shows that the large grained alloy should be able to be heavily worked and the grain size remain stable. This was to an extent confirmed in that the alloys showed no sign of grain coarsening when processed in exactly the same manner as the fine-grained alloy with the 1μm grain size.

If the dislocation density in the rapidly solidified alloys was determined for a given processing routine (such as hot isostatic pressing of powder, extrusion of powder, or rolling of a spray-deposit), then it would be useful to know which particle size and spacing is necessary in the alloy to prevent grain boundary detachment and abnormal grain growth. Figure 6.5 shows Equation 15 plotted for various critical dislocation densities in an alloy with a 1μm grain size. For a given dislocation density, regions above the corresponding line indicate combinations of particle size and spacing that stabilize the grain boundaries. In the shaded region, the particle radius is greater than twice the particle spacing and therefore has no physical significance. Superimposed on the plot are volume fractions of second phase particles given by the relationship

$$r = \left(\frac{3}{4} \frac{f_v x^2}{\pi} \right)^{1/3} \qquad (16)$$

The diagram in Figure 6.5 could be used in a number of ways as a processing guide for the rapidly solidified Fe-Cr-Al-Ti-B alloys. Both the powder processed and spray-formed alloys had a grain size of about 1μm so Figure 6.5 can be directly applied to alloys processed by both methods. If the dislocation density in an alloy was known for a given thermo-mechanical treatment, then the attempt could be made to control particle size and particle spacing to place the alloy in the region where grain boundary detachment would not occur. As an example, for the fine-grained rapidly solidified alloys processed in this work, the grain size and particle spacing were not easily adjusted but essentially fixed by the processing method, Figure 6.3 could be used to determine the volume fraction of second phase that must be present to obtain a particle radius that prevents abnormal grain growth.

Since the powder-processed alloy retained the amorphous phase to room temperature, it might be possible to control the nucleation rate of TiB_2, and therefore, the particle spacing by heat treatment of the powder prior to consolidation, as previously discussed. As shown in Figure 6.5, this may be the most effective method for stabilizing the grain size if the particle coarsening rate is very low. For example, the location marked with the X in Figure 6.5 indicates the particle spacing and particle size for the powder-processed and fine-grained, spray-formed alloys processed in this work. As shown, a dislocation density much above $10^{15}m^{-2}$ in this alloy should result in abnormal grain growth. However, if the powdered alloy could be annealed so as to obtain a particle spacing of 0.05μm at the same 0.03 volume fraction of TiB_2(indicated by an O) and then consolidated, the alloy should resist abnormal grain growth even with an extremely high dislocation density in the alloy.

The critical dislocation density was calculated for the case of the large-grained, spray-formed alloy. A grain size of 10μm with a particle radius of 1μm

was used for the calculation. It was found that a dislocation density of $3.22X10^{16}m^{-2}$ is required for abnormal grain growth in the alloy. This shows that the large grained alloy should be able to be heavily worked and the grain size remain stable. This was to an extent confirmed in that the alloys showed no sign of grain coarsening when processed in exactly the same manner as the fine-grained alloy with the 1μm grain size.

6.2. Alloy Oxidation

The oxidation of the conventionally processed alloys at temperatures below 800°C will be discussed first followed by a comparison of the oxidation of the rapidly solidified alloys oxidized at the same temperatures. The oxidation results at 900 and 1000°C will then be discused along with the effect of titanium on oxidation at these temperatures. To help clarify the discussion, a summary of the oxidation products formed on the alloys is presented in Table 6.1.

6.2.1. Oxidation of Conventionally Processed Alloys Between 400 and 800°C

The results obtained in this work for the oxidation of conventionally processed alloys between 400 and 800°C agrees with the results obtained by Boggs[62] and Saegusa and Lee[61] for Fe-Al alloys and Tomaszewicz and Wallwork[59] for Fe-Cr-Al alloys. Particularly, a maximum in the oxidation rate that can be associated with iron oxide formation was found at intermediate temperatures, in this work 600 to 700°C. The oxide scale morphology that was observed on the conventionally processsed alloys oxidized in this temperature range can be divided into four distinct types that are designated types I through IV for discussion. The type I oxide scale consists of an external iron-rich oxide that comprises an outer layer of Fe_2O_3 and an inner layer of Fe_3O_4. In addition, oxide particles rich in aluminum and chromium that were formed by internal oxidation were present in the alloy matrix adjacent to the external scale. The type II oxide consisted of a continous, external layer of iron-rich oxide that comprised three layers, an inner layer of $Fe(Al,Cr)_2O_4$, a middle layer of Fe_3O_4, and outer layer of Fe_2O_3. Alloys that formed the type III scale morphology were covered primarily by an external α-Al_2O_3 oxide scale but also had present on the alloy surface iron-rich oxide mounds. Type IV consists of a homogeneous α-Al_2O_3 layer that on the exterior surface of the alloy. Figure 6.2 indicates the scale formed on the two conventionally processed alloys at each temperature.

Factors that favor the formation of an aluminum oxide scale, and are important in this work, include a high concentration of aluminum and high a diffusion coefficient of aluminum in the alloy, a low concentration and a low diffusion coefficient for oxygen in the alloy, and a low rate of growth of iron oxide. The ratio ($D_{Al}C_{Al}/D_OC_O$) in the alloy is important with respect to control of the supply of aluminum to the surface of the alloy, which is important in determining whether or not an aluminum oxide scale forms on the alloy surface. Figure 6.6 shows the diffusion coefficient of oxygen and aluminum in α-iron as a function of temperature. Also shown are diffusion coefficients for various elements in the grain boundary region of α-iron. Data was not found for to the grain boundary diffusion of aluminum in α-iron; however, the data obtained for grain boundary diffusion of various substitutional elements in α-iron is closely grouped, and the corresponding value for aluminum is assumed herein to be in this range.

6.2.1.1 Type I Scale

This scale morphology was observed only on the conventionally processed Fe-2.5Cr-2.5Al alloy when oxidized at 700°C and fits the classic picture of internal oxidation of a reactive element with simultaneous growth of an external oxide of the more noble base metal. The internal oxide particles are a definite indication if oxygen diffusion into the alloy. In this case, the internal oxide particles are isolated from each other and ineffective in blocking transport of oxygen into the alloy, which would protect the alloy from further internal oxidation. The alloy and internal oxide particles become incorporated into the external iron oxide scale as it thickens.

Figure 5.81 shows clearly the effect of a grain boundary intersecting the alloy surface on the formation of both the external scale and the internal oxide region. A schematic of the micrograph is shown in Figure 6.7. A very thin, continuous oxide formed in the internal oxide region on either side of the grain boundary. The continuous internal scale prevented oxygen diffusion into the alloy,

and thus, prevented formation of internal oxide precipitates. That the grain boundary acted to protect the alloy from oxidation is shown by the thinner external scale that formed over the grain boundary. This is essentially the same effect of grain boundaries on oxidation that was described by Giggens and Pettit for Ni-20Cr alloys.[128]

Away from the grain boundary region aluminum is depleted from the alloy matrix by the formation of oxide particles. The oxygen flux into the alloy is greater than the aluminum flux outward and the internal oxidation front advances into the alloy, generally at a parabolic rate. In the grain boundary, the diffusion coefficient of aluminum is much greater than in the matrix, so aluminum is transported toward the alloy surface along the boundary. As shown in Figure 6.7, aluminum also diffused laterally and intercepted the oxygen, thereby forming a continuous aluminum-rich scale.

Wagner[129] examined internal oxidation of binary alloys and the transition to continuous external cale growth for the case where only one species was oxidized. He determined the critical concentration of reactive element that was required in the alloy to form a sufficient volume fraction of oxide particles near the alloy surface so that oxygen penetration into the alloy is blocked. In the present case, however, an external scale forms on the alloy surface and consumes the surface region of the alloy that contains the oxide particles. This makes these particle and the amount of reactive element that formed them ineffective in aiding in the formation of a blocking layer. When an external scale forms simutaneously with internal oxides, a higher concentration of the reactive element is required in the alloy to form an internal oxide blocking layer.

Mack[130] and reciently Gesmundo and Viani[131] have analyzed the requirments for the formation of a protective blocking layer in the pesence of an external scale. The oxidation results of the conventionally processed Fe-2.5Cr-

2.5Al alloy at 700°C can be analyzed by the methods of these authors and estimates made conerning the necessary diffusion of aluminum required in the alloy to form a protective blocking layer. Figure 6.8 shows a schematic diagram of the oxidation product and representative concentration profiles for aluminum and oxygen in the alloy during oxidation. The internal oxide precipitates were determined to be rich in aluminum and chromium but the oxide phase was not identified. Smeltzer[132] identified the internal, rod-like oxides in an Fe-Al alloy to be of Al_2O_3 at ends of the rod and $FeAl_2O_4$ near the metal/external scale interface. It is likely that a similar situation occured here with $Fe(Cr,Al)_2O_4$ at the metal/external oxide interface.

Following the work of Gesmundo and Viani[133], internal oxidation is assumed to proceed according to a parabolic growth law and is expressed by Wagner's equation

$$\xi^2 = 4\gamma^2 D_0 t \qquad (17)$$

where ξ is the position of the internal oxide front as measured from the original gas/metal interface, D_O is the diffusion coefficient of oxygen in the alloy, γ is a dimensionless parameter related to the parabolic rate constant for internal oxidation, and t is the time that oxidation has taken place. The parabolic growth rate for the outer oxide is given by

$$X^2 = 2 K_c t \qquad (18)$$

where X is the thickness of the metal consumed and K_C is the parabolic growth rate constant for the external oxide scale. The effective thickness of the internal oxide zone is therefore ξ-X.

It is convenient to define a term u as

$$u = \left[K_c / (2\, D_0)\right]^{1/2} \tag{19}$$

The concentration profile of O in the alloy takes the form

$$N_0 = N_0^S \frac{\mathrm{erf}(\gamma) - \mathrm{erf}\left[\, x/2(D_0 t)^{1/2}\right]}{\mathrm{erf}(\gamma) - \mathrm{erf}(u)} \quad \text{for } X \le x \le \xi, \tag{20}$$

and the profile of Al takes the form

$$N_{Al} = N_{Al}^0 \left\{ 1 - \mathrm{erfc}\left[x / 2(D_{Al} t)^{1/2}\right] / \mathrm{erfc}\left(\gamma\theta^{1/2}\right) \right\} \quad \text{for } \xi \le x, \tag{21}$$

where

$$\theta = D_o / D_A \tag{22}$$

By equating the fluxes of O and Al at the internal oxide front the following relation is obtained

$$\frac{N_0^S}{\nu N_{Al}^0} = \frac{\mathrm{erf}(\gamma) - \mathrm{erf}(u)}{\mathrm{erf}(\gamma)} \frac{G(\gamma)}{F\left(\gamma\theta^{1/2}\right)} \tag{23}$$

The auxilary functions G(r) and F(r) are defined as

$$G(r) = \pi^{1/2}\, r \exp\left(r^2\right) \mathrm{erf}(r) \text{ , and} \tag{24}$$

$$F(r) = \pi^{1/2}\, r \exp(r^2)\, \mathrm{erfc}(r) \qquad (25)$$

The positions of the interfaces were measured from Figure 5.80 (ξ=15.2μm, X=11) and the diffusion coefficient for oxygen taken from Figure 6.6 (D_O=$10^{-7}cm^2/s$). The rate constant for the growth of the external scale was calculated from Equation 17, γ can be calculated from Equation 18 and u can be calculated from Equation 19. The metal ressession rate, which is needed to calculate Equation 19, was determine by dividing the scale thickness by the average of the Pilling Bedsworth Ratio for hematite (PBR=2.10) and magnetite (PBR=2.14). The diffusion coefficient for aluminum is taken as $8x10^{-17}cm^2/s$ from Figure 6.6 and the mole fraction of aluminum was calculated to be 0.059 for the Fe-2.5Cr-2.5Al alloy. A value of 1.5 was chosen for v by assuming Al_2O_3 forms the blocking layer. This is a reasonable assumption because there in evidence in Figure 5.80 for the formation of an aluminum-rich blocking layer in the internal oxide zone. Insertion of the appropriate values into Equation 23 gives the molar fraction of oxygen at the scale/external metal interface as $1.57x10^{-6}$.

Due to the outward diffusion of an element being internally oxidized, Wagner defined an enrichment factor

$$\alpha = \frac{f}{N_{Al}^{0}} \qquad (26)$$

which may also be expressed as

$$\alpha = \frac{1}{F(\gamma\theta^{1/2})} \qquad (27)$$

As previously discussed, the condition for a transition from internal to external oxidation has been related to the formation of a critical volume fraction of the internal oxide near the alloy surface. The critical volume fraction of oxide is related to the critical mole fraction, given in Equation 26, by

$$f_v^* = f^* \rho \tag{28}$$

where ρ is the ratio between molar volume of the oxide and the molar volume of the alloy.

Finally, combination of Equations 26, 27, and 28 gives

$$N_{Al}^{0*} = \frac{1}{\rho} f_v^* F\left(\gamma\theta^{1/2}\right), \tag{29}$$

which allows calculation of the critical concentration of aluminum to from the critical volume fraction of Al_2O_3 necessary to form a protective blocking layer if the critical volume fraction is known along with the other parameters.

Equation 29 can also be used to calculate the volume fraction of oxide that has formed in the internal oxidation zone of the Fe-2.5Cr-2.5Al alloy oxidized at 700°C. Using the values for θ, γ, and N_{Al} previously determined gives a value of f_v equal to 0.18. This is below the 0.3 value determined for the criticial volume fraction by Wagner[57] for the internal oxidation of Ag-In alloys.

If it is assumed in this case that a volume fraction of 0.3 is required to form a blocking oxide layer in the Fe-2.5Cr-2.5Al alloy oxidized at 700°C, then either the critical concentration of Al required to form that layer may be directly calculated from Equation 29 or the critical diffusion coefficient of aluminum necessary to produce the same effect may be found by back calculation through the various

equations. Calculation for the critical mole fraction of aluminum by Equation 29 gives 0.097 which equals approximatelly 4.1 wt% Al .

Determination of the critical diffusion coefficient of Al is carried out by first assuming $f_v = 0.3$ and solving Equation 29 for $F(\gamma\theta^{1/2})$. This value is inserted into Equation 23 and the equation then solved for γ. All other parameters in the equation were perviously determined. The value for γ is then inserted into equation 29 to determine θ. Once θ is known, equation 22 can be used with the value for D_O to determine D_{Al}^*. Carrying out this procedure yields a critical diffusion coefficient of $4.3X10^{-12}cm^2/s$. This value is more than four orders of magnitude greater than the lattice diffusion coefficent of aluminum at this temperature.

6.2.1.2. Type II Scale

The type II scale morphology was formed on the conventionally processed Fe-2.5Cr-2.5Al alloy when oxidized at 500 and 600°C. This differs from the type I scale in that there was no indication of internal oxide particles and the external scale consited of the three iron-rich oxide layers. The lack of internal oxide particles might indicate that the penetration of oxygen into the alloy at this lower temperature was lower than the growth of the external scale. Essentially the scale metal interface moves into the alloy at a greater rate than the internal oxide front. However, one common observation for all the alloys tested was that whenever a continuous $Fe(Cr,Al)_2O_4$ layer was in contact with the alloy surface, internal oxide particles were not detected. $Fe(Cr,Al)_2O_4$ has a greater affinity for oxygen than Fe_3O_4 and will therefore maintain a lower concentration of oxygen at the scale metal/interface. This would certainlly lower the transport of oxygen into the alloy and aid in preventing internal oxidation.

As previously noted the mixed spinel layer in Fe-Al and Fe-Cr-Al alloys gradually becomes inriched in aluminum along the scale/metal interface and eventually forms a contiuous alumina scale that seals off the alloy and slows

oxidation. In the present work, the alloys were not oxidized long enough to obtain this result.

6.2.1.3. Type III Scale

Alloys that formed the third type of oxide consisted of the conventionally processed Fe-2.5Cr-2.5Al that was oxidized at 800°C and the conventionally processed Fe-4Cr-4Al alloy that was oxidized at 500, 600, and 700°C. The oxidation behavior of these alloys compared with the alloys that formed type I and II scales show the effects of temperature and alloy content on the transition from iron oxide formation to protective alumina scale formation.

The increase in temperature from 700 to 800°C for the Fe-2.5Cr-2.5Al alloy increased the diffusion of Al in the alloy enough that an alumina scale was formed over most of the alloy surface. As shown in Figure 6.6, the value of the diffusion coefficient of Al in α-iron is increased by about two orders of magnitude by raising the oxidation temperature from 700 to 800°C.

The increase in aluminum and chromium contents of the alloy effectively promoted the formation of an alumina scale at 500, 600, and 700°C. The formation of iron oxide at some regions of the alloy surface indicates the alloys still have marginal oxidation resistance. Under more severe oxidation testing, such as subjecting the alloys to thermal cycling, the alumina scale may breakdown with the formation of faster growing iron oxides. A result of the analysis of the oxidation of the conventionally processed Fe-2.5Cr-2.5Al alloy was that approximately 4wt% Al was required to form a continuous alumina scale. Neglecting the effect of chromium, this result appears to be confirmed by the appearance of an alumina scale over most of the surface of the conventionally processed Fe-4Cr-4Al alloy oxidized at 700°C.

6.2.1.4. Type IV Scale

This type of scale formed on the conventionally processed Fe-2.5Cr-2.5Al only at 400°C and on the conventionally processed Fe-4Cr-4Al alloys at both 400 and 800°C. It was not expected that a very protective alumina scale would form on both of the conventionally processed alloys at at 400°C. Assuming that the diffusion data in Figure 6.6 can be extrapoilated to 400°C, the aluminum lattice diffusion in α-iron should decrease by more than three orders of magnitude with a decrease in temperature from 500 to 400°C. This indicates that an alumina scale should be less likely to form on the alloy at 400°C than at 500°C. The results show, however, that iron oxides formed on both conventionally processed alloys at 500°C, but did not form on the alloys at 400°C. A probable cause for the alumina scale formation on the alloys at 400°C is that a pre-exsisting tarnish layer was formed on the alloy prior to oxidation and protected the surface when exposed to the high temperature. Confirmation of this would require more experimentation, such as abrading the alloy surface at temperature.

The homogeneous, adherent alumina scale formed on the conventionally processed Fe-4Cr-4Al alloy at 800°C is in direct ageement with the results of Tomaszewicz and Wallwork[134] which are shown in Figure 2.11. Also in agreement with their work is the finding that lowering both the Cr and Al concentration each to 2.5 wt. % results in the formation of iron oxide nodules at 800°C.

6.2.2. Oxidation of Rapidly Solidified Fe-2.5Cr-2.5Al-1Ti-0.6B Alloys at 600 and 700°C.

The improved oxidation resistance of the Fe-2.5Cr-2.5Al-1Ti-0.6B alloys can be directly attributed to grain boundary diffusion of aluminum and chromium in the alloys. The aluminum-rich scale that formed over the grain boundaries of the alloy that had a 10μm grain size (Figure 5.87) is a clear indication of aluminum diffusion from the alloy interior to the alloy surface along grain boundaries. Although these RS alloy showed much improved oxidation resistance compared to the conventionally processed alloys containing the same concentrations of aluminum and chromium, a significant amount of iron oxide formed on the RS alloys, especially at 700°C.

Using the values from Figure 6.6 for the lattice diffusion of aluminum in α-iron ($D_{Al,lattice} = 10^{-18}cm^2/s$ at 600°C and $D_{Al,\ lattice} = 10^{-16}cm^2/s$ at 700°C) and an estimate of grain boundary diffusion of aluminum in α-iron also from Figure 6.6 ($D_{Al,g.b.} = 10^{-12}cm^2/s$ at 600°C and $D_{Al,\ g.b.} = 10^{-11}cm^2/s$ at 700°C). The effective grain boundary diffusion of alumium in α-iron can be estimated using the Hart equation[74]

$$D_{eff} = f D_{gb} + (1 - f) D_l \qquad (4)$$

(the terms were defined in section 2.2.4). The volume fraction of grain boundary material in an alloy with an equiaxed grain structure is calculated by multiplying the grain boundary width (taken as 5Å) by the grain boundary area per unit volume (S), given by

$$S=2/L \qquad (30)$$

where L is the average grain diameter. The values for the effective diffusion coefficient of aluminum at 600 and 700°C in iron alloys is given in Table 6.2. At 700°C the 10μm grain size alloy has an effective diffusion coefficient for aluminum that is about one order of magnitude greater than the lattice diffusion coefficient while a reduction in grain size to 1μm increases the coefficient one more order of magnitude. Both of these diffusion coefficients are well below the value of 10^{-12} cm^2/s calculated in section 6.2.1 to be required in order to obtain a continuous alumina scale. This could account for the fact that iron oxides formed on the alloys and some regions of limited internal oxidation were observed.

The calculated value of the critical diffusion coefficient ($10^{-12}cm^2/s$) is close to the value of the grain boundary diffusion coefficients at 600°C and shown in Figure 6.6. The observation that alumina was able to form over the grain boundaries of the large-grain, spray-formed alloy, is probably due to grain boundary diffusion and indicates that the calculation is valid.

Using the Hart equation, the grain size necessary to obtain the critical aluminum diffusion coefficient of $10^{-12}cm^2/s$ at 700°C is calculated to be 10nm. This fine grain size would be difficult to process and stabilize at high temperatures. Campbell[135] has shown that the Hart equation is an over simplification in the limit that the lattice penetration distance is much larger than the grain boundary spacing; i.e.,

$$\frac{L}{\sqrt{D\,t}} << 1 \qquad (31)$$

In this case, the average concentration profile is typical of a homogenous medium with the grain boundary diffusion coefficient as the effective diffusion coefficient. For the range of grain sizes of diffusion coefficients of alloy studied here

$$\frac{L}{\sqrt{D\,t}} > 25 \qquad (32)$$

so the use of the Hart equation is a valid. For equation 31 to be valid for the Fe-Cr-Al alloys, the grain size would also have to be reduced to the tens of nanometers range.

It would be difficult to obtain the high diffusion coefficient necessary to form an exclusive alumina scale on these alloys by a reduction in grain size. However, the alloys all had very low oxidation rates compared to the conventionally processed alloys and the iron oxides formed primarily during the early, transient period of oxidation. An aluminum- and chromium-rich layer undercut much of the iron oxides and sealed of the alloy. Further testing would be required to determine the protectiveness of the scale at longer times and during thermal cycling.

It was unusual finding that for both the 1μm and 10μm grain sized alloys, much less iron oxide formed during oxidation at 600°C than at 700°C. The activation energy for oxygen lattice diffusion and aluminum grain boundary diffusion is about equal so the relative rates of diffusion of the two species should be about equal at both temperatures and the oxidation behavior similar. Actually, the greater value of the lattice diffusion of aluminum at 700°C should improve oxidation resistance at that temperature. A possible explanation for the observation is that a decrease in the growth rate of the iron oxides at the lower temperature allows aluminum time to diffuse to the surface and form an alumina scale.

6.2.3. Oxidation of Rapidly Solidified Fe-4Cr-4Al-1Ti-0.6B Alloys From 400 to 800°C.

Oxidation of the spray-formed Fe-4Cr-4Al-1Ti-0.6B alloy in the temperature range of 400 to 800°C differed from that of the conventionally processed Fe-4Cr-4Al alloys in that iron oxides in the form of patches or nodules did not form. A small amount of iron oxide did develop on the spray-formed alloy samples oxidized at 600 and 700°C and this appeared to be associated with preferential oxidation at prior particle boundaries in the alloy.

The suppression of nodule growth on fine-grained, rapidly solidified alloys has been documented by many investigators.[136,137,138,139] Nobel[140] found that a rapidly solidified Fe-6Al alloy with a 7μm grain size that was stabilized by MnS precipitates formed fewer iron oxide nodules than a conventionally processed, large-gained, Fe-6Al alloy when both alloys were oxidized at 800°C. He attributed the tendency of the rapidly solidified alloy to form the more protective alumina scale to three factors that related to alloy microstructure. First, it was reasoned that the large number of grain boundaries and MnS precipitates in the alloy acted as preferential nucleation sites for Al_2O_3. If a large number of high density of Al_2O_3 nuclei formed on the alloy surface during the initial stages of oxidation, then very little lateral growth of alumina would be necessary in order for the alumina to form a continuous oxide scale. Secondly, the alloy grain boundaries act as rapid diffusion paths for aluminum in the alloy and promote the growth of the Al_2O_3 nuclei on the alloy surface. Scanning Auger spectroscopy was unsuccessful in determining whether Al_2O_3 grew preferentially over alloy grain boundaries in either the rapidly solidified or conventional alloys. Thirdly, it was believed that the greater chemical homogeneity in the rapidly solidified alloy resulted in the formation of a more uniform oxide scale with less internal stress, and therefore, better resistance to

scale spallation. From this work, only the second factor, that grain boundaries act as high diffusivity paths, can be substantiated.

In the work carried out with the spray-formed Fe-4Cr-4Al-1Ti-0.6B alloy there was no direct evidence that the alloy grain size had any bearing on the improvement in oxidation resistance relative to that of the conventionally processed Fe-4Cr-4Al alloy. The chemical effect due to the presence of titanium and boron in the alloy cannot be ignored. Both titanium and boron form very stable oxides and titanium diboride is readily oxidized in the presence of pure oxygen at 400-800°C. It is quite possible that the dispersion of fine TiB_2 particles in the alloy matrix acted as a secondary getter for oxygen, in the same manner as chromium, and promotedthe formation of an alumina scale. The fine alloy grain size of the spray-formed alloy probably does increase the diffusivity of chromium and aluminum in the alloy at these low temperature, but the prevention of the formation of iron oxides which were observed to form on the conventionally processed alloy, cannot be attributed to enhanced diffusion based on these experiments. The effect of grain boundaries on protectve oxide scale formation was more important for the Fe-2.5Cr-2.5Al alloys, which were much less reistant to oxidation in the conventionally processed form.

6.2.4. Oxidation of Conventionally Processed Fe-4Cr-4Al and Rapidly Solidified Fe-4Cr-4Al-1Ti-0.6B Alloys at 900 and 1000°C.

The convoluted α-Al_2O_3 scales that formed on the conventionally processed Fe-4Cr-4Al alloy oxidized at 900 and 1000°C are typical morphologies for alumina scales that form on iron, nickel, and cobalt-base alloys when oxidized above 900°C. The growth of these types of oxides have been described in detail by Wood and Stott.[141] Lateral growth of the oxide apparentlly causes compressive stresses to develop in the scale. The cohesive strength of convoluted oxides is greater than the strength of adhesion between the alloy and the oxide and bilateral compressive

stresses produce extensive detachment of the oxide from the alloy followed by buckling of the oxide. Folds have been found to form preferentially over alloy grain boundaries and scratches in the alloy surface that originated from polishing during sample preparation. These features are present in Figure 5.52. The convolutions became more extensive with increasing time and temperature, resulting in a progressive increase in the surface area of the oxide but little change in oxide thickness. The dependence on temperature of the extent of convolutions is evident by comparison of the scale morphology shown in Figures 5.51 and 5.52 and by comparison of the difference in weight gain shown in Figure 5.35.

The conventionally processed Fe-2.5Cr-2.5Al alloys that were oxidized at 900 and 1000°C behaved in a manner similar to the conventionally processed Fe-4Cr-4Al alloy except that the iron-rich nodules formed along the specimen edges. As the scale attemps to spread laterally across the surface and side of the oxidation coupon, it will buckle and expose the alloy surface to the oxidizing gas. Apparentlly, the Fe-2.5Cr-2.5Al alloy contained insufficient aluminum and chromium to form an alumina scale in this region and iron oxides formed in the shape of mounds along the edges of the specimens.

The major improvements in oxidation resistance observed for the spray-formed Fe-4Cr-4Al-1Ti-0.6B alloy over the conventionally processed Fe-4Cr-4Al alloy occurred at 900 and 1000°C. The alloy oxidized at 900°C had been annealed at 900°C and was fine grained as were the alloy samples oxidized at lower temperatures, but the alloy that was oxidized at 1000°C had undergone extensive abnormal grain growth during annealling at 1000°C and was large grained. The absence of a convoluted, nonadherent scale formed on the spray-formed Fe-4Cr-4Al-1Ti-0.6B alloy oxidized at 900 and 1000°C was essentially the same result as that obtained by Guruswamy et al.[142] with a rapidly solidified Fe-8Al alloy that had a 1μm grain size stabilized by a dispersion of fine TiB_2 particles.

Guruswamy et al. found that after a brief transition period the oxidation rate decreased to an extremely low value, in agreement with the results of this work. At both 900 and 1000°C the rapidly solidified Fe-8Al alloy formed an adherent alumina scale. The excellent oxidation resistance was attributed to a high rate of alumina nucleation at alloy grain boundaries and rapid diffusion of aluminum in the fine grained rapidly solidified alloy.

Clearly, grain boundaries play no role in the observed improvement in oxidation of the spray-formed and recrystallized Fe-4Cr-4Al-1Ti-0.6B alloy that was oxidized at 1000°C. It is possible that TiB_2 particles in the alloy served as nucleation sites for alumina formation; however, experimental evidence to support this speculation is difficult to obtain. The adherence of the alumina scale that was observed on the spray-formed alloy oxidized at 900 and 1000°C is typical for alumina-forming alloys that contain small concentrations of reactive elements such as yittrium, lanthinum, and cerium.[143] The improvement in oxidation resulting from the addition of these elements in usually referred to the "reactive element effect". Several theories have been proposed over the last two decades to account for the observed improvement in alumina scale adhesion, but the general consensus at this point is that the mechanism may involve several factors.[144]

6.2.5. The Effect of Titanium on a Conventionally Processed Fe-4Cr-4Al Alloy at 900 and 1000°C.

The oxidation of the conventionally processed Fe-4Cr-4Al-1Ti alloy was undertaken to determine the effect of titanium on the formation of an alumina scale at 900 and 1000°C. The results show that titanium alone has a very beneficial effect on the adhesion of an alumina scale. The scale that formed on the alloy when oxidized at both temperatures was completely adherent to the alloy and showed absolutely no sign of the formation of folds. The alloy that Guruswamy oxidized contained a concentration of titanium greater than that necessary to getter

the boron in the alloy so that the alloy matrix contained about 0.5 wt. % titanium in solution. The improvement in oxidation observed by Guruswamy[145] could very likely be due to the presence of titanium in the alloy, and the conclusions of that work should be modified to take this into account. It appears that TiB_2 particles serve a dual purpose by stabilizing the alloy grain size and by acting as a source for titanium for improved scale adhesion. The important factor in the oxidation of iron-base alloys that contain these levels of chromium and aluminum when oxidized at temperatures above 900°C is not the formation of the alumina scale, as Guruswamy had stated, but the adherence of the alumina scale to the alloy substrate and the growth rate of the oxide. Clearly, the addition of 1wt% titanium to a conventionally processed Fe-4Cr-4Al alloy resulted in the formation of an adherent alumina scale during oxidation at 900 and 1000°C and the thickness of the alumina scale that formed on the Fe-4Cr-4Al-1Ti alloy was on the same order as that which formed on the Fe-4Cr-4Al alloy but was not convoluted.

Although, much work has been carried out on investigating the "reactive element effect" as it pertains to the formation of alumina scales, very little has been done with titanium and the work that has been carried out is contradictory.[146,147,148,149] Titanium does not really fulfill the accepted requirements for being considered a "reactive element" because aluminium forms a more stable oxide than titanium. Shoji et al.[150] found that the addition of up to 0.4 wt.% had little effect on the formation of an alumina scale on a Fe-18Cr-3Al alloy oxidized at 1000°C. Only a slight reduction in the tendency for the scale to spall was reported. Lagrange et al.[151] found that addition of 0.2 wt% titanium to an Fe-37Ni-20Cr-5Al alloy actually enhanced scale spallation when the alloy was thermally cycled between 1200 and 260°C. Titanium was found to be concentrated in the outer scale layer on the alloys. Taniguchi et al.[152,153] found that 1.6 wt%

titanium added to an Ni_3Al intermetallic alloy caused repeated scale spallation when cyclically oxidized between 1027 and 127°C.

A predominate feature of the scale formed on the Fe-4Cr-4Al-1Ti alloy oxidized at 900 and 1000°C is the presence of large, titanium-rich nodules. The growth of the nodules is responsible for the greater weight gains of the conventionally processed Fe-4Cr-4Al-1Ti alloy compared to the spray-formed Fe-4Cr-4Al-1Ti-0.6B alloy oxidized at both 900 and 1000°C. No reference in the literature has been found describing the formation of such nodules. This type of nodule did not form on the spray-formed Fe-4Cr-4Al-1Ti-0.6B alloy that contained approximately the same total concentration of titanium. The spray-formed alloy, however, contains a much lower concentration of titanium in solid solution in the alloy matrix. A delineation of the growth characteristics of these nodules, such as how they form initially, how their growth is sustained, and how long they continue to grow, would require more detailed study. It is likely, however, that they form because of the fairly high concentration of titanium in solid solution in the alloy and because titanium has a diffusion coefficient in α-iron that is about an order of magnitude greater than that of aluminum.

6.2.6. Cyclic Oxidation

The conventionally processed Fe-4Cr-4Al-1Ti and spray-formed Fe-4Cr-4Al-1Ti-0.6B alloys showed excellent resistance to oxidation throughout the cyclic oxidation tests. The α-Al_2O_3 scale that formed on the spray-formed alloy had a very slow growth rate and it is surprising that the scale was only slightly thicker than the scale that formed on the same alloy when it was oxidized isothermally for 50h at 1000°C. The few titanium-rich oxide particles observed on the alloy surface indicates that titanium is transported through the scale from the alloy. The conventionally processed Fe-4Cr-4Al-1Ti gained slightly more weight than the spray-formed alloy during the first 75 thermal cycles. This is in agreement with the

larger weight gain experienced by this alloy during the 50h isothermal oxidation experiment. The Fe-4Cr-4Al-1Ti alloy did not gain any further weight after 75 thermal cycles which indicates that nodule growth ceased at that point and an alumina layer had formed beneath the nodule, thereby sealing it from the alloy.

The conventionally processed Fe-4Cr-4Al alloy formed the same type of scale during cyclic oxidation that it had under isothermal oxidation conditions; however, during thermal cycling the α-Al_2O_3 scale flaked off the alloy repeatedly and reformed. This process continued up until approximately 200 cycles. During this period aluminum was constantly being lost from the alloy until after 200 cycles, the specimen began to form iron oxides due to the depletion of aluminum in the alloy. Correspondingly the oxidation specimen began to gain weight rapidly. As was the case with the formation iron oxide nodules on this alloy during isothermal oxidation at 600 and 700°C, oxidation resistance was poorest at the specimen edges where more alumina scale was lost and iron oxides formed initially.

7. SUMMARY

A premise of this work was that a fine grain size would lead to the formation of a protective aluminum oxide scale on Fe-Cr-Al steels that contain low concentrations of aluminum and chromium when the alloys are exposed to high temperatures. This work has shown that the rate of growth of normally fast-growing iron oxides at intermediate temperatures (600 to 700°C) can be diminished greatly by reducing alloy grain size, thereby increasing the transport of aluminum in the alloy to the alloy surface during oxidation. The use of alloy processing to control microstructure and to obtain an improvement in oxidation resistance as an alternative to increasing the concentration of Cr and Al in an alloy has been demonstrated. The results indicate that in certain applications where highly alloyed stainless steels are presently used, these materials can be replaced with rapidly solidified, low-alloy steels, which can result in improvements in the lifetimes of alloys and in a reduction of the consumption of critical and/or strategic elements. Where low alloy steels are presently used, the substitution of fine-grained, rapidly solidified alloys with better oxidation resistance can lead to increases in service life of components and, in the operation of coal-fired power generation plants, these alloys could allow the use of higher operating temperatures for more efficient combustion. The potential for cost savings caused by increased alloy lifetimes and decreased use of expensive elements such as chromium and nickle, would have to be weighed against the added cost of rapid solidification processing.

An unanticipated result of this research was the finding that titanium greatly improved the adherence of the aluminum oxide scale formed on the alloys, which improved the oxidation resistance of both conventionally processed and rapidly solidified alloys at temperatures above 900°C. Although it was shown that grain size probably had little effect on oxidation at these high temperatures, rapid solidification was beneficial to the oxidation resistance by enabling formation of a

dispersion of fine titanium boride particles that suppled titanium to the scale during oxidation. Rapid solidification could probably be used to produce fine dispersions of other titanium containing compounds to yield the same improvement in scale adhesion.

The tendency for abnormal grain growth, which was observed to occur for the alloys with a one micron grain size when annealed at 900 and 1000°c, could be used to advantage to obtain a large-grained, dispersion-strengthened alloy with good high temperature creep resistance and excellent oxidation resistance. Such an alloy would contain sufficient aluminum and chromium to prevent formation of iron oxide at intermediate or low temperatures.

The initial goal of this work was to produce a fine-grained, low alloy steel with a dispersion of fine, stable particles that would effectively prevent grain coarsening at elevated temperatures. This was accomplished using two separate rapid solidification processing methods, spray-forming and powder processing. Spray-forming of materials has been utilized in the manufacture of coatings for tubing, plate and sheet. The powder processing method has been utilized for the production of coextruded tubing and bulk forms with consolidation by hot isostatic pressing. There are no technological barriers to the use of these processing methods for production of either dispersion-containing, fine-grained alloys requiring aluminum oxide scale formation at low temperatures, or for dispersion-containing, large-grained alloys where high strength and an improvement in aluminum oxide adherence are required at high temperatures.

8. CONCLUSIONS

1. Microcrystalline Fe-Cr-Al alloys that contain a dispersion of fine titanium diboride particles can be formed by both spray-forming and powder processing techniques.

2. The stability of the titanium diboride dispersion and its effectiveness in preventing normal grain growth make these alloys suitable for service at temperatures up to at least 1000°C.

3. The fine-grained, rapidly solidified alloys underwent abnormal grain growth if severely worked during processing. This probably rules out the processing of powders by extrusion and points to spray-forming as the preferred rapid solidification processing method, if a fine grain size is desired.

4. The use of rapid solidification processing to produce oxidation resistant Fe-Cr-Al alloys that contain low concentrations of chromium and aluminum was demonstrated.

5. Titanium diboride is an excellent choice for a dispersoid in this system because of its effectiveness in stabilizing a fine-grained microstructure for oxidation resistance at intermediate temperatures and because of the effectiveness of titanium in improving scale adhesion at high temperatures.

9. SUGGESTIONS FOR FURTHER WORK

1. Redesign of the atomization nozzle to aid aspiration of the melt from the crucible during atomization and thereby simplify and improve the reliability of the atomization process. The major modification to the atomization nozzle would consist of changing the gas jet angle to decrease the included angle at the gas jet apex.

2. Proceed with the processing and oxidation of alloys containing an oxide dispersion using an alloy/oxide system that is wetting. A favorable system is an Fe-Cr-Al alloy that contains an alumina dispersion.

3. A more extensive study of the oxidation of conventionally processed Fe-Cr-Al alloys is needed to understand and document the formation of the complex oxide scales that form on these alloys as a function of temperature and alloy composition. Of particular interest is the very protective α-alumina tarnish layer observed to form at 400°C and the unexpectedly favorable oxidation behavior of the Fe-4Cr-4Al alloy at temperatures less than 800°C.

4. The beneficial effect of titanium on the adhesion of aluminum oxide scales to alloys at 900 and 1000°C that was found in this work should be further studied since this element is useful as an alloying addition to steel. The effect of titanium on the formation and growth of alumina scales has been studied very little.

5. The interdendritic amorphous phase that was discovered in the atomized powder makes further control over alloy microstructure possible. The powder particles could be annealed at a low temperature to crystallize TiB_2 prior to high temperature consolidation. This could increase the number and decrease the size of the boride particles and therefore make the dispersion more effective in preventing grain boundary migration and abnormal grain growth. Furthermore, since a number of elements have limited solubility in α-iron and would likely be

segregated to the amorphous phase during solidification, the possibility exists to form various boride and intermetallic compounds during processing.

APPENDIX 1

Reaction	Free Energy Change	Reference
$Ti_{(s)} + 2B_{(s)} = TiB_{2(s)}$	-78,172 + 4.73 T (cal/mole)	110
$Ti_{(s)} = Ti_{(i.d., wt. \%, liq.)}$	-6,000 - 10.75 T (cal/mole)	111
$B_{(s)} = B_{(i.d., wt. \%, liq.)}$	-15,600 - 5.15 T (cal/mole)	111

First Order Interaction Coefficients, e_i^j , in Liquid Iron.

i \ j	Al	B	Cr	Ti
Al	0.045			
B		0.038		
Cr			-0.0003	0.059
Ti			0.055	0.013

REFERENCES

1. D. P. Whittle and J. Stringer: *Philos. Trans. R. Soc. London*, Ser. A, vol. 295, 1980, pp. 191.
2. S. C. Giggens and F. S. Pettit: *Trans. TMS-AIME*, vol. 245, 1969, pp. 2509.
3. P. Duwez: *Trans. TMS-AIME*, vol. 60, 1967, pp. 607.
4. R. Mehrabian: *Inter. Metals Rev.*, vol. 27, no. 4, 1982, pp.185.
5. A. Lawley: *Advances in Metal Processing*, 1981, pp. 91.
6. R. Mehrabian, S. C. Hsu, C. G. Levi, and S. Kou: *Advances in Metals Processing*, 1981, pp. 13.
7. H. Matyja, B. C. Giessen, and N. J. Grant: *Jour. Inst. Metals*, vol. 96, 1968, pp. 30.
8. V. K. Sarin: *Trans. TMS-AIME*, vol. 3, 1972, pp. 757.
9. J. Megusar, L. Arnberg, J. Vander Sande and N. J. Grant: *J. of Nuclear Materials*, vol. 99, no. 2 and 3, 1981, pp. 190.
10. G. Rai, E. Lavernia, and N. J. Grant: *J. of Metals*, vol.37, no. 8, 1985, pp. 22.
11. M. J. Couper and R. F. Singer, in: *Rapidly Quenched Metals*, eds.S. Steeb and H. Warlimont, 1985, pp. 1737.
12. W. B. James, *International Journal of Powder Metallugy and Techology*, vol. 21, no.3, 1985, pp. 163-182.
13. E. J. Lavernia, and N. J. Grant: *Met. Powder Rep.*, vol. 4, 1986, pp. 225.
14. R. W. Evans, A. G. Leatham, and R. G. Brooks: *Powder Metallurgy*, vol. 28, no. 1, pp.13.
15. G. Gillen, P. Mathur, D. Apelian, and A. Lawley: Paper Presented at the Annual Powder Metallurgy Conference, Metal Powder Industries Federation, Boston MA., May 18-21, 1986.
16. E.J. Lavernia. E.M. Guteirrez, J. Szekely, and N.J. Grant: (PM Conference Dallas 1986)
17. T. W. Clyne, R. A. Ricks and P.J. Goodhew: *International Journal of Rapid Solidification*, vol. 1, no. 1, 1984, pp. 59-80.
18. A. I. Taub, in *Rapidly Quenched Metals*, S.Steeb and H. Warlimont eds., Elsevier Science Publishers, New York, 1985, pp. 1611-1618.
19. I.M. Allam, D.P. Whittle, and J. Stringer: *Oxidation of Metals,* vol.13, no. 4, 1979, pp. 381-401.
20. M.S Selter, B.A. Wilcox, and R.I. Jaffe: *Metall. Trams.*, vol. 3, 1972, p.2390.
21. J.S. Benjamin: *Met. Trans.*, vol.1, 1970, pp. 2943-2951.
22. M. Cohen: in *Specialty Steels and Hard Materials*, N. R. Comins and J. B. Clark eds., Pergamon Press, Oxford, 1983, pp. 1-22.
23. H. Kimura, T. Masumoto, W. N. Myung, and S. Furukawa, in *Rapidly solidified Materials*, P. W. Lee and R. S. Carbonara eds., ASM, Metals Park, OH, 1985, pp. 303-309.
24. R. G. Roe, A. G. Jackson, E. F. Koch, and F. H. Froes, in *Rapidly Solidified Materials: Properties and Processing*, P. W. Lee and J. H. Moll eds., ASM International, 1988, pp. 99-106.
25. S. M. L. Sastry, P.J. Meschter, and J. E. O'Neal: *Met. Trans.*, vol. 15A, 1984, pp. 1451-1463.

26. D. Eliezer, S. J. Savage, Y. R. Mahajan, and F. h. Froes: in *Rapidly Solidified Alloys and Their Mechanical and Magnetic Properties*, MRS Symposia Proceedings, vol. 58, B. C. Giessen, D. E. Polk, and A. I. Taub eds., 1985, pp. 293-304.
27. R. Meherabian: *International Metals Review*, vol. 27, no.4, 1982, pp.185-208.
28. F. H. Froes and R. G. Rowe: inin *Rapidly Solidified Alloys and Their Mechanical and Magnetic Properties*, MRS Symposia Proceedings, vol. 58, B. C. Giessen, D. E. Polk, and A. I. Taub eds., 1985, pp.309-334.
29. T. F. Kelly, Ph.D. Thesis, MIT, 1983.
30. B.L. Mordike and H.W. Bergman: in *Rapidly Solidified Amorphous and Crystalline Alloys*, B.H. Kear, B.C. Giessen, and M. Cohen eds., Elsevier Science Publishing, New York, 1982, p.423-427.
31. D.G. Konitzer, B.C. Muddle, R. Kircheim, and H.L. Frazer: in *Rapidly Quenched Metals,* S. Steeb and H. Warlimont eds., Elsevier Science Publishers, 1985, pp.953-956.
32. M. Cohen: in *Specialty Steels and aHard Materials*, N.R. Comins and J.B. Clark, Pergamon Press, Oxford, 1983, pp. 1-22.
33. M. Hasegawa and K. Takeshita: *Metall. Trans.*, Vol. 9B, 1978, pp. 383-388.
34. M. Hasegawa and M. Osawa: *Metall. Trans.*, vol. 16A, 1985, pp. 1043-1048.
35. E.T. Turkdogan, *Arch. Eisenhuttenwes.*, vol 54, no. 1, 1983, pp.1-10.
36. V.H. Knuppel, K. Brotzmann, and N.W. Forster, *Stahl u. Eisen,* no. 11, 1965, pp. 675-688.
37. C. Gatellier and M. Olette: in *Chemical Metallugy of Iron and Steel*, ISI, London, 1973, pp. 191-194.
38. P. Kozakevitch and M. Olette: in *Production and Applications of Clean Steels*, ISI, London, 1972, pp.42-49.
39. V.H. Knuppel, K. Brotzmann, and N.W. Forster, *Stahl u. Eisen,* no. 11, 1965, pp. 675-688.
40. E.T. Turkdogan, in *Chemical Metalurgy of Iron and Steel*, ISI, London, 1973, pp. 153-170.
41. A.A. Chernov and D.E. Temkin: in *1976 Crystal Growth and Materials*, E. Kaldis and H.J. Scheel eds., North-Holland Publishing, 1977, pp. 3-75.
42. P. Cotterill and P.R. Mould: in *Recrystallization and grain growth in Metals*, John Wiley & Sons, New York, 1976, p. 233.
43. C. Zenner, quoted by C.S. Smith, *Trans. Met. Soc.*, AIME, vol. 175, 1949, p. 15.
44. T. Gladman, *Proc. Roy. Soc.*, vol, A294, 1966, p.298.
45. N.A. Haroun and D.W. Budworth, *J. Mater. Sci.*, no. 3, 1968, p. 326.
46. M.F. Ashby: in *Recrystallization and Grain Growth in Multiphase and Particle Containing Materials*, N. Hanson A.R. Loris, and T. Leffes eds., 1978, pp. 325-336.
47. M.F. Ashby and R.M.A. Centamore, *Acta. Met.*, vol. 16, 1968, 1081.
48. E. Grant, Angus Porter, and Brian Ralph: *J. Mater. Sci.*, vol. 19, 1984, pp.3554-3573.
49. S.K. Bhattacharyya and K.C. Russel, *Met. Trans.*, vol.3, 1973, p. 2195.
50. H. Jones: in *Rapid Solidification Processing: Principals and Technologies*, Clator's Publishing, Baton Rouge, 1980, pp. 306-316.
51. N. Birks and G.H. Meier: in *Introduction to High Temperature Oxidation of Metals*, Erward Arnold Publishers, London, 1983, p. 104.

52. J.L. Smialek and G.H. Meier: in *Super Alloys* , C.T. Sims, N. Stoloff, W.Hagel, eds. J. Wiley and Sons, New York, NY, 1987.
53. D.P. Whittle: in *High Temperature Corrosion*, R.A. Rapp ed., NACE, Houston, 1981, pp. 171-183.
54. D.P. Whittle and H, Hindam, in *Proceedings Corrosion-Erosion-Wear of Materials in Emerging Fossile Energy Systems*, A.V. Levy ed., NACE, Houston, 1892, pp. 54-99.
55. D.P. Whittle: in *High Temperature Corrosion*, R.A. Rapp ed., NACE, Houston, 1981, pp. 171-183.
56. C. Wagner: *Z. Electrochem.*, vol. 63 1959, p. 772.
57. P. Tomaszewicz and G.R. Wallwork: *Corrosion*, vol. 40, no, 4, 1984, pp. 152-157.
58. P. Tomaszewicz and G.R. Wallwork: *Oxidation of Metals*, vol. 19, no. 5/6, 1983. pp. 165-185.
59. P. Tomaszewicz and G.R. Wallwork: in *High Temperature Corrosion*, R.A. Rapp ed., NACE, Houston, 1981, pp. 258-266.
60. F. Saegusa and L. Lee: *Corrosion*, vol. 22, no. 6,1966, pp. 168-177.
61. W.E. Boggs: J. Electrochem. Soc., vol. 118, no. 6, 1971, pp.906-913.
62. F.H. Stott, G.C. Wood, and M.G. Hobby, *Oxidation of Metals*, vol. 3, no. 2, 1971, pp.103-113.
63. P. Tomaszewicz and G.R. Wallwork: *Oxidation of Metals*, vol.20, no. 3/4, 1983, pp. 75-109.
64. C. Wagner, *Corr. Sci.*, 1965, vol. 21, p. 382.
65. N.A. Gjostine: in Diffusion, ASM, Metals Park OH., 1973, pp.241-71.
66. J.L. Bocquet, G. Brebec, and Y. Limoge: in *Physical Metallurgy*, R.W. Cahn and P. Haasen eds., Elsevier Science Publishers, p. 451.
67. R.W. Balluffi: in *Diffusion in Crystalline Solids*, Academic Press, Inc., 1984, pp.319-377.
68. N.L. Peterson: *International Metals Reviews*, vol. 28, 1983, pp.65-91.
69. D. Gupta: in *Thin Films-Interdiffusion and Reactions,* J.M. Poate, K.N. Tu, and J.W. Mayer eds., The Electrochemical Society, Princeton, 1978, pp. 161-242.
70. G. Martin and B. Perrallon: in *Grain Boundary Structure and Kinetics*, ASM, Metals Park, OH, 1979, pp. 239-295.
71. J.L. Bocquet, G. Brebec, and Y. Limoge: in *Physical Metallurgy*, R.W. Cahn and P. Haasen eds., Elsevier Science Publishers, p. 451.
72. E.W. Hart: *Acta Met.,* vol.5, 1957, p.597.
73. N.L. Peterson: *International Metals Reviews*, vol. 28, 1883, pp.65-91.
74. C.S. Giggens and F.S. Pettit: *Trans. AIME*, vol. 245, 1969, pp.2495-2507.
75. C.S. Giggens and F.S. Pettit: *Trans. AIME*, vol. 245, 1969, pp.2509-2514.
76. B. Chattopadhyay and G.C. Wood: *J. Electrochemical Society* , vol. 117, no. 9, 1970, pp.1164-1171.
77. M.K. Hossain, Corr. Sci., vol. 119, 1979, pp.1031- 1045.
78. N. Wade, T. Koshihama, and Y. Hosoi, *Scripta met.*, vol. 19, 1985, pp. 859-864.
79. G.J. Yurek, D. Eisen, and A. Garrat-Reed, *Metal. Trans.*, vol. 13A, 1982, pp. 473-485.
80. G.J. Yurek and D.L. Cocke, paper no. 18 presented at the NACE Corrosion 85 conference, Boston, MA, March 1985.
81. N.J. Grant, *Journal of Metals*, no. 1, 1983, pp. 20-27.

82. S. Guruswamy, J.P. Hirth, and G.W. Powell, *Oxidation Metals,* no.19, vol. 3/4, 1983, pp. 77-98.
83. D.B. Noble, M.S. Thesis, MIT, 1981.
84. K. Barmak, M.S. Thesis, MIT, 1984.
85. G. Rai, E. Lavernia, and N.J. Grant: *J. of Metals*, no.8, 1985, pp.22-26.
86. J.A. Beattie and H.P. Julien, Ind. and Eng. Chem., vol. 46, no. 2, pp. 1668-9.
87. U. Backmark, N. Backstrom, and L. Arnberg: Swedish Institute for Metals Research, unpublished research.
88. United States Atomic Energy Commision Report NYO-1583.
89. A.J. Morehead: Advanced Ceramic Materials, vol. 2, no. 2,1987, pp. 159-166.
90. S. Guruswamy, J.P. Hirth, and G.W. Powell, *Oxidation Metals,* no.19, vol. 3/4, 1983, pp. 77-98.
91. ASTM Standard E 407-70
92. T. F. Kelly, Ph.D. Thesis, MIT, 1983.
93. M. Humenik, Jr. and W. D. Kingery: *Journal of the American Ceramic Society*, vol. 37, no. 1, 1954, pp.18-45.
94. Steven Ridder, NBS, Gathersberg WA., Private Comunication.
95. Flemmings, *Solidification Processing*, McGraw-Hill, New York, 1974.
96. R . Meherabian: in *Rapid Solidification Processing: Principals and Properties and Technologies*, Claitor's, Baton Rouge, LA, 1978, pp. 9-27.
97. R. J. Patterson, II: in Rapidly Solidified Amorphous and Crystalline Alloys, B. H. Kear, B. C. Giessen, and M. Cohen, eds., Elsevier Science, New York, pp. 123-129.
98. M. J. Couper and F. Singer: in *Rapidly Quenched Metals*, S. Steeb and H. Warlimont eds., Elsevier Science, New York, pp. 1737-1742.
99. T. W. Clyne, R. A. Ricks, and P. J. Goodhew, *International Journal of Rapid Solidification*, vol. 1, no. 1, 1984, pp. 59-80.
100. S.C. Hsu, S. Chakravorty, and R. Mehrabian: *Met. Trans. B.* vol. 9B, pp.
101. J.V. Wood and R.W.K. Honeycomb: in *Ultra Rapid Quenching Metals*, H. Herman ed., Academic Press, New York,
102. B. Cantor: in *Rapidly Solidified Amporpous and Crystalline Alloys* , B.H. Kear, B.C. Geissen, and M. Cohen eds., Elsevier Publishing Co., 1982, pp. 317-330.
103. E.R. Slaughter and S.K. Das: in *Rapid Solidification Processing, P Principals and Technologies II*, R. Mehrabian, B.H. Kear, and M. Cohen, Claitors Publishers, Baton Rouge, 1980, pp. 354-363.
104. E.S. Powell and G.W. Powell: in *Microstructural Science*, vol. 10, Elsevier Publishing Co., 1982. pp. 3-24.
105. A. Brown: Ph.D. Dissertation, 1973, University of Cambridge.
106. J. Campbell and J.W. Bannister: *Metals Technology*, no.9, 1975, pp. 409-415.
107. C.R. Shastry, R.M. Latanision, and H. E. Townsend: in *Rapidly Solidified Matastable Materials*, MRS Symposia Proceedings, vol. 28, Boston, MA, 1983, pp. 217-225.
108. T.F. Kelly and J.B. Van der Sande: in *Rapid Solidification Processing: Principles and Technologies* , ed. by R. Mehrabiun, B.H. Kear and M. Cohen, (Claitor's, Baton Rouge, LA, 1980) pp. 100-111.
109. T.F. Kelly, Ph.D. Thesis, 1983, Massachusetts Institute of Technology.

110. Janaf Thermochemical Tables, Third Edition, vol. 14, Suppliment no. 1, 1985.
111. J.F. Elliott: in Proceedings, Electric Furnace Conference, Iron and Steel Society, AIME, vol. 32, 1974, pp. 62-73.
112. M.J. Maloney and G.J. Yurek: EPRI Report, Contract No. RP2278-2, 1-1-87 to 12-31-87.
113. L. Arnberg, L. Backerud, and H. Klang: in *Solidification Technology*, The Metals Society, 1983, pp. 89-92.
114. J. Wood: in *Solidification and Casting of Metals*, The Metals Society, 1979, pp. 179-183.
115. V.G. Rivlin and G.V. Raynor: *International Metals Reviews*, no. 4, 1980, pp.139-157.
116. G. E. McGanna, *The Making, Shaping, and Treating of Steel*, Eight Edition, 1964, p. 1033.
117. H.J. Goldschmidt: *Interstitial Alloys*, Plenum Press, NY, 1967, p. 276.
118. G.M. Michal, T.K. Glasgow, and T. J. Moore: in *Rapidly Solidified Materials*, P. U. Lee and R. S. Carbonara eds., ASM, 1985, pp. 255-271.
119. E.R. Slaughter and S.K. Das: in *Rapid Solidification Processing Principles and Technologies, II*, R. Mehrabian, B.H. Kear, and M. Cohen eds., Claitor's, Baton Rouge, 1980, pp. 354-363.
120. G.B. Olsen, H.C. Ling, J.S. Montgomery, J.B. Vander Sande, and M. Cohen: in Rapidly Solidified Amorphous and Crystalline Alloys, B.H. Kear, B.C. Giessen, and M. Cohen eds., Elsevier Science Publishers, New York, 1982, pp. 355-362.
121. S.H. Moll and R.E. Ogilvie: *Trans. AIME*, vol.215, 1959, pp. 613-618.
122. P.E. Busby and C. Warga: *Trans. AIME*, Vol. 197, 1953, p. 1463.
123. Handbook of Binary Metallic Systerms, Structures and Properties, U.S. Department of Commerce, 1967, p. 637.
124. E.D. Hondros: in Precipitation processes in Solids, K.C. Russel and H.I. Aaronson eds., TMS-AIME, 1978, pp.1-30.
125. J. A. Schey: in *Metal Deformation Process*, Marcel Dekker Inc., New York, 1970, p. 31.
126. M.H. Ashby: in Recrystallization and Grain Growth of Multiphase and Particle Containing Materials, N. Hansen ed.,1978, pp. 325-36.
127. J. Friedel, Dislocations, Pergamon Press, Oxford, 1964, pp. 211
128. C.S. Giggens and F.S. Pettit: *Trans. AIME*, vol. 245, 1969, pp.2495-2507.
129. C. Wagner, *Corr. Sci.*, 1965, vol. 21, p. 382.
130. Maak, F., *Z. Metallkde.*, vol. 53, (1961), p. 545.
131. Gesmundo, F., and F. Viani, *Oxid. Met.*, vol. 25, nos. 5/6, (1986) pp. 269-282.
132. W.W. Smeltzer, P.R.S. Jackson and H.A. Ahemd: in Transport in Nonstochiometric Compounds, Plenum Press, New York, 1984, pp.481-493.
133. F. Gemundo and F. Viani, *Oxid. Met.*, vol. 25, nos. 5/6, (1986) pp. 269-282.
134. P. Tomaszewicz and G.R. Wallwork: *Oxidation of Metals*, vol. 19, no. 5/6, 1983. pp. 165-185.
135. D.R. Campbell, *Bull. Am. Phys. Soc.* 19 (1974) p. 347
136. D.B. Noble, M.S. Thesis, MIT, 1981.
137. S. Guruswamy, J.P. Hirth, and G.W. Powell, *Oxidation Metals,* no.19, vol. 3/4, 1983, pp. 77-98.

138. G.J. Yurek, D. Eisen, and A. Garrat-Reed, *Metal. Trans.*, vol. 13A, 1982, pp. 473-485.
139. N. Wade, T. Koshihama, and Y. Hosoi, *Scripta met.*, vol. 19, 1985, pp. 859-864.
140. D.B. Noble, M.S. Thesis, MIT, 1981.
141. G. C. Wood and F. H. Stott: in High Temperature Corrosion, National Association of Corrosion Engineers, Houston, TX, 1983, pp. 227-250.
142. S. Guruswamy, J.P. Hirth, and G.W. Powell, *Oxidation Metals,* no.19, vol. 3/4, 1983, pp. 77-98.
143. D.P. Whittle and J. Stringer: *Trans. Roy. Soc.*, Lomdon, ser. A, 1980, vol. 295, p. 309.
144. P. Kofstad: High Temperature Corrosion, Elsevier Applied Science, London, 1988, pp. 410-411.
145. S. Guruswamy, J.P. Hirth, and G.W. Powell, *Oxidation Metals,* no.19, vol. 3/4, 1983, pp. 77-98.
146. Y. Shoji, S. Akiyama, M. Kisaichi, K. Nagatoshi, and H. Hoshi:, J. Iron and Steel Inst. of Japan,vol. 62, 1976, pp. 108-125.
147. M. H. Lagrange, A. M. Huntz, and J. H. Davidson: Corrosion Science, vol. 24, 1984, pp. 613-627.
148. S. Taiguchi, T. Shibata, and Hiroshi Tsurvoka: Oxidation of Metals, vol. 26, no. 1/2, 1986, pp. 1-17.
149. S. Taniguchi and T. Shibata: Oxidation of Metals,, vol. 25, no. 3/4, 1986, pp. 201-216.
150. Y. Shoji, S. Akiyama, M. Kisaichi, K. Nagatoshi, and H. Hoshi:, J. Iron and Steel Inst. of Japan, vol. 62, 1976, pp. 108-125.
151. M. H. Lagrange, A. M. Huntz, and J. H. Davidson: Corrosion Science, vol. 24. 1984, pp. 613-627.
152. S. Taniguchi, T. Shibata, and Hiroshi Tsurvoka: Oxidation of Metals, vol. 26, no. 1/2, 1986, pp. 1-17.
153. S. Taniguchi and T. Shibata: Oxidation of Metals, vol. 25, no. 3/4, 1986, pp. 201-216.
154. J. Hirvonen and J. Raisanen, J. Appl. Phys., vol. 53, no. 4, April 1982, pp. 3314-3316.
155. R.B. McLellan, Proc. Int. Symp. on Chemical Metalurgy of Iron and Steel, Sheffield, July 1971, pp. 337-343.
156. J. Takada and M. Adachi, *J. Mater. Sci.,* vol. 21, no. 6, 1986, pp.2133-2137

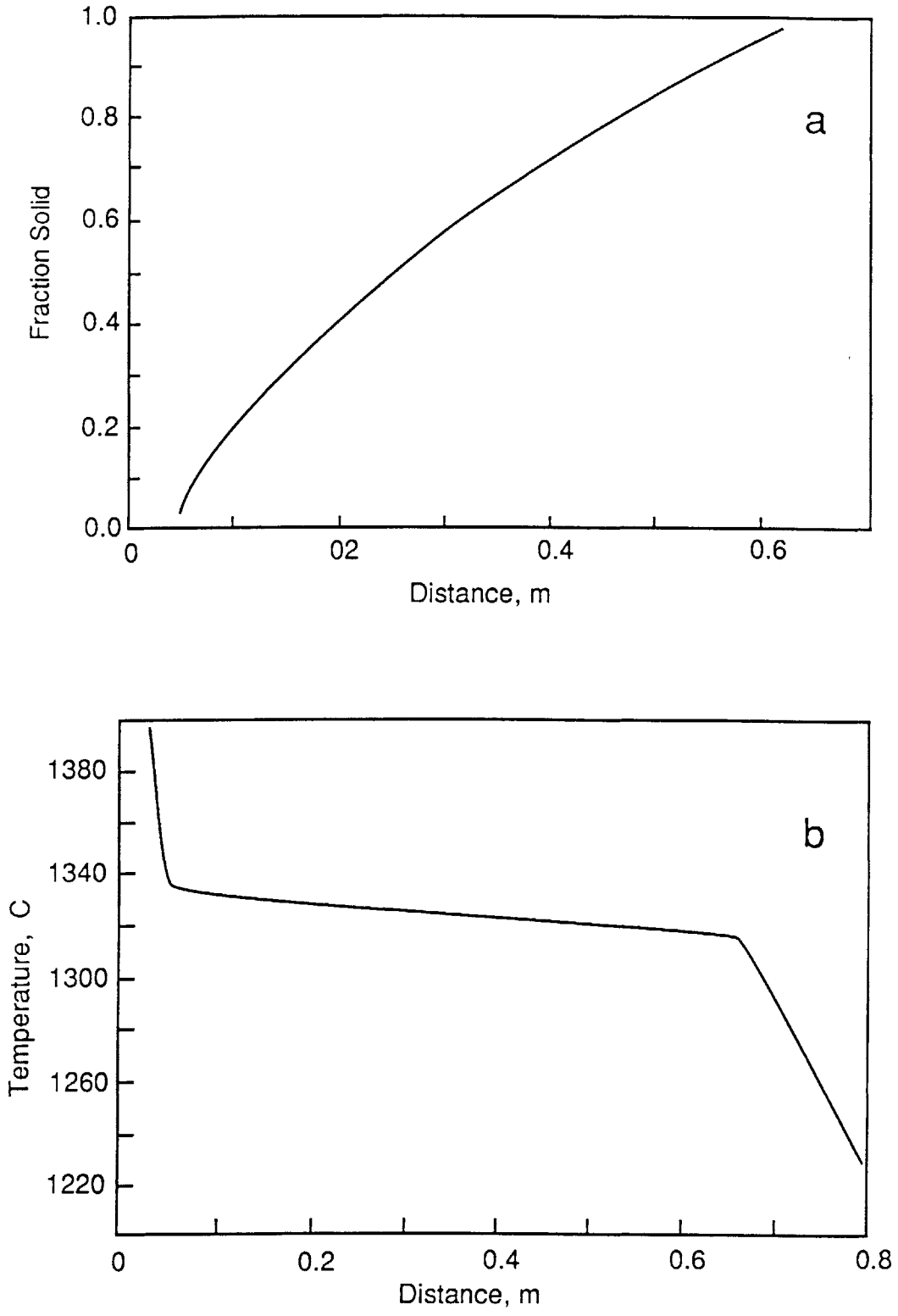

Figure 2.1—Computed (a) fraction of solid and (b) temperature as a function of flight distance for a 50 m nickle base superalloy powder particle (16).

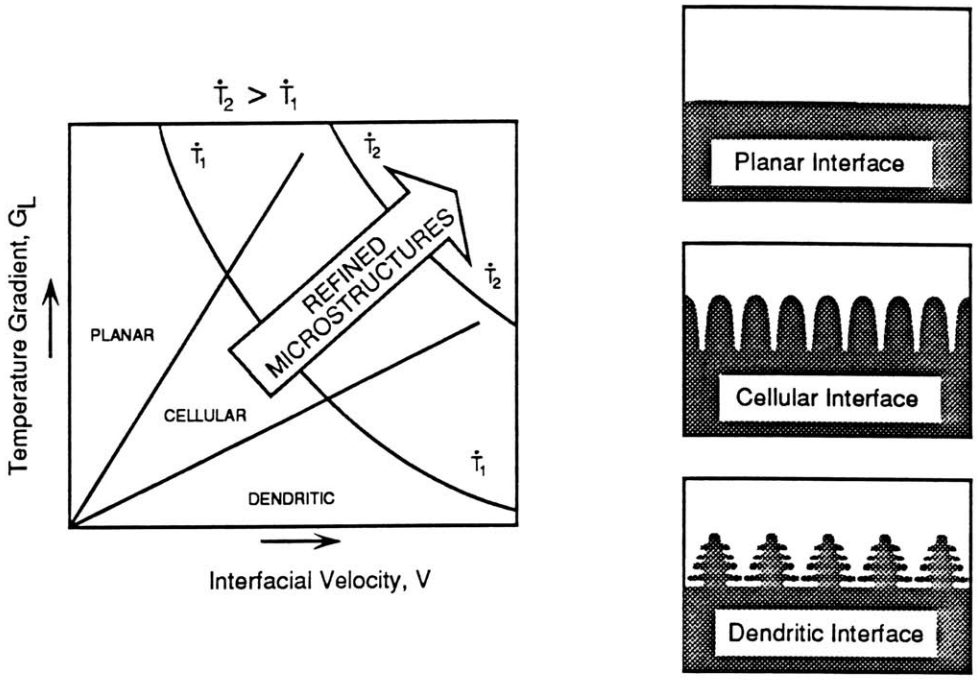

Figure 2.2—Dependence of solidification morphology on temperature gradient G and interfacial solidification velocity V (4).

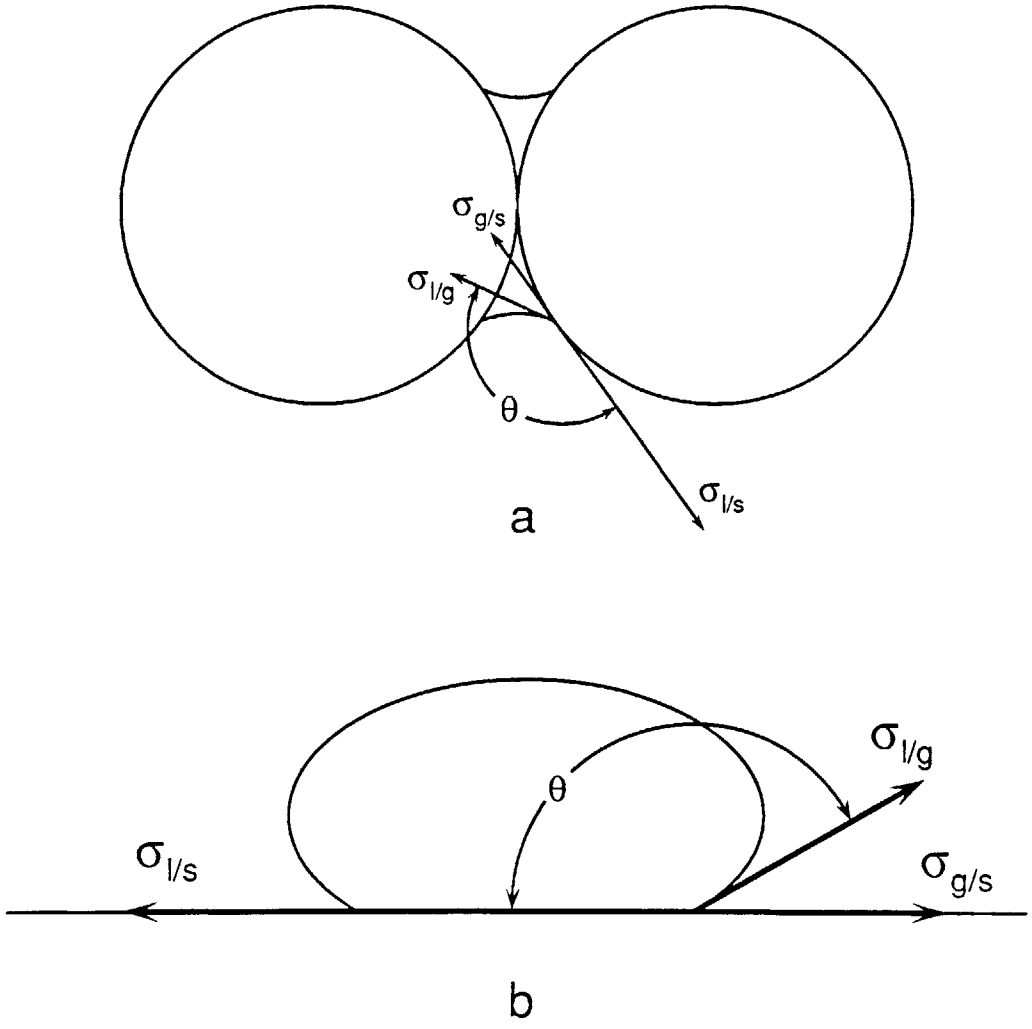

Figue 2.3—Balance of surface tension forces between solid, liquid and gas for (a) the vacuum miniscus and (b) the sessile drop configurations.

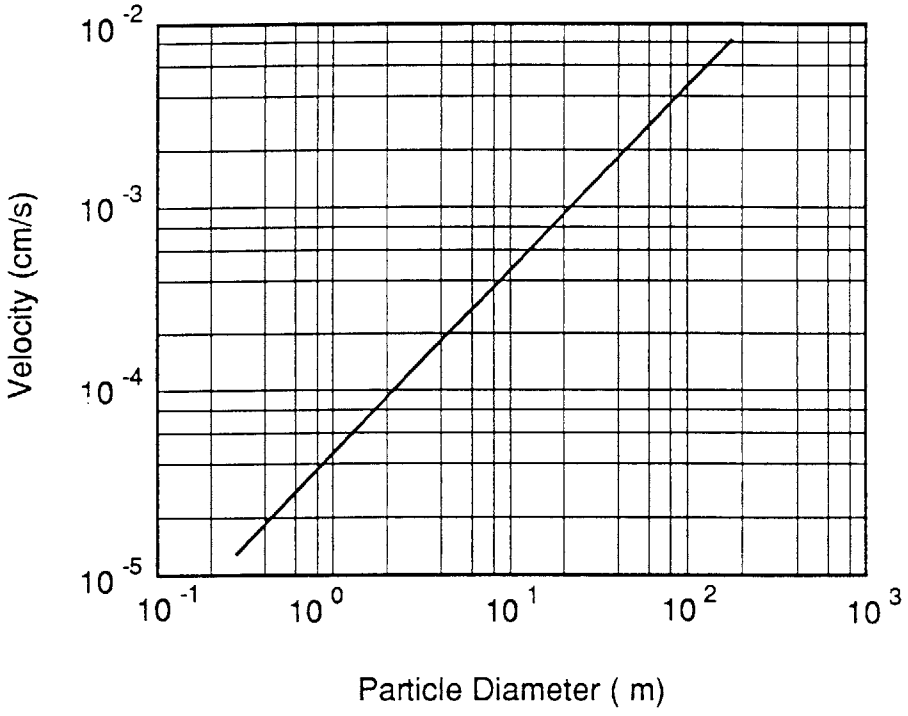

Figure 2.4—Rising velocity of alumina particles in liquid iron according to Stoke's Law (36).

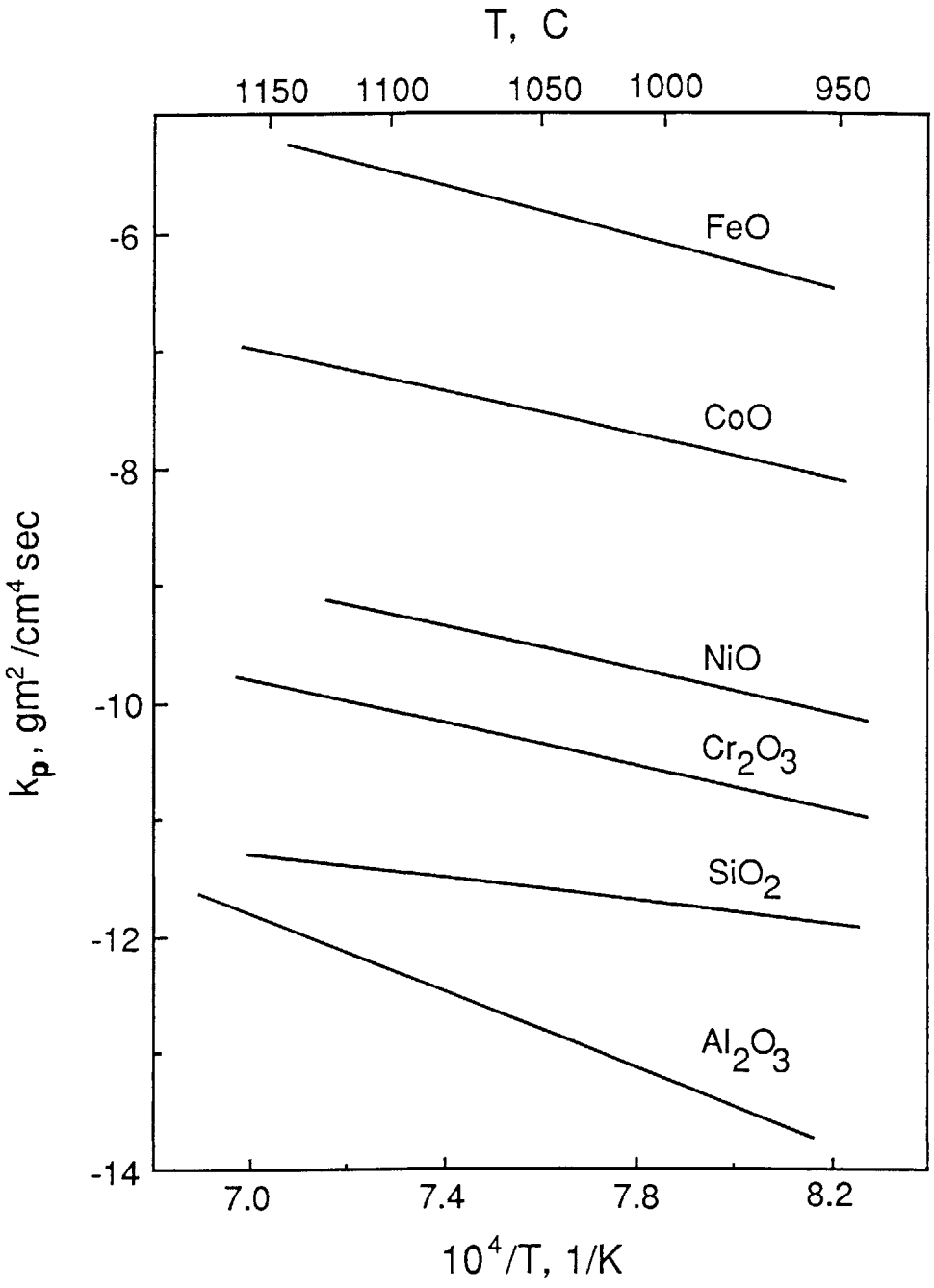

Figure 2.5—Temperature dependence of the parabolic rate constants for various oxides (52).

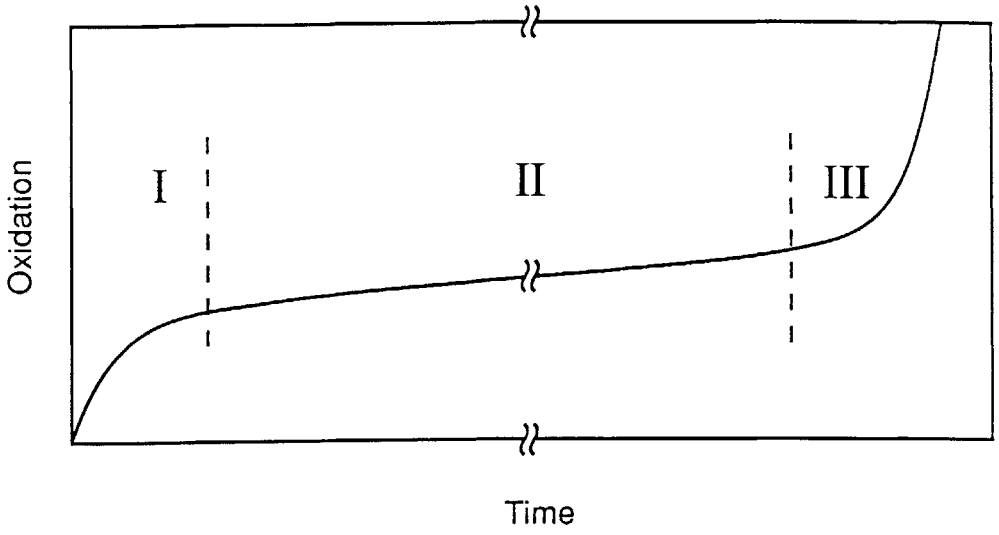

Figure 2.6—Transient, steady state, and breakaway stages of oxidation.

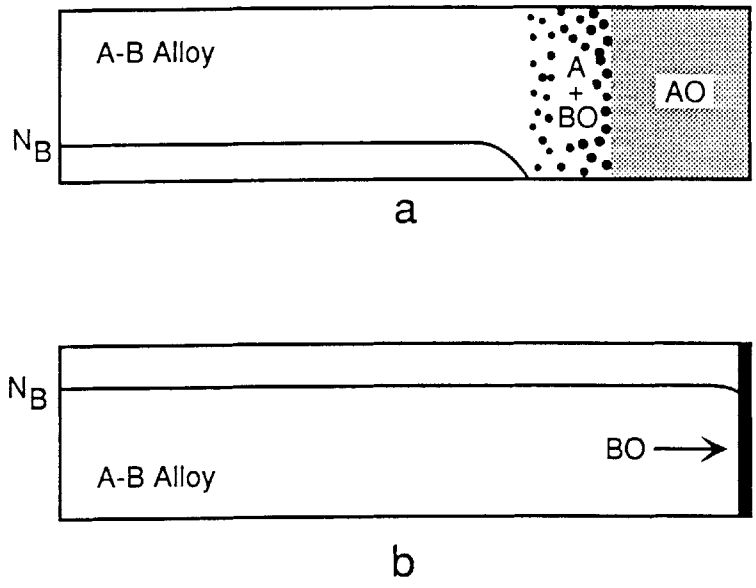

Figure 2.7—Effect of concentration on oxide scale formation. (a) Formation of an external layer AO and internal precipitates of BO at concentrations of low concentrations of B. (b) Sufficient concentration of B in alloy to form an external scale of BO.

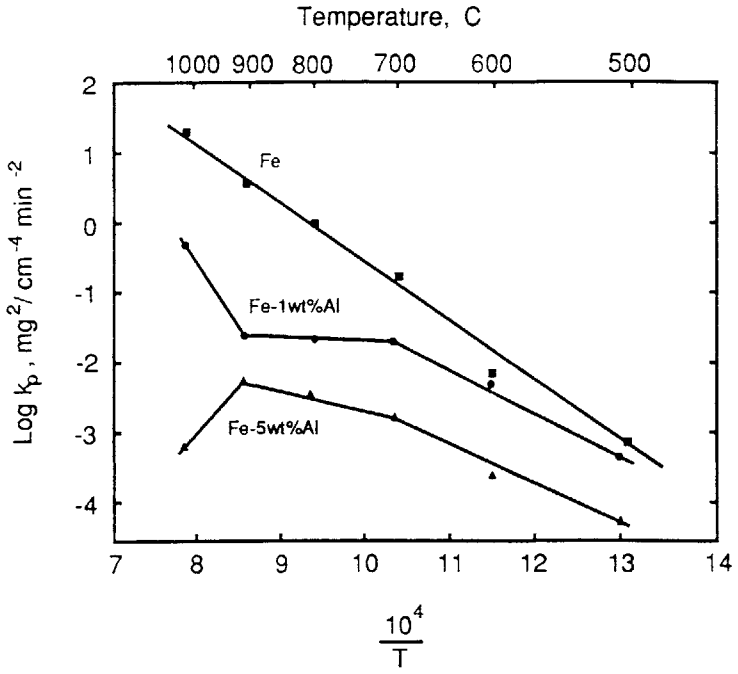

Figure 2.8—Temperature dependence of parabolic rate constant of Fe, Fe-1wt%Al, and Fe-5wt%Al alloys (60).

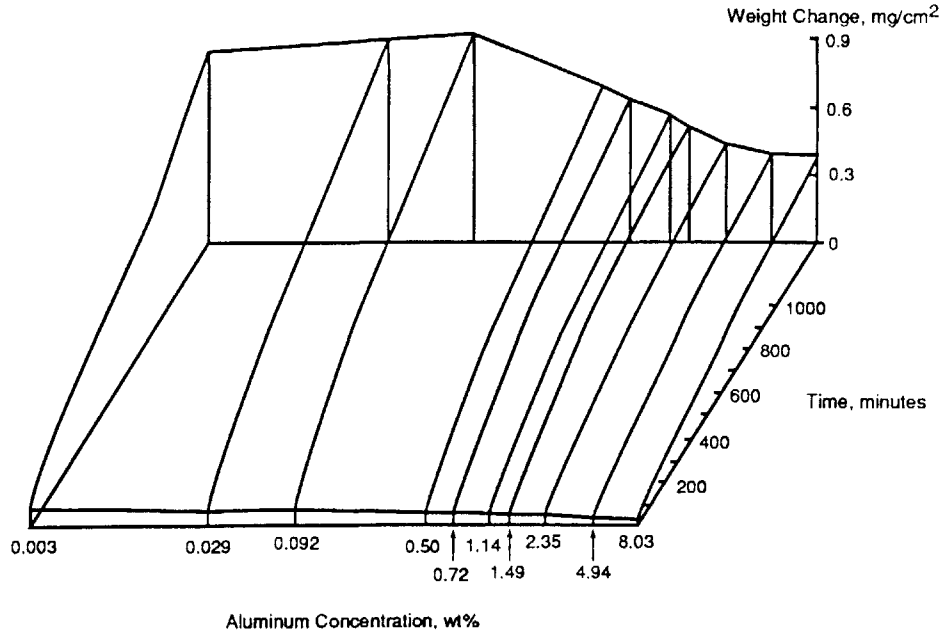

Figure 2.9—The effect of aluminum concentration on the oxidation rate of Fe-Al alloys at 500 C (61).

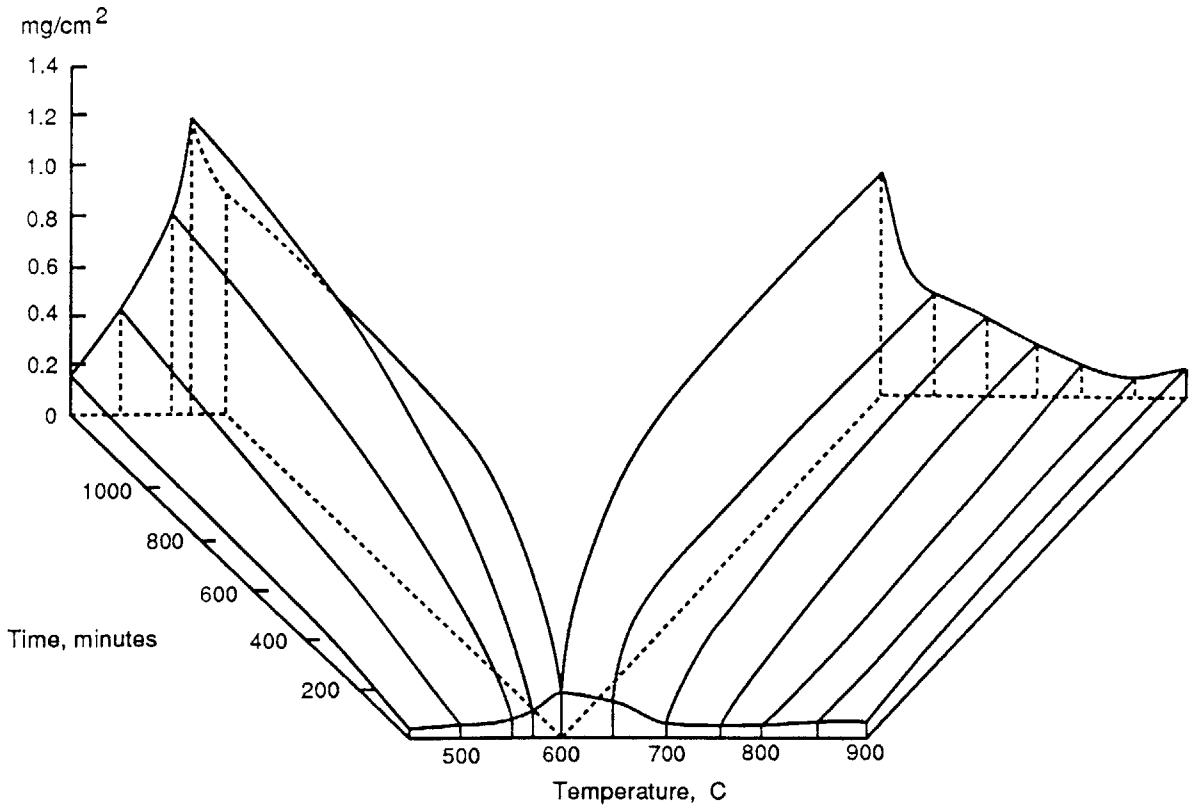

Figure 2.10—Effect of temperature on the oxidation of an Fe-4.94 wt%Al alloy (61).

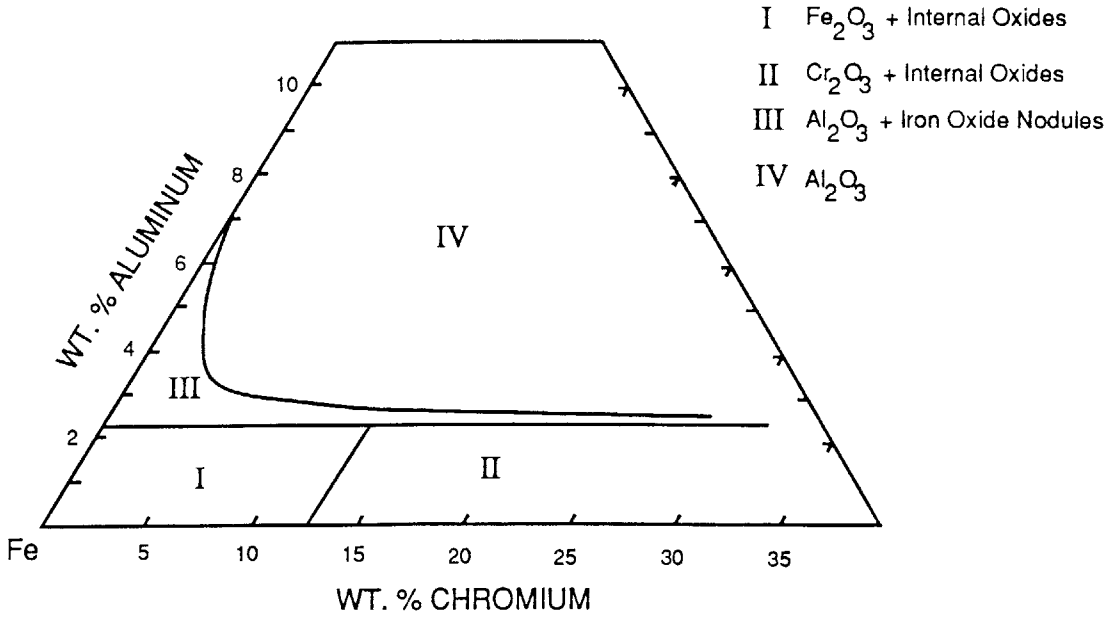

Figure 2.11—Oxide map for the oxidation of Fe-Cr-Al alloys at 800 C (63).

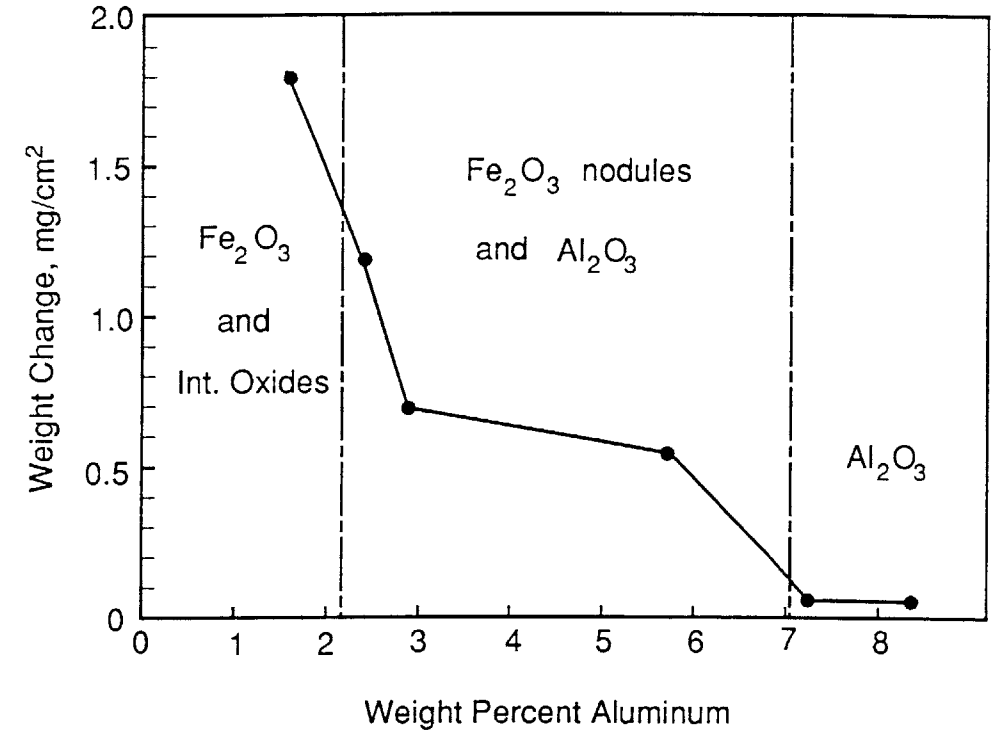

Figure 2.12—The effect of aluminum concentration on the final weight gains of a series of Fe-Al allloys after 25 hours of oxidation at 800 C (63).

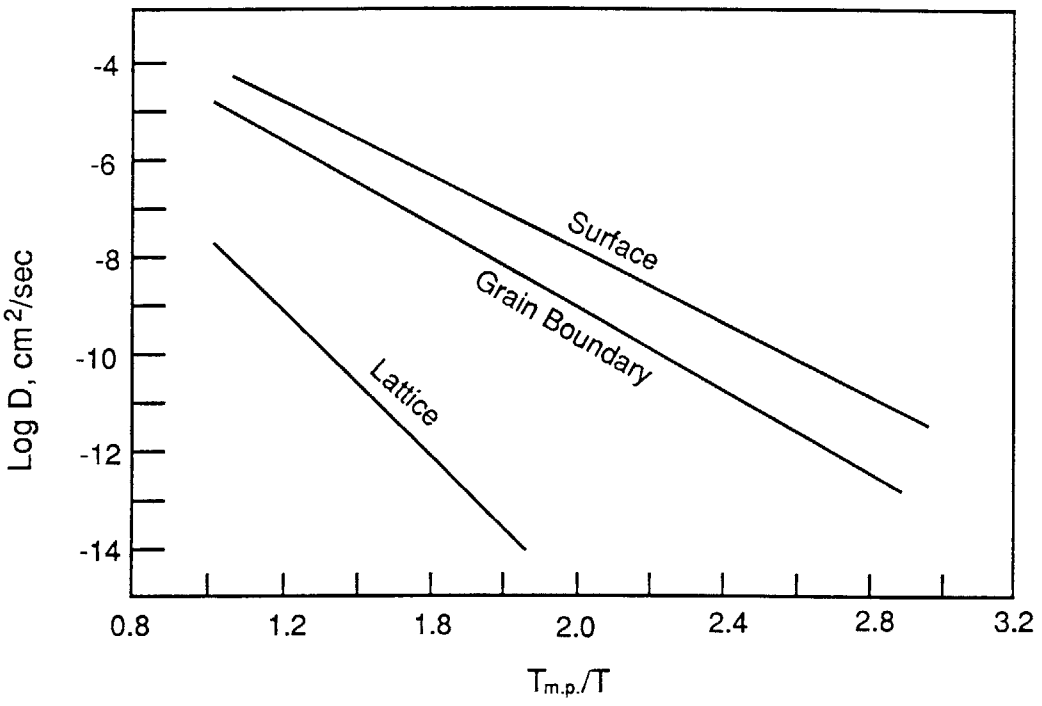

Figure 2.13—Diffusion coefficient for surface, grain boundary and lattice diffusion (65).

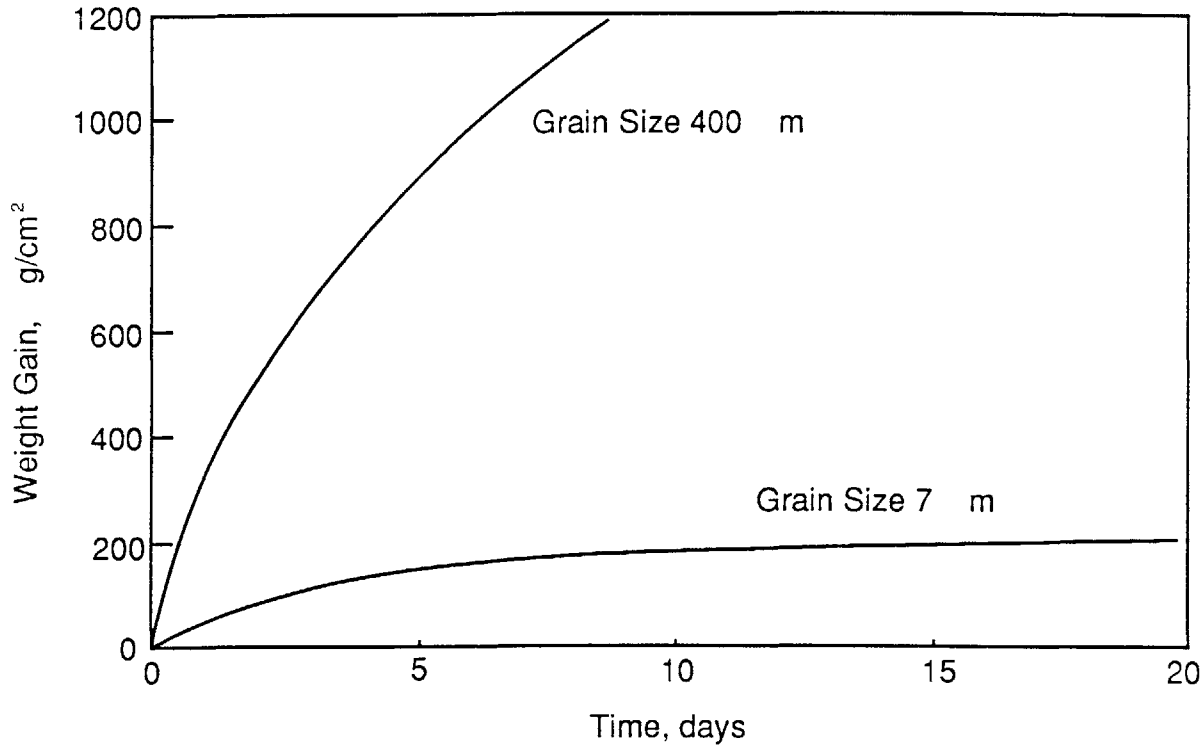

Figure 2.14—Weight gain as a function of time for coarse and fine grained Fe-10wt%Cr alloys oxidized at 600 C (77).

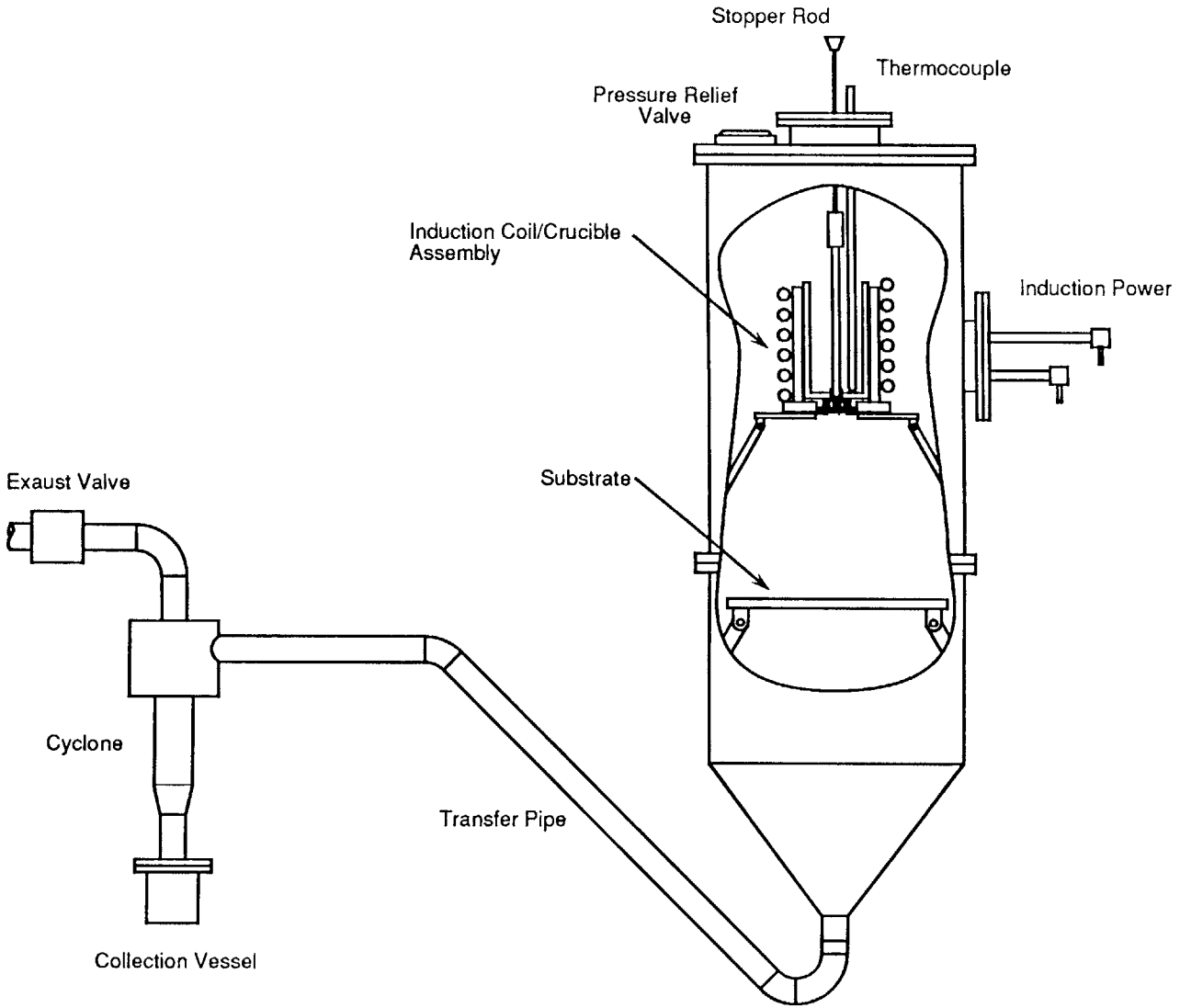

Figure 4.1a—Schematic diagram of gas atomization system.

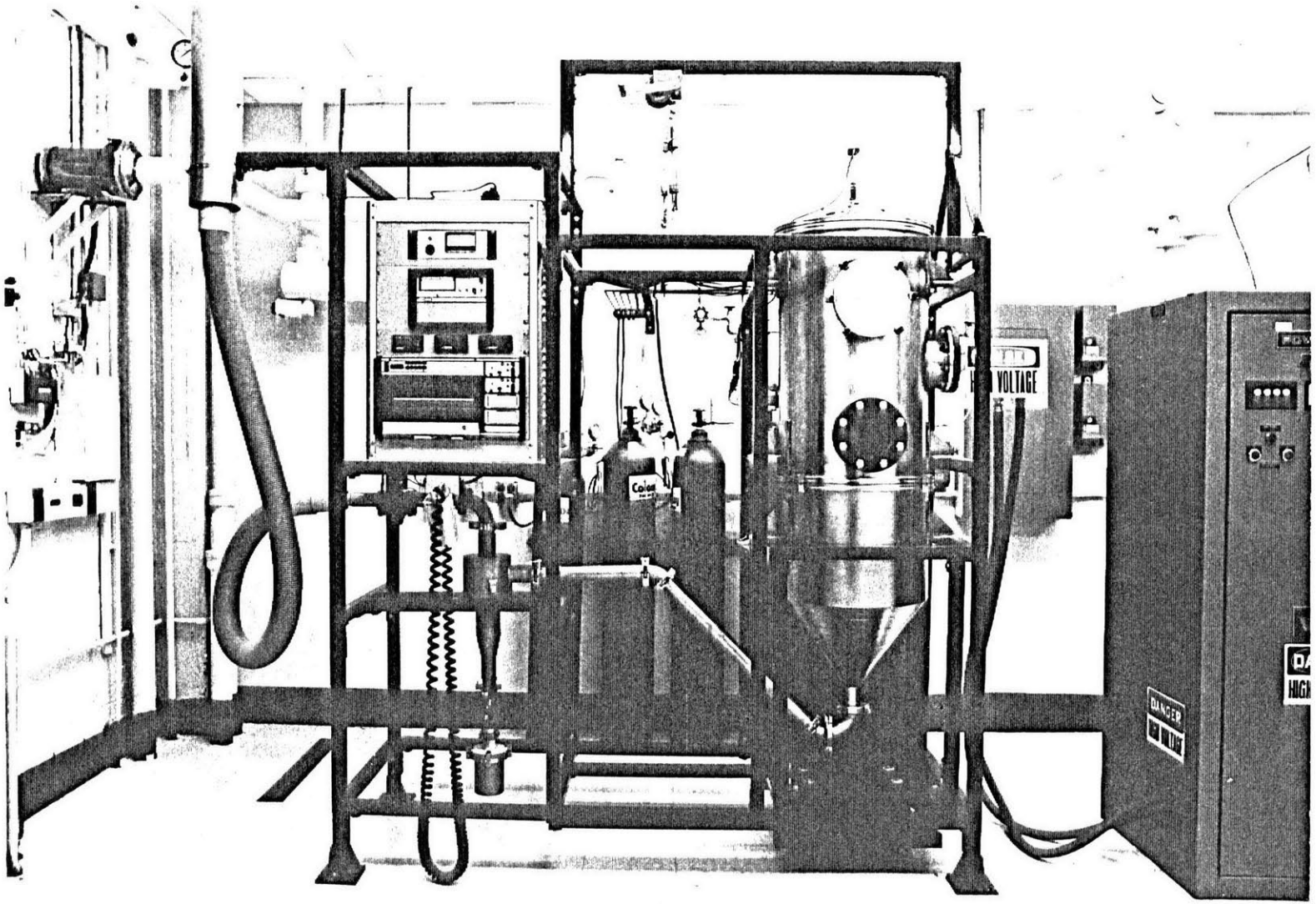

Figure 4.1b—Photograph of gas atomization system.

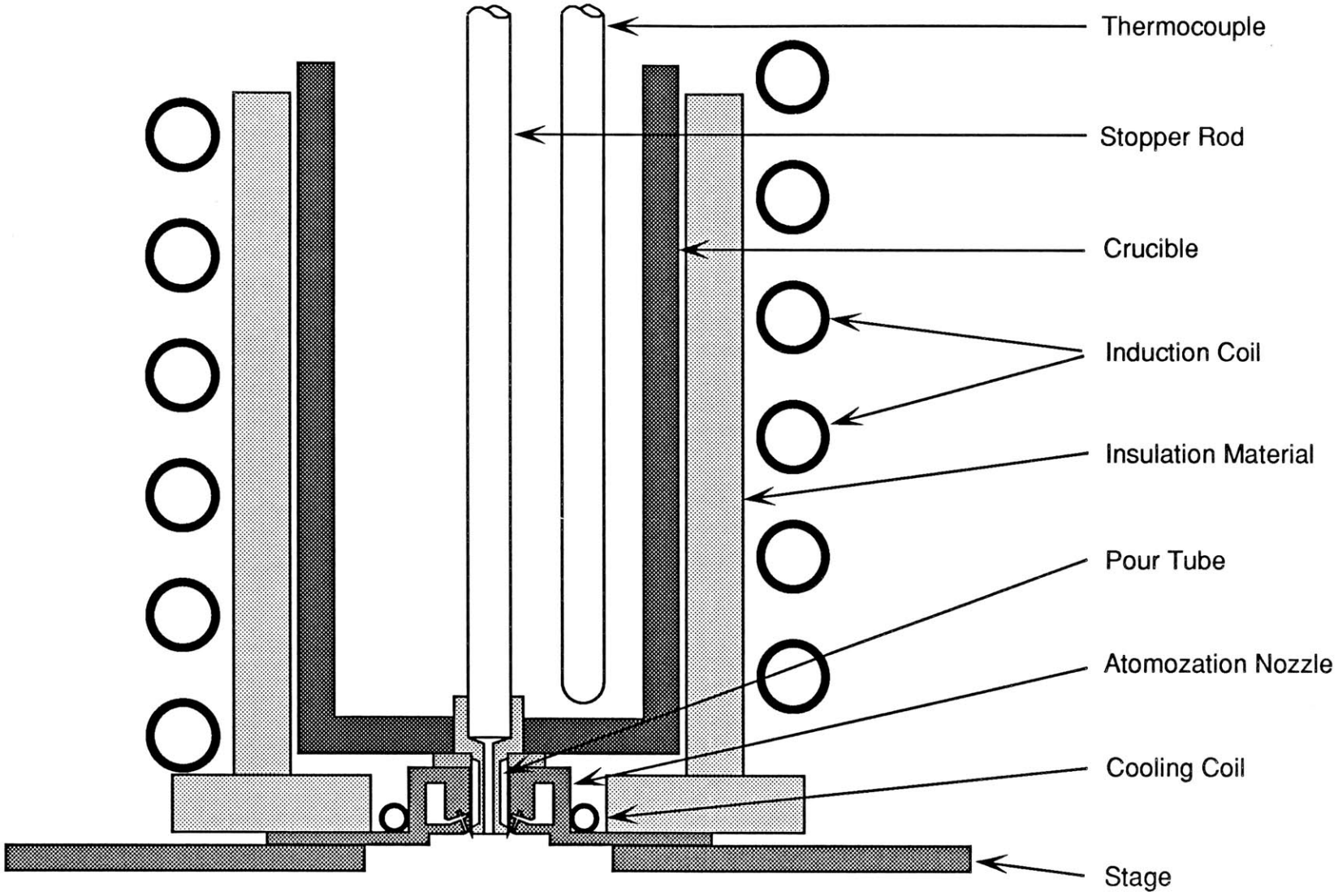

Figure 4.2—Schematic of induction coil/crucible assembly.

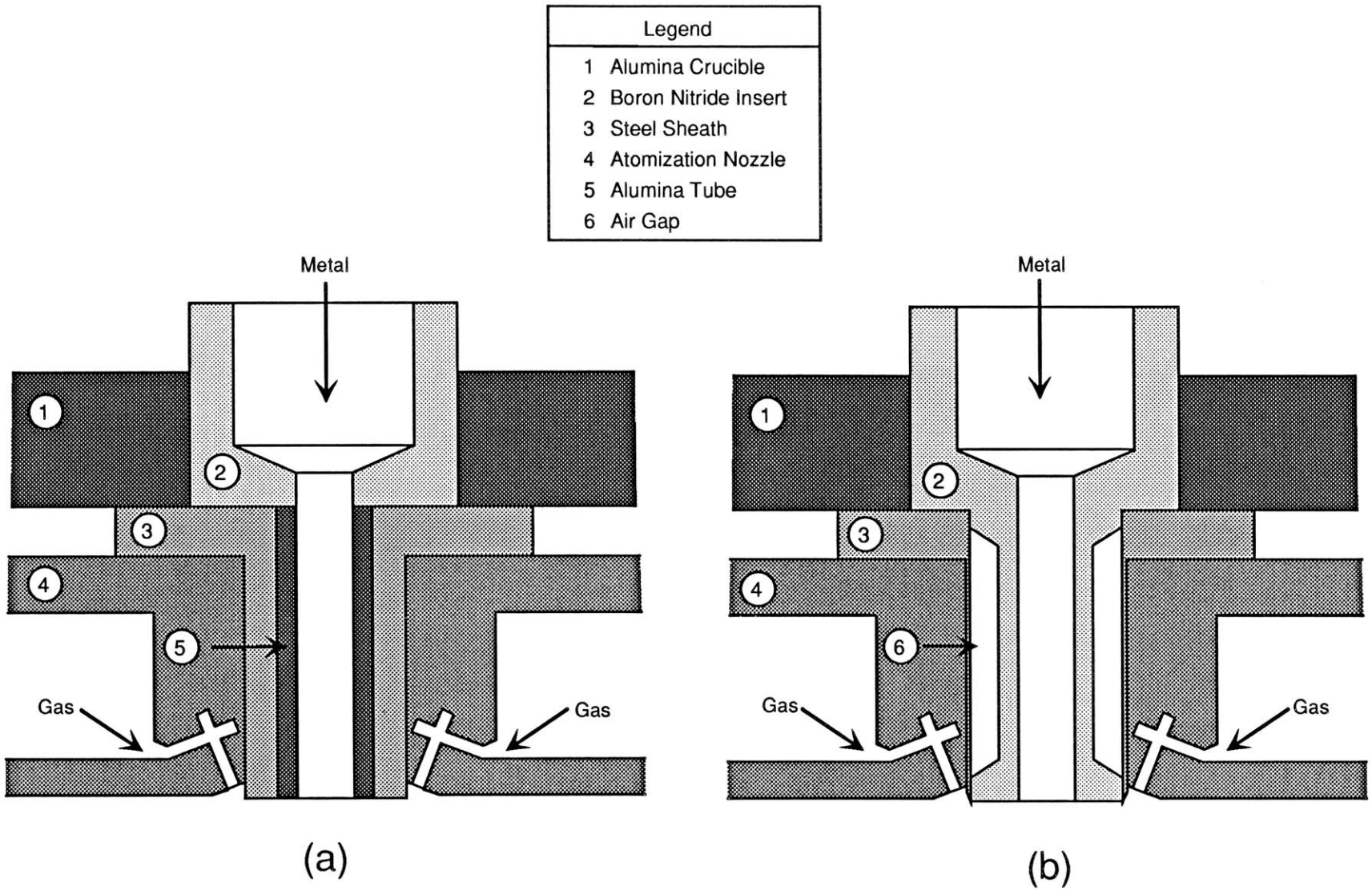

Figure 4.3—Atomization melt pour tubes showing (a) noninsulating and (b) insulating type designs.

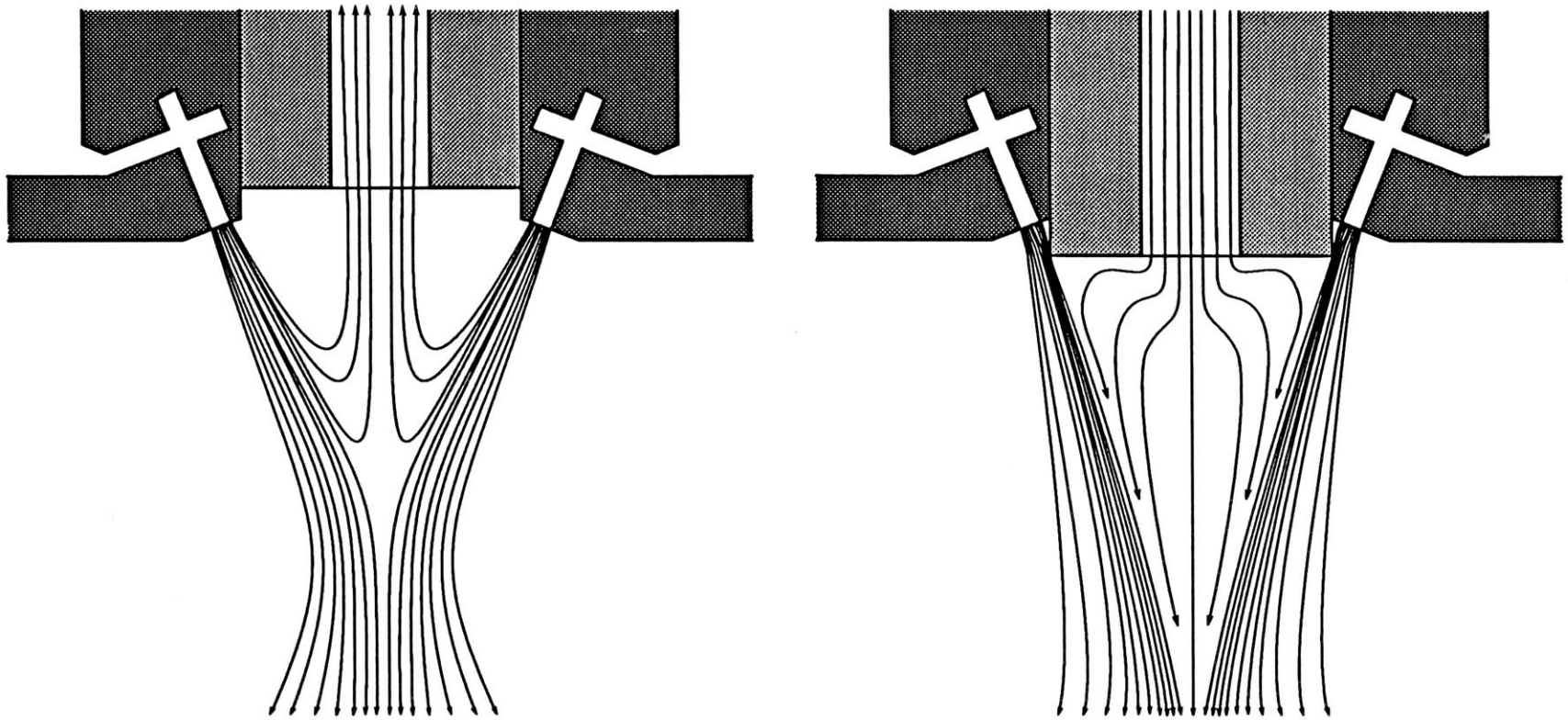

Figure 4.4—Schematic diagram of atomization gas flow out of USGA nozzle for (a) reverse flow condition and (b) aspiration condition.

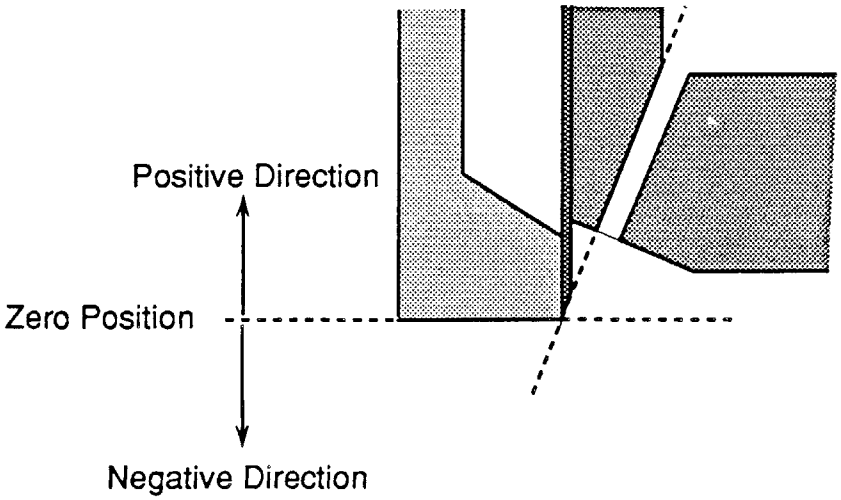

Figure 4.5—Pour tube zero position used for pressure measurements shown in figure 4.6.

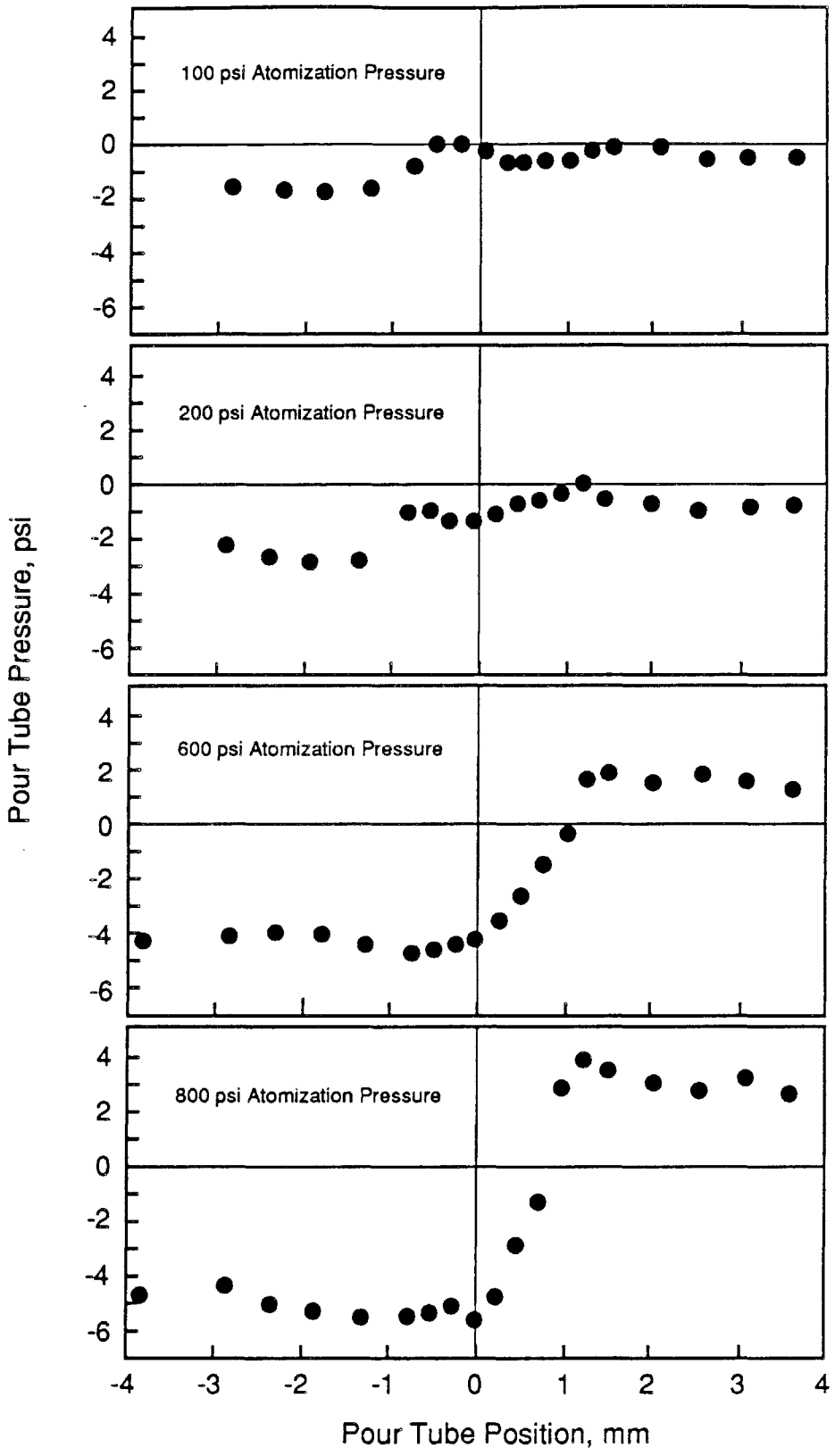

Figure 4.6—Pressure at pour tube opening as a function of pour tube length for atomization pressures of 100, 200, 600 and 800 psi.

	2.5Cr-2.5Al Series	4Cr-4Al Series
Conventionally Processed Alloys	Fe-2.5Cr-2.5Al	Fe-4Cr-4Al Fe-4Cr-4Al-1Ti
Spray Formed Alloys	Fe-2.5Cr-2.5Al-1Ti-0.6B *	Fe-4Cr-4Al-1Ti-0.6B **
Powder Processed Alloys	Fe-2.5Cr-2.5Al-1Ti-0.6B	

* Alloys produced at 9, 11, 15, 19 and 25in substrate positions.
** Alloy produced at a 9in substrate position.

Table 4.1—Conventionally processed and rapidly solidified alloys.

Element	Supplier	Purity
Iron	Johnson Matthey, Inc.	99.98%*
Chromium	Morton Thiokol, Inc.	99.5%**, 99.9%*
Aluminum	Johnson Matthey, Inc.	99.95%*
Titanium	Morton Thiokol, Inc.	99.7%*
Boron	Morton Thiokol, Inc.	99.0%*

* Does not include nonmetallic impurities.
** Includes metallic and nonmetalic impurities.

Table 4.2—The purity and supplier of elements used in the processing of alloys.

	Cr	Al	Ti	B	C	S	N	Fe
Conventionally Processed Fe-4Cr-4Al Alloy	4.13	4.11	0.008	0.002	0.006	0.003	0.0010	bal.
Conventionally Processed Fe-4Cr-4Al-1Ti Alloy	4.54	4.30	1.11	0.58	0.022	0.005	0.0024	bal.
Spray-Formed Fe-4Cr-4Al-1Ti-0.6B Alloy	4.36	4.29	0.99	0.002	0.004	0.007	0.0010	bal.
Conventionally Processed Fe-2.5Cr-2.5Al Alloy	2.79	2.39	0.004	0.002	0.006	0.006	0.006	bal.
Spray Formed Fe-2.5Cr-2.5Al-1Ti-0.6B Alloy*	2.65	2.29	1.25	0.58	0.006	0.002	0.0010	bal.
Spray Formed Fe-2.5Cr-2.5Al-1Ti-0.6B Alloy**	2.67	2.37	1.29	0.58	0.006	0.005	0.0016	bal.
Powder Processed Fe-2.5Cr-2.5Al-1Ti-0.6B Alloy	2.73	2.40	1.35	0.46	0.004	0.005	0.0014	bal.

*Alloy spray-formed at a 9in substrate distance.
**Alloy spray-formed at a 25in substrate distance.

Table 4.3—Elemental analysis of the conventionally processed and rapidly solidified alloys in weight percent.

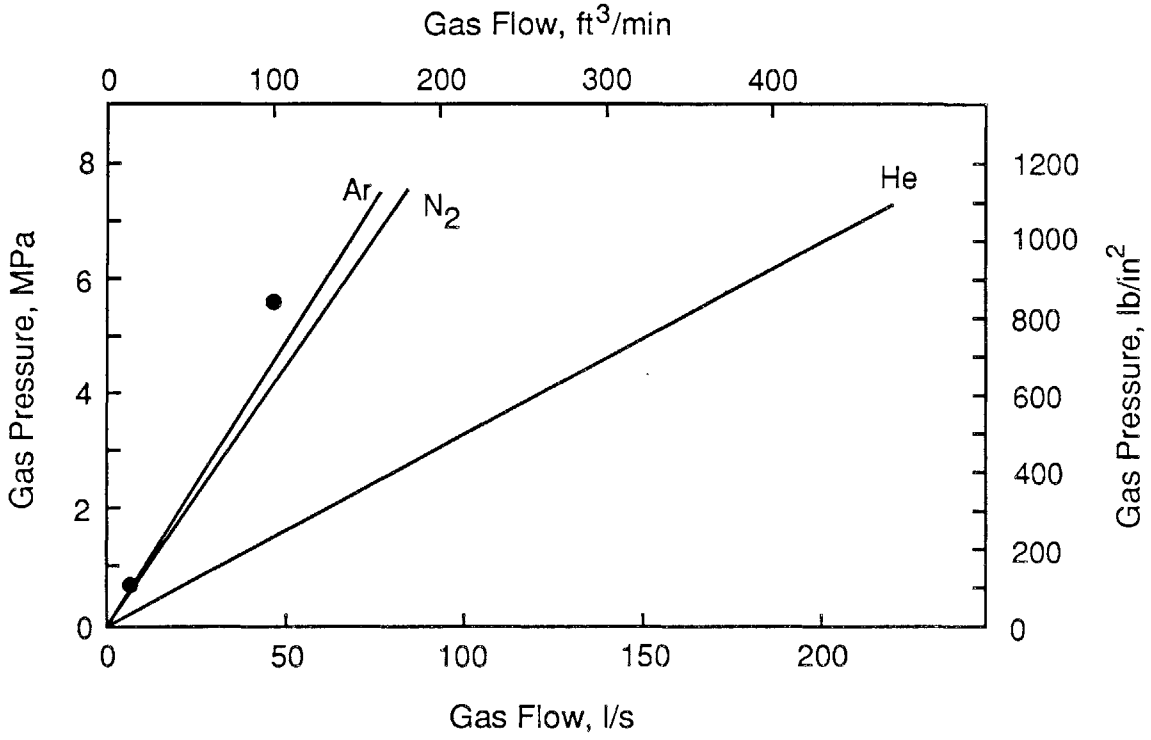

Figure 4.7—Gas flow through USGA nozzle as a function of atomization gas pressure. Points indicated are calculated flows from this work (87).

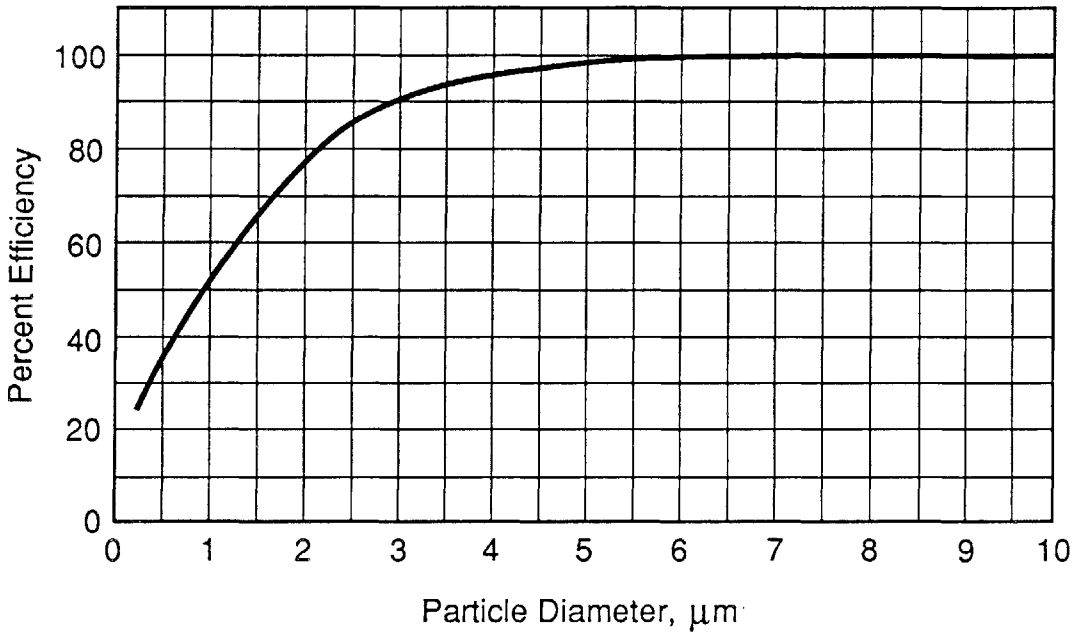

Figure 4.8—Particle size efficiency curve for iron powder at a gas flow rate of 40 scfm (88).

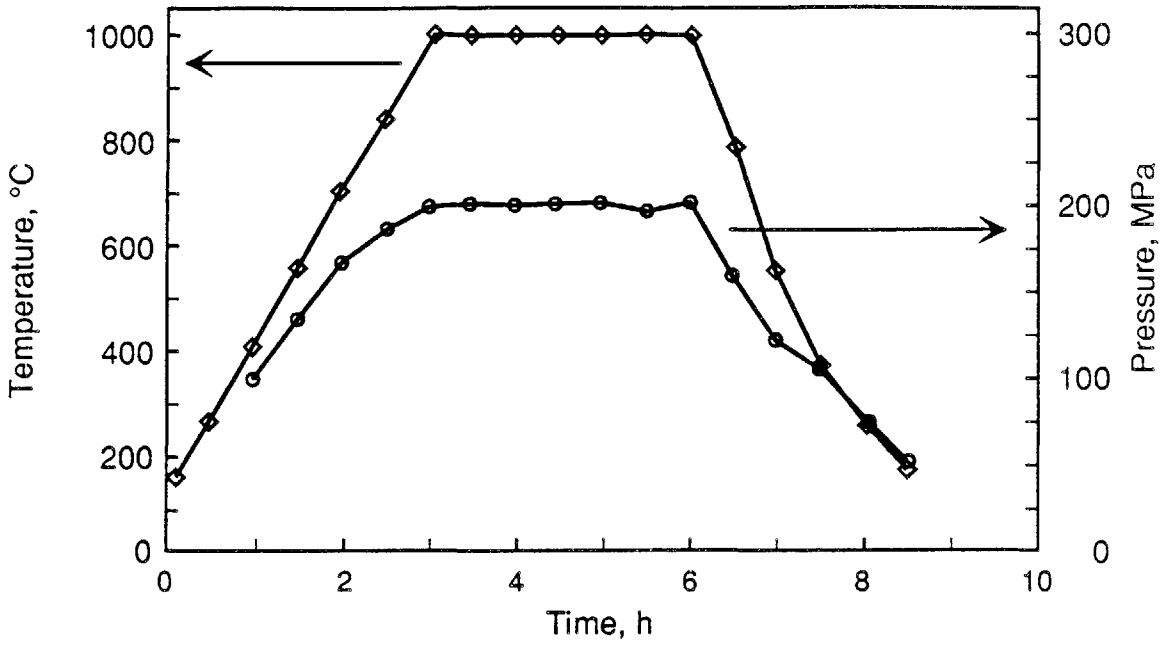

Figure 4.9—Temperature and pressure cycle for hot isostatic pressing of rapidly solidified Fe-2.5Cr-2.5Al-1Ti-0.6B powder.

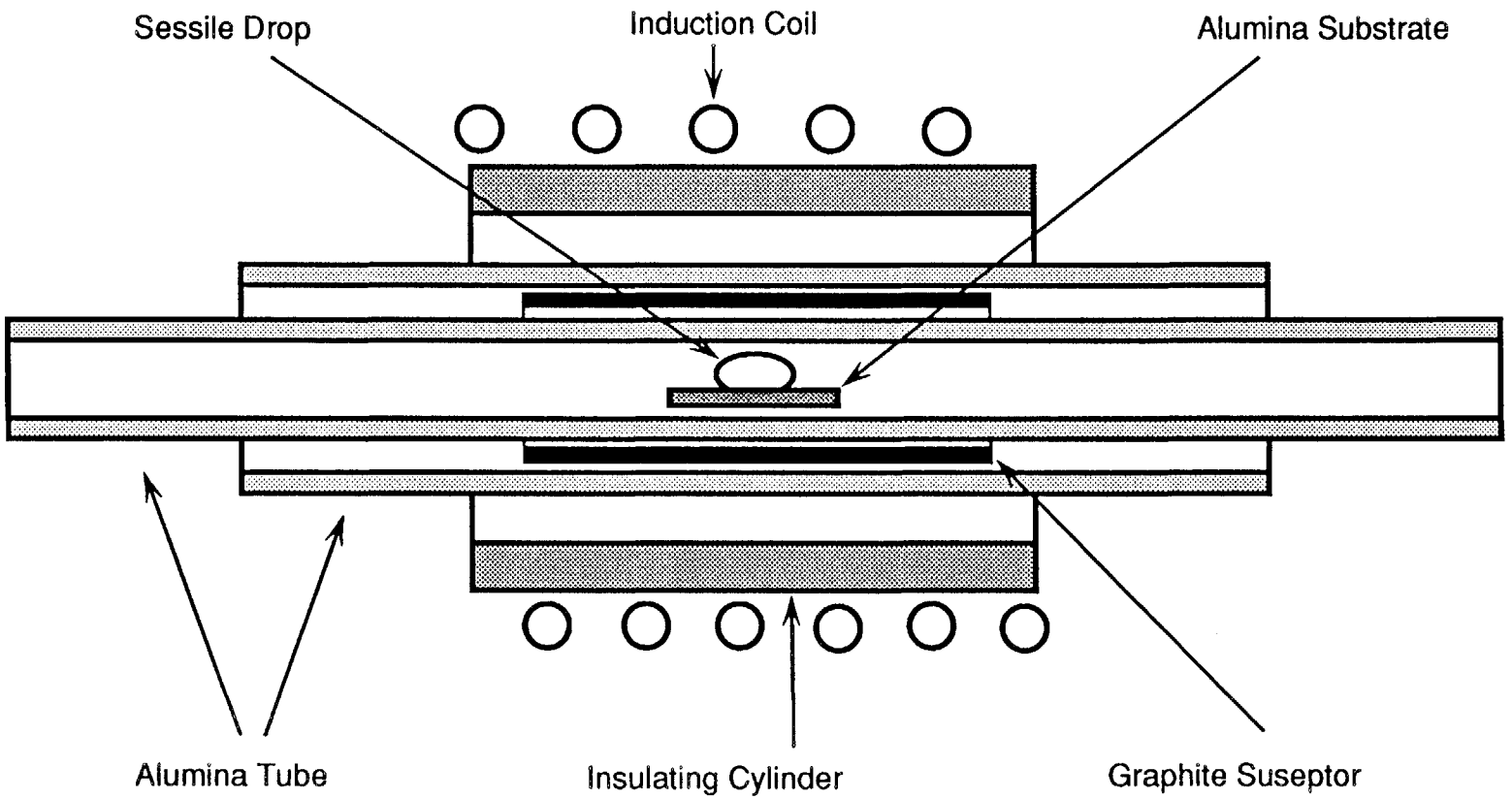

Figure 4.10—Sessile drop apparatus.

	2.5Cr-2.5Al Series			4Cr-4Al Series		
	Conventionallly Processed Fe-2.5Cr-2.5Al	Spray Formed* Fe-2.5Cr-2.5Al-1Ti-0.6B	Powder Processed Fe-2.5Cr-2.5Al-1Ti-0.6B	Conventionally Processed Fe-4Cr-4Al	Conventionally Processed Fe-4Cr-4Al-1Ti	Spray Formed Fe-4Cr-4Al-1Ti-0.6B
400°C						
500°C						
600°C						
700°C						
800°C						
900°C						
1000°C						

* Alloys tested were spray formed at 9 and 25 inch substrate positions.

Table 4.4—Matrix of isothermal oxidation experiments.

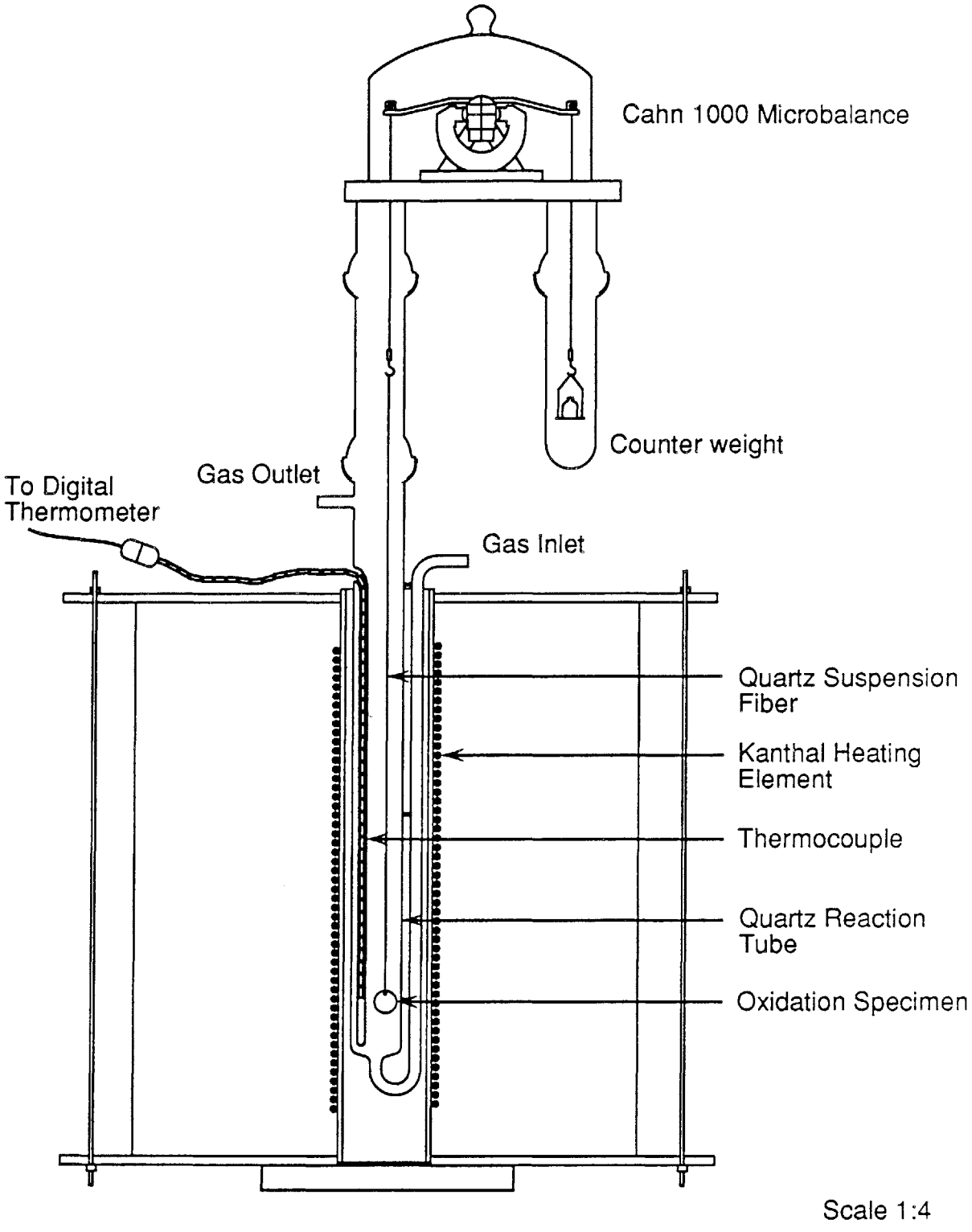

Figure 4.11—Schematic of thermogravimetric apparatus (TGA).

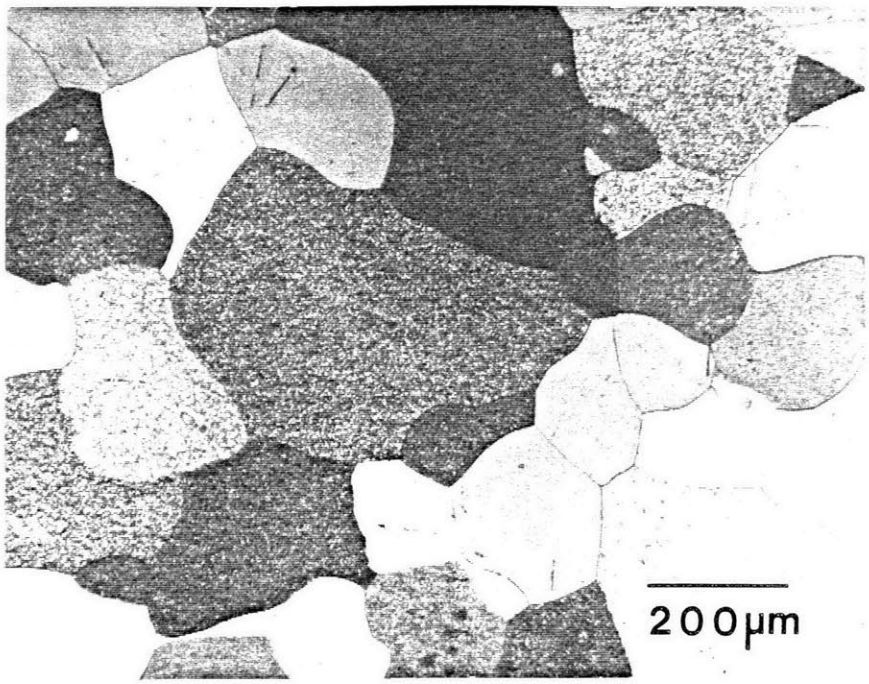

Figure 5.1—Polarized light optical micrograph of conventionally processed Fe-2.5Cr-2.5Al alloy.

Figure 5.2—Spray forming process.

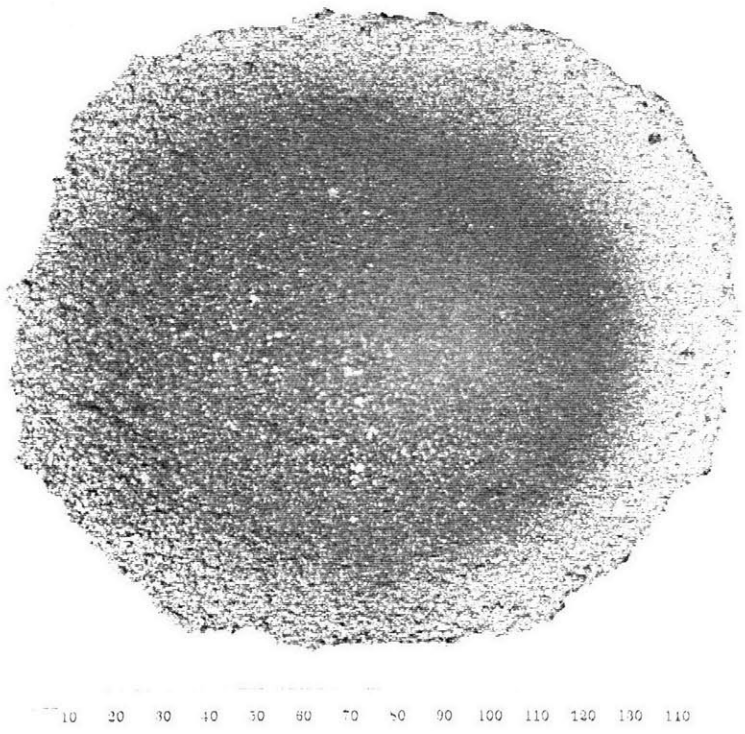

Figure 5.3—Spray formed deposit.

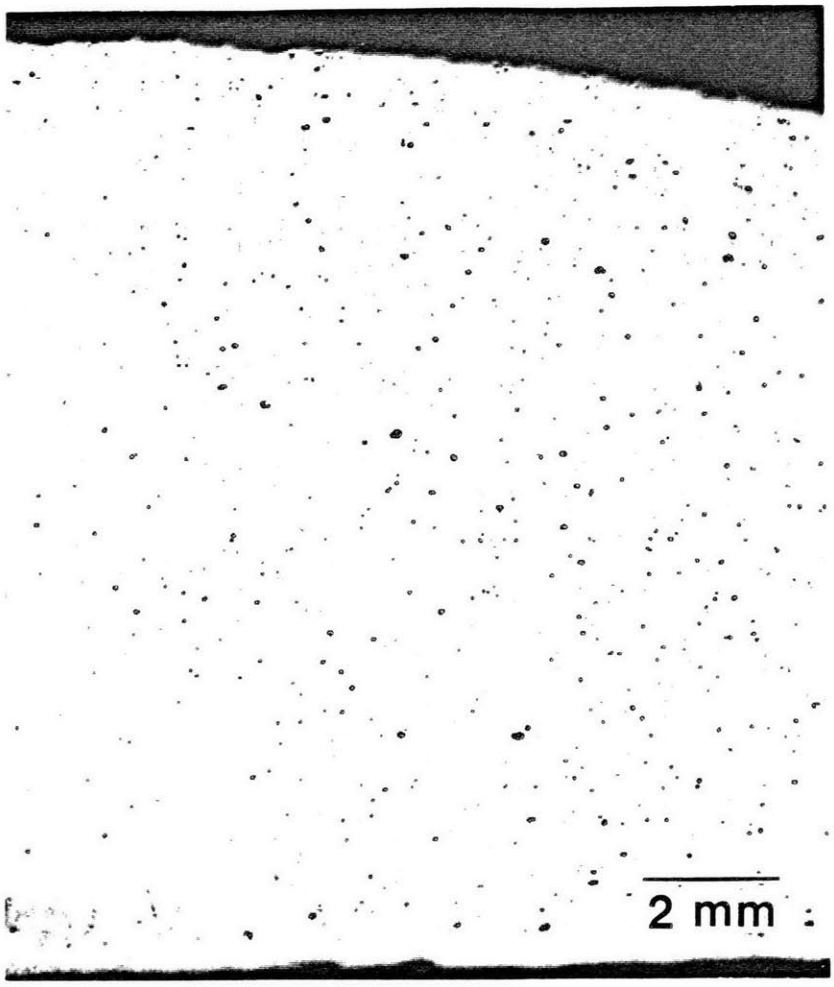

Figure 5.4—Cross-section through spray formed Fe-4Cr-4Al-1Ti-0.6B alloy showing distribution of porosity in deposit.

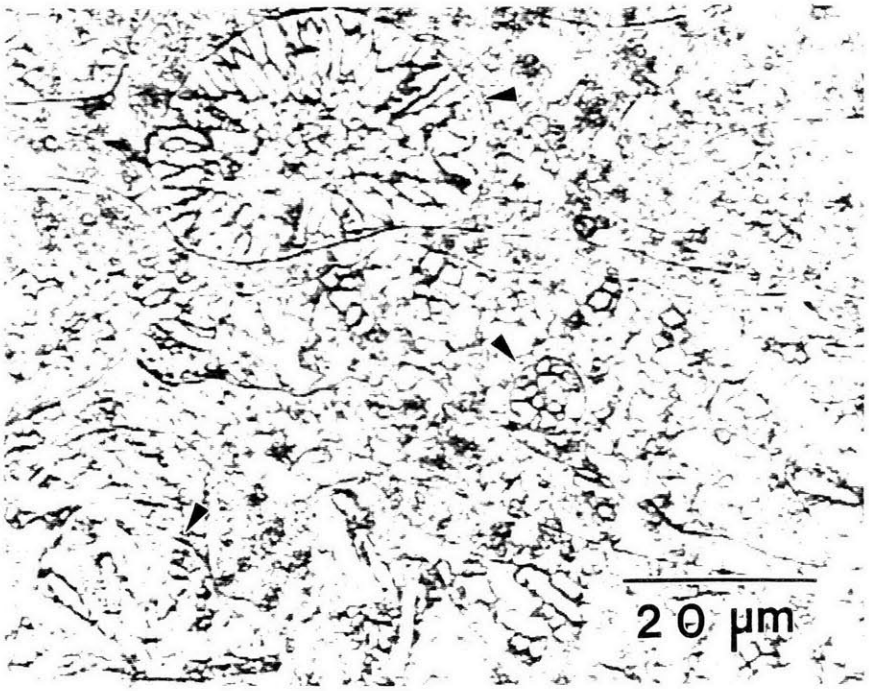

Figure 5.5—Optical micrograph of spray formed Fe-4Cr-4Al-1Ti-0.6B alloy showing entrapped powder particles (arrows) and splat boundaries.

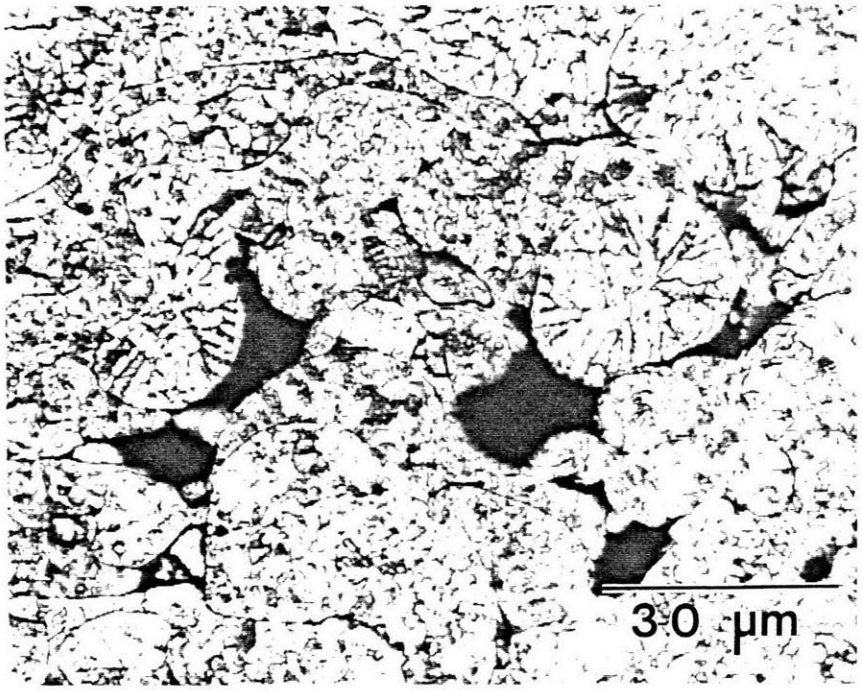

Figure 5.6—Optical micrograph of spray fromed Fe-4Cr-4Al-1Ti-0.6B alloy showing porosity associated with presolidified powder particle.

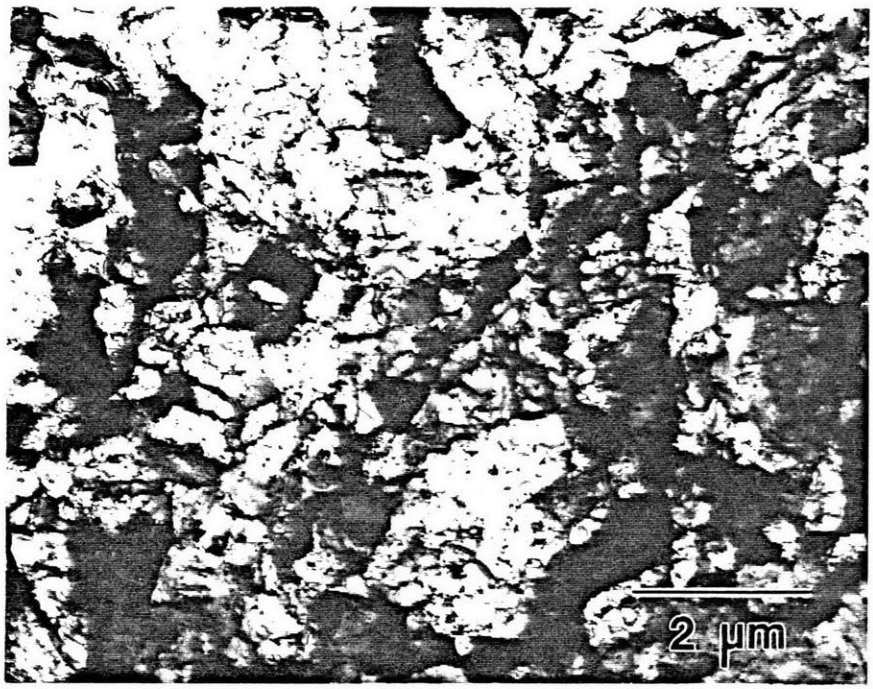

Figure 5.7—Bright-field TEM image of spray formed Fe-4Cr-4Al-1Ti-0.6B alloy after hot rolling to a 50% reduction in area and annealing at 900°C for 100h.

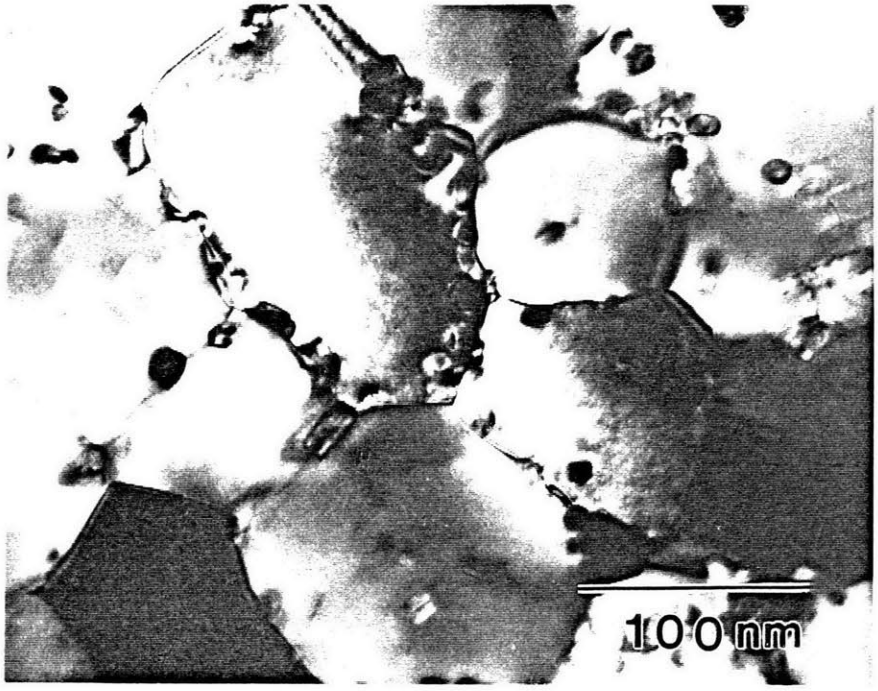

Figure 5.8—Bright-field TEM image of region in figure 5.7 showing alloy grain size and precipitate distribution.

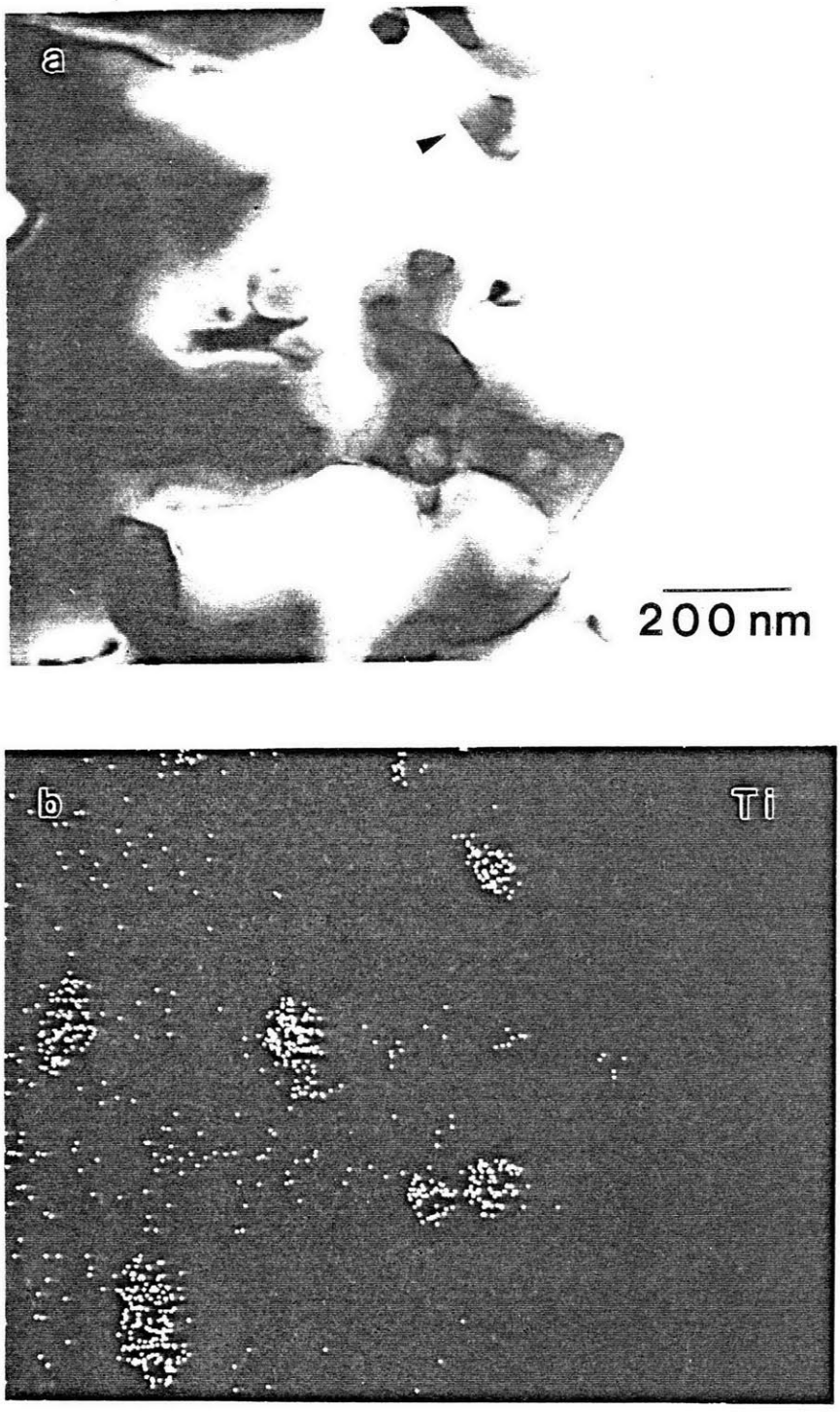

Figure 5.9—Bright-field STEM image (a) and titanium X-ray intensity map (b) of spray formed Fe-4Cr-4Al-1Ti-0.6B alloy after hot rolling to a 50% reduction in cross-sectional area and annealing at 900°C for 100h.

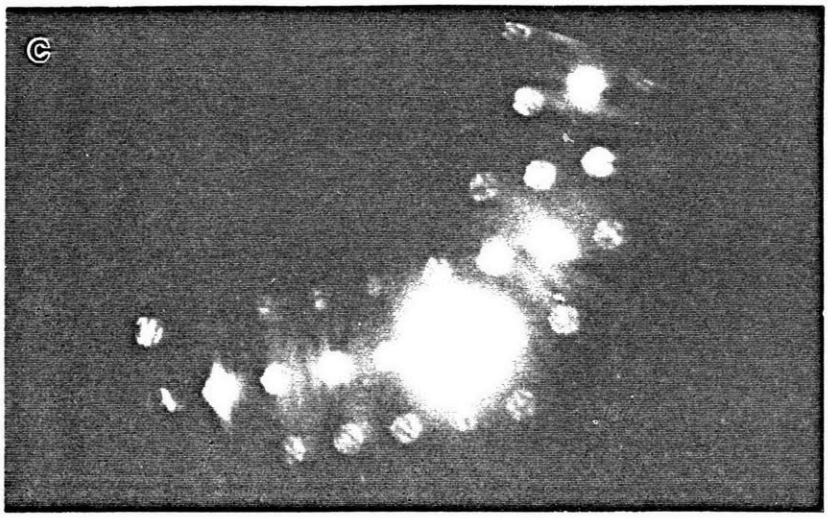

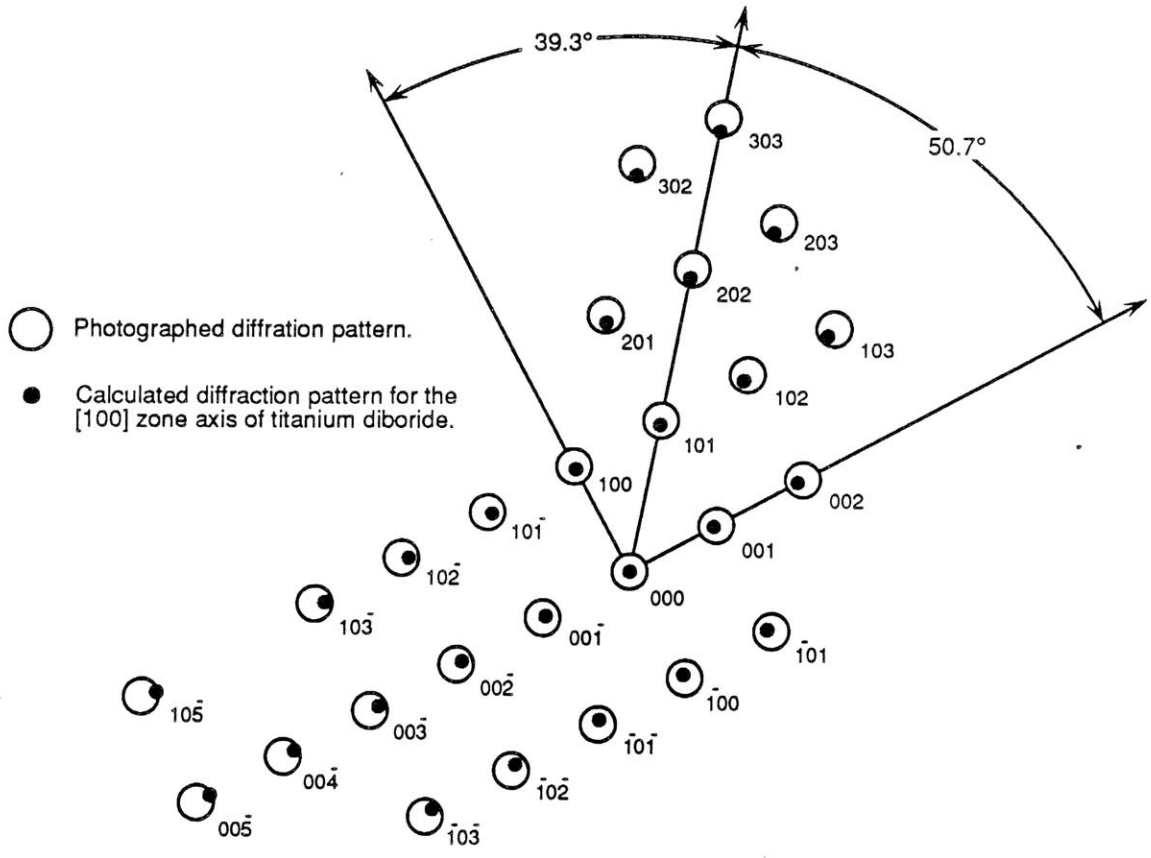

d

Figure 5.9 continued—Convergent beam electron diffraction pattern of particle indicated by arrow in figure 5.9 (c) and index of the pattern to the [010] zone axis of titanium diboride (d).

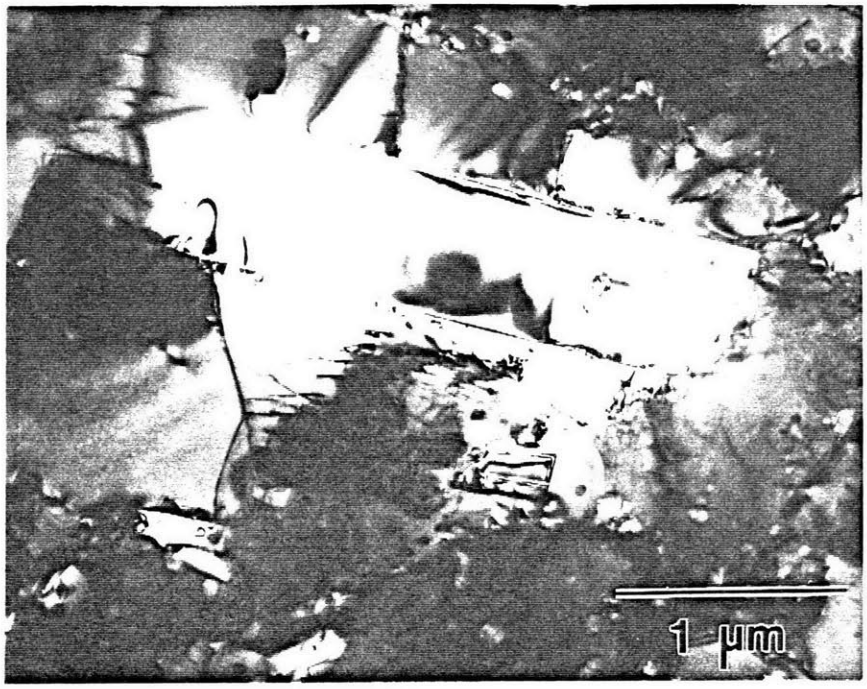

Figure 5.10—Dark-field TEM image of coarse boride particles in spray formed and thermo-mechanically processed Fe-4Cr-4Al-1Ti-0.6B alloy.

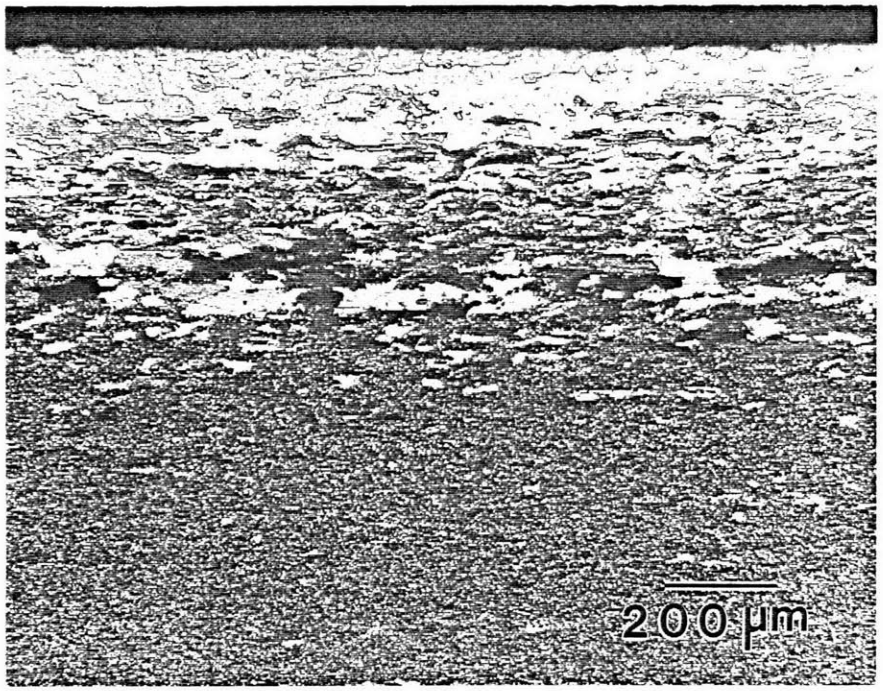

Figure 5.11—Optical micrograph of spray formed Fe-4Cr-4Al-1Ti-0.6B alloy after hot rolling to a 50% reduction in cross-sectional area and annealing at 900°C for 300h. Field of view at edge of rolled strip showing abnormal grain growth penetrating into the alloy from the surface.

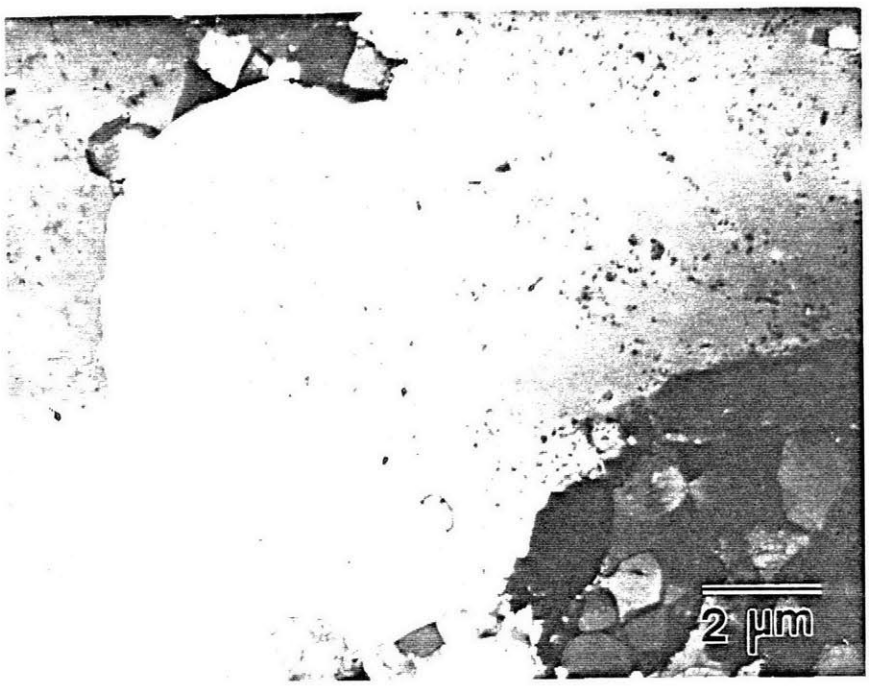

Figure 5.12—Bright-field STEM image of anormal grain growth region shown in figure 5.13.

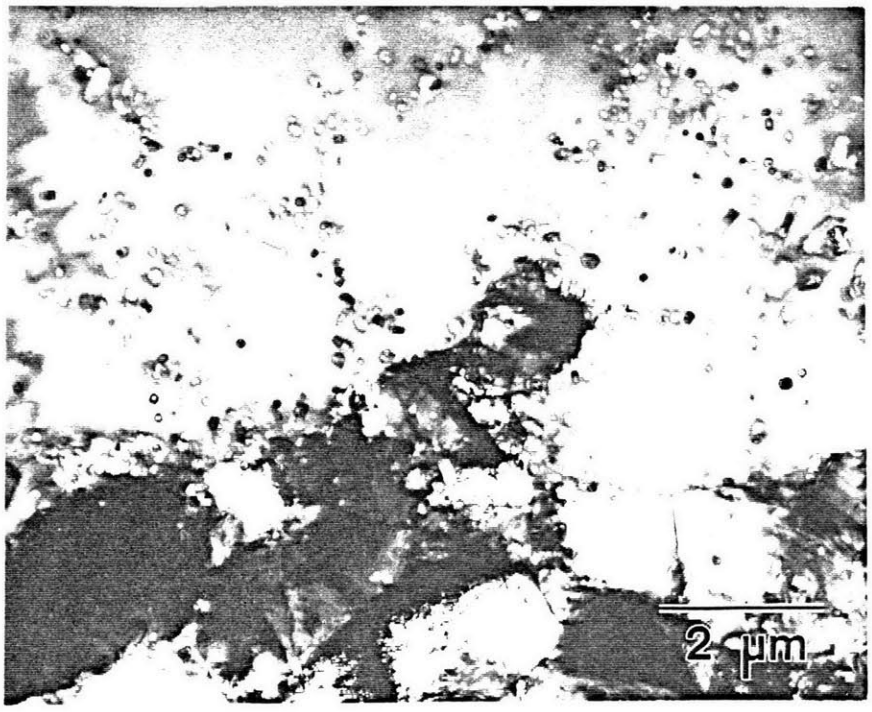

Figure 5.13—Bright-field TEM image of interface between a fine grained region and a large recrystallized grain.

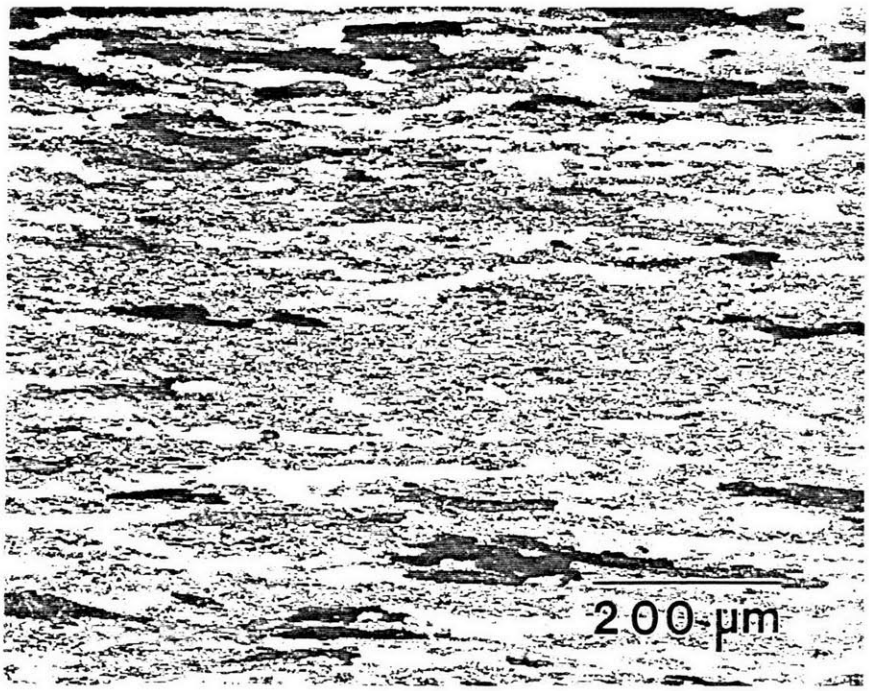

Figure 5.14—Optical micrograph of spray deposited Fe-4Cr-4Al-1Ti-0.6B alloy after hot rolling to a 50% reduction in cross-sectional area and annealing at 1000°C for 100h. Field of view is at the center of the rolled strip showing abnormal grain growth having consumed almost the entire alloy.

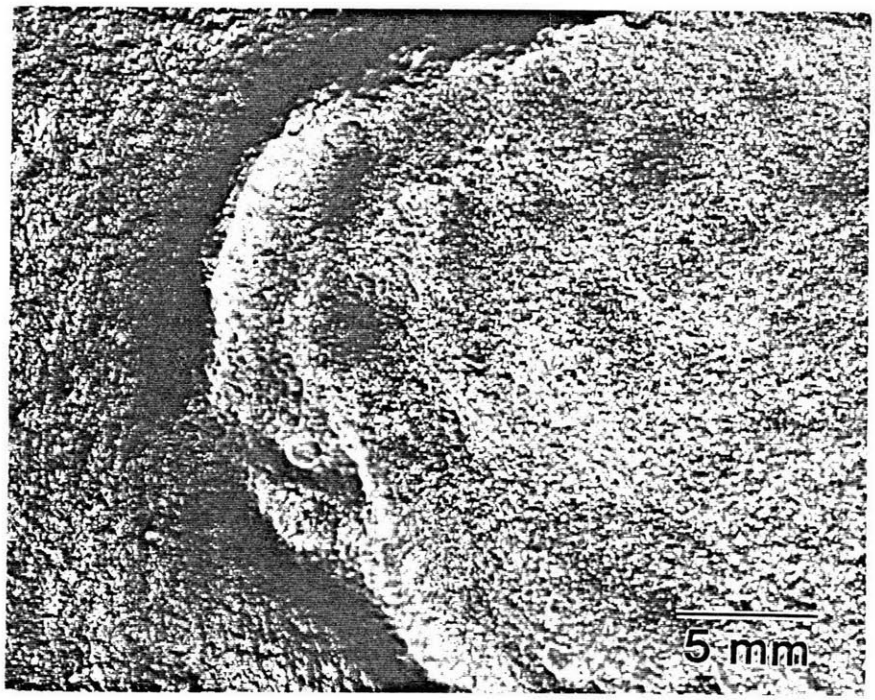

Figure 5.15—Photograph of surface of spray formed Fe-2.5Cr-2.5Al-1Ti-0.6B alloy processed at a 0.22m (9in) substrate position showing rippled surface caused by formation of a liquid puddle in the deposit during spray forming.

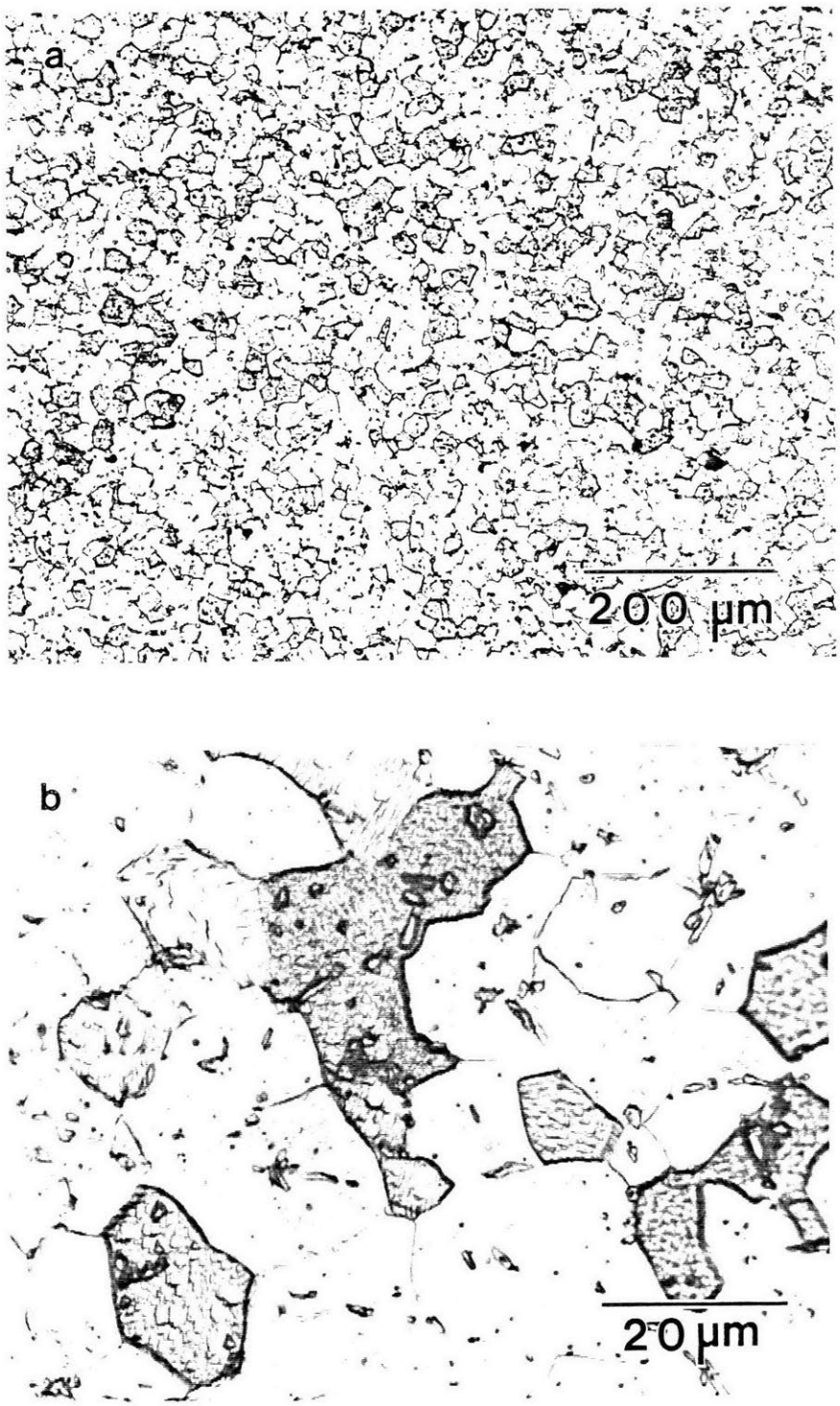

Figure 5.16—Optical micrograph of spray formed Fe-2.5Cr-2.5Al-1Ti-0.6B alloy processed at a 0.22m (9in) substrate position: (a) low magnification and (b) high magnification.

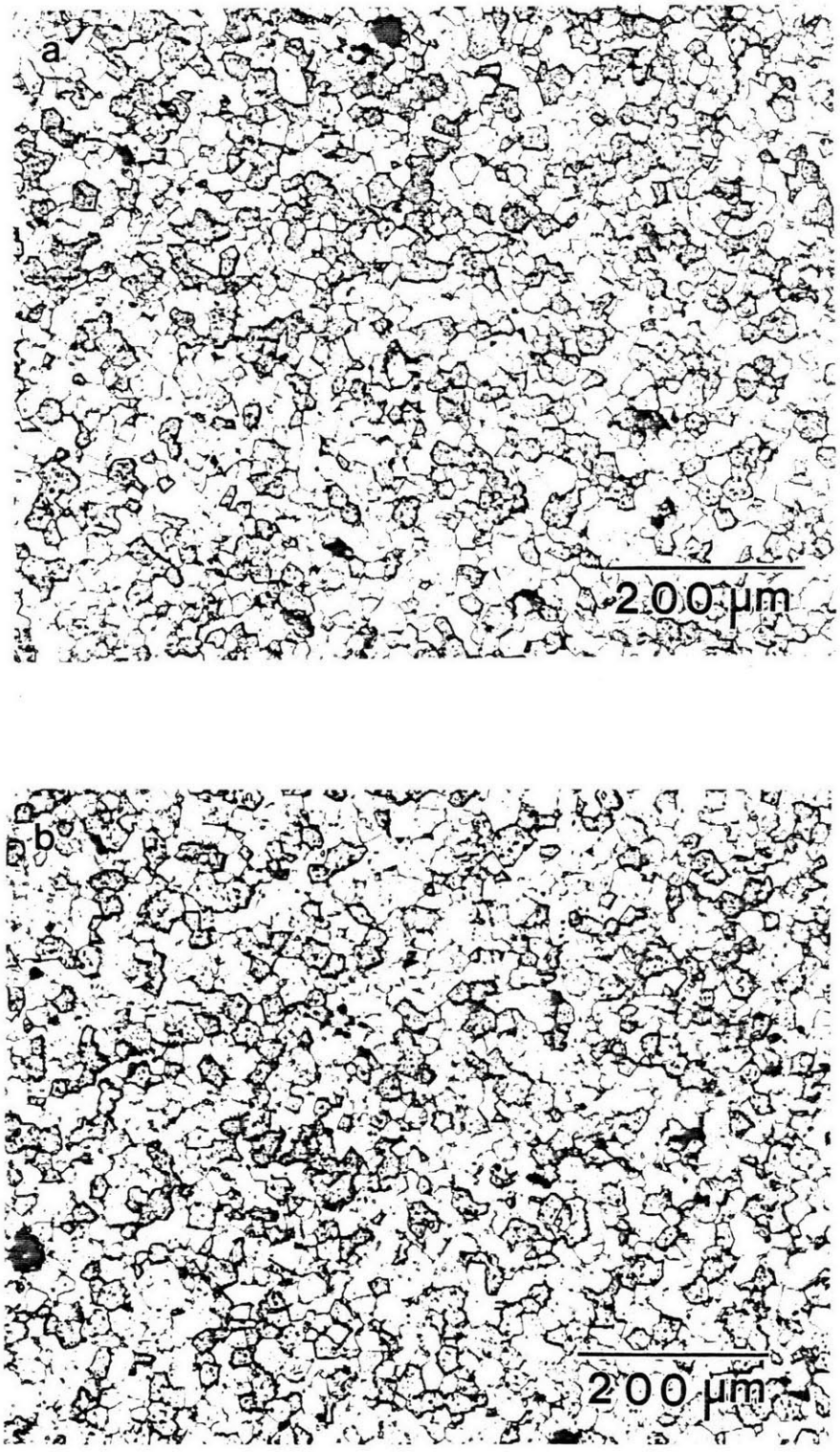

Figure 5.17—Optical micrograph of spray formed Fe-2.5Cr-2.5Al-1Ti-0.6B alloy processed at (a) 0.27m (11in) and (b) 0.38m (15in) substrate positions.

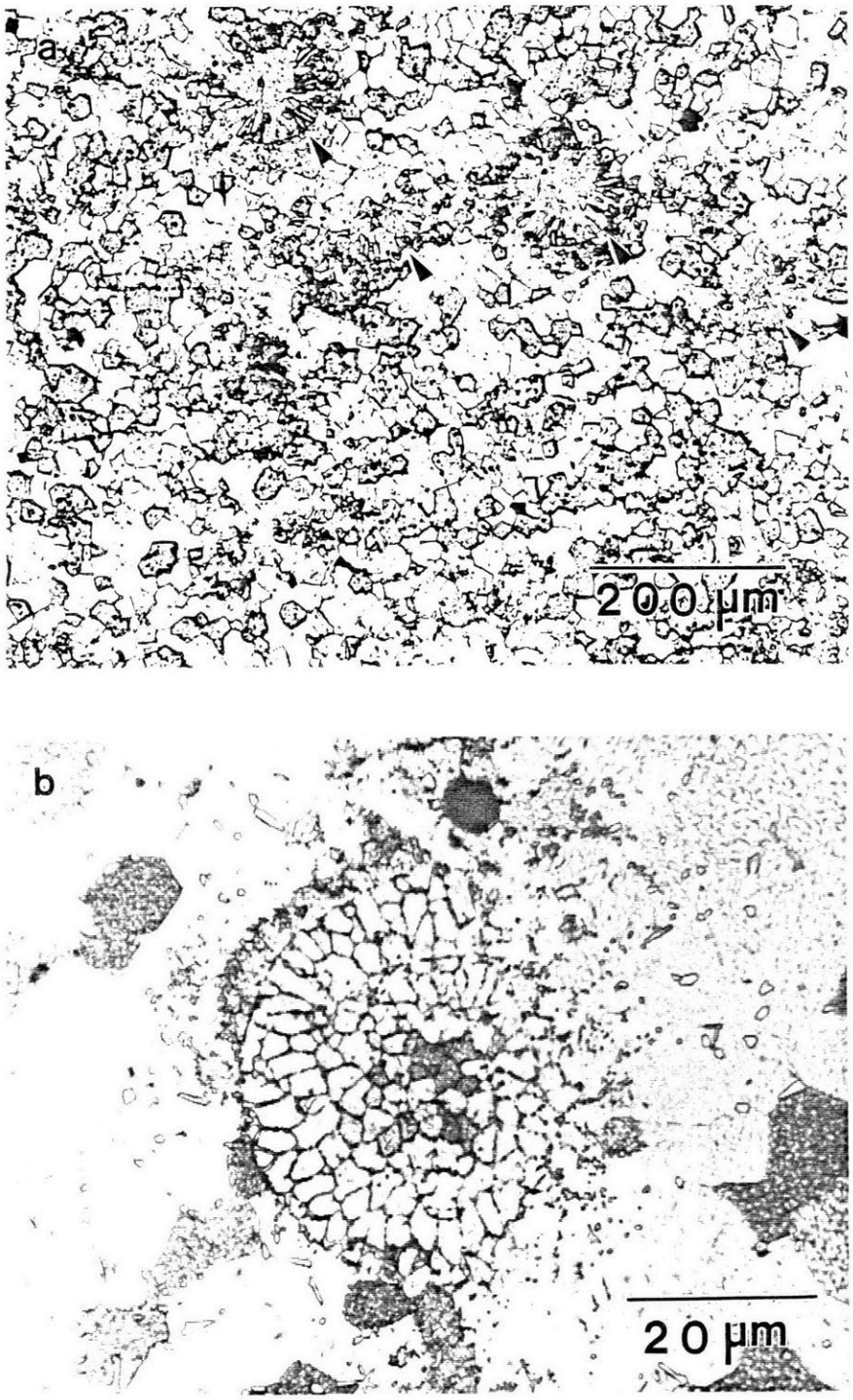

Figure 5.18—Optical micrograph of spray formed Fe-2.5Cr-2.5Al-1Ti-0.6B alloy processed at a 0.48m (19in) substrate position: (a) low magnification view showing four entrapped powder particles (indicated by arows) and (b) high magnification view of a partially melted, entrapped powder particle.

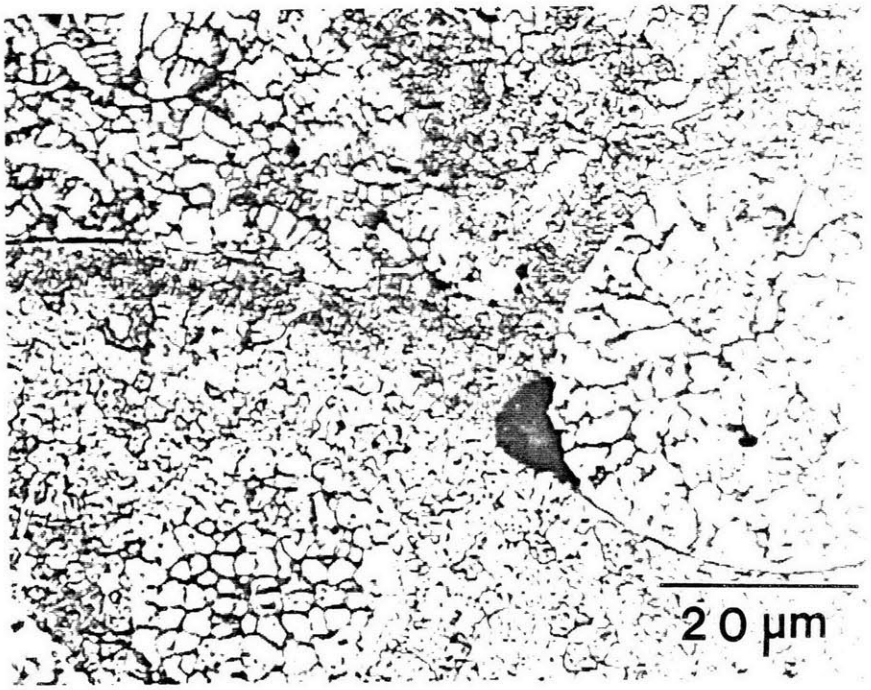

Figure 5.19—Optical micrograph of spray formed Fe-2.5Cr-2.5Al-1Ti-0.6B alloy processed at a 0.63m (25in) substrate position showing entrapped powder particles and splat boundaries.

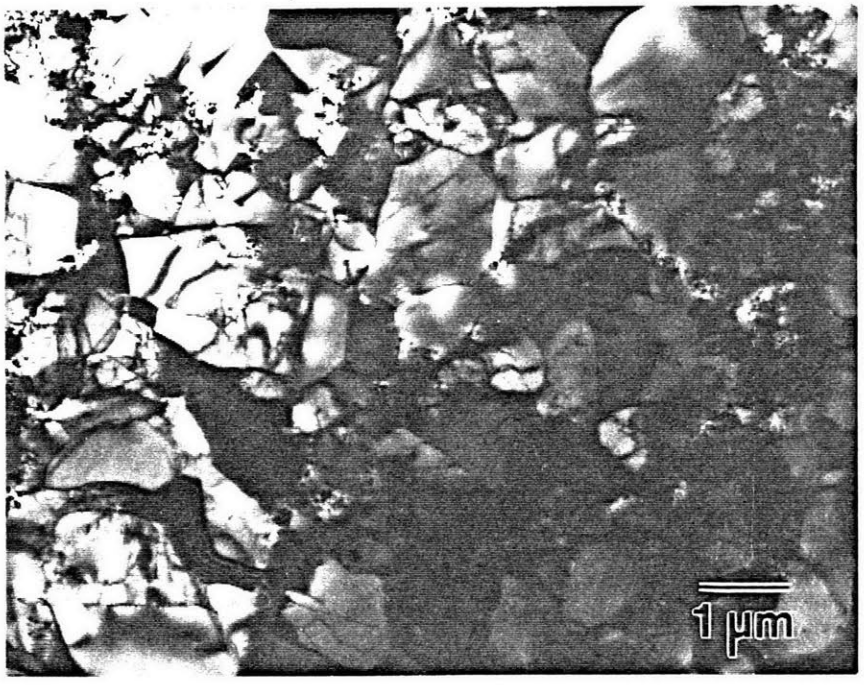

Figure 5.20—Bright-field TEM micrograph of spray formed Fe-2.5Cr-2.5Al-1Ti-0.6B alloy processed at a 0.63m (25in) substrate position after being hot rolled to a 50% reduction in cross-sectional area and annealed at 900°C for 100h.

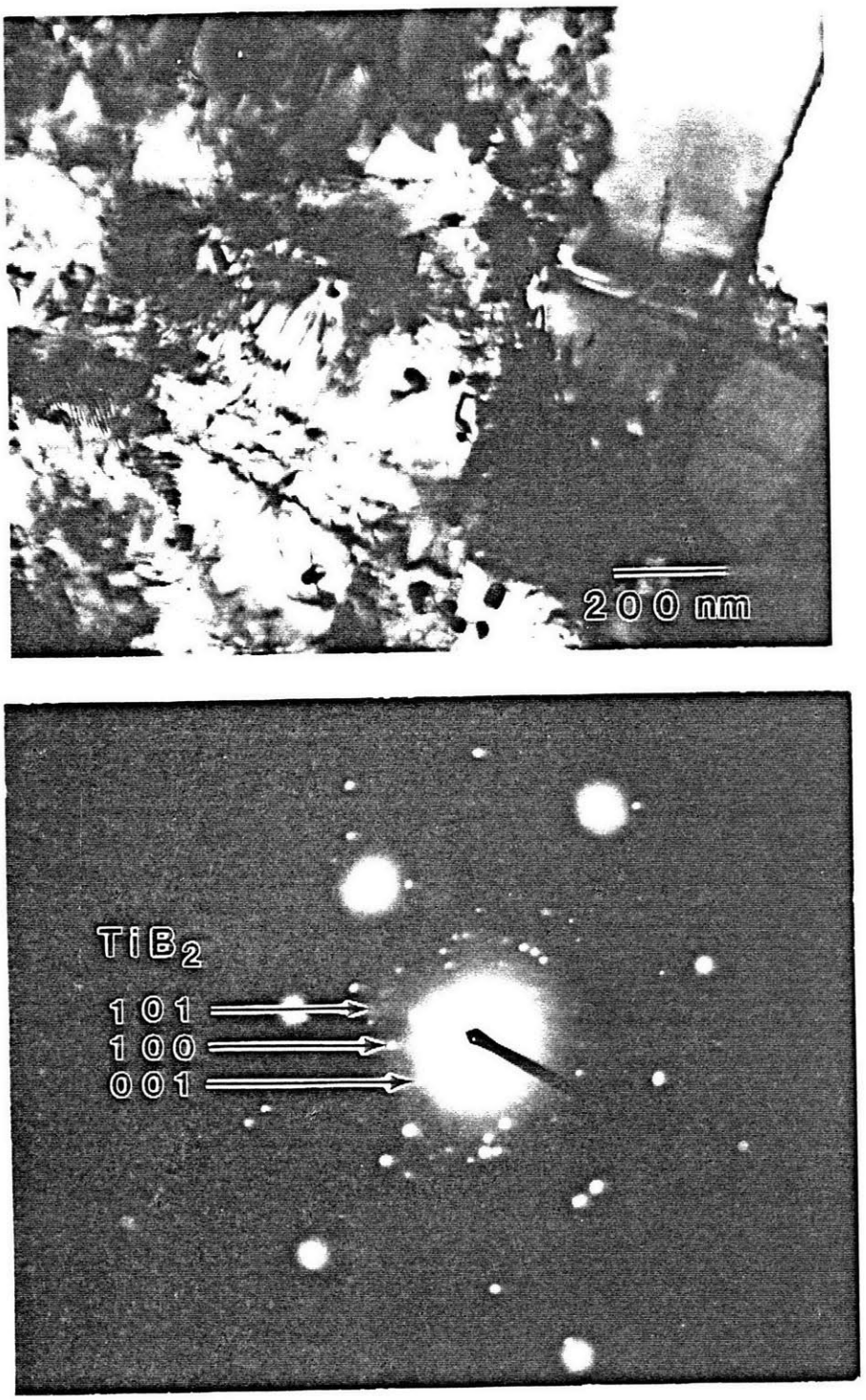

Figure 5.21—Bright field TEM image (a) and selected area diffraction pattern (b) of a region containing a high concentration of TiB_2 particles in a spray formed Fe-2.5Cr-2.5Al-1Ti-0.6B alloy processed at a 0.63m (25in) substrate position.

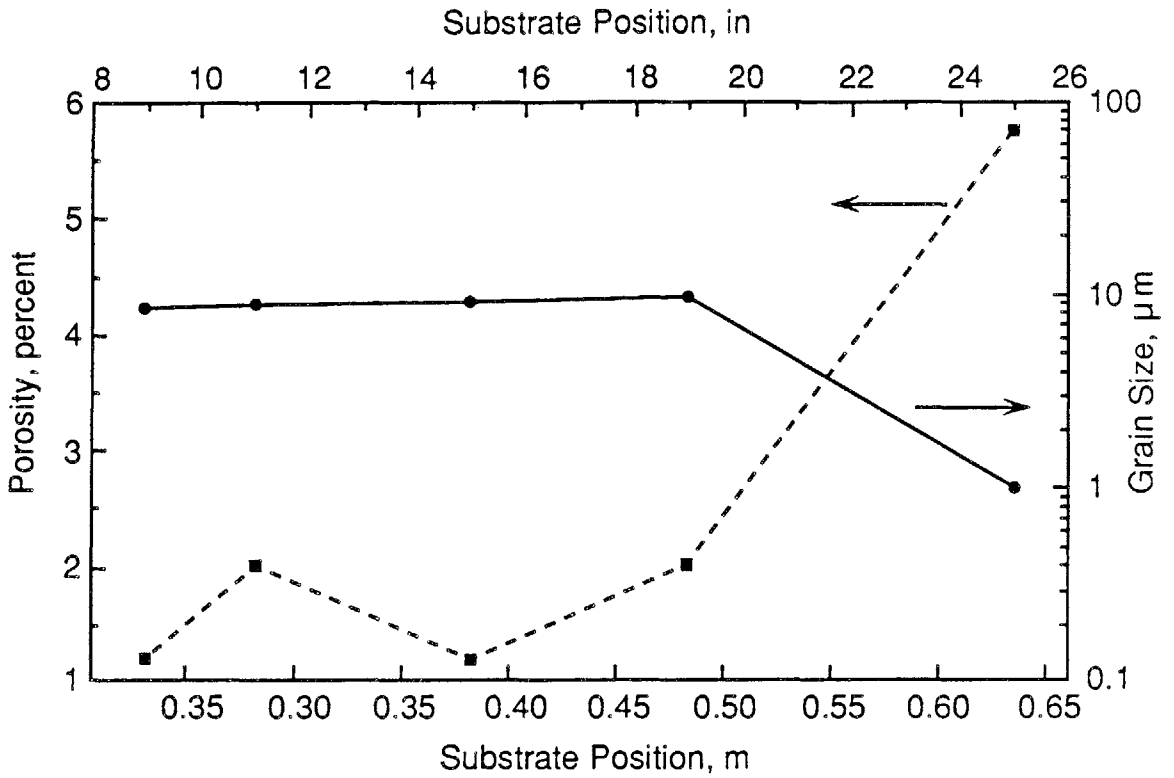

Figure 5.22—Porosity and grain size of spray formed Fe-2.5Cr-2.5Al-1Ti-0.6B alloys as a function of substrate position.

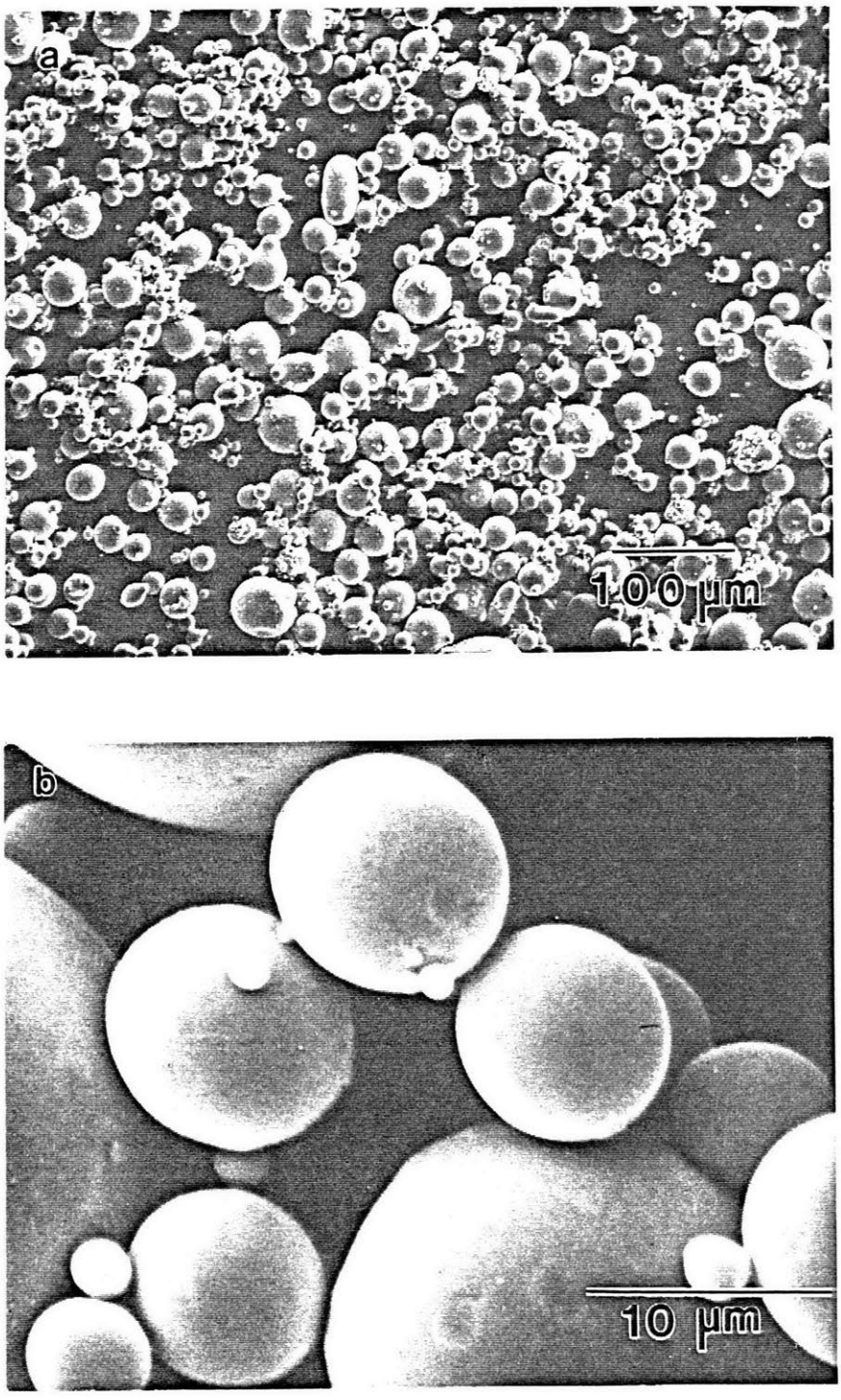

Figure 5.23—Secondary SEM electron image of gas atomized Fe-2.5Cr-2.5Al-1Ti-0.6B alloy: (a) low magnification and (b) high magnification.

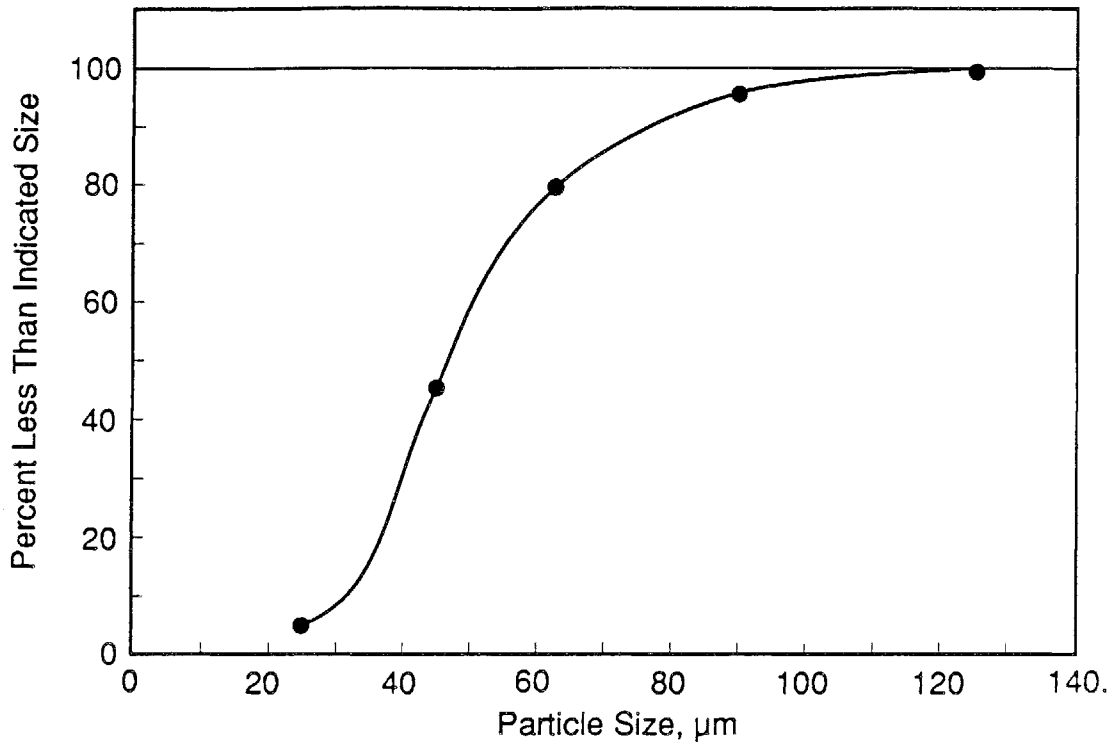

Figure 5.24—Particle size distribution of gas atomized Fe-2.5Cr-2.5Al-1Ti-0.6B alloy powder.

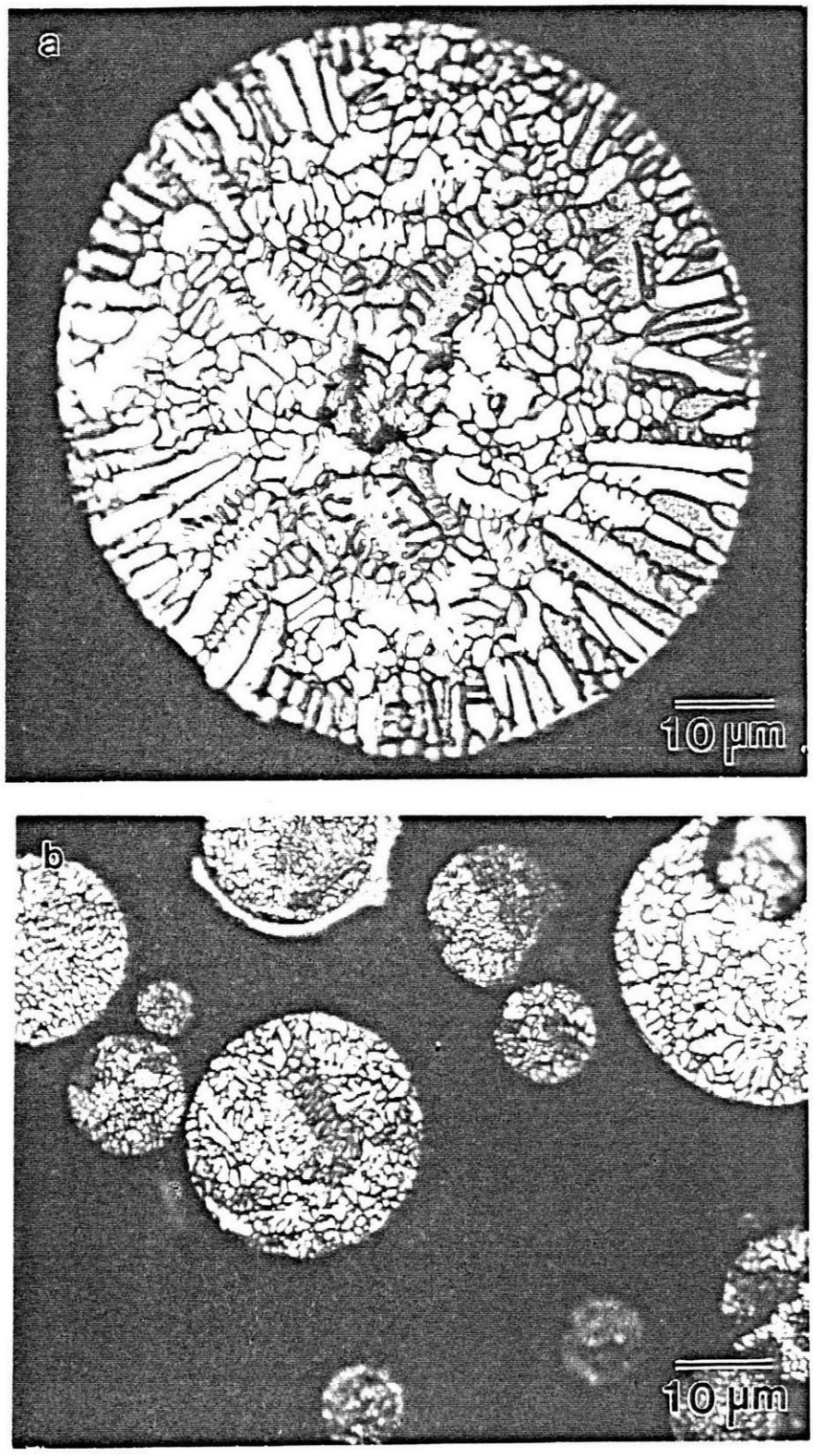

Figure 5.25—Optical micrograph of cross-section through gas atomized Fe-2.5Cr-2.5Al-1Ti-0.6B alloy powder: (a) large sized powder particle and (b) small sized powder particles.

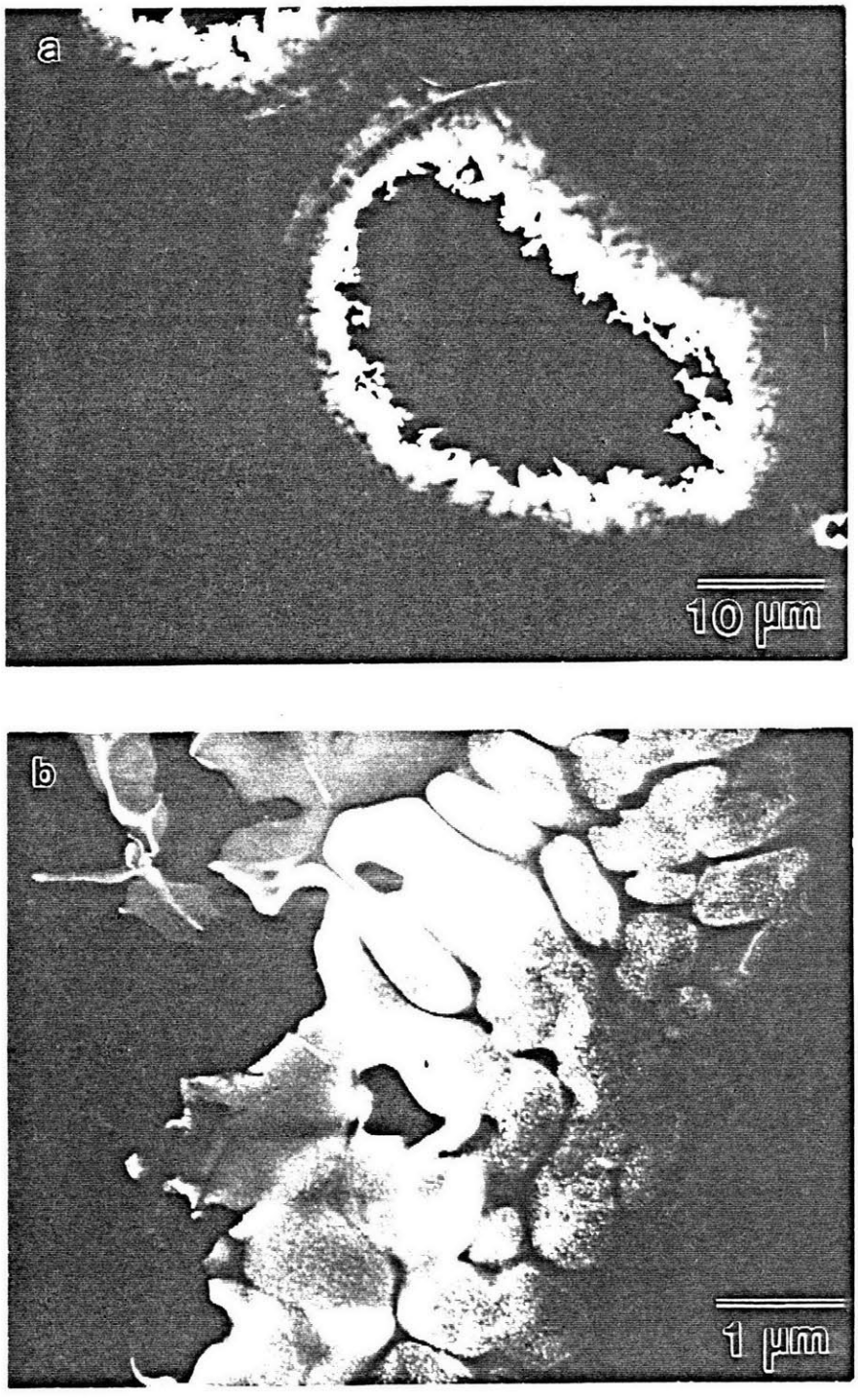

Figure 5.26—Annular dark-field STEM image of gas atomized Fe-2.5Cr-2.5Al-1Ti-0.6B alloy powder: (a) low magnification and (b) high magnification.

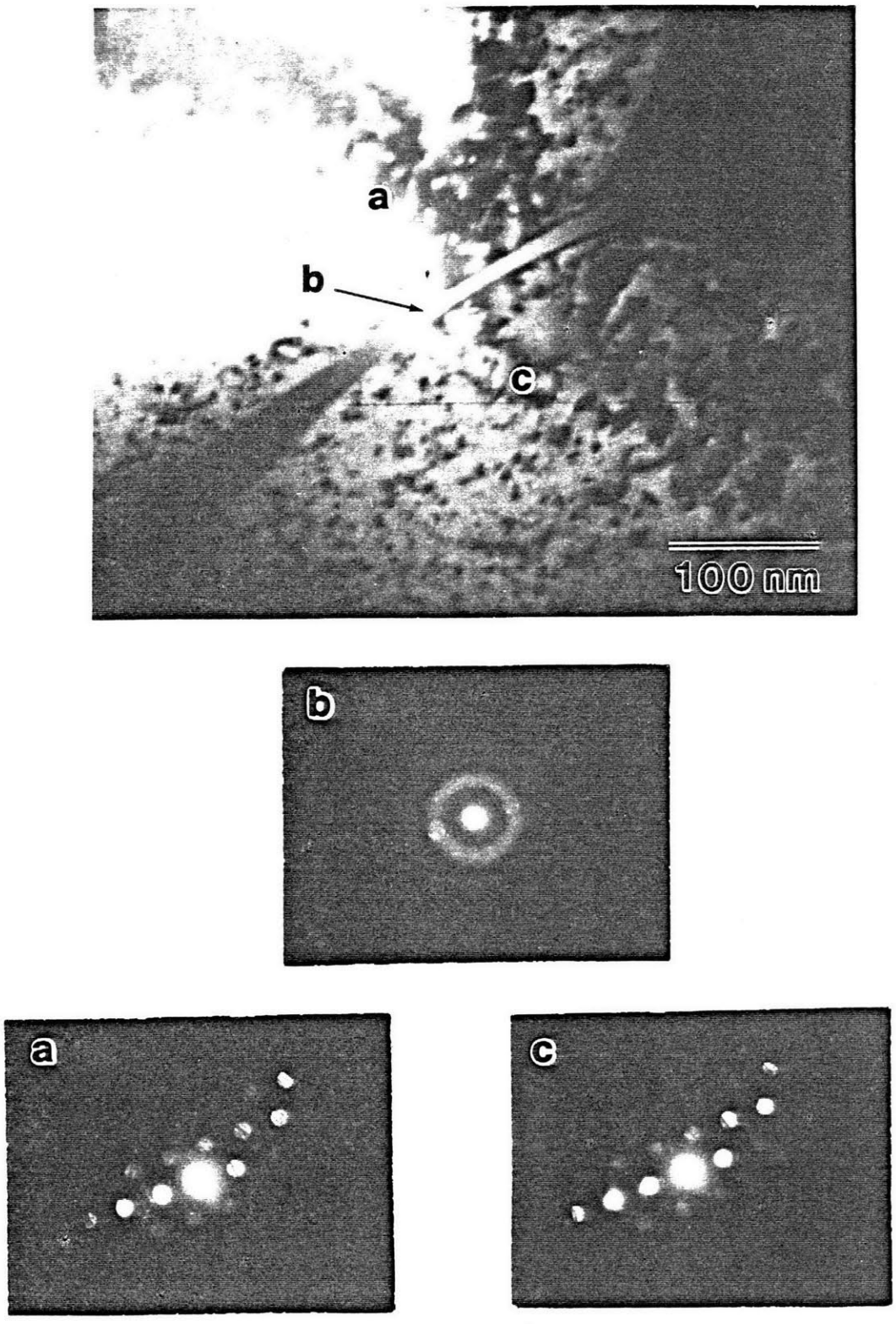

Figure 5.27—Bright-field STEM image and convirgent beem diffraction pattern of interdendritic phase and adjoining dendrite arms.

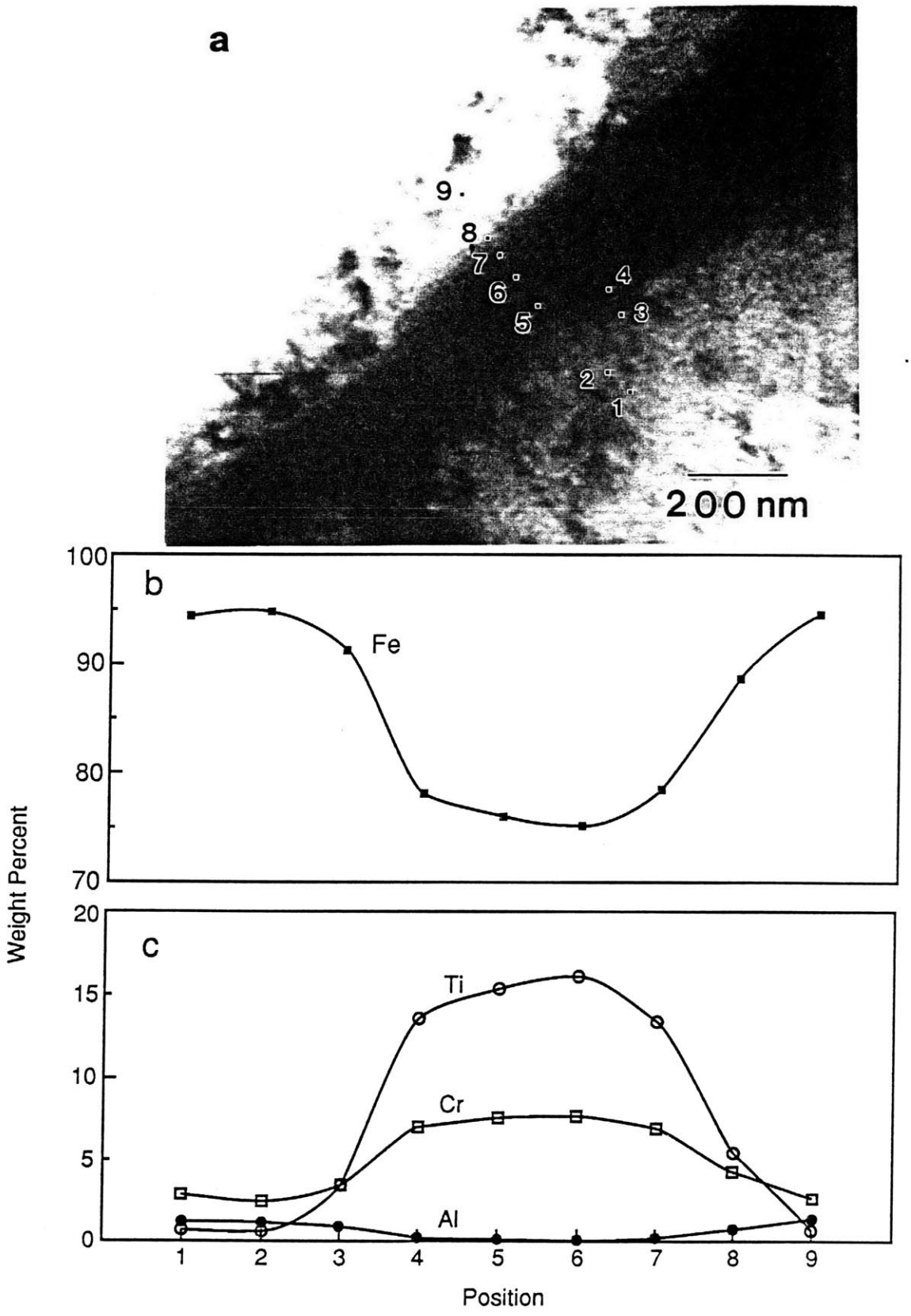

Figure 5.28—Bright-field STEM image of interdendritic amorphous phase (a) and composition profiles across the amorphous phase for (b) Fe and (c) Al, Cr, and Ti.

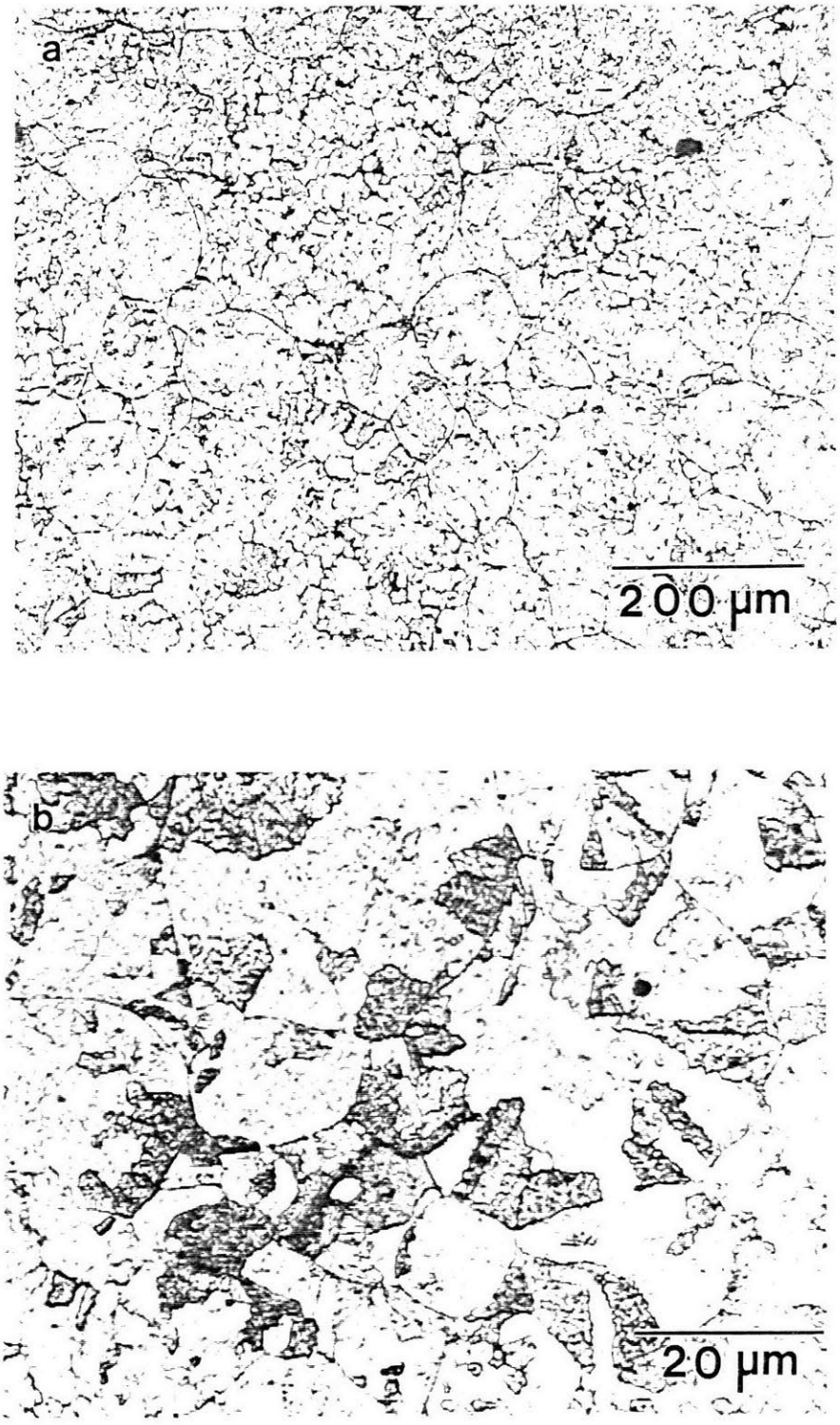

Figure 5.29—Hot isostatically pressed Fe-2.5Cr-2.5Al-1Ti-0.6B alloy powder: (a) low magnification and (b) high magnification.

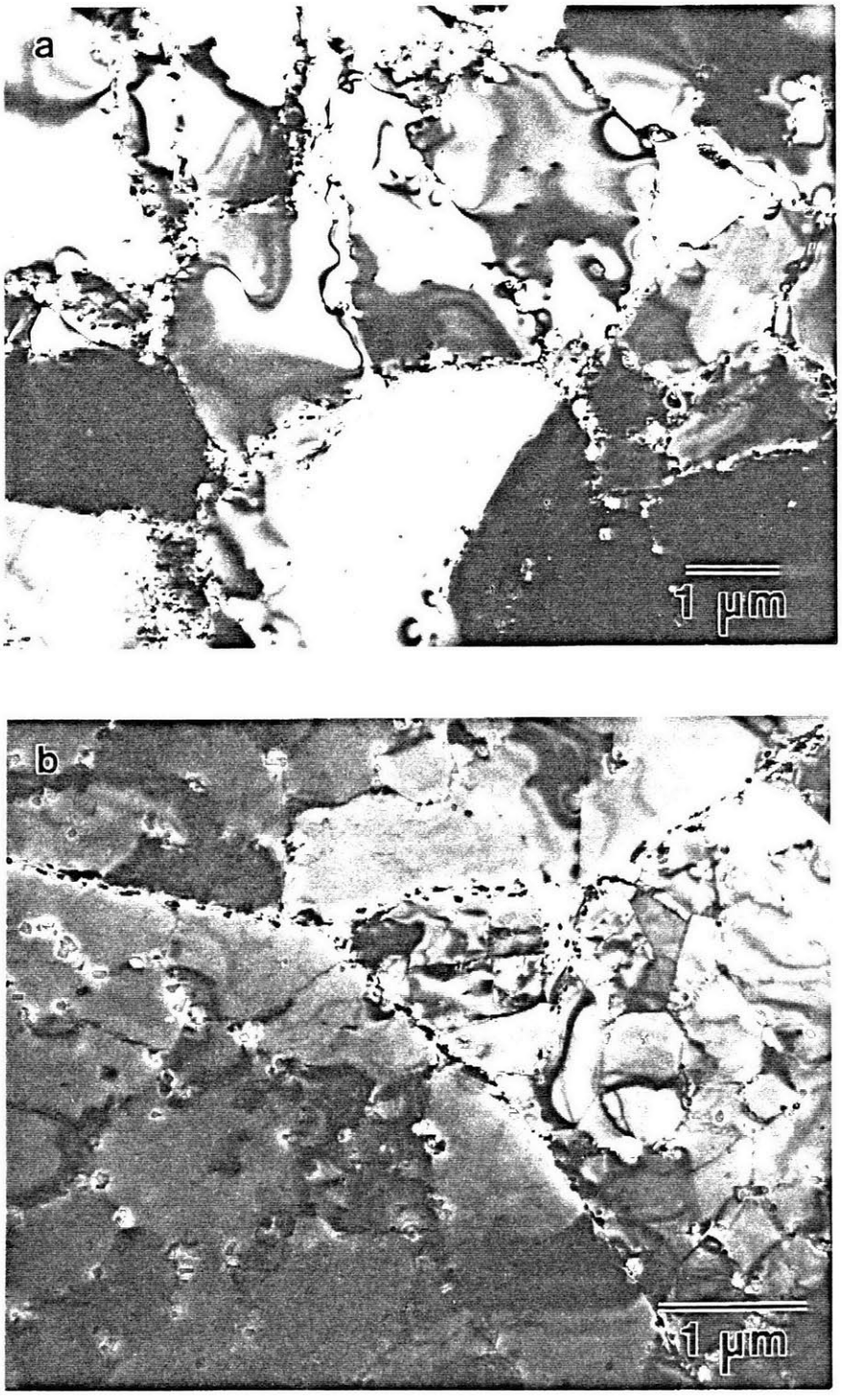

Figure 5.30—Bright-field TEM images of consolidated Fe-2.5Cr-2.5Al-1Ti-06B alloy powder after annealing at 900°C for 100h showing (a) clusters of boride particles and (b) linear arrays of boride particles along prior particle boundaries.

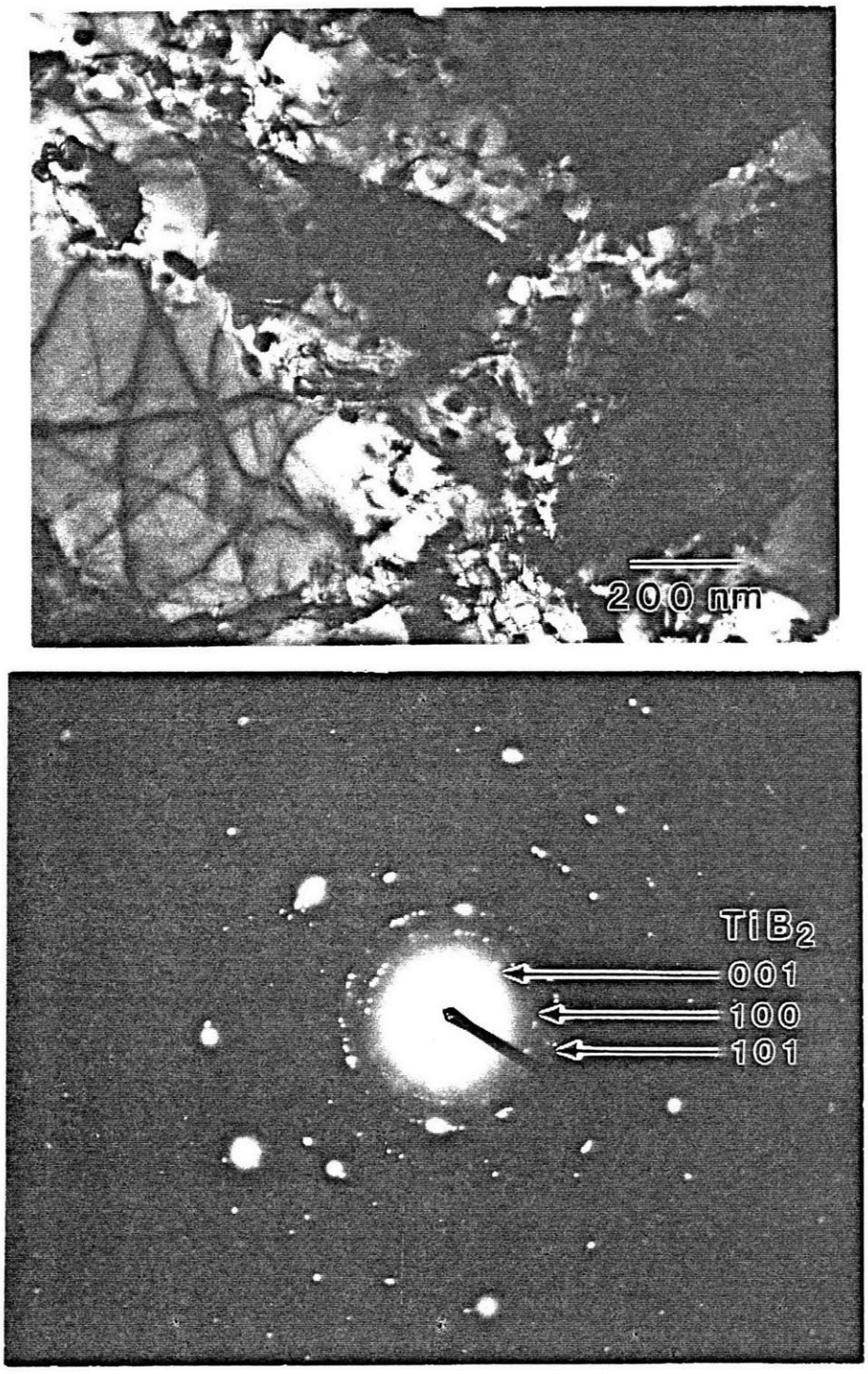

Figure 5.31—Bright field TEM image (a) and selected area diffraction pattern (b) of a region containing a high concentration of TiB_2 particles in a hot isostatically presssed Fe-2.5Cr-2.5Al-1Ti-0.6B alloy.

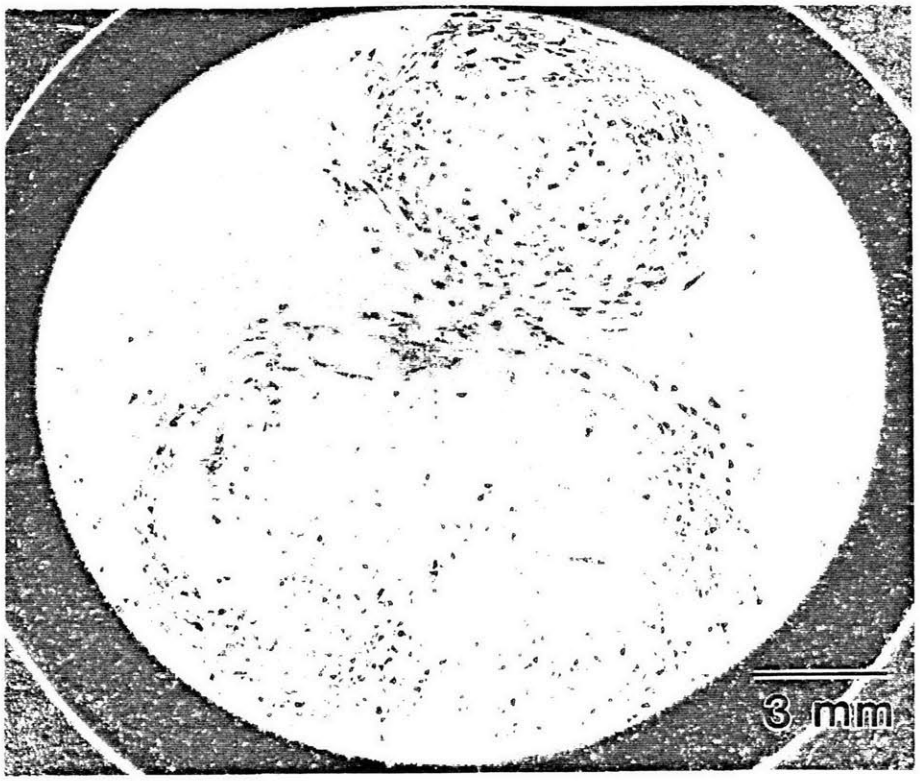

Figure 5.32—Photograph of cross-section through hot isostatically pressed Fe-2.5Cr-2.5Al-1Ti-0.6B alloy powder. View is at the crimped end of the canning tube showing pattern of recrystalized bands.

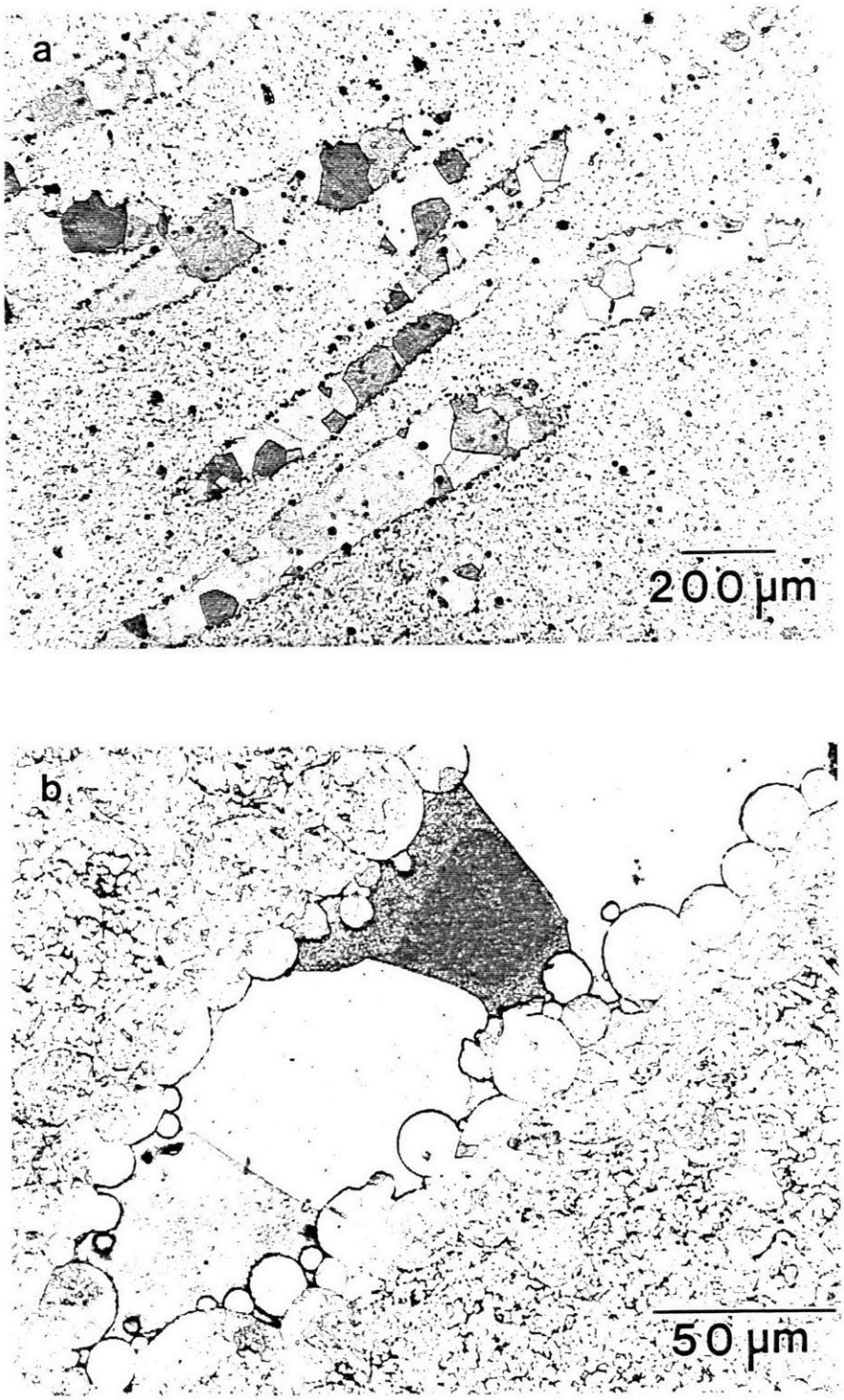

Figure 5.33—Optical micrograph of recrystalized bands shown in figure 5.31: (a) low magnification and (b) high magnification.

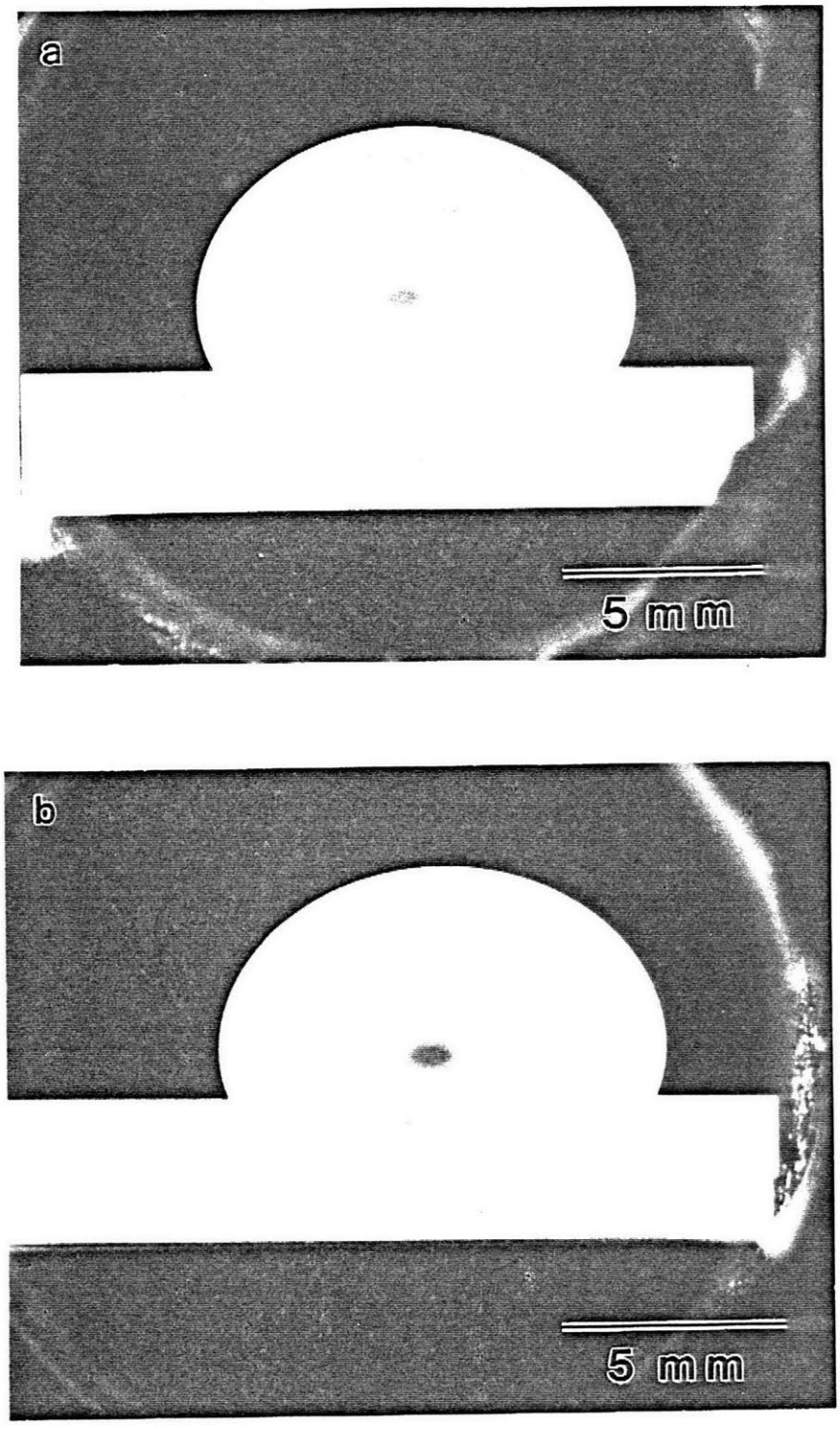

Figure 5.34—Sessile drop of (a) pure iron and (b) Fe-4Cr-4Al alloy on an alumina substrate at 1600°C.

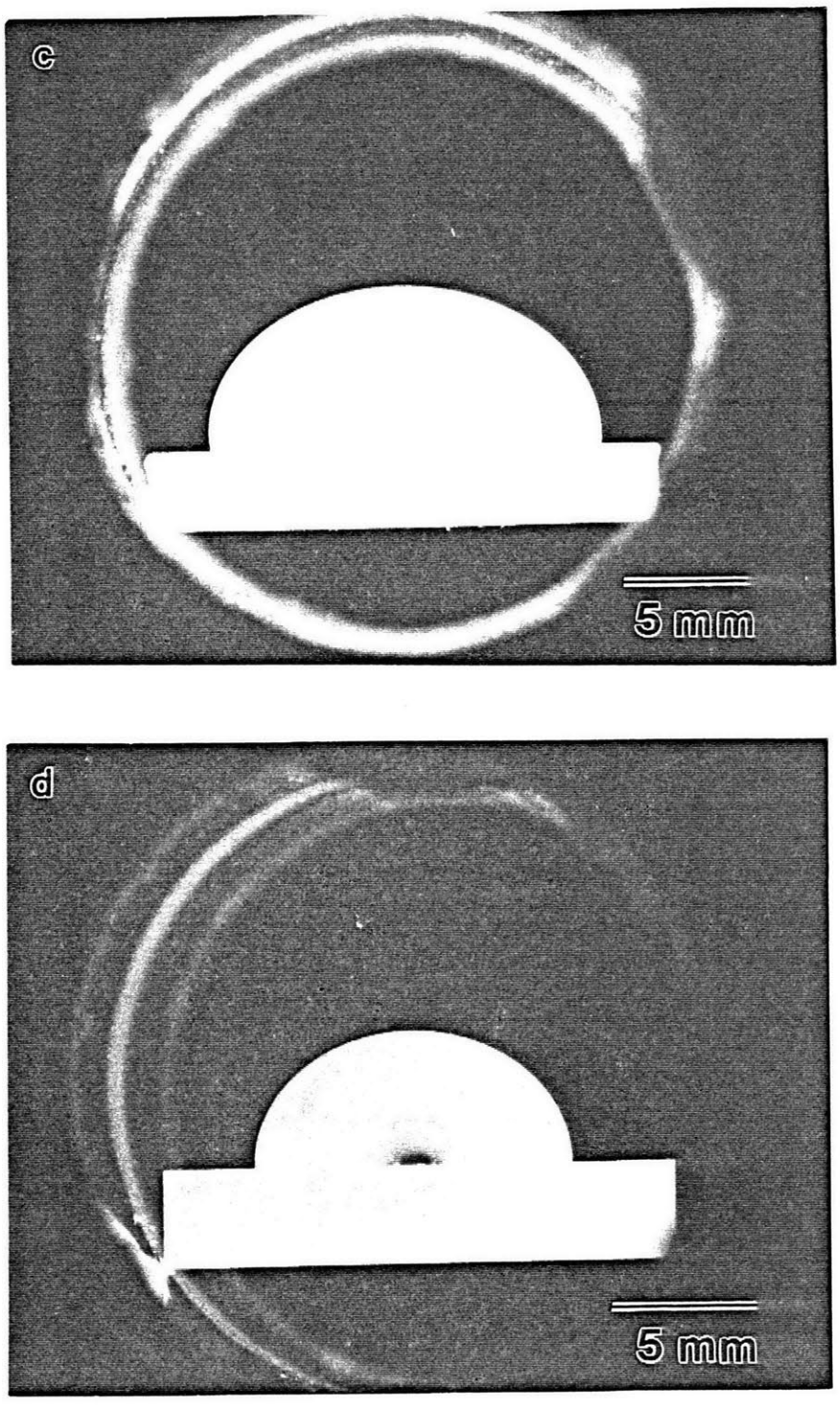

Figure 5.34 continued—Sessile drop of (c) Fe-4Cr-4Al-1Ti and (d) Fe-4Cr-4Al-1.5Ti alloy on an alumina substrate at 1600°C.

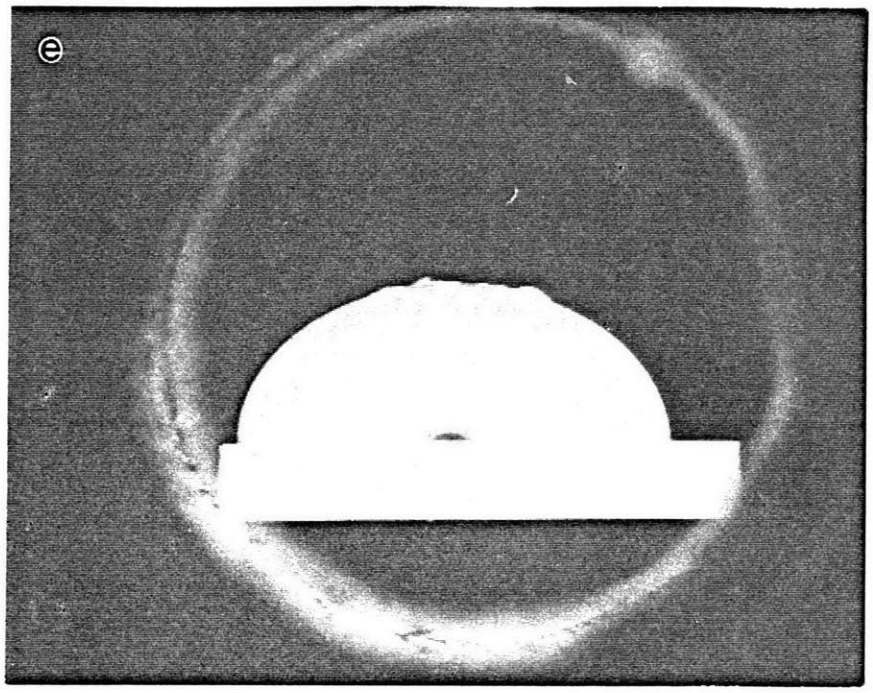

Figure 5.34 (e)—Sessile drop of Fe-4Cr-4Al-2.0Ti on an alumina substrate at 1600°C.

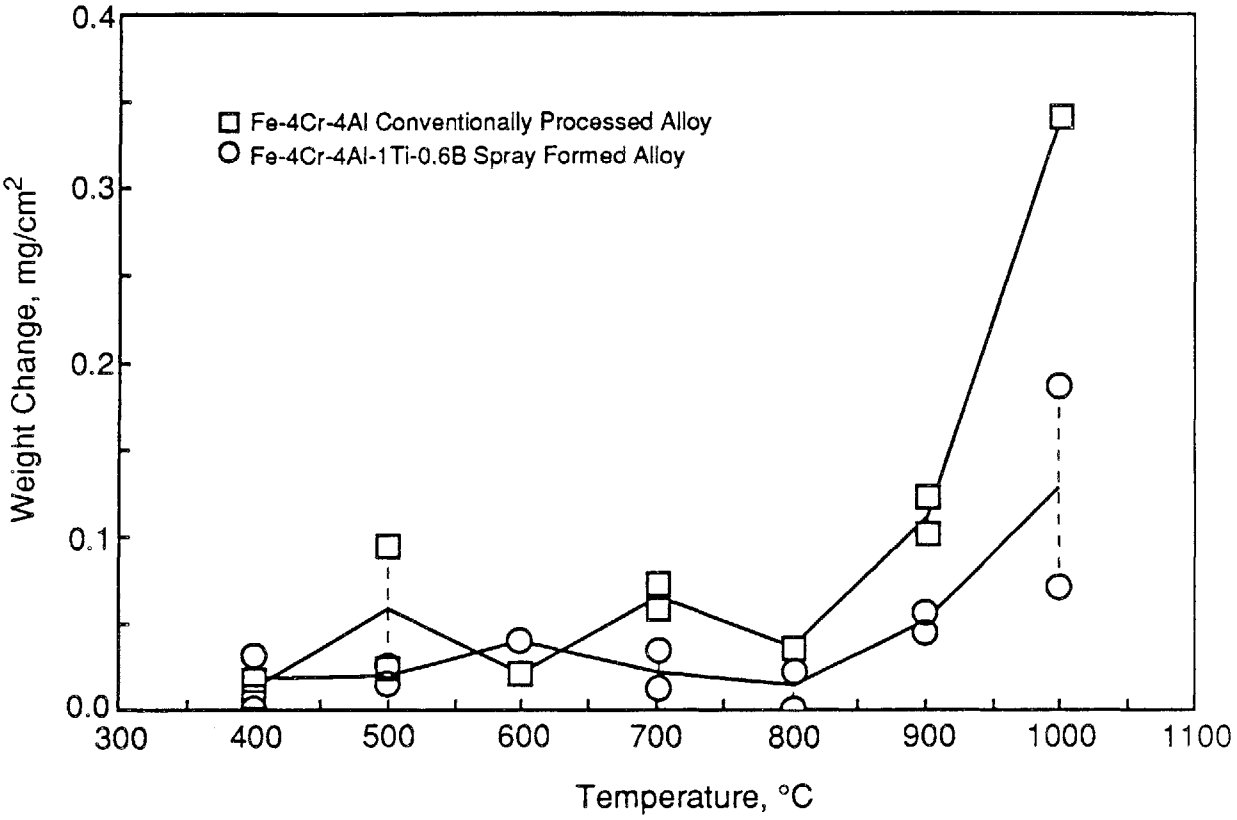

Figure 5.35—Weight change of conventionally processed Fe-4Cr-4Al and rapidly solidified Fe-4Cr-4Al-1Ti-0.6B alloys after 50h of oxidation.

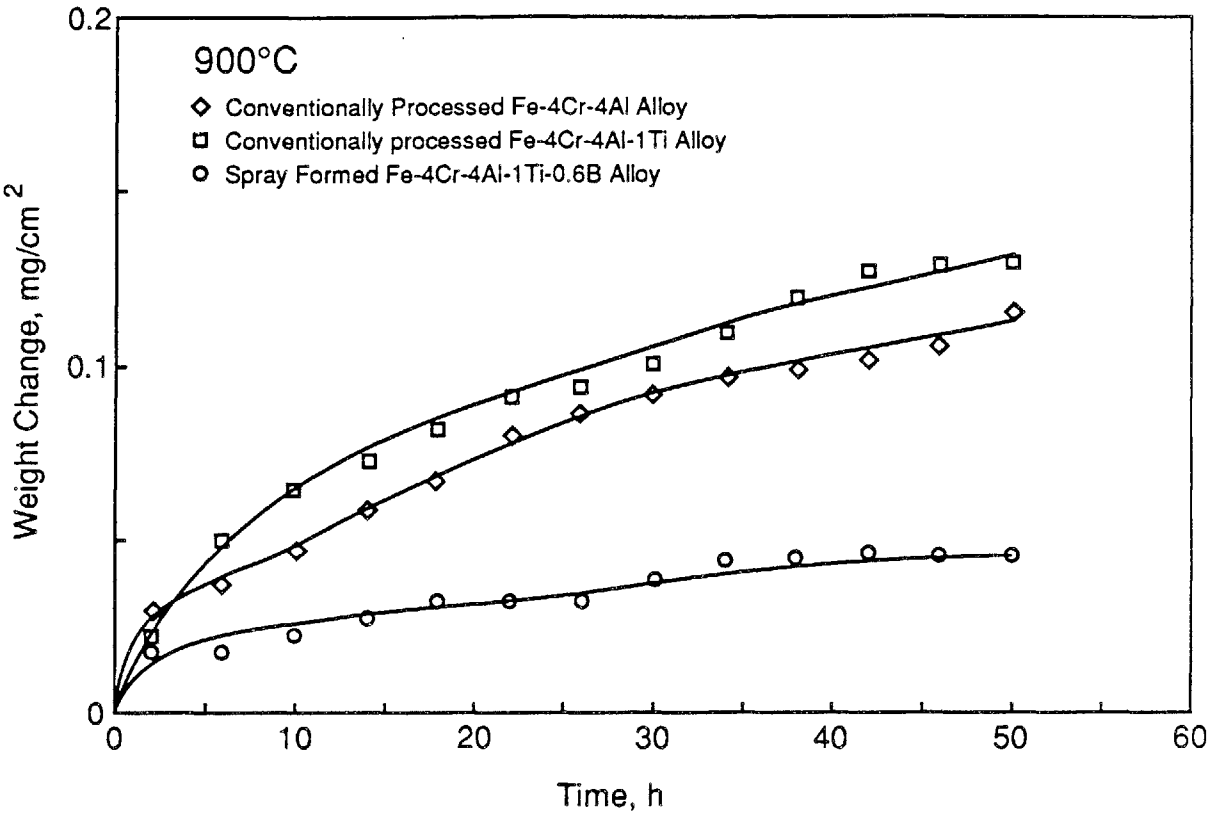

Figure 5.36—Weight change as a function of time for conventionally processed Fe-4Cr-4Al and Fe-4Cr-4Al-1Ti alloys and a rapidly solidified Fe-4Cr-4Al-1Ti-0.6B oxidized at 900°C.

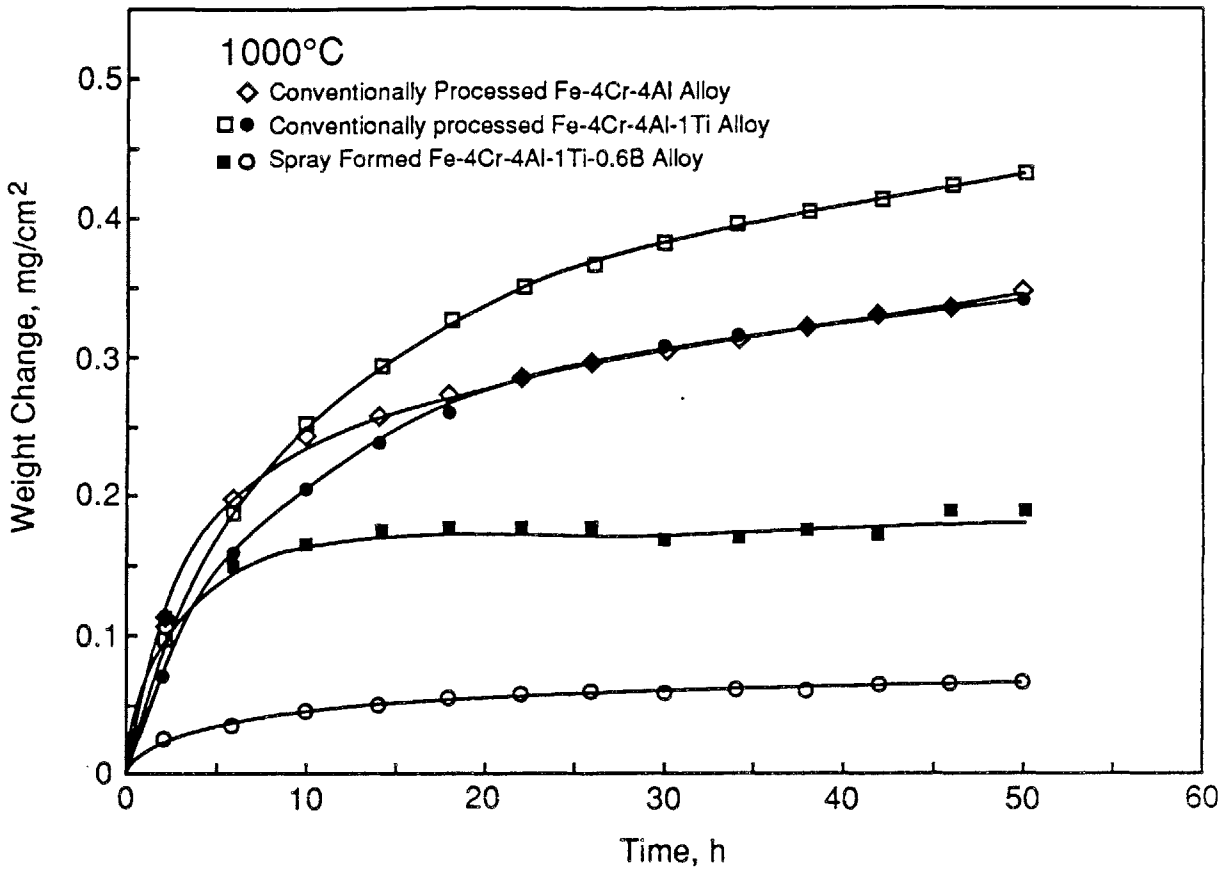

Figure 5.37—Weight change as a function time for conventionally processed Fe-4Cr-4Al and Fe-4Cr-4Al-1Ti alloys and a rapidly solidified Fe-4Cr-4Al-1Ti-0.6B oxidized at 1000°C.

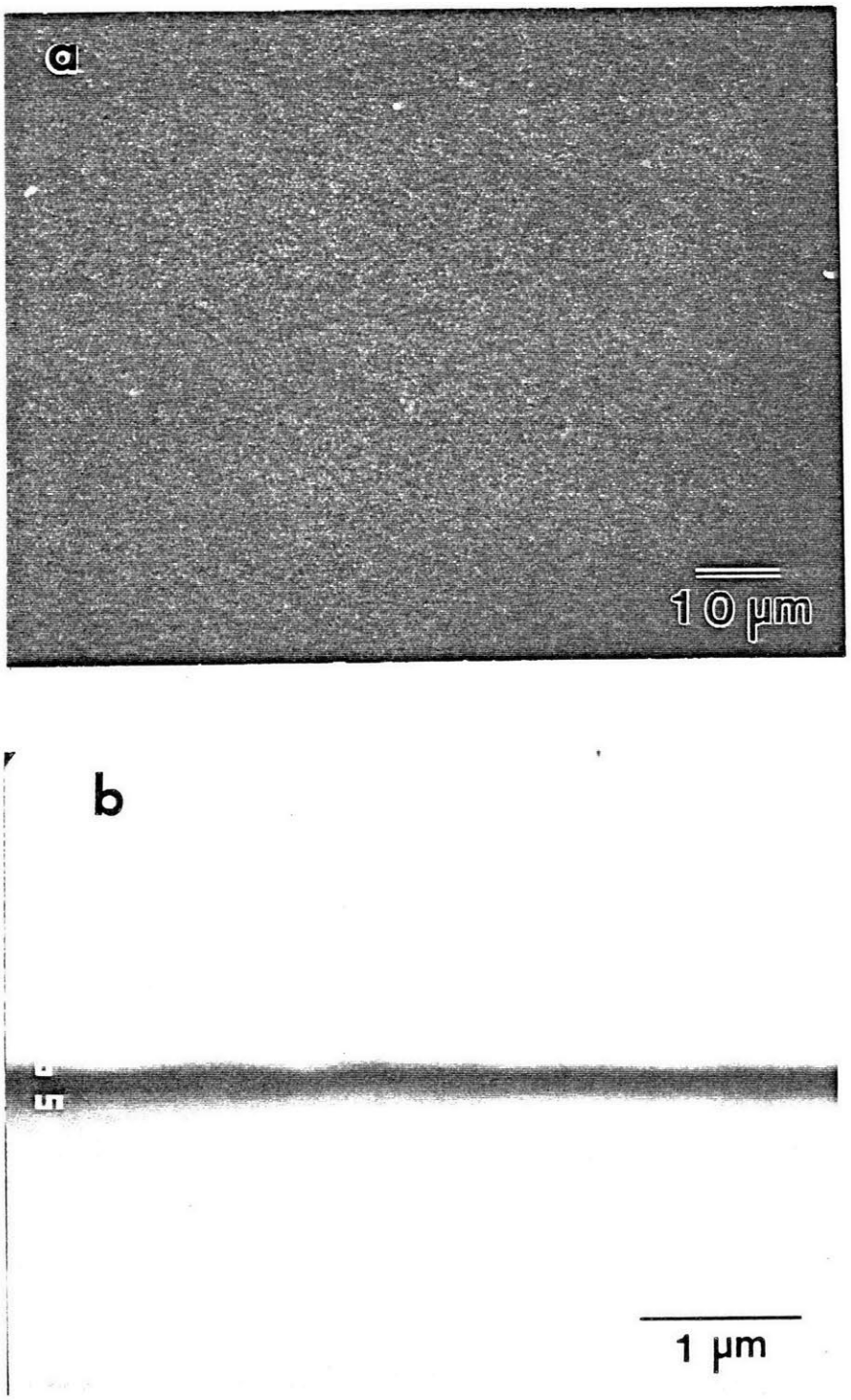

Figure 5.38—Scale formed on a conventionally process Fe-4Cr-4Al alloy oxidized at 400°C for 50h: (a) SEM seconary electron image of scale surface and (b) EPMA back scattered electron image of scale cross-section.

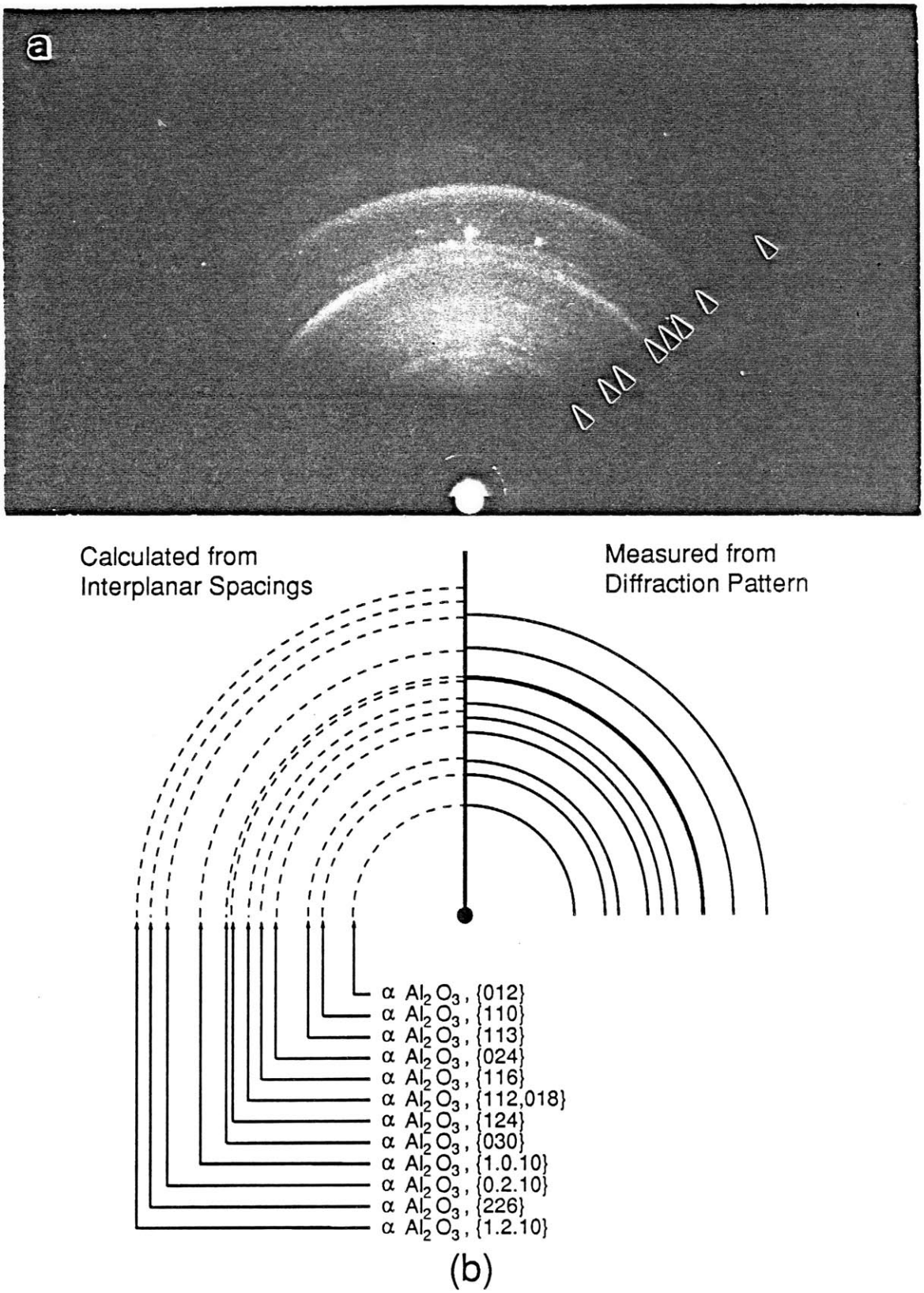

Figure 5.39—Reflected high energy electron diffraction pattern from the surface of a conventionally processed Fe-4Cr-4Al alloy that was oxidized at 400°C for 50h (a) and index of pattern (b).

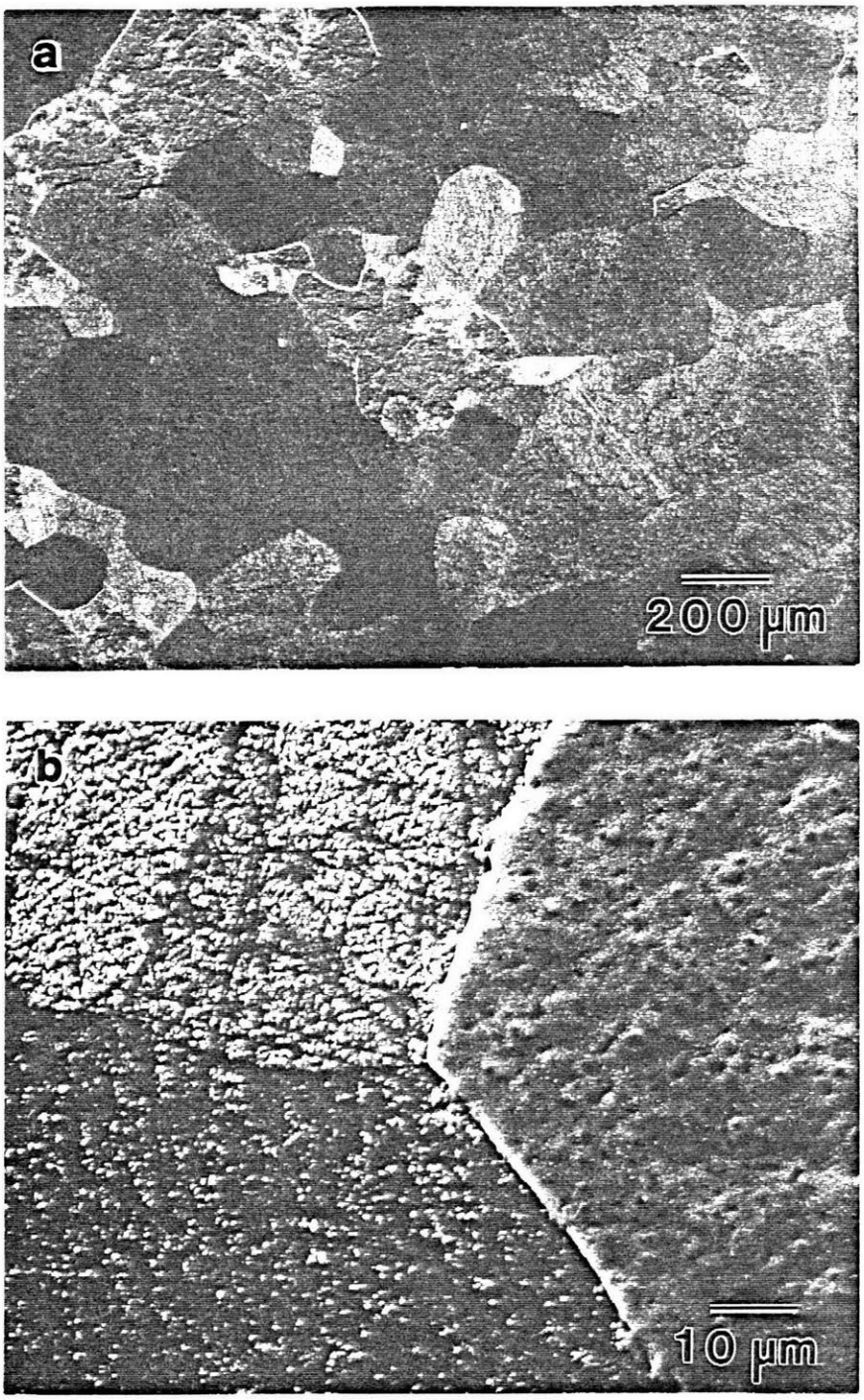

Figure 5.40—SEM secondary electron image of the scale formed on a conventionally processed Fe-4Cr-4Al alloy after oxidation at 500°C for 50h: (a) low magnification and (b) high magnification.

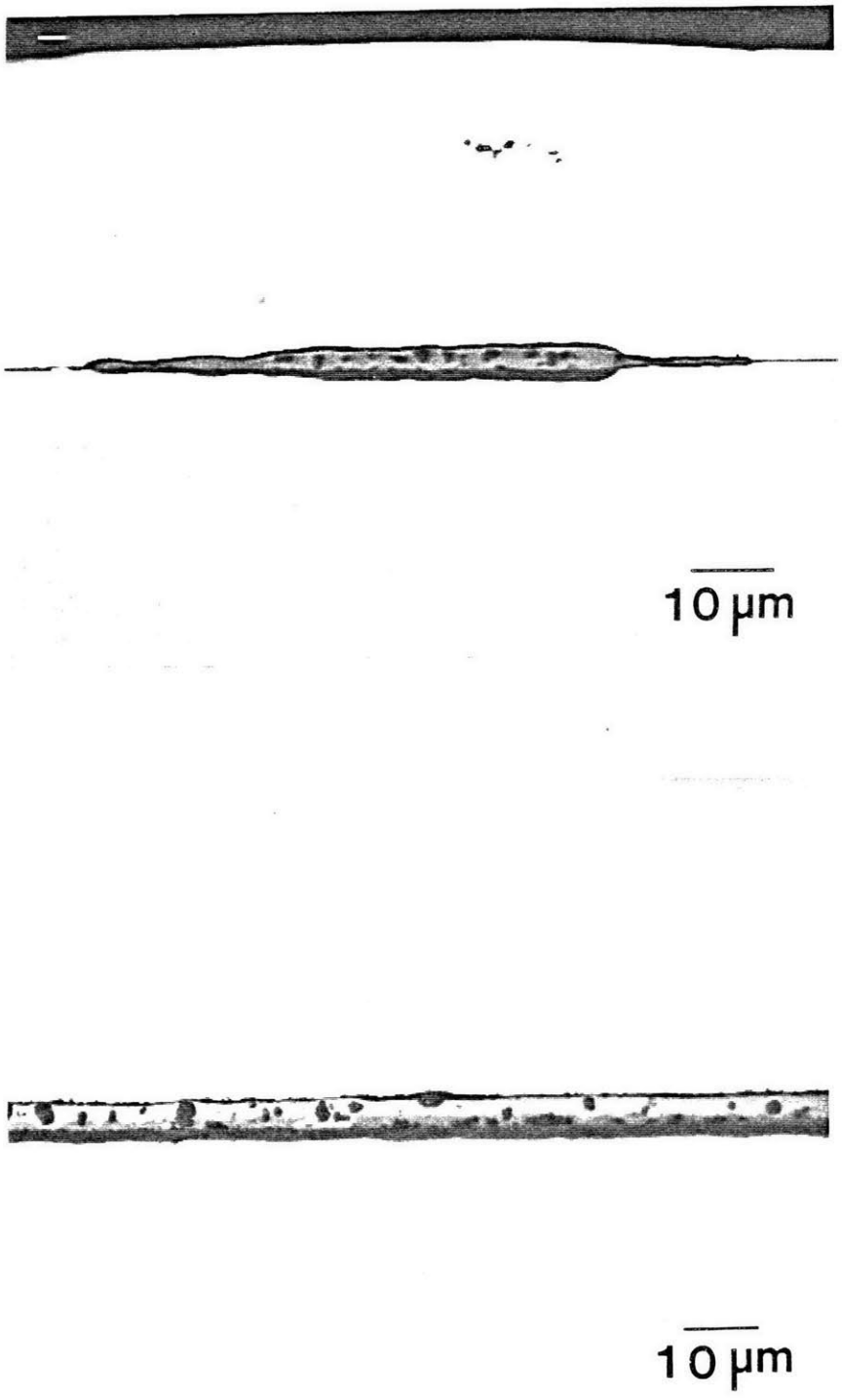

Figure 5.41—Cross-section through scale shown in figure 5.40: (a) EPMA backscattered electron image and (b) optical micrograph.

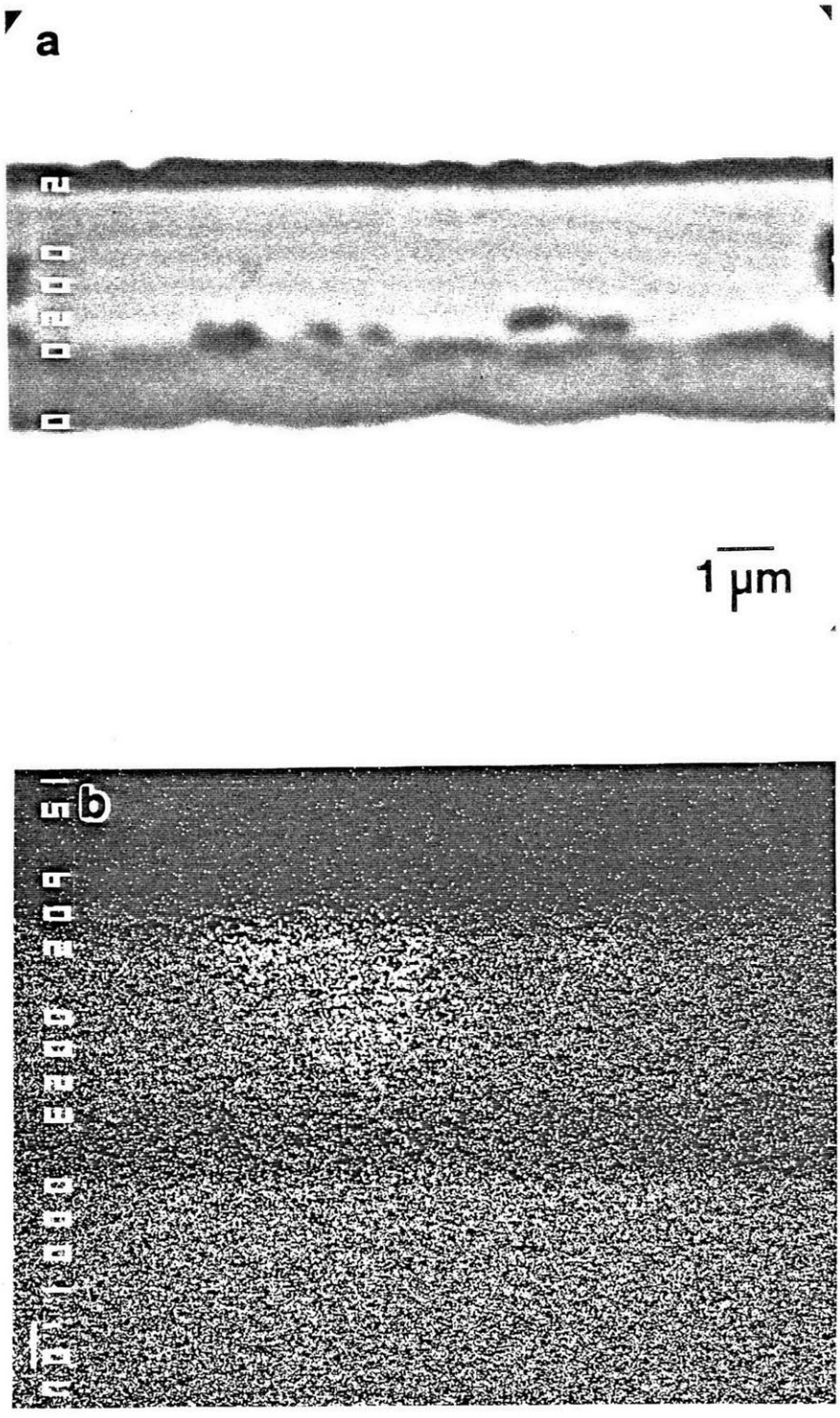

Figure 5.42—EPMA images of a cross-section through an oxide mound shown in Figure 5.40: (a) backscattered electron image and (b) elemental X-ray intensity map for iron.

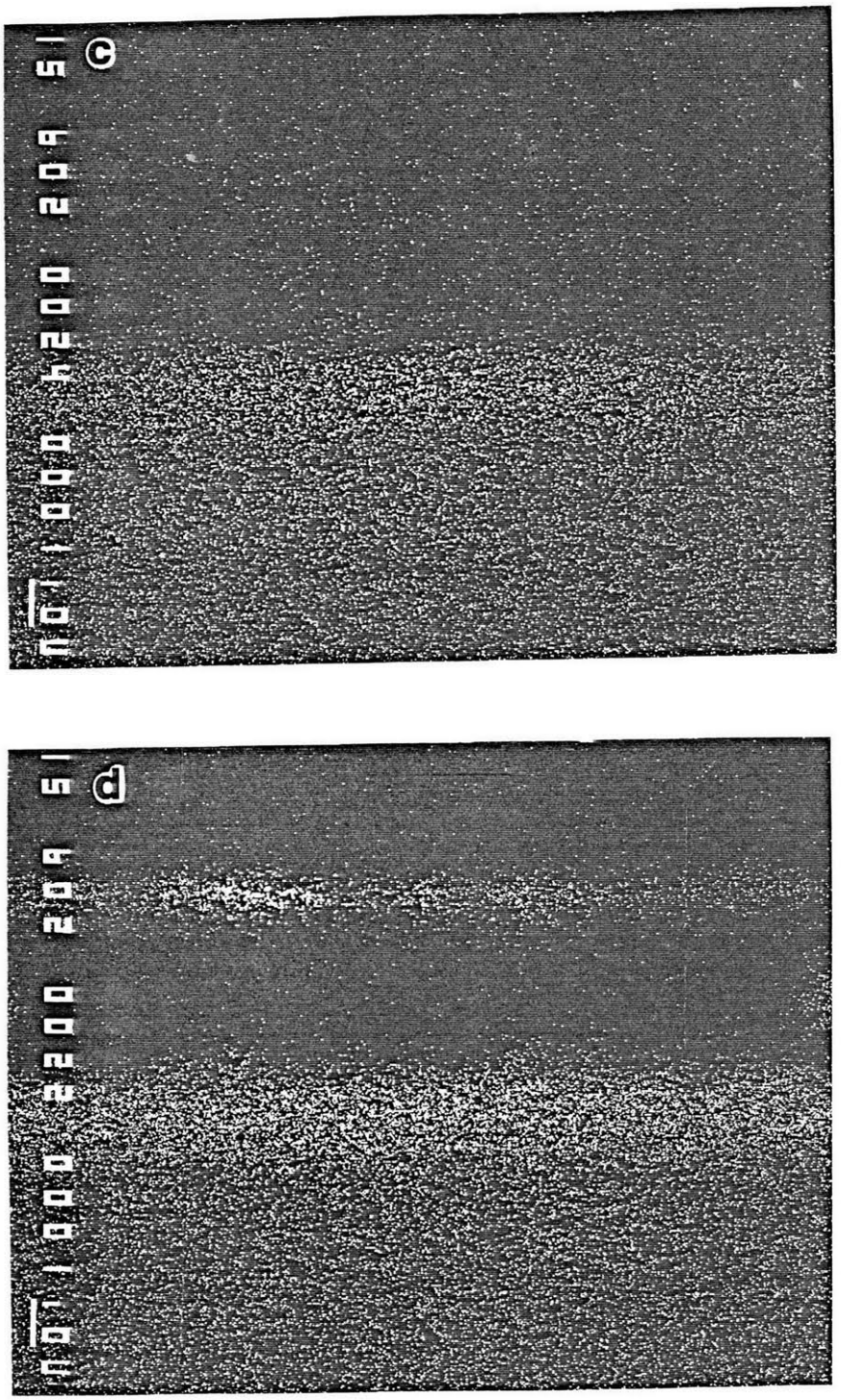

Figure 5.42 Cont.—Elemental X-ray intensity maps for (c) chromium and (d) aluminum.

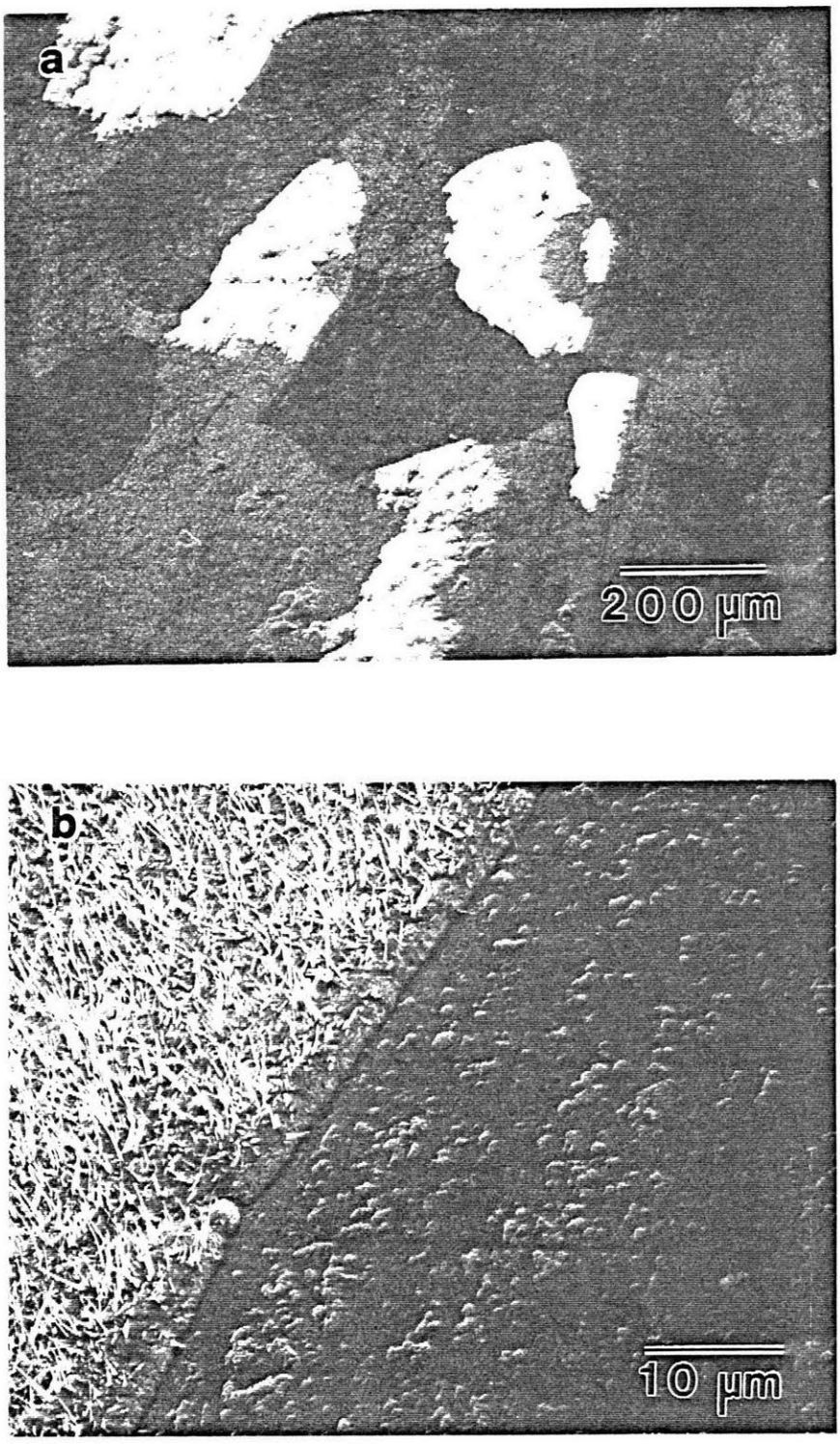

Figure 5.43—SEM secondary electron images of the oxide scale formed on a conventionally processed Fe-4Cr-4Al alloy oxidized at 600°C for 50h: (a) low magnification and (b) high magnification.

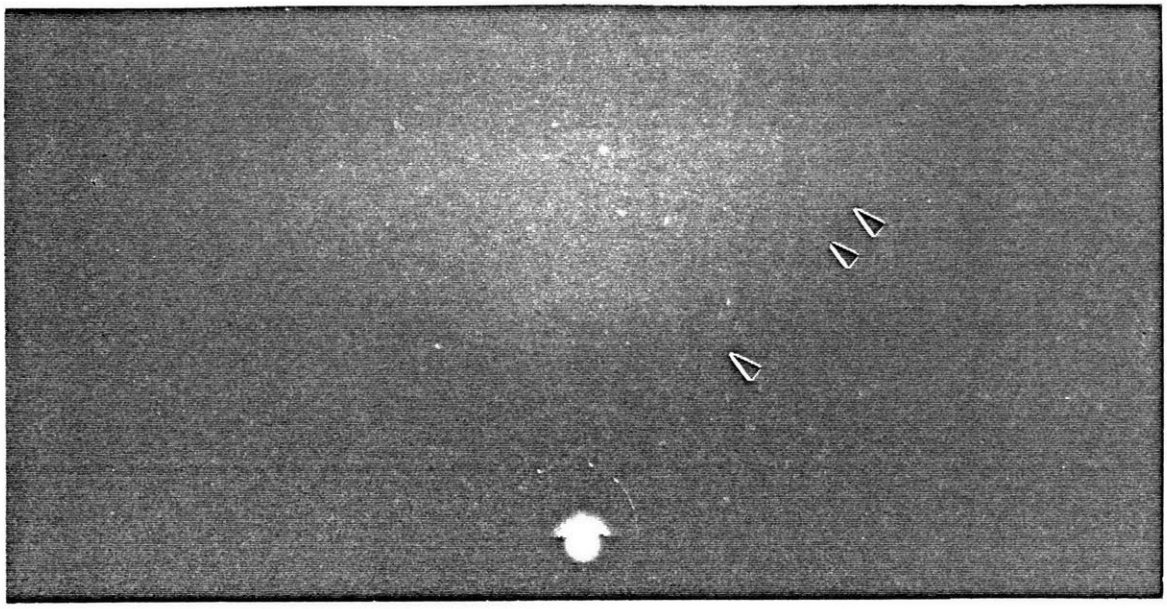

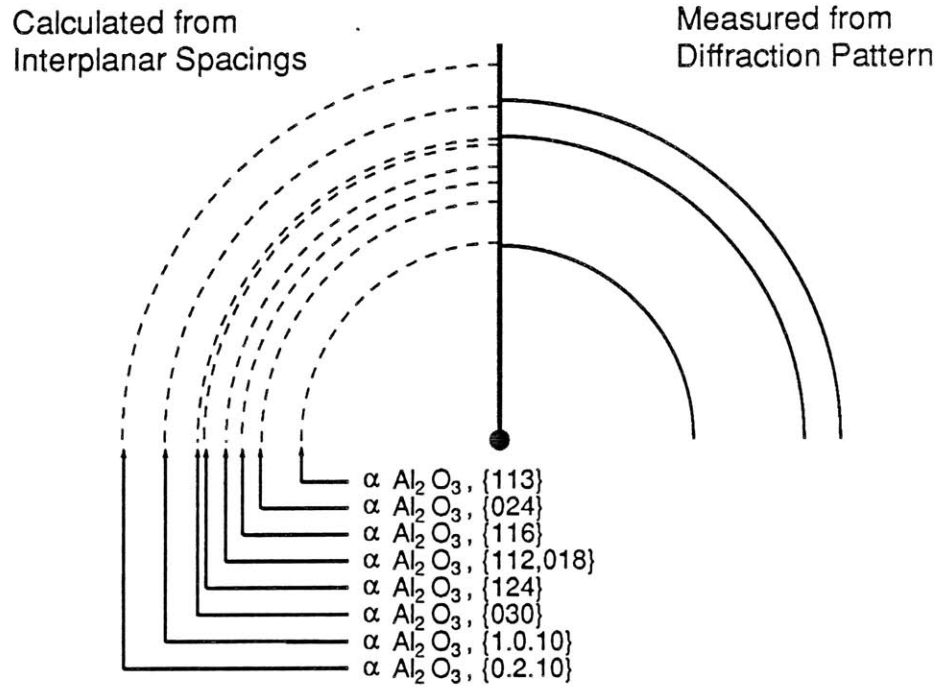

(b)

Figure 5.44—Reflected high energy electron diffraction pattern from the surface of a conventionally processed Fe-4Cr-4Al alloy that was oxidized at 600°C for 50h (a) and index of pattern (b).

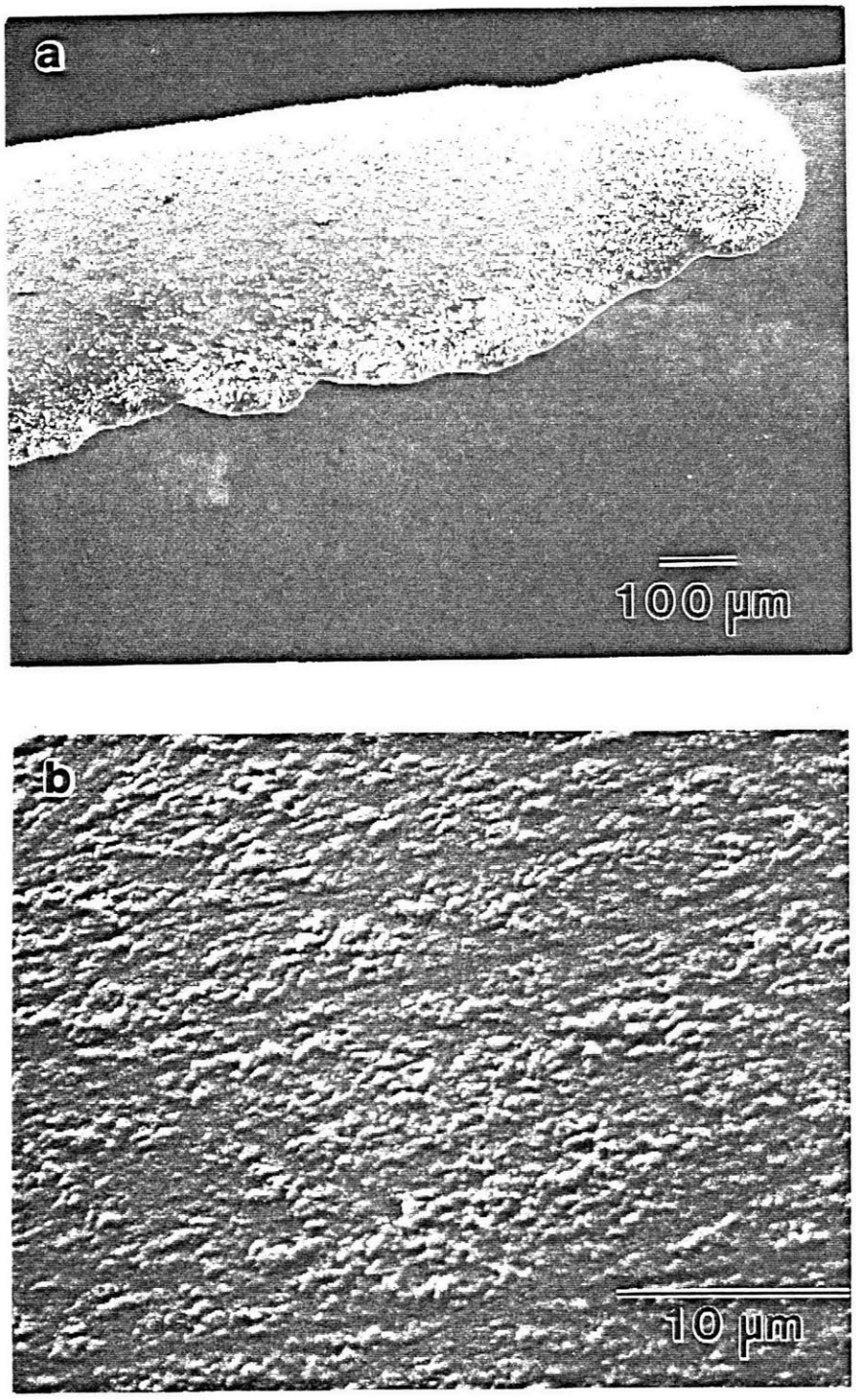

Figure 5.45—SEM secondary electron images of the oxide scale formed on a conventionally processed Fe-4Cr-4Al alloy oxidized at 700°C for 50h: (a) low magnification and (b) high magnification.

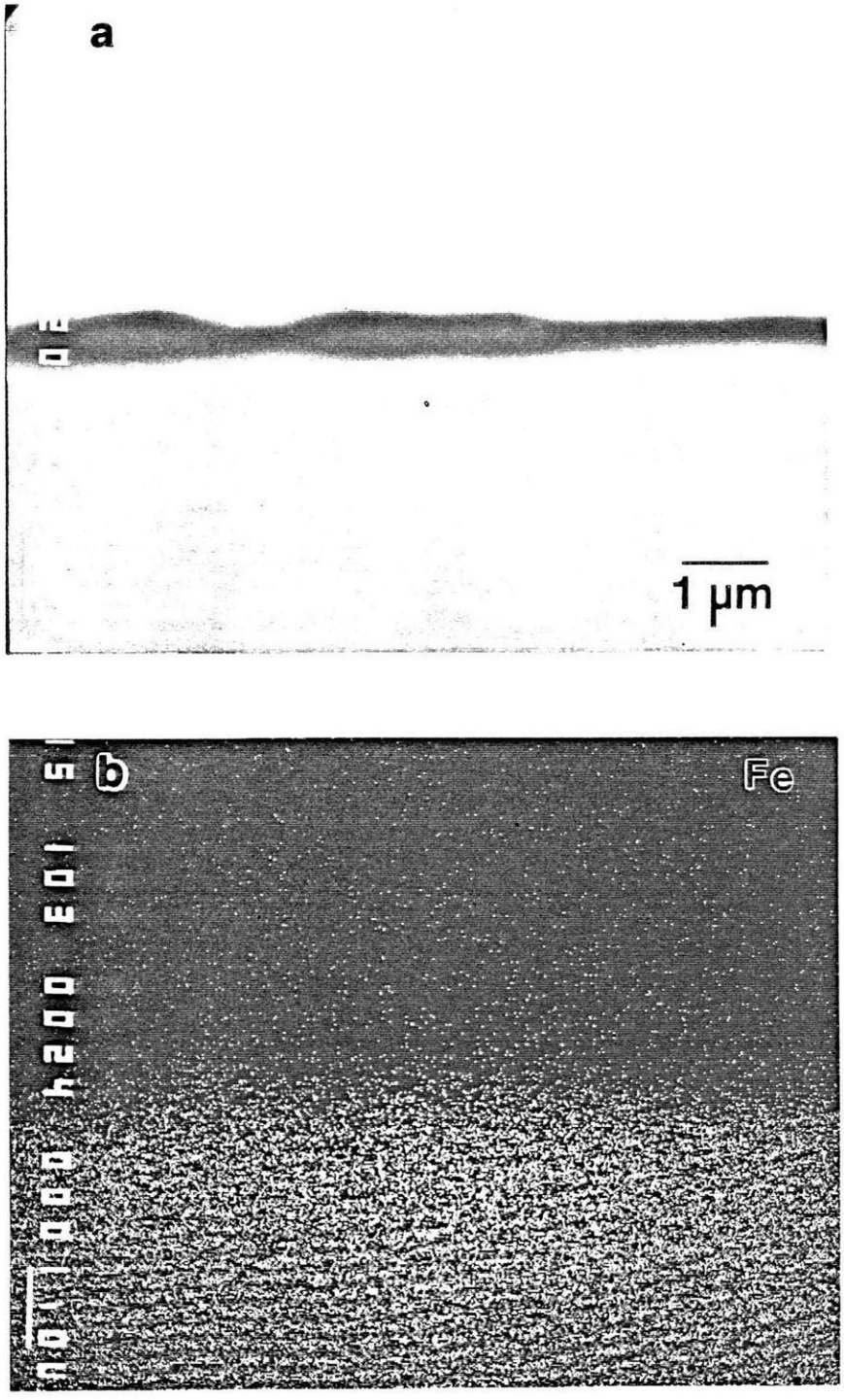

Figure 5.46—EPMA images of a cross-section through the thin oxide scale shown in Figure 5.45: (a) backscattered electron image and (b) elemental X-ray intensity map for iron.

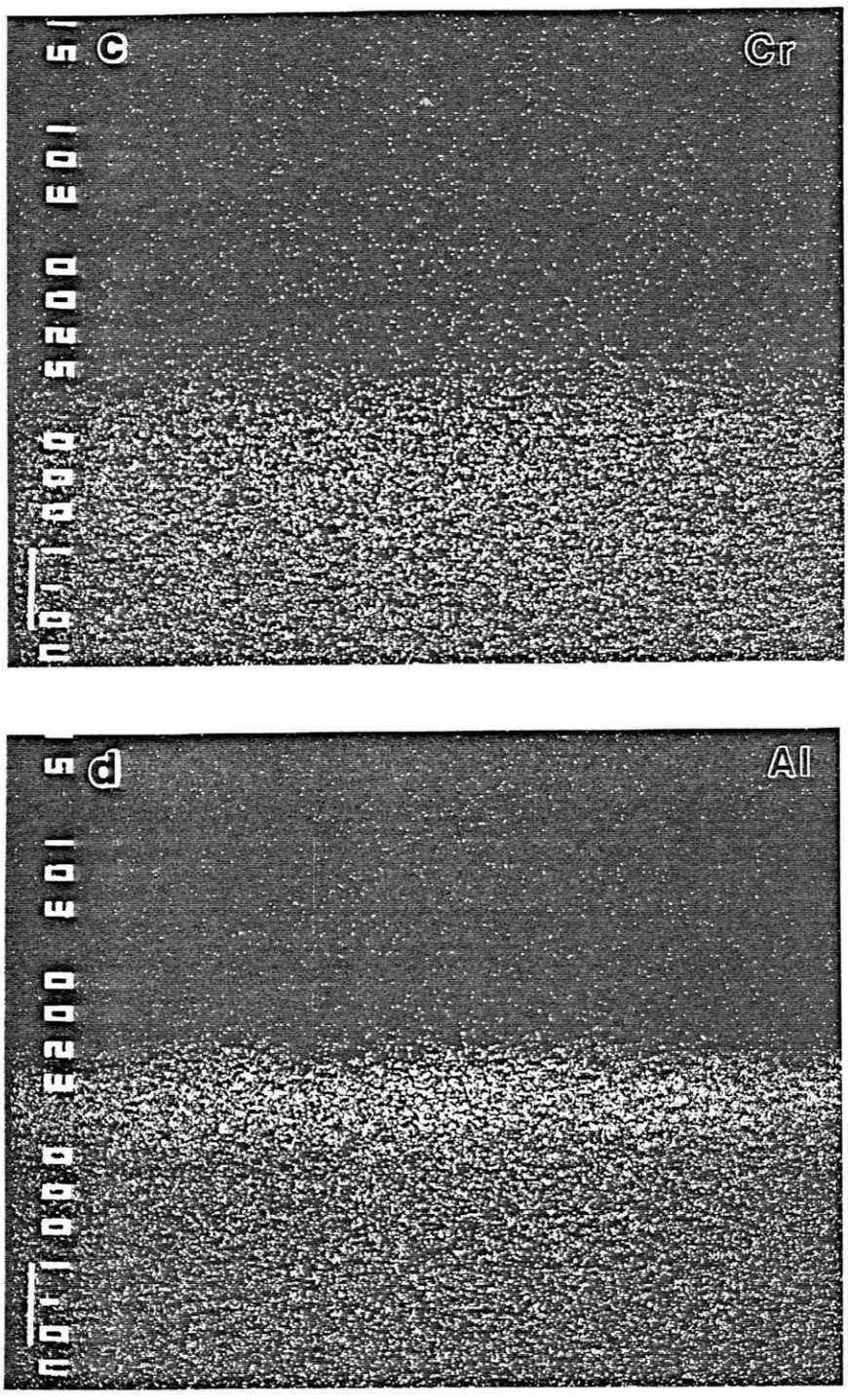

Figure 5.46 Cont.—Elemental X-ray intensity maps for (c) chromium and (d) aluminum.

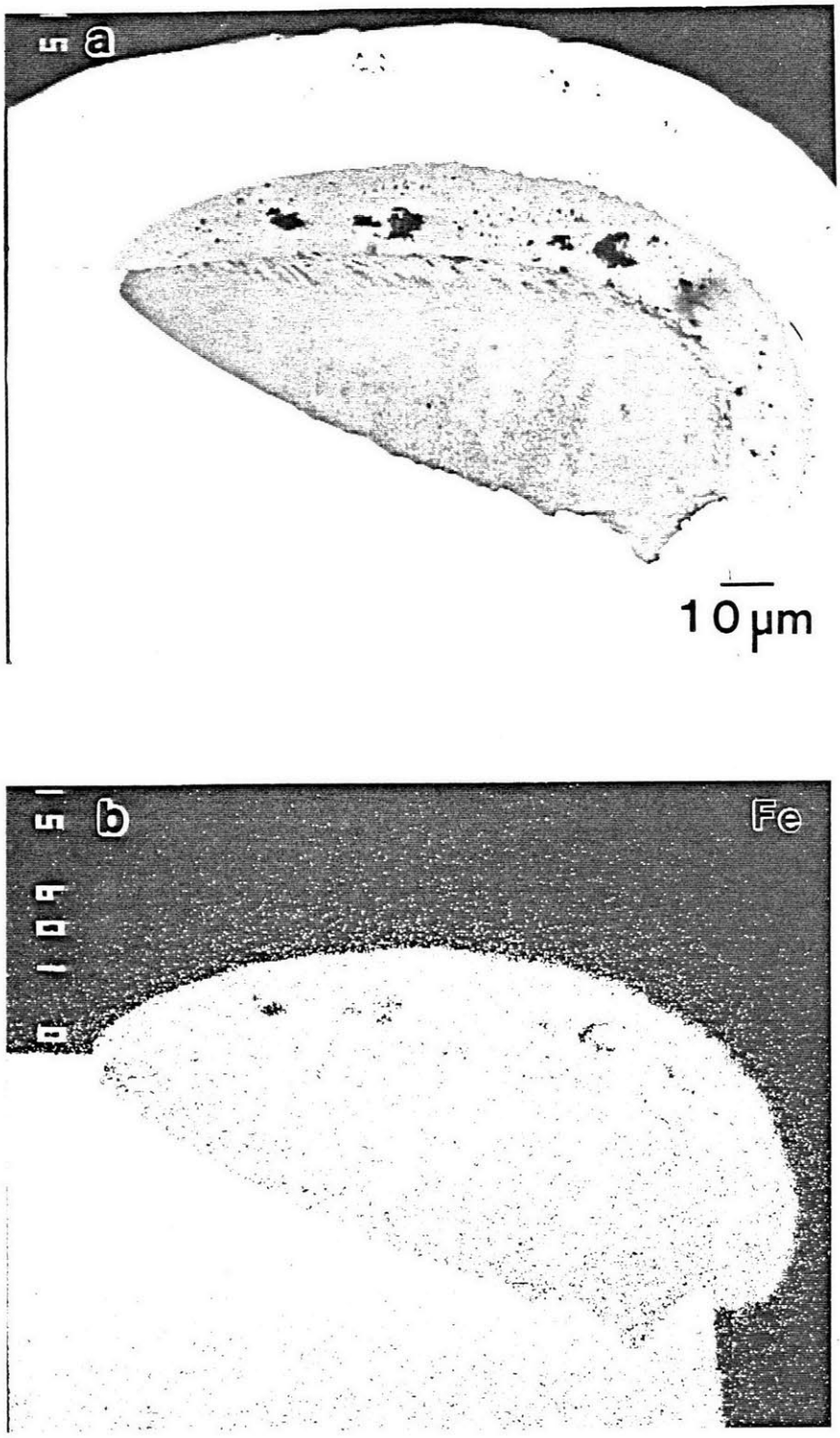

Figure 5.47—EPMA images of a cross-section through the oxide nodule shown in Figure 5.45: (a) back scattered electron image and (b) elemental X-ray intensity image for iron.

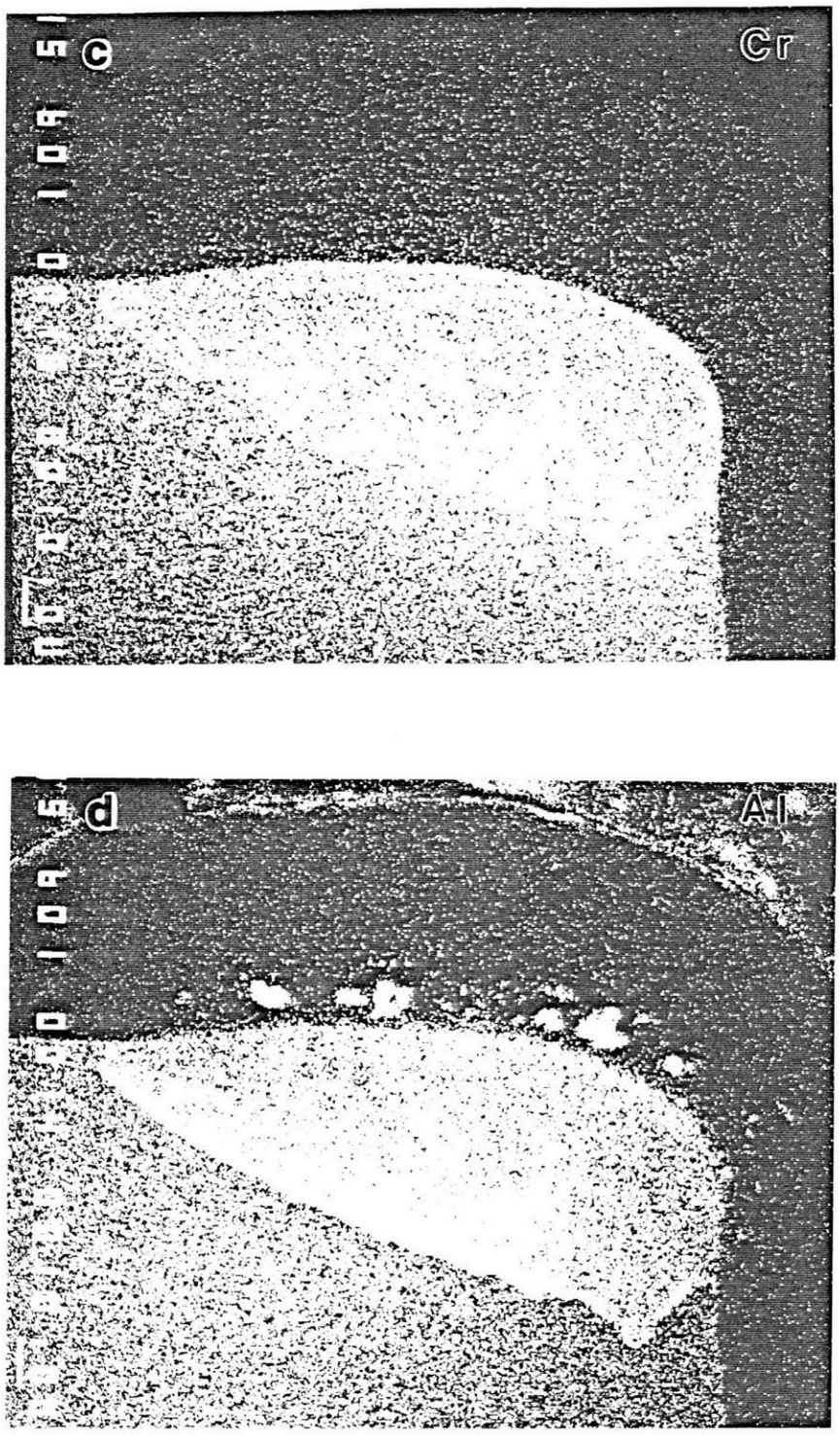

Figure 5.47 Cont.—Elemental X-ray intensity maps for (c) chromium and (d) aluminum.

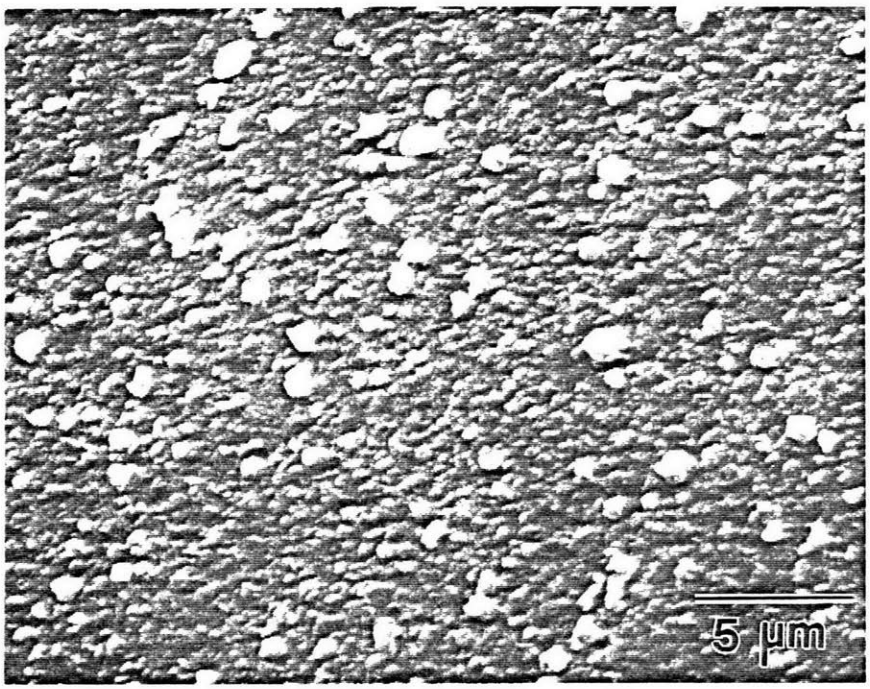

Figure 5.48—SEM secondary electron image of the oxide scale formed on a conventionally procesed Fe-4Cr-4Al alloy oxidized at 800°C for 50h.

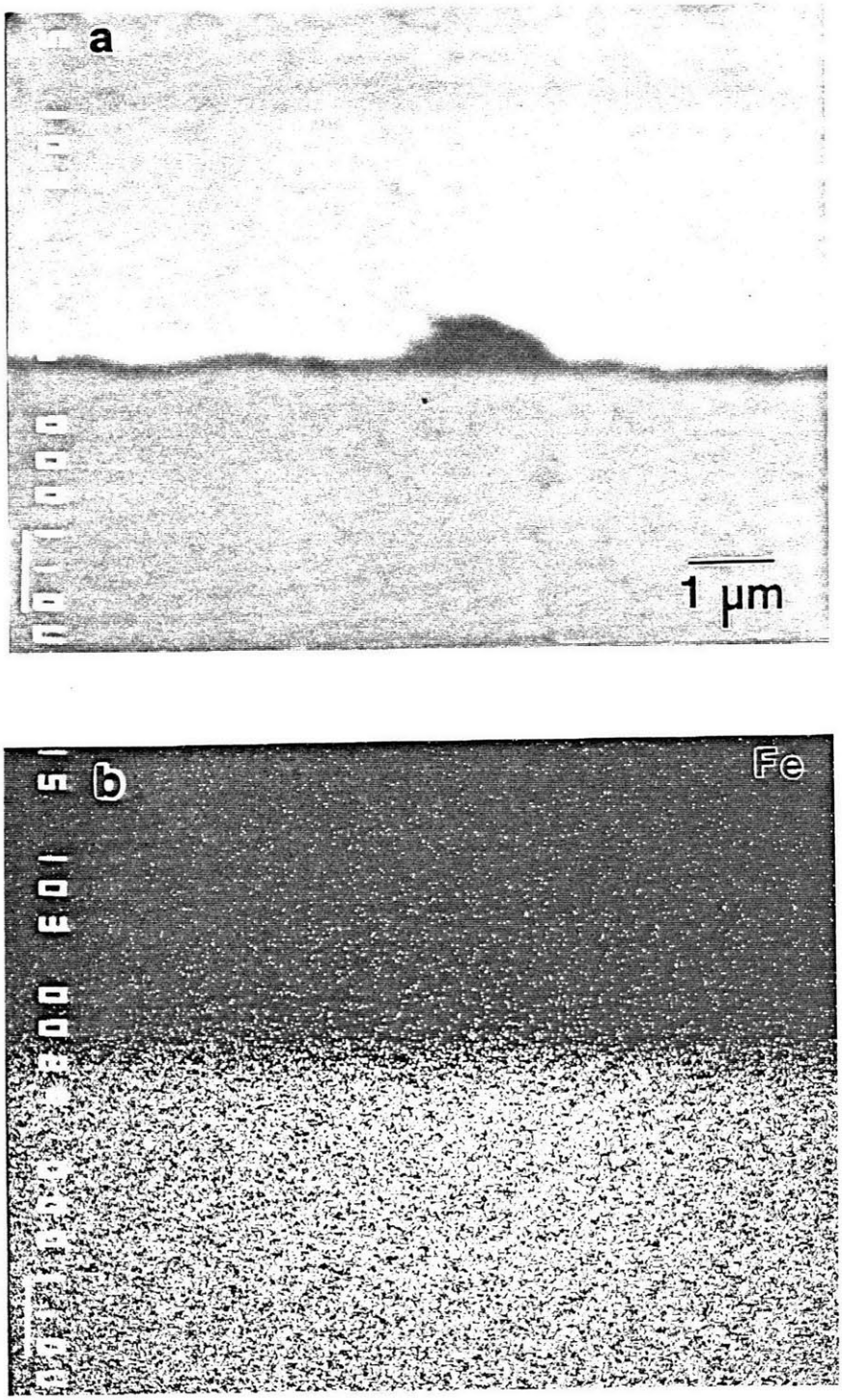

Figure 5.49—EMPA image of the cross-section through the scale shown in Figure 5.48: (a) back scattered electron image and (b) elemental X-ray intensity map for iron.

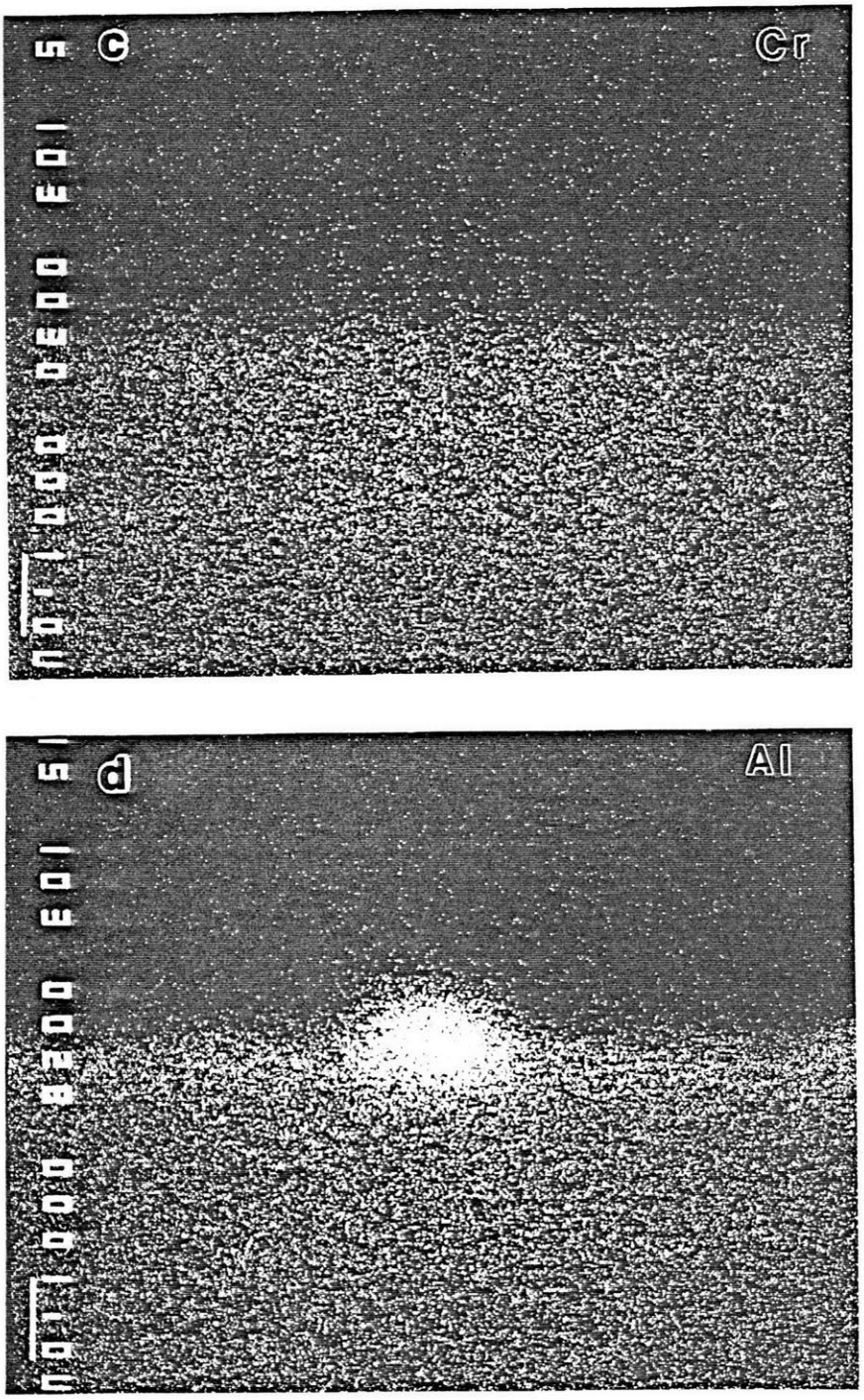

Figure 5.49 Cont.—Elemental X-ray intensity maps for (c) chromium and (d) aluminum.

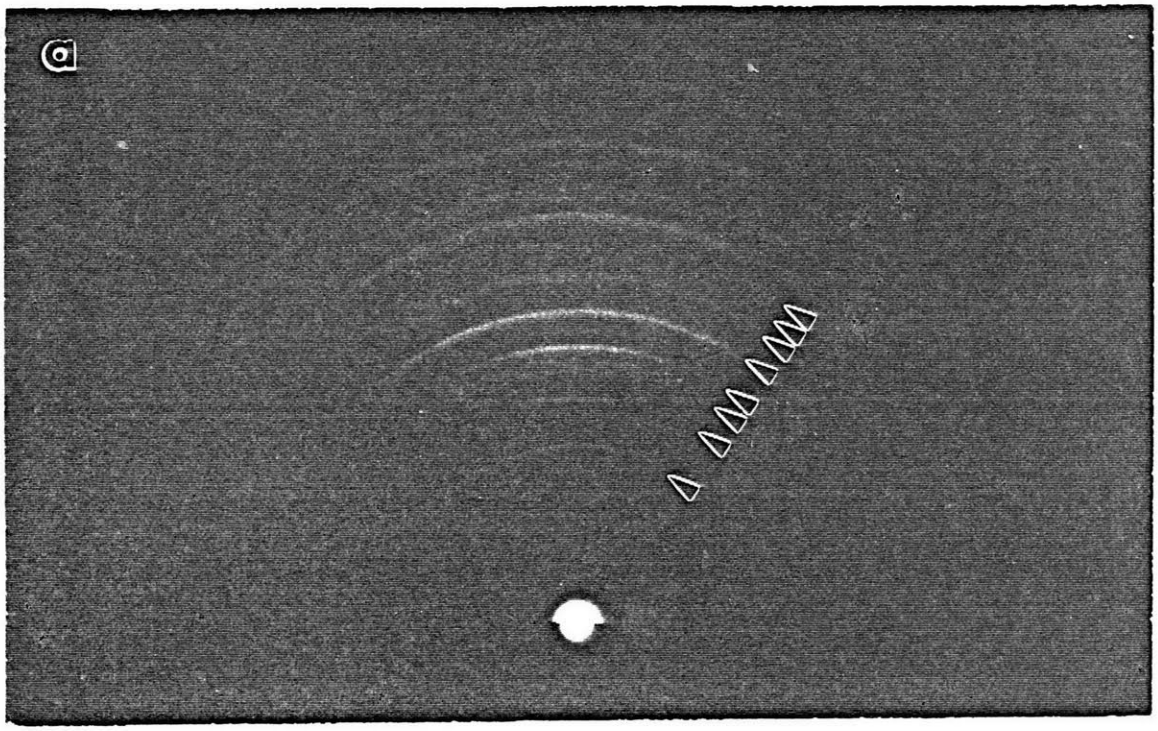

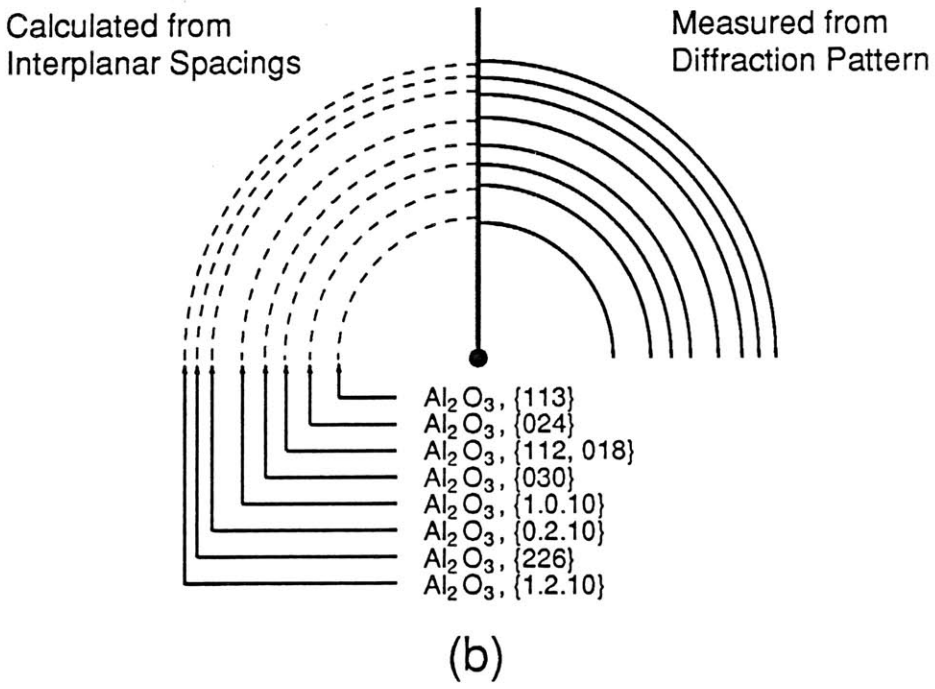

Figure 5.50—Reflected high energy electron diffraction pattern from the surface of a conventionally processed Fe-4Cr-4Al alloy that was oxidized at 800°C for 50h (a) and index of pattern (b).

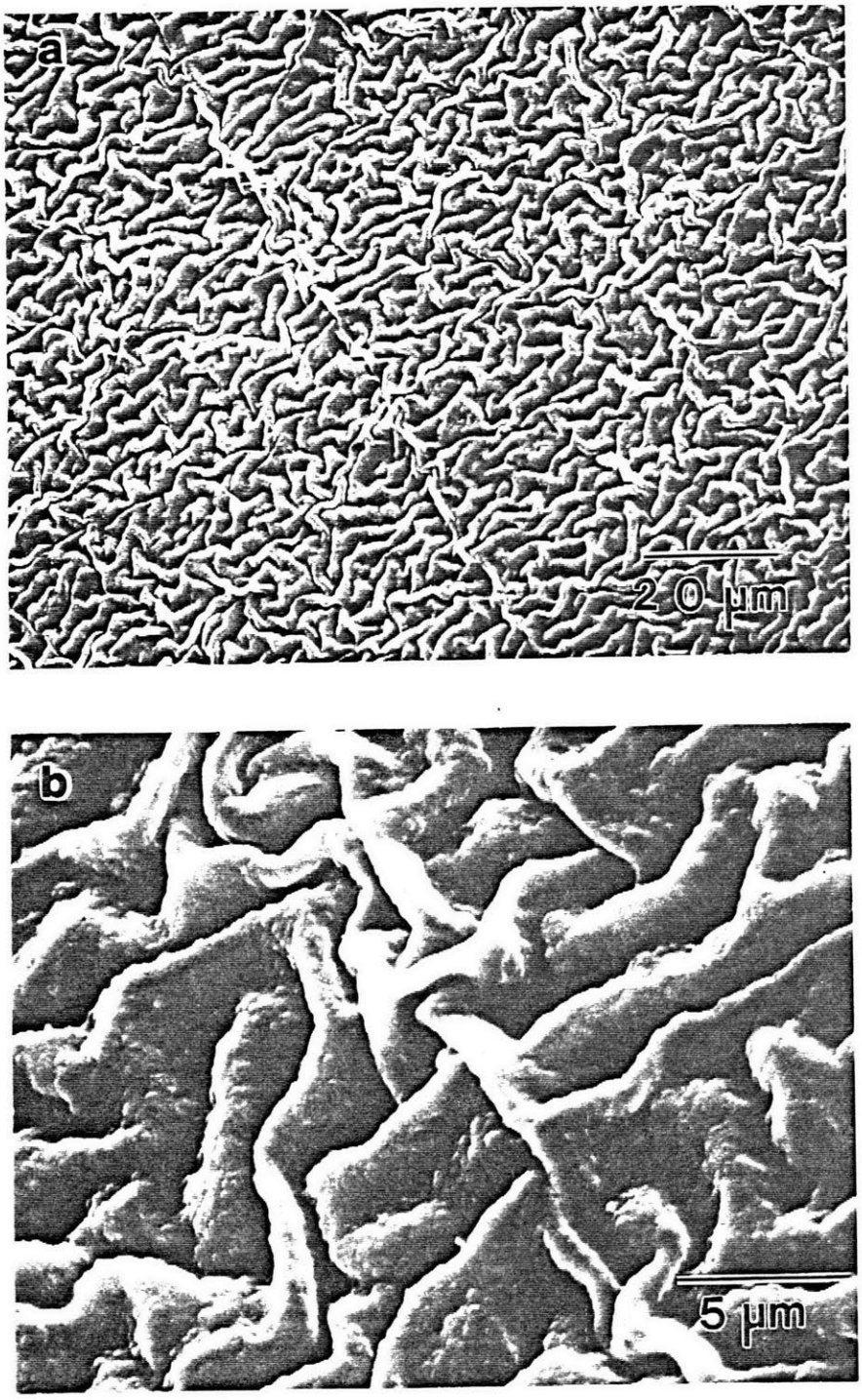

Figure 5.51—SEM secondary electron images of the scale formed on a conventionally processed Fe-4Cr-4Al alloy oxidized at 900°C for 50h: (a) low magnification and (b) high magnification.

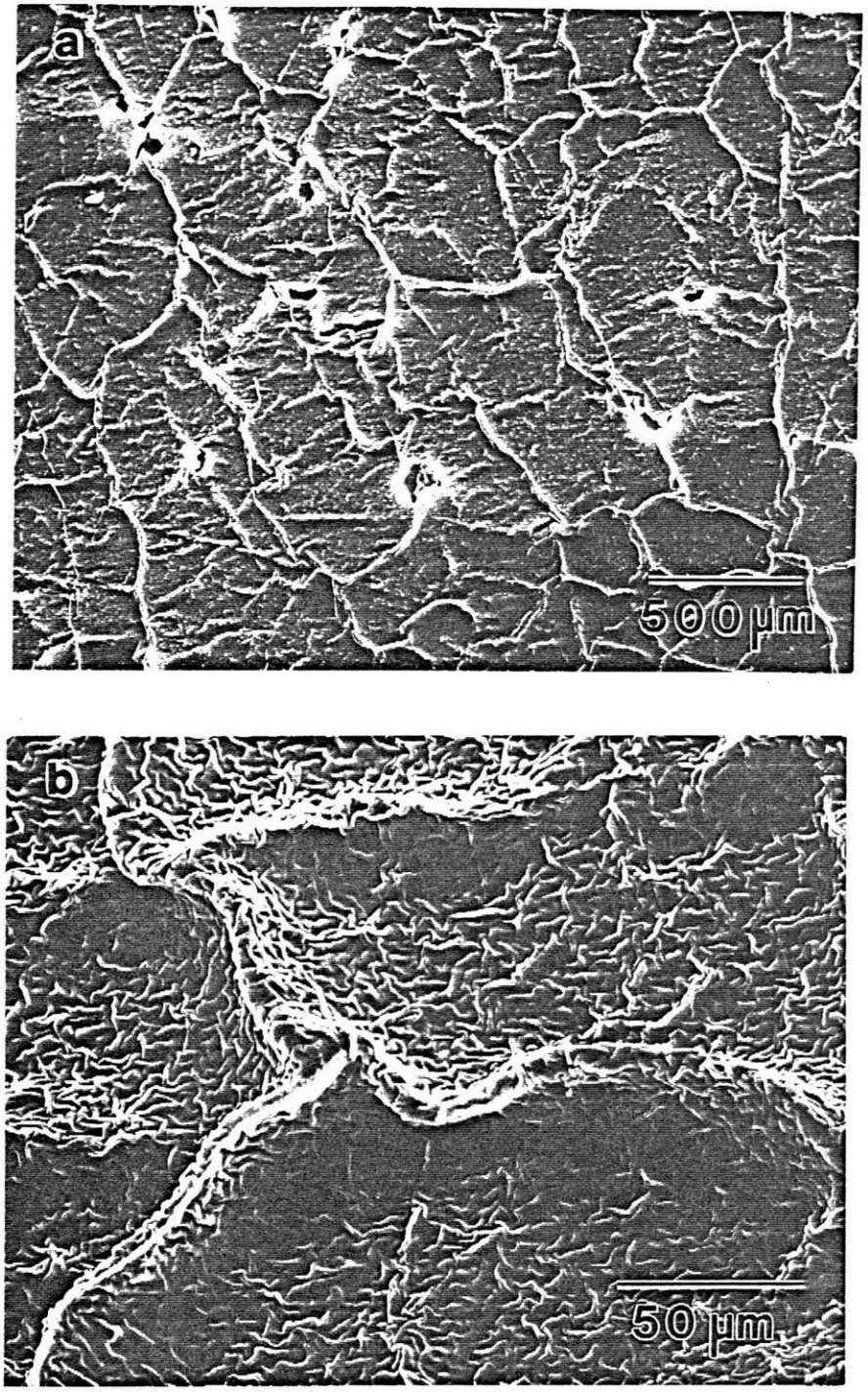

Figure 5.52—SEM secondary electron images of the scale formed on a conventionally processed Fe-4Cr-4Al alloy oxidized at 1000°C for 50h: (a) low magnification (b) high magnification.

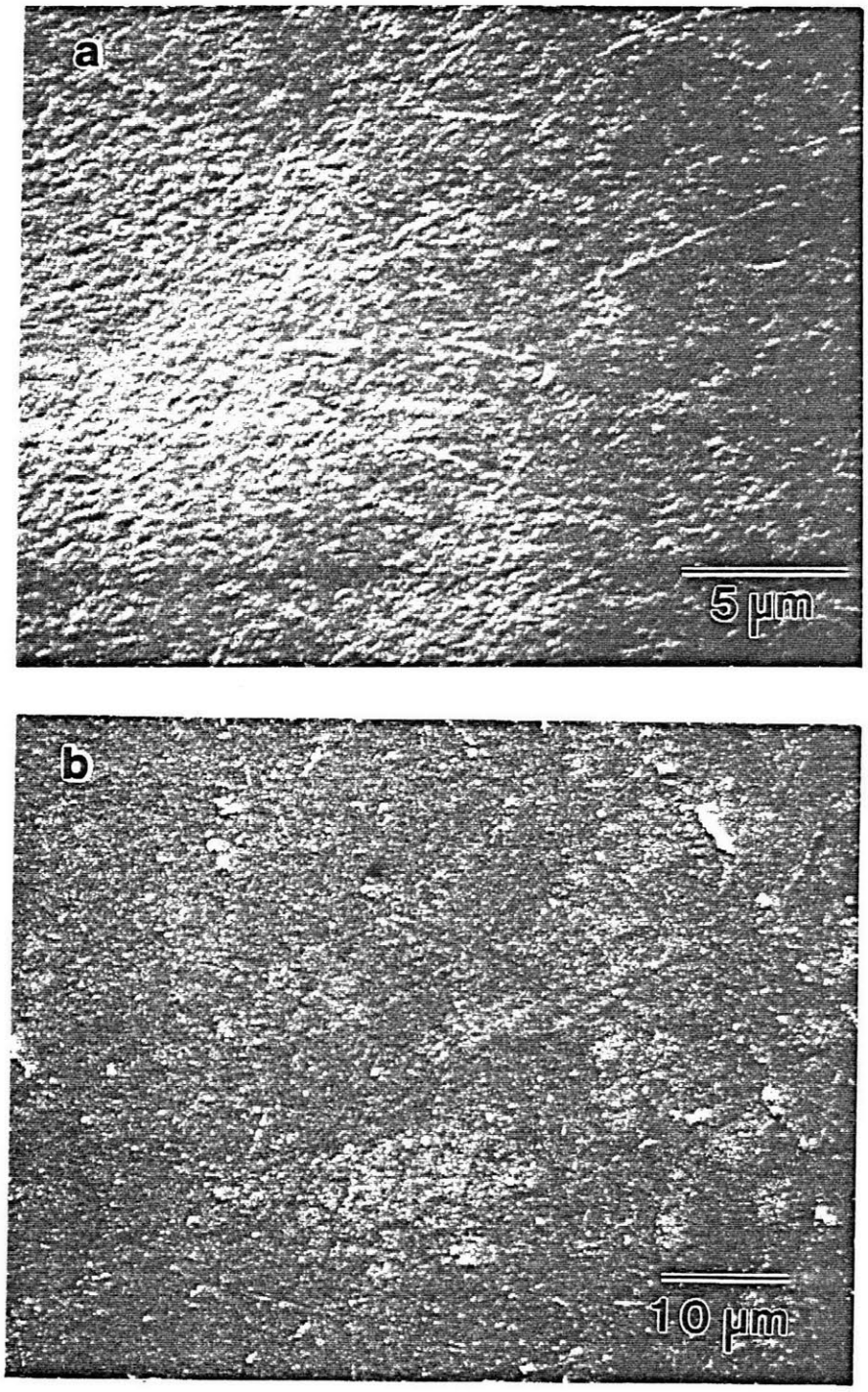

Figure 5.53—SEM secondary electron images of the scale formed on a spray formed Fe-4Cr-4Al-1Ti-0.6B alloy oxidized for 50h at (a) 400 and (b) 500°C.

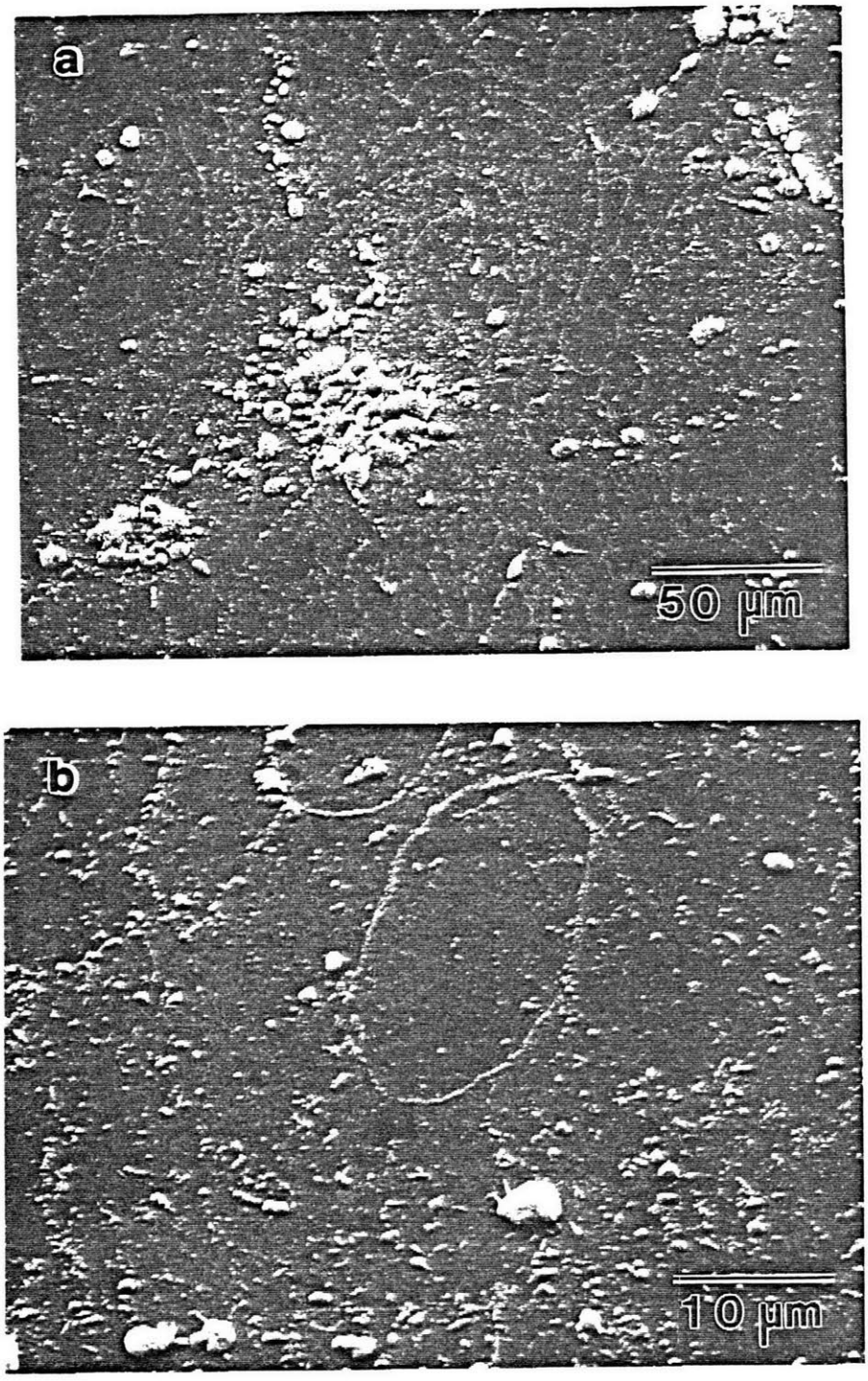

Figure 5.54—SEM secondary electron images of the scale formed on a spray formed Fe-4Cr-4Al-1Ti-0.6B alloy oxidized at 600°C for 50h: (a) low magnification and (b) high magnification.

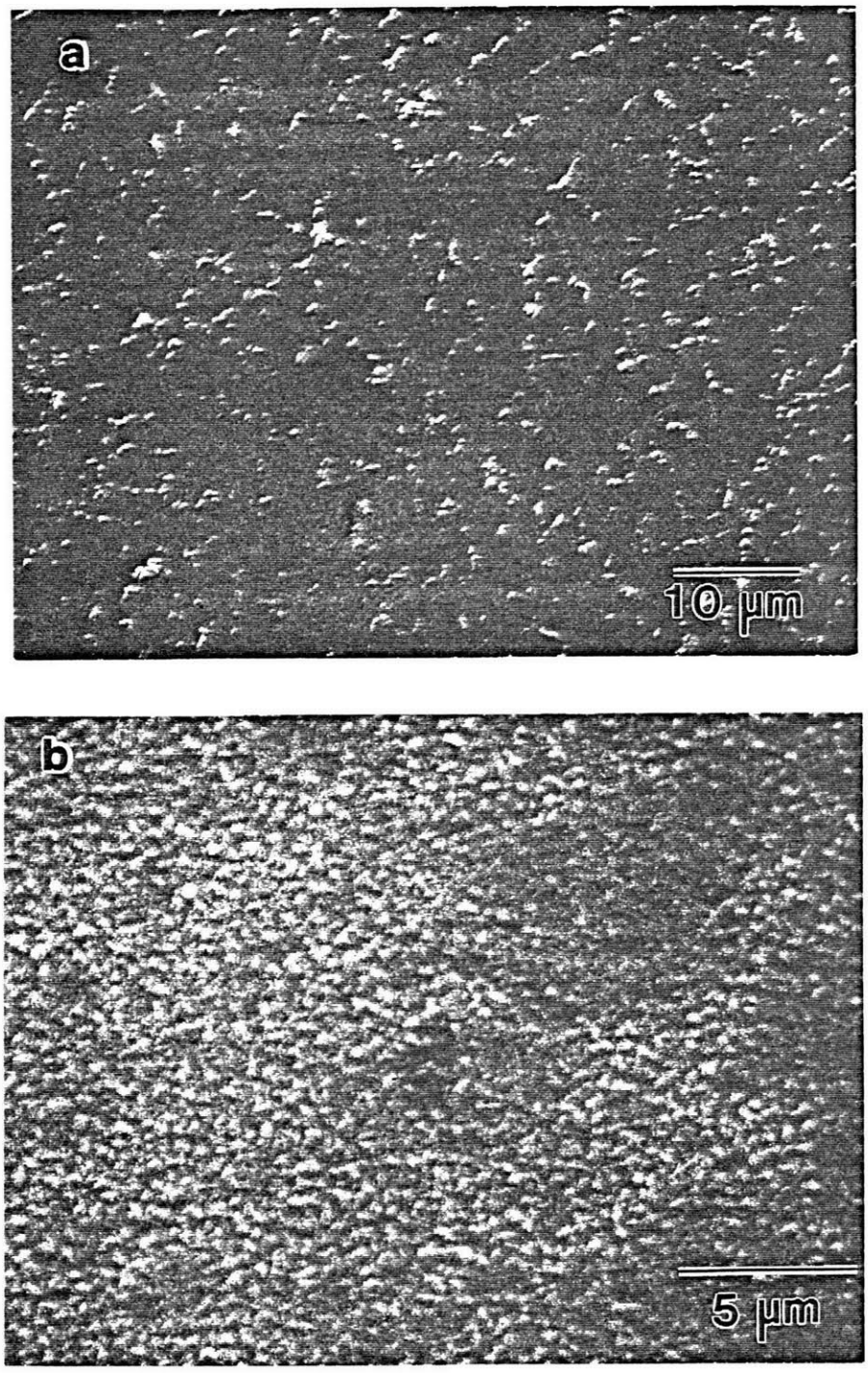

Figure 5.55—SEM secondary electron images of the scale formed on a spray formed Fe-4Cr-4Al-1Ti-0.6B alloy oxidized for 50h at (a) 700 and (b) 800°C.

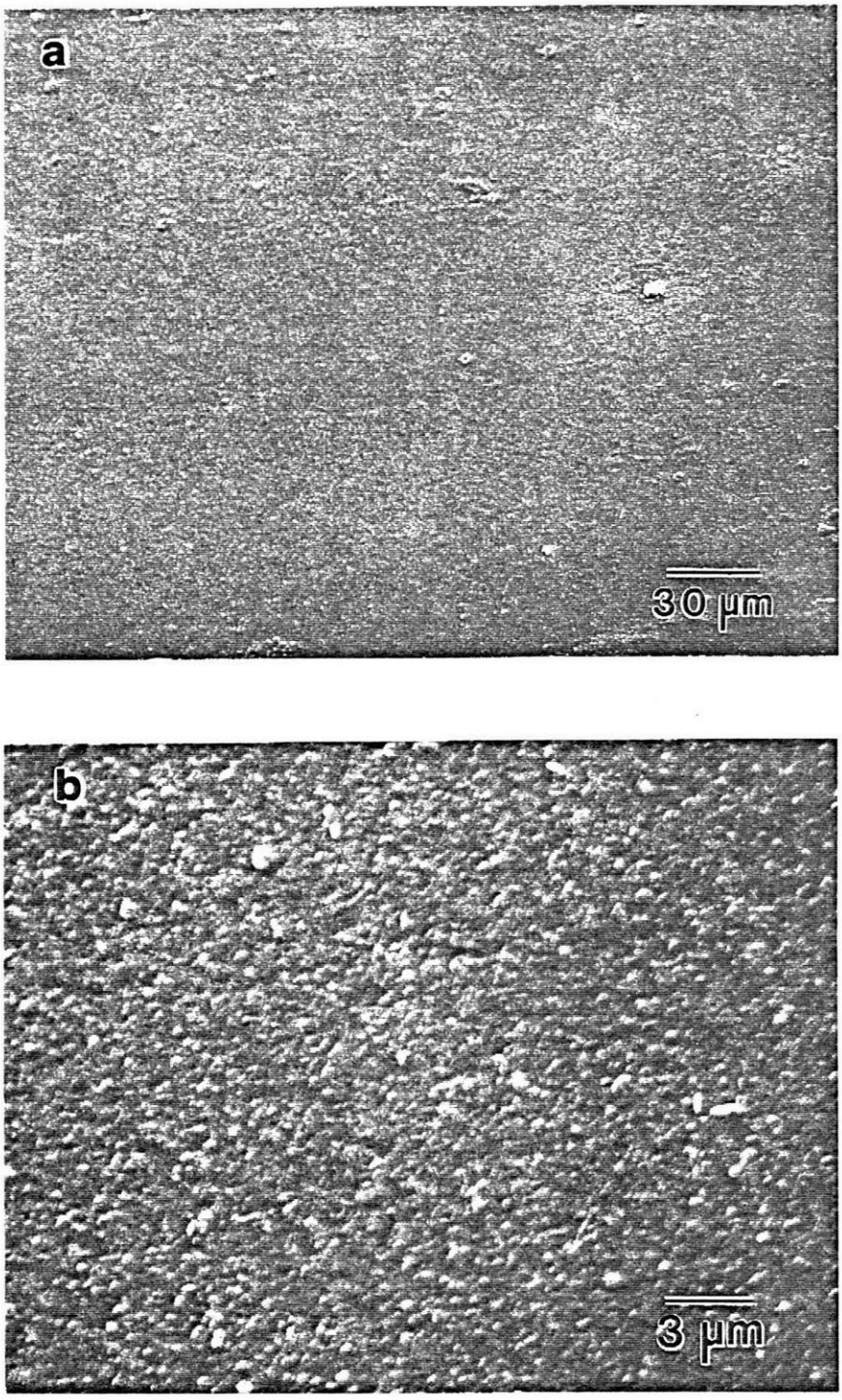

Figure 5.56—SEM secondary electron images of the scale formed on a spray formed Fe-4Cr-4Al-1Ti-0.6B alloy oxidized at 900°C for 50h: (a) low magnification and (b) high magnification.

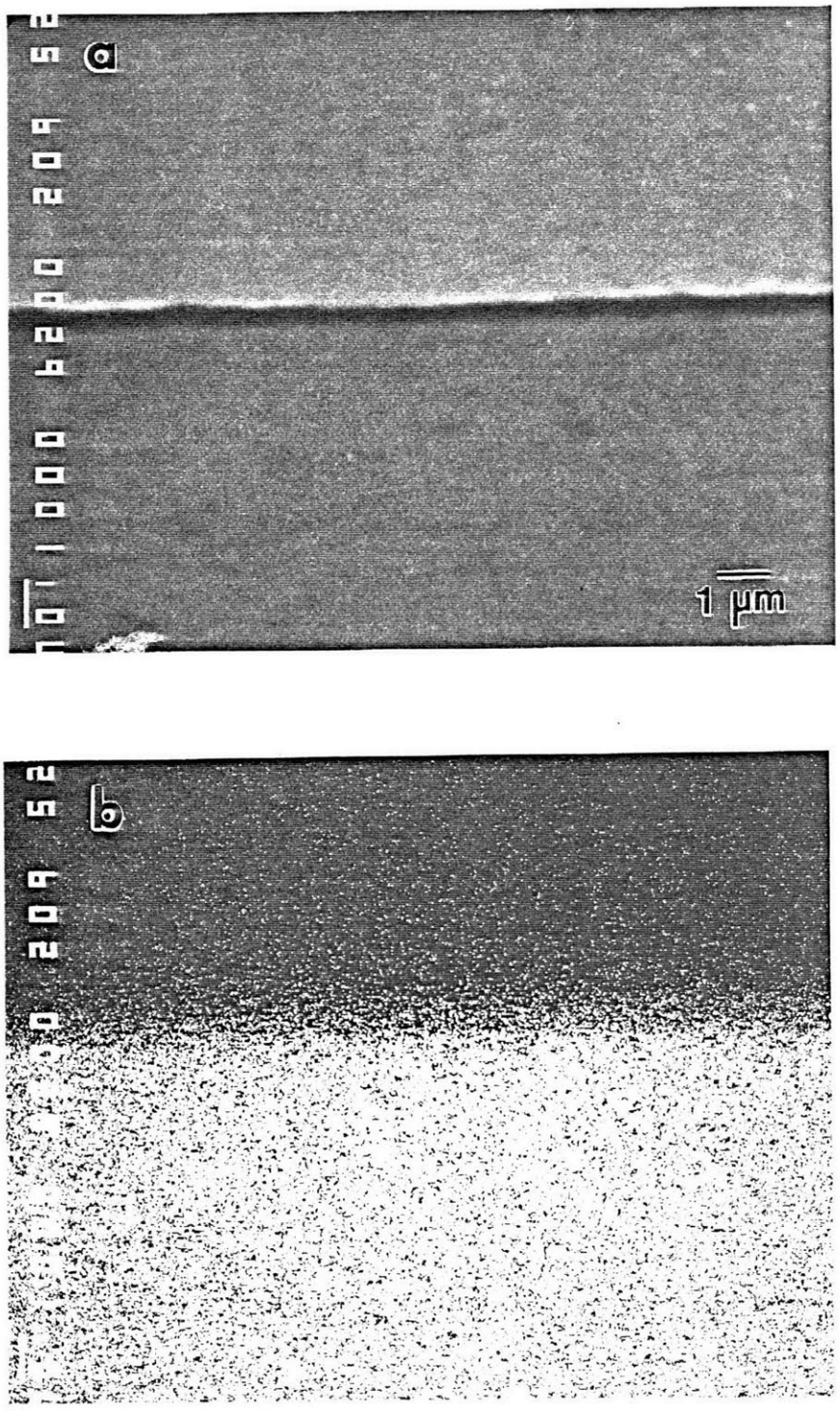

Figure 5.57—EPMA images of a cross-section through the scale shown in Figure 5.59: (a) back scattered electron image and (b) elemental x-ray intensity map for iron.

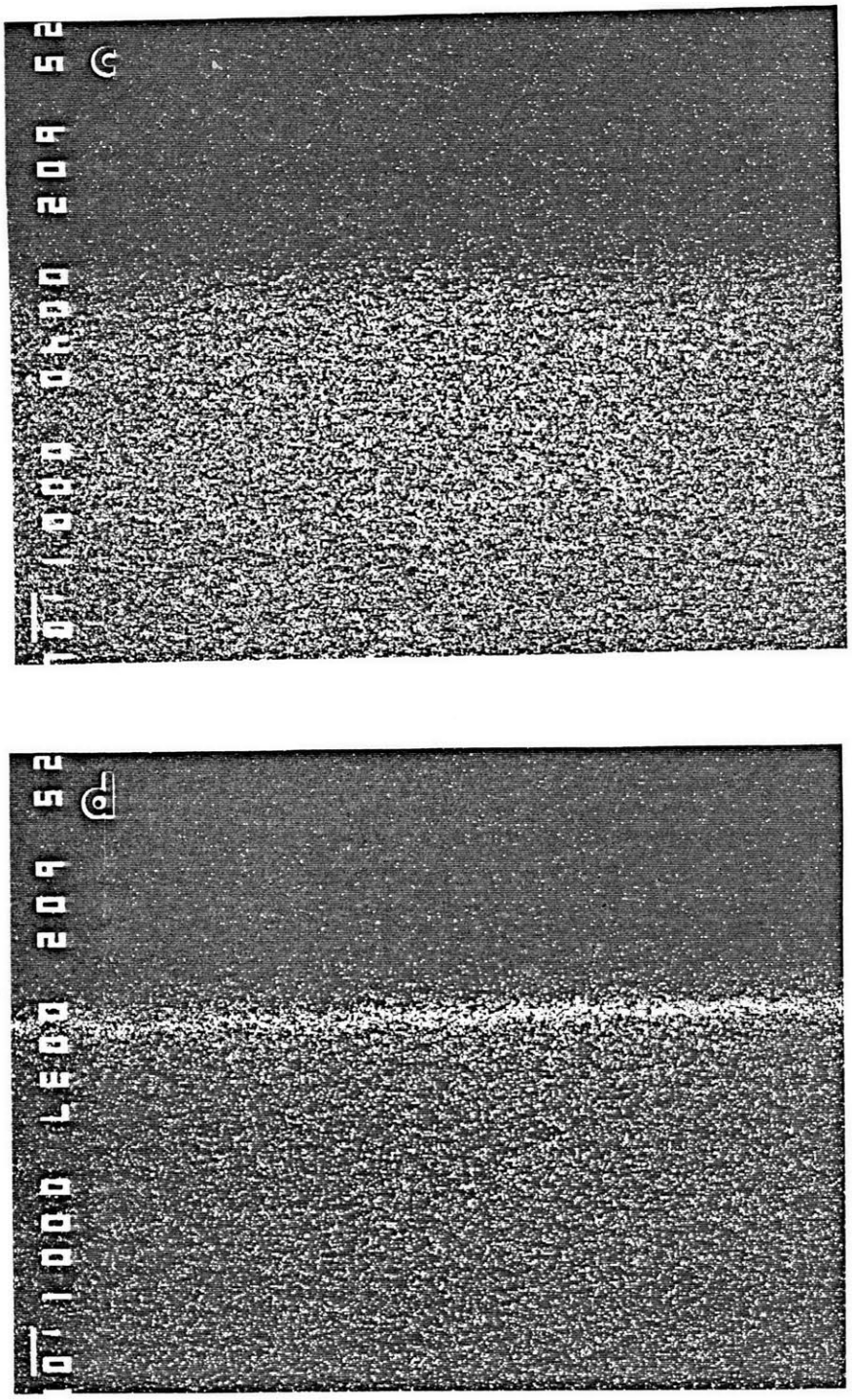

Figure 5.57 Cont.—Elemental X-ray intensity map for (c) chromium and (d) aluminum.

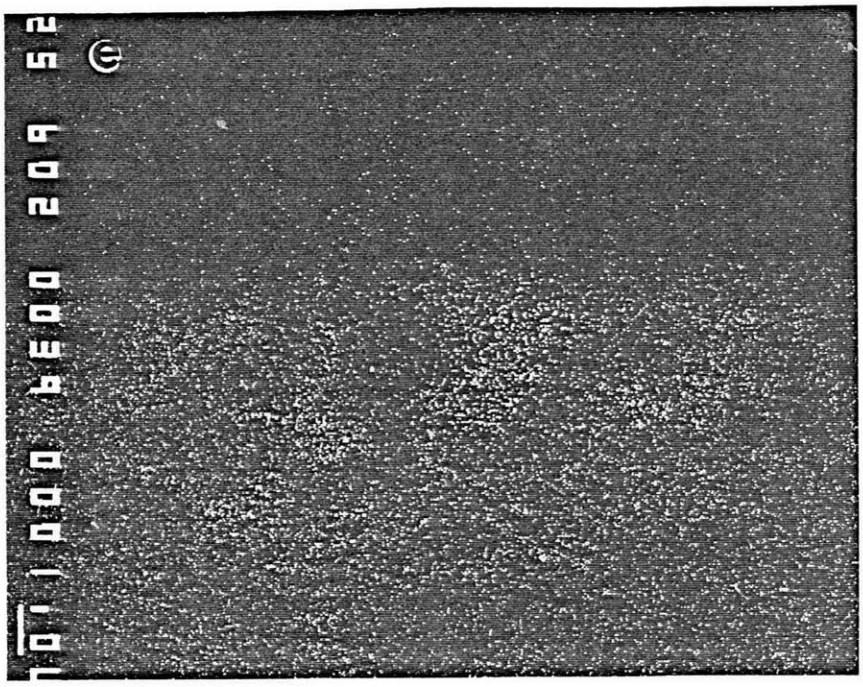

Figure 5.57 Cont.—(e) Elemental X-ray intensity map for titanium.

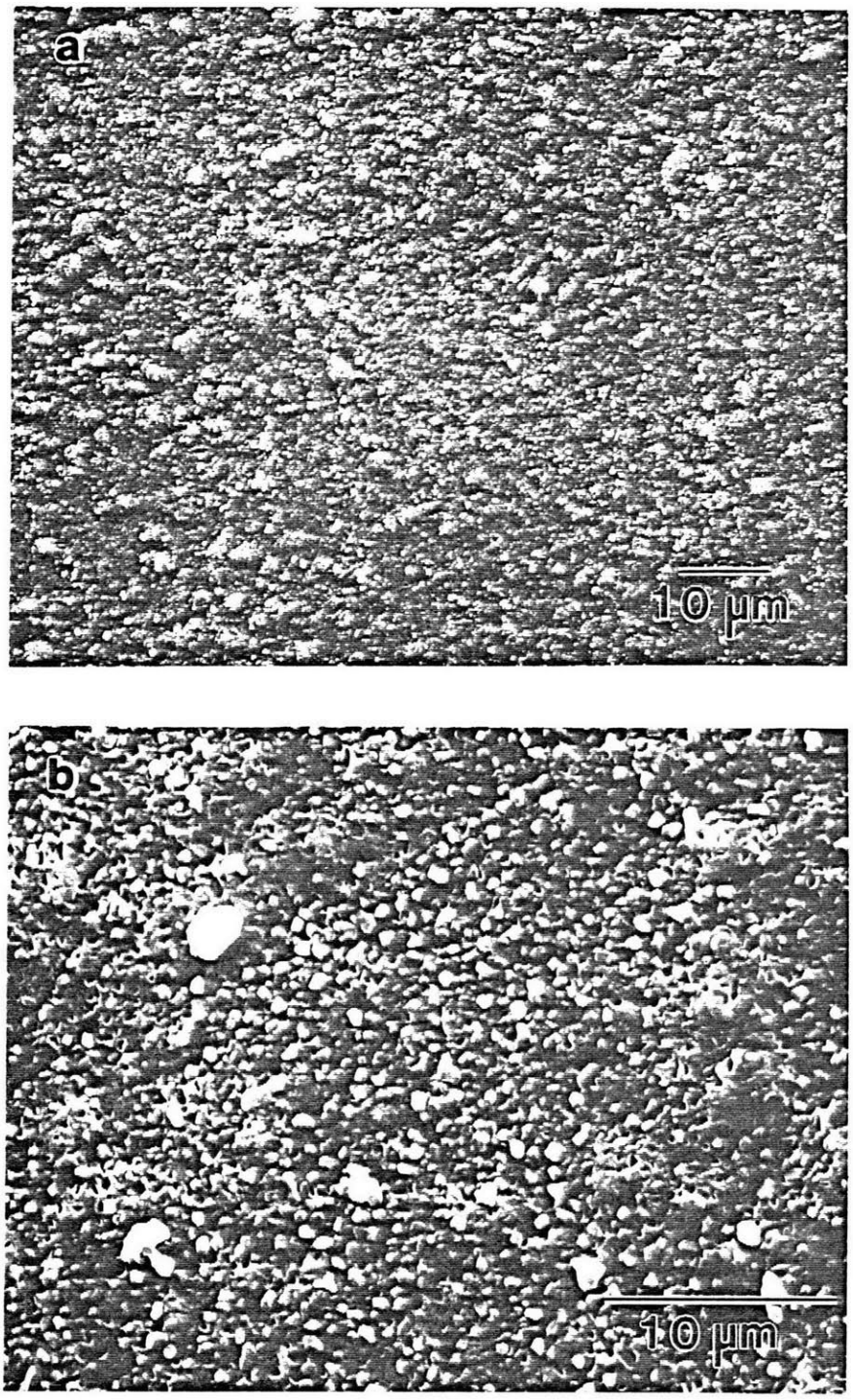

Figure 5.58—SEM secondary electron images of the scale formed on a spray formed Fe-4Cr-4Al-1Ti-0.6B alloy oxidized at 1000°C for 50h: (a) low magnification and (b) high magnification.

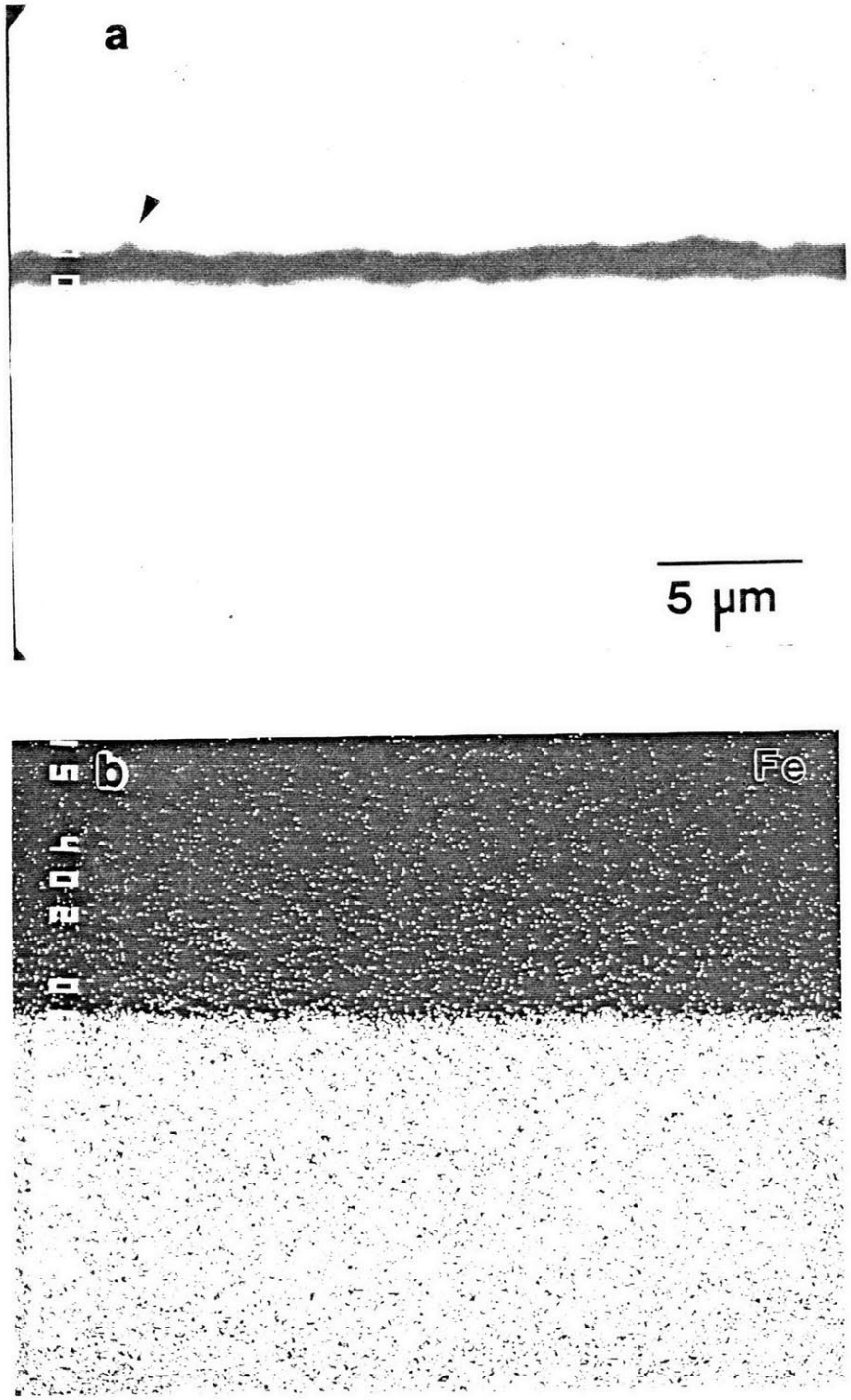

Figure 5.59—EPMA images of a cross-section through the scale shown in Figure 5.58: (a) backscattered electron image and (b) elemental intensity image for iron.

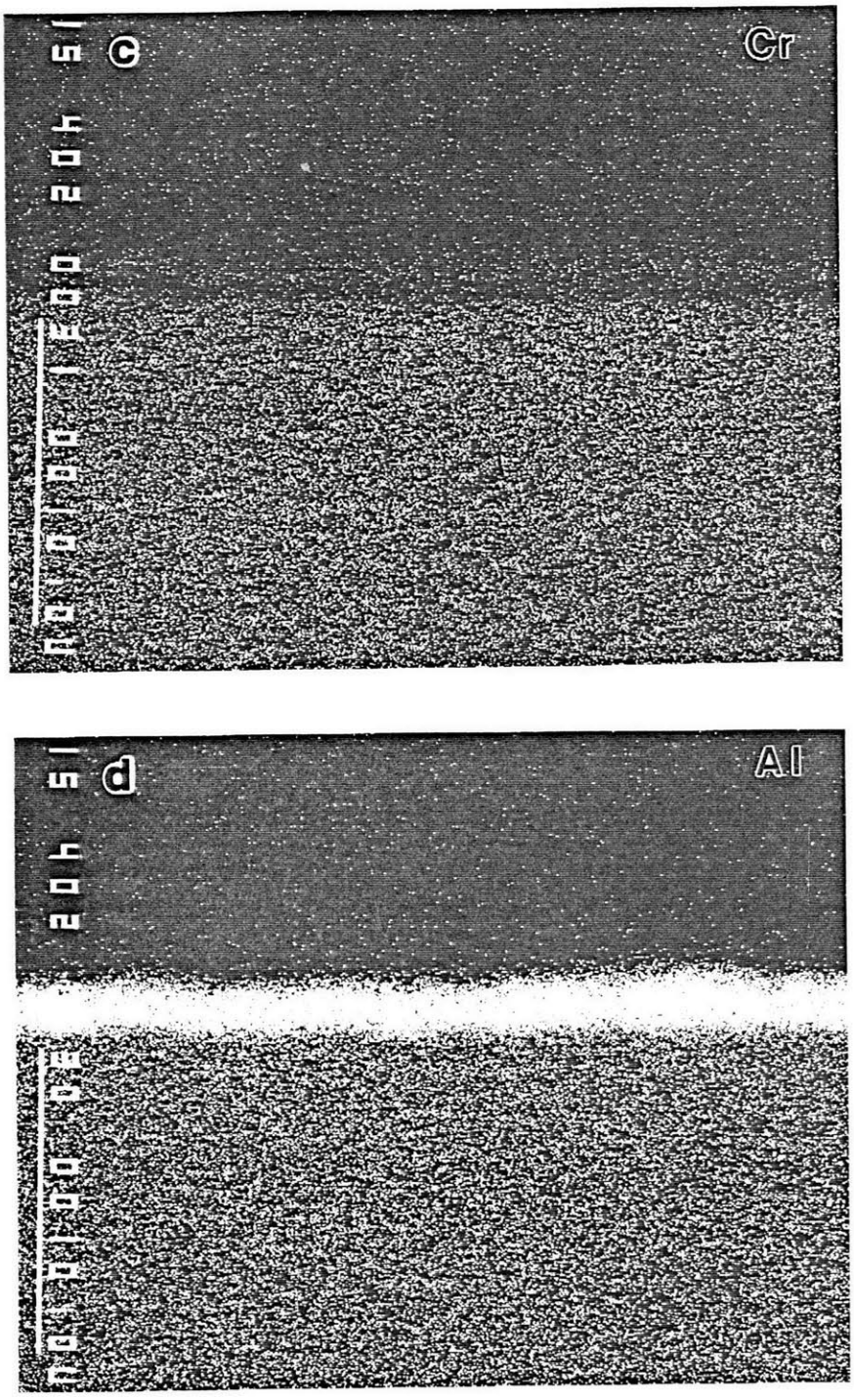

Figure 5.59 Cont.—Elemental X-ray intensity maps for (c) chromium and (b) aluminum.

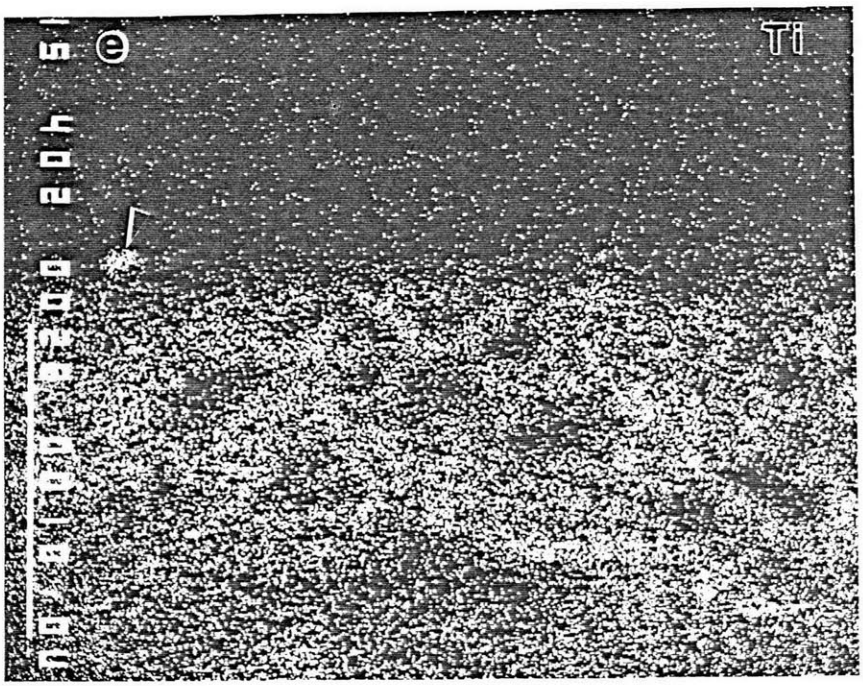

Figure 5.59 Cont.—(e) Elemental X-ray intensity map for titanium.

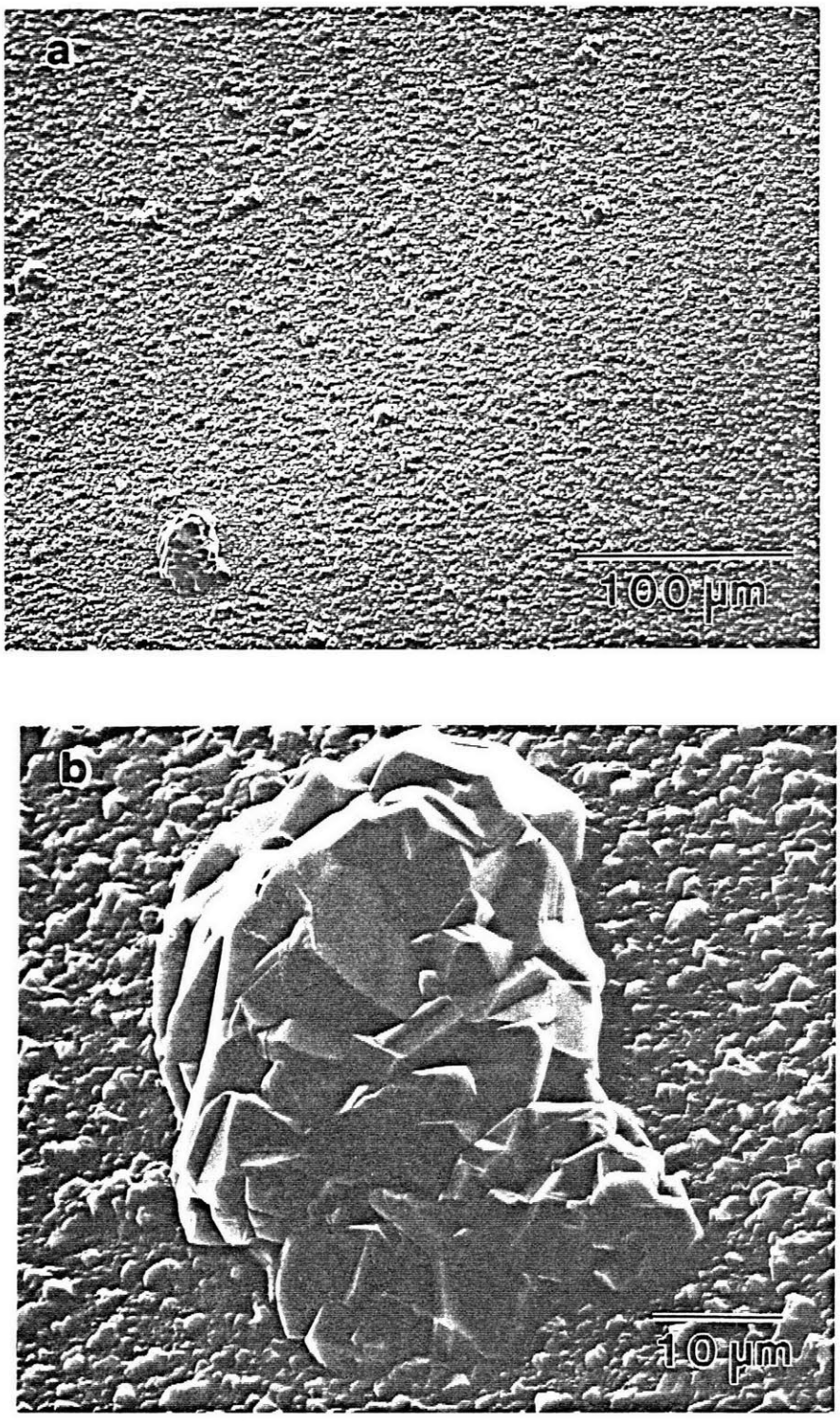

Figure 5.60—SEM secondary electron images of the scale formed on a conventionally processed Fe-4Cr-4Al-1Ti-0.6B alloy oxidized at 900°C for 50h: (a) low magnification and (b) high magnification.

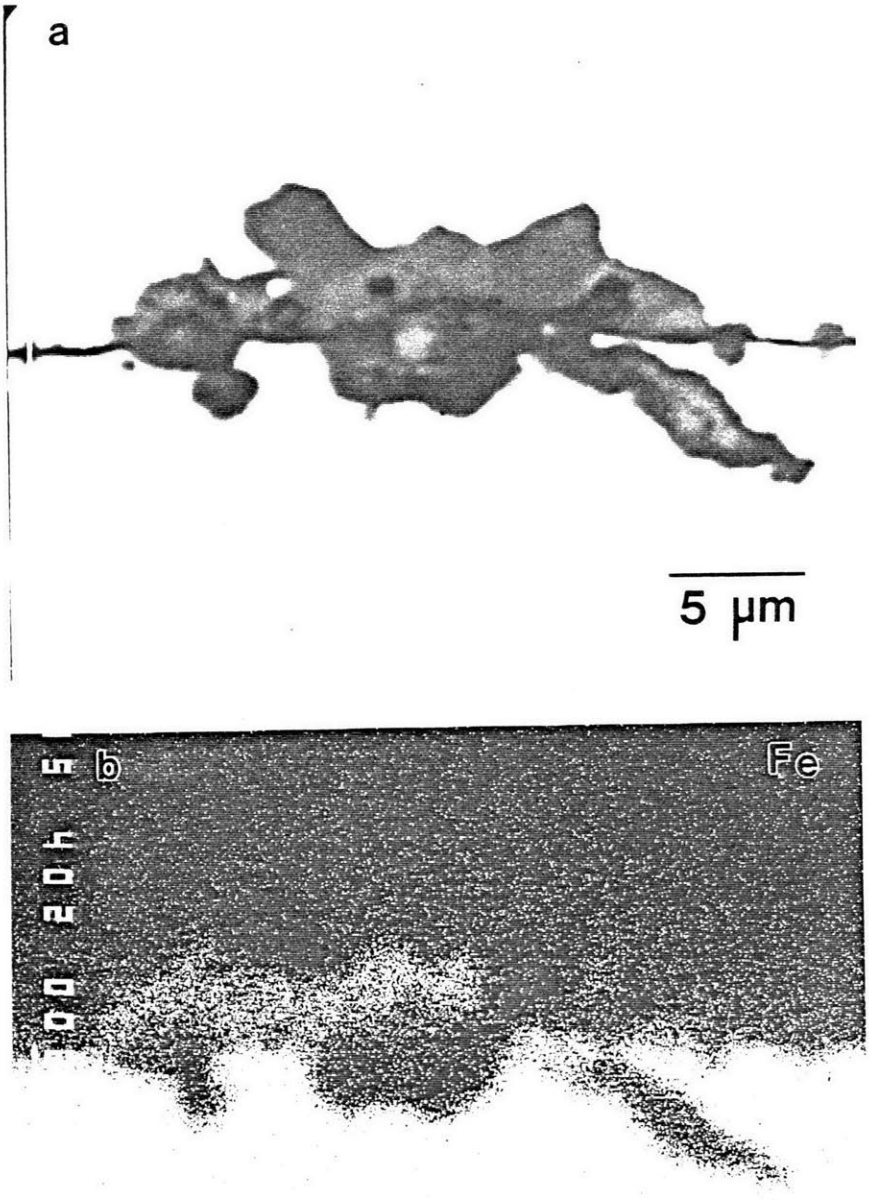

Figure 5.61—EPMA images of a cross-section through a nodule on the specimen shown in Figure 5.60: (a) back scattered electron image and (b) elemental X-ray intensity map for iron.

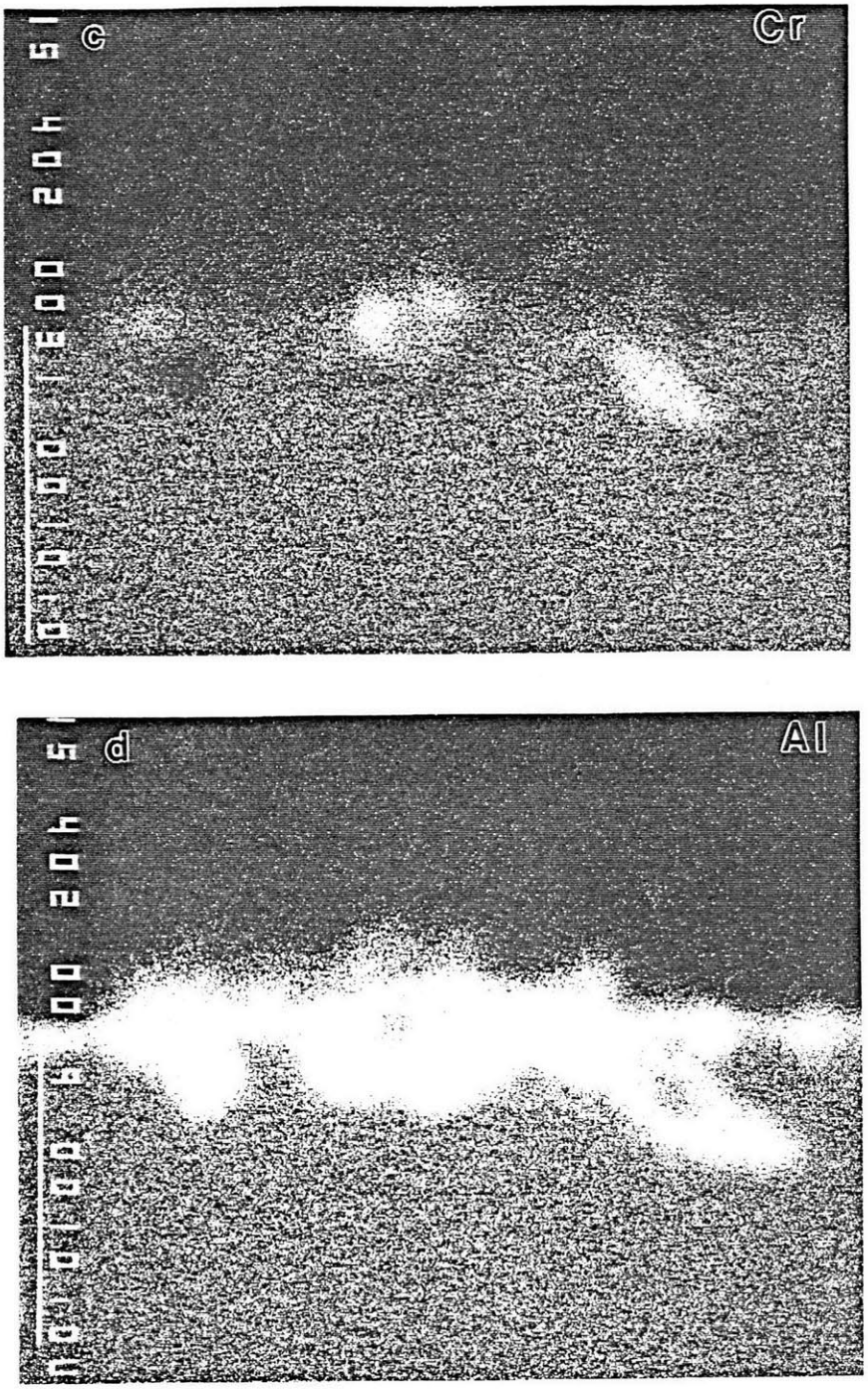

Figure 5.61 Cont.—Elemental X-ray intensity maps for (c) chromium and (d) aluminum.

Figure 5.61 Cont.—(e) Elemental X-ray intensity map for titanium.

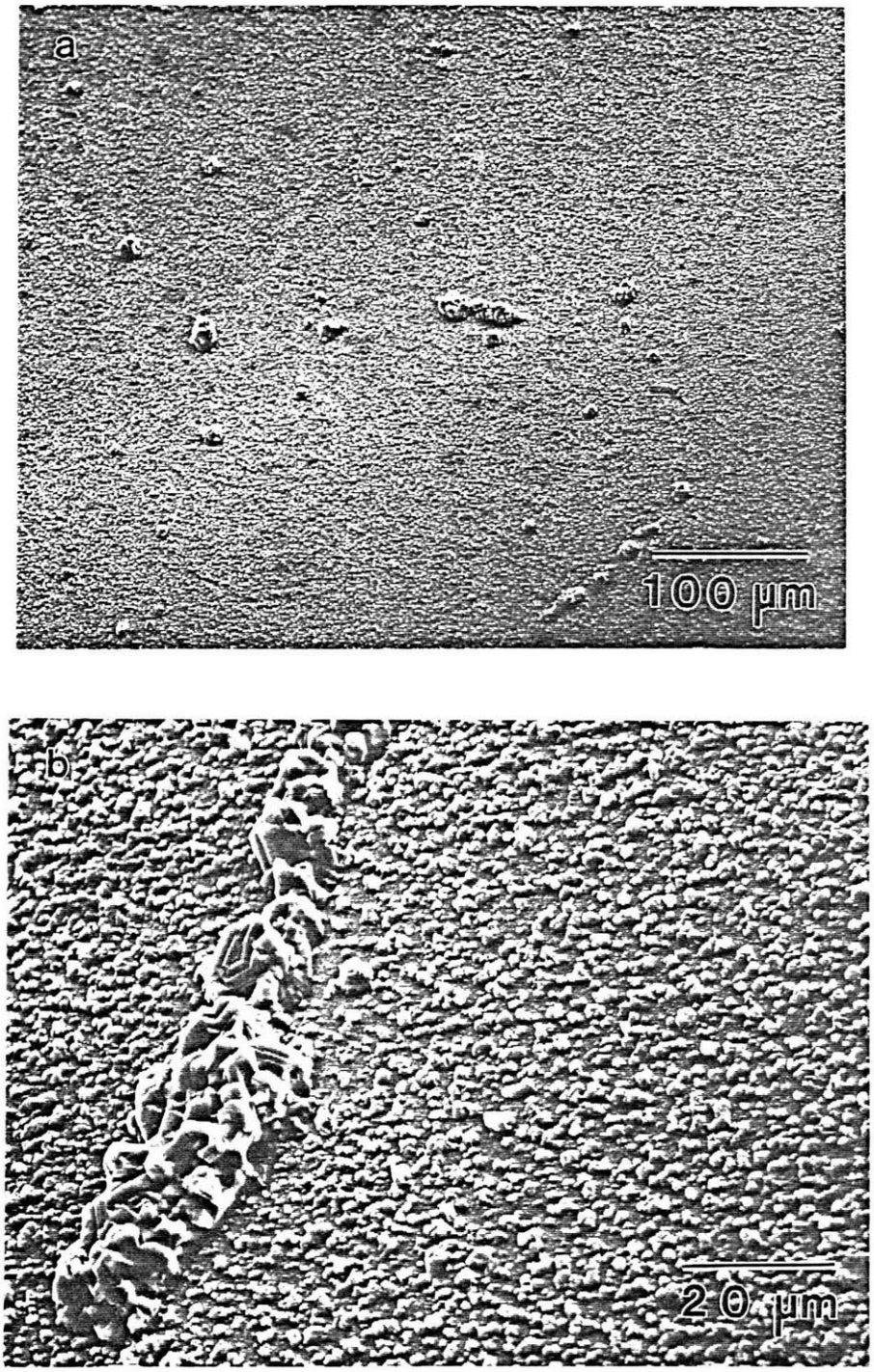

Figure 5.62—SEM secondary electron images of the scale formed on a conventionally processed Fe-4Cr-4Al-1Ti alloy oxidized at 1000°C for 50h: (a) low magnification and (b) high magnification.

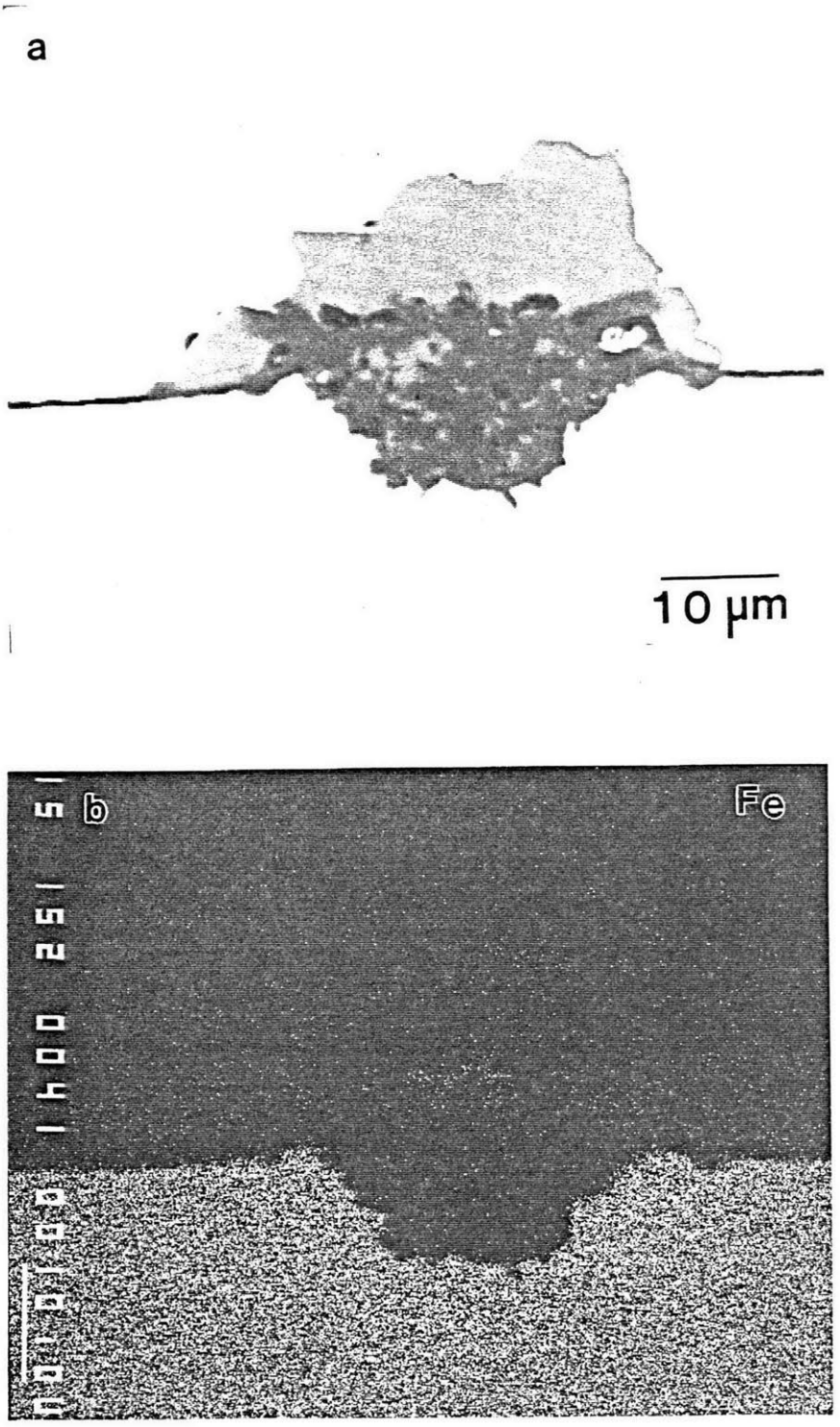

Figure 5.63—EPMA images of a cross-section through the scale shown in Figure 5.62: (a) back scattered image and (b) elemental X-ray intensity map for iron.

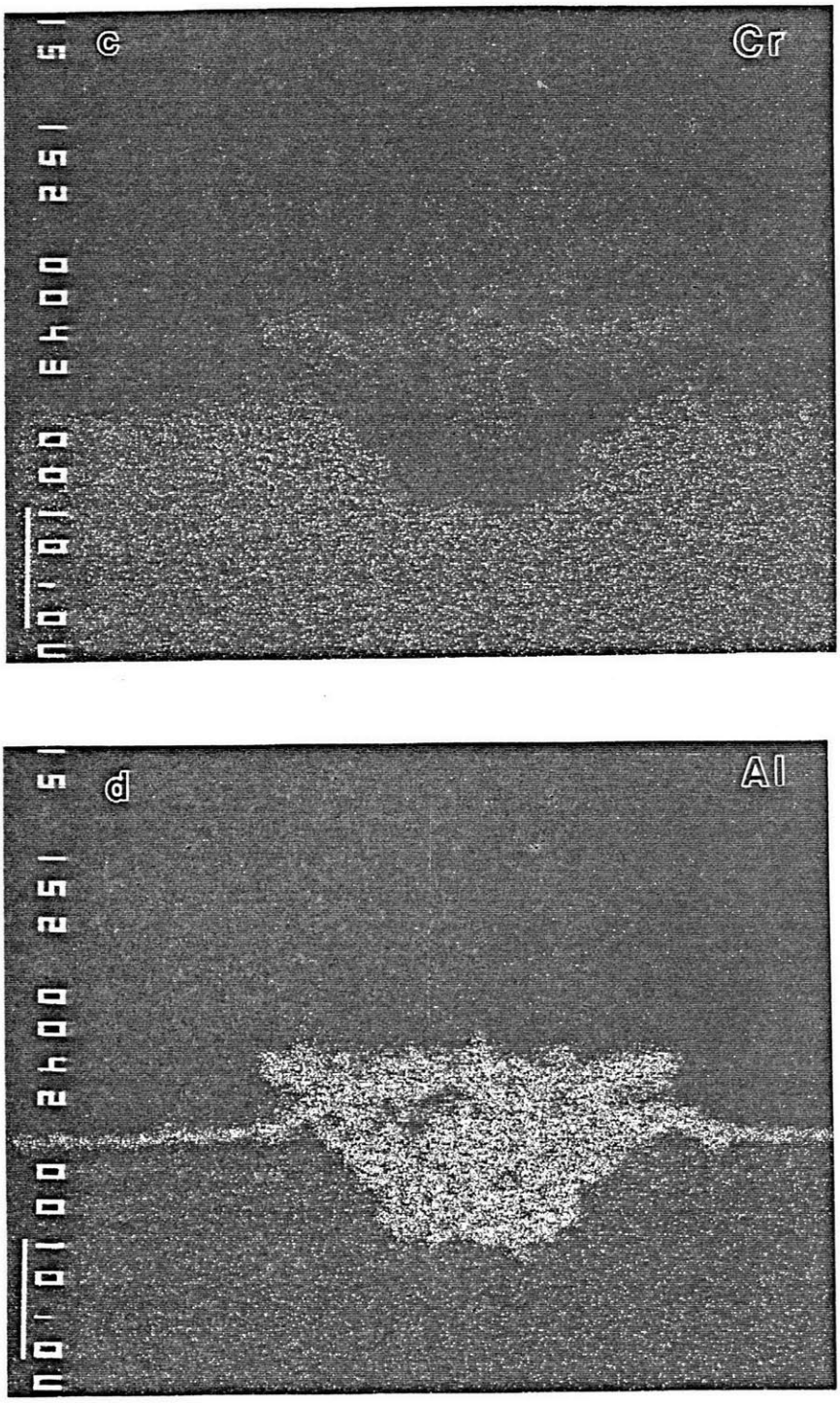

Figure 5.63 Cont.—Elemental X-ray intensity maps for (c) chromium and (d) aluminum.

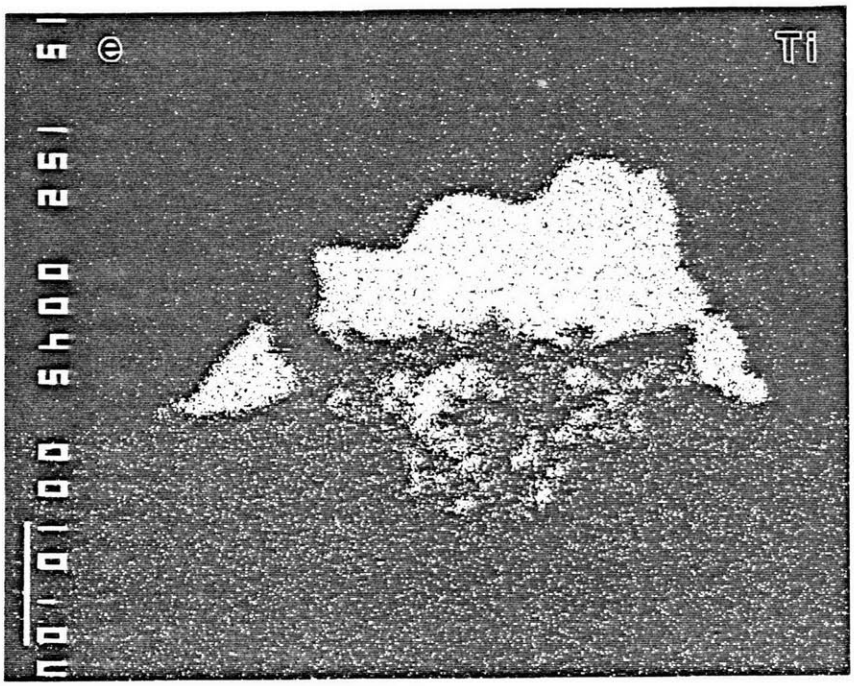

Figure 5.63 Cont.—(e) Elemental X-ray intensity map for titanium.

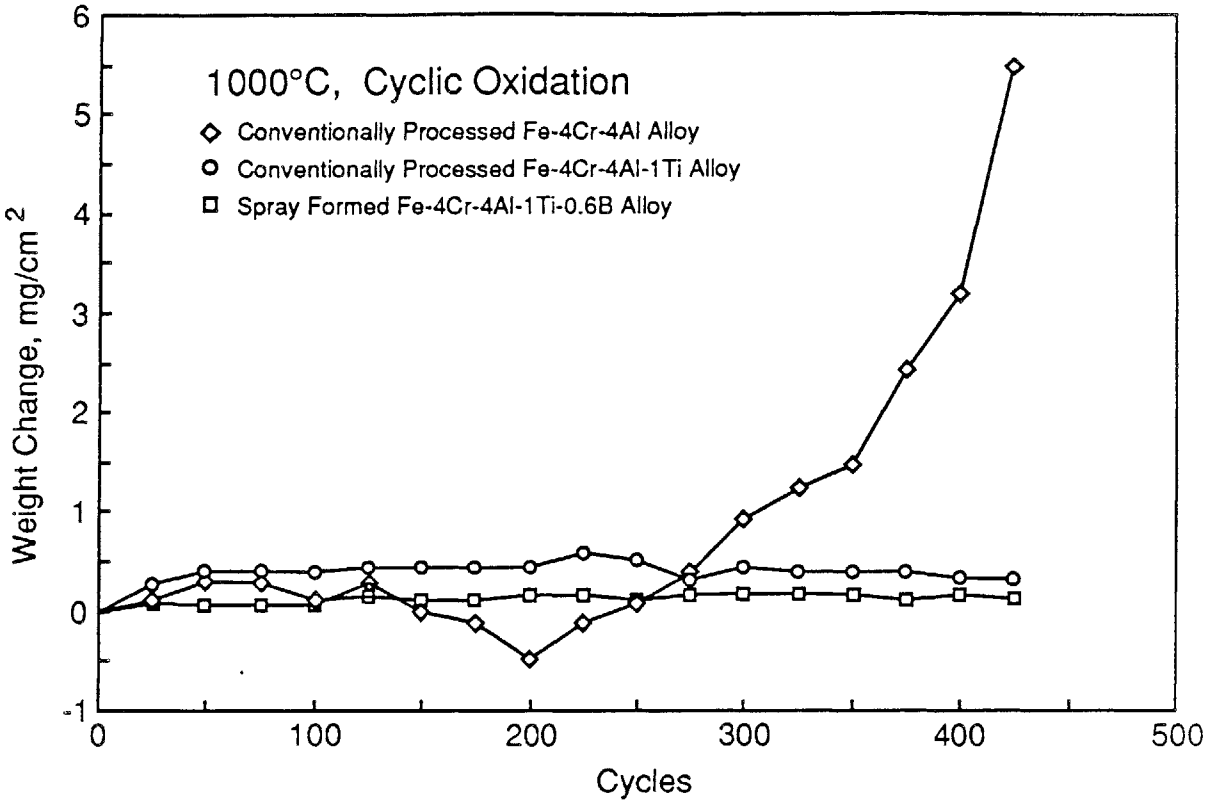

Figure 5.64—Weight change as a function of number of thermal cycles from 1000°C to room temperature for Fe-4Cr-4Al and Fe-4Cr-4Al-1Ti conventionally processed alloys and Fe-4Cr-4Al-1Ti-0.6B alloy.

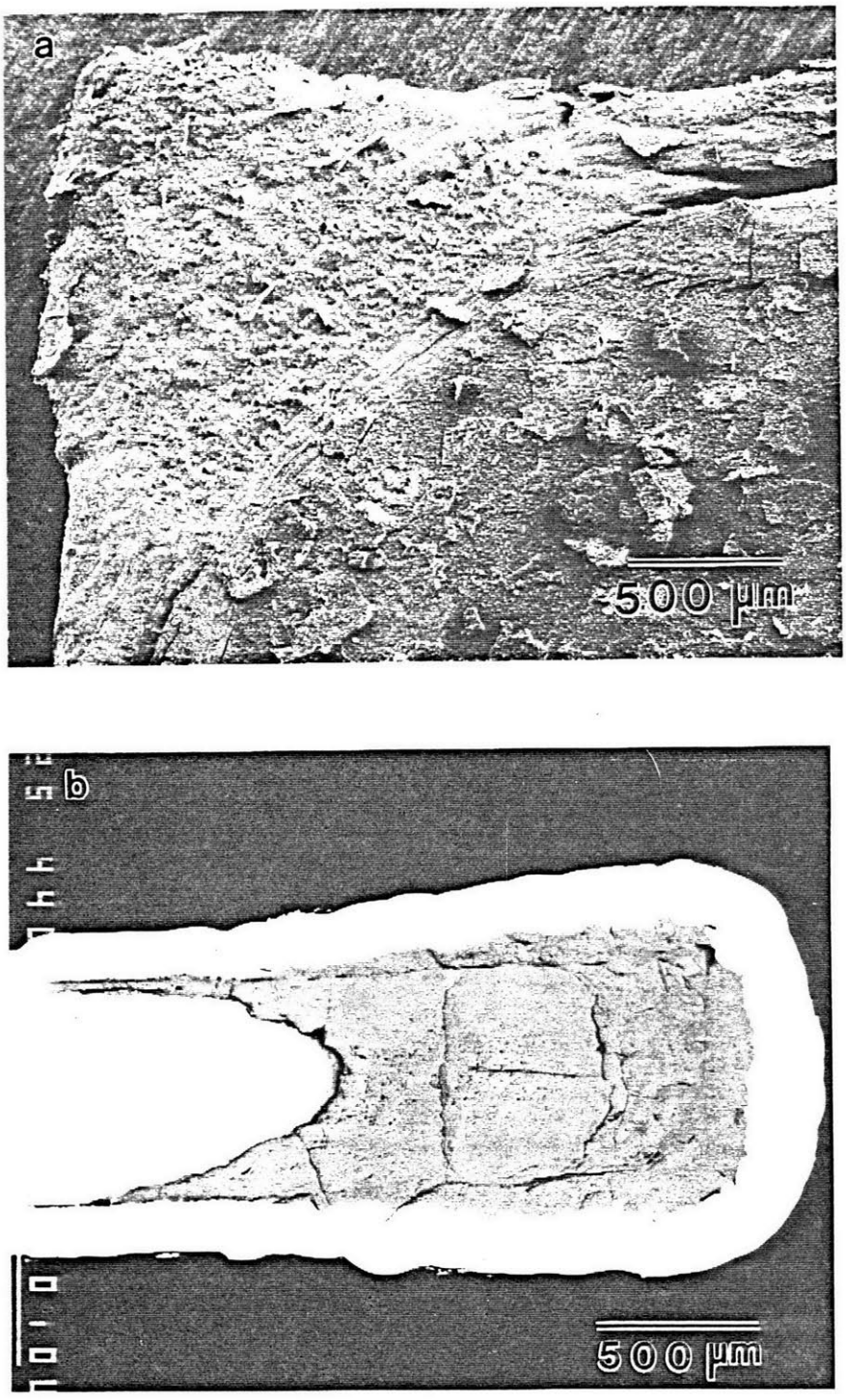

Figure 5.65—Scale formed on a conventionally processed Fe-4Cr-4Al alloy after undergoing 425 thermal cycles from 1000°C to room temperature: (a) SEM secondary electron image of scale surface and (b) EPMA back scattered electron image of a cross-section through the scale.

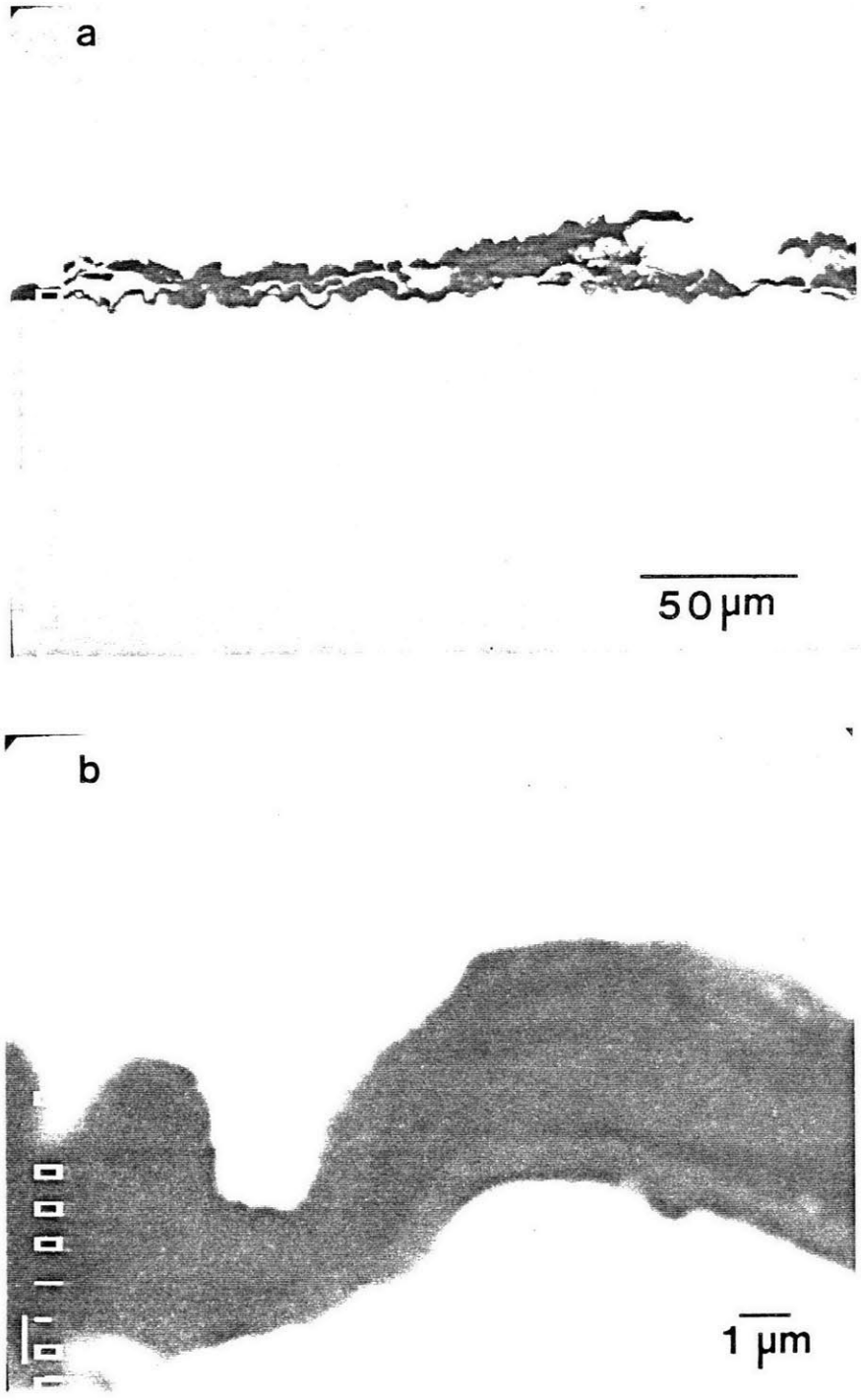

Figure 5.66—EPMA back scattered electron images of a cross-section through the scale shown in Figure 5.65: (a) low magnificaton and (b) high magnification.

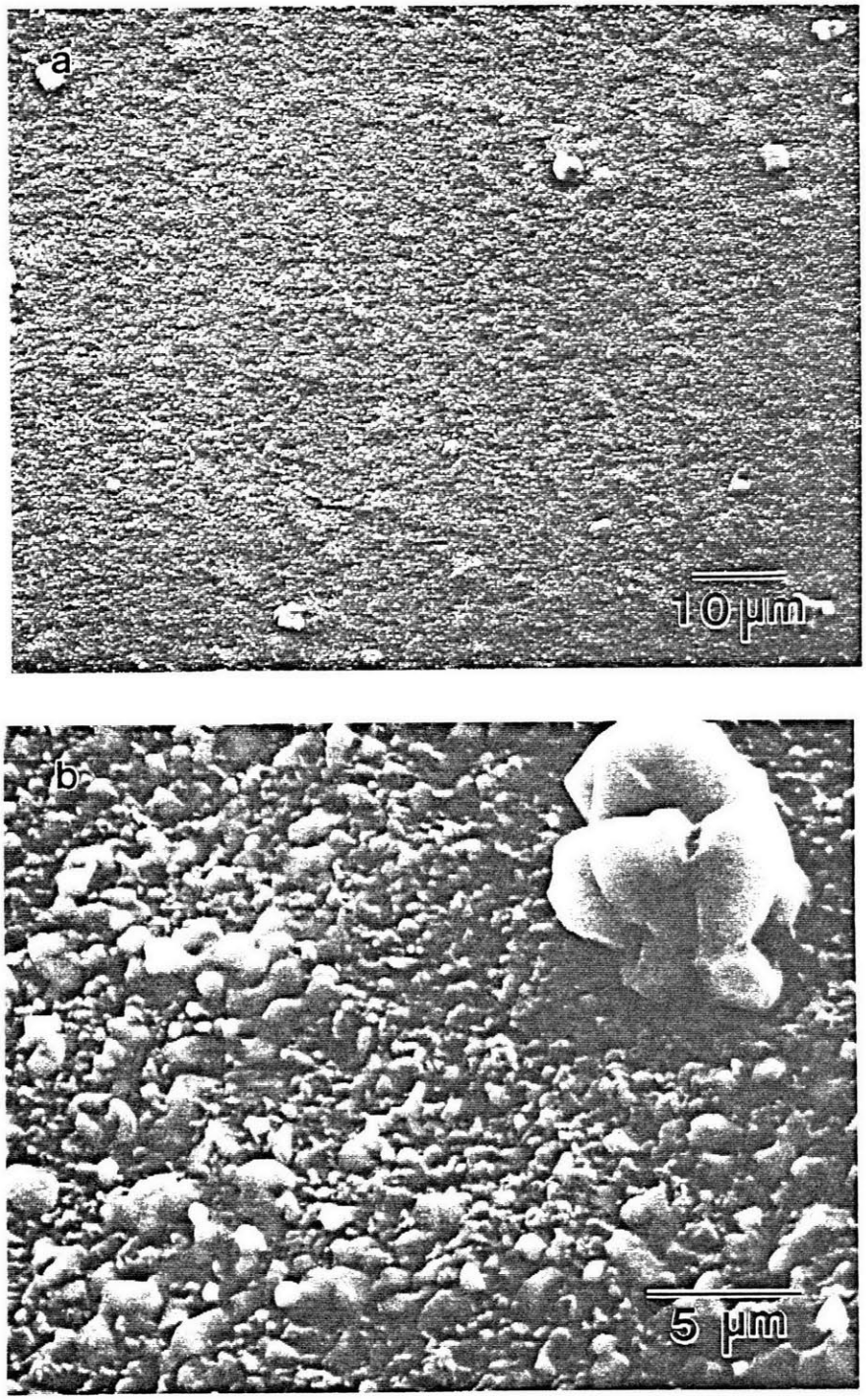

Figure 5.67—SEM secondary electron images of the scale formed on a spray formed Fe-4Cr-4Al-1Ti-0.6B alloy after undergoing 425 thermal oxidation cycles from 1000°C to room temperature: (a) low magnification and (b) high magnification.

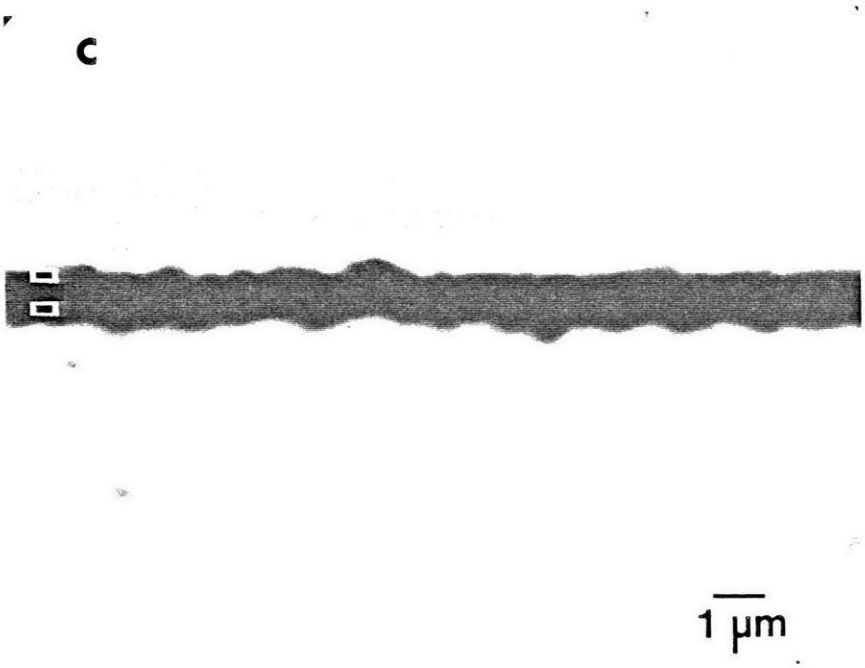

Figure 5.67 Cont.—(c) EPMA back scattered electron image of a cross-section through the scale.

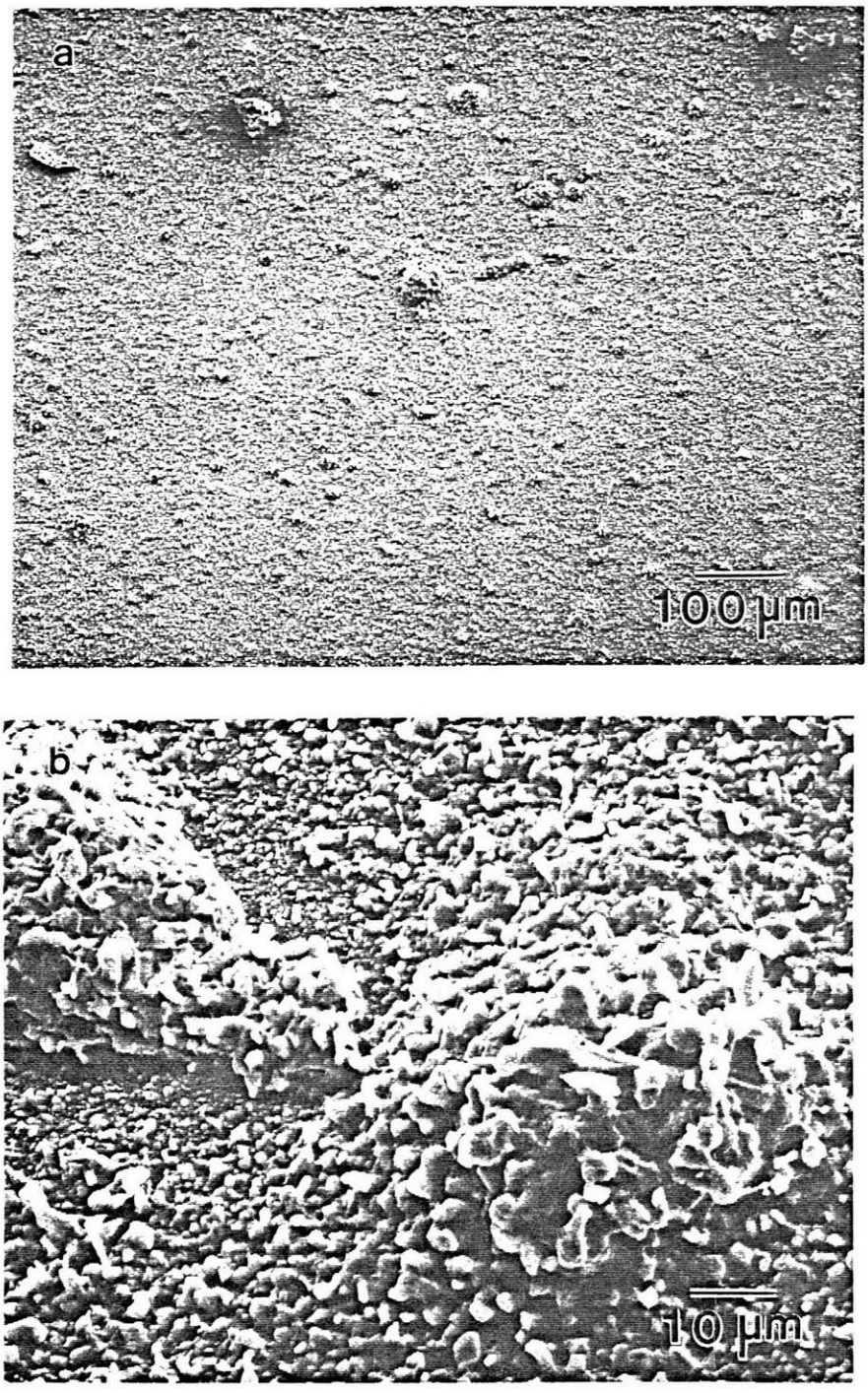

Figure 5.68—SEM secondary electron image of the scale formed on a conventionally processed Fe-4Cr-4Al-1Ti alloy after undergoing 425 thermal oxidation cycles from 1000°C to room temperature: (a) low magnification and (b) high magnification.

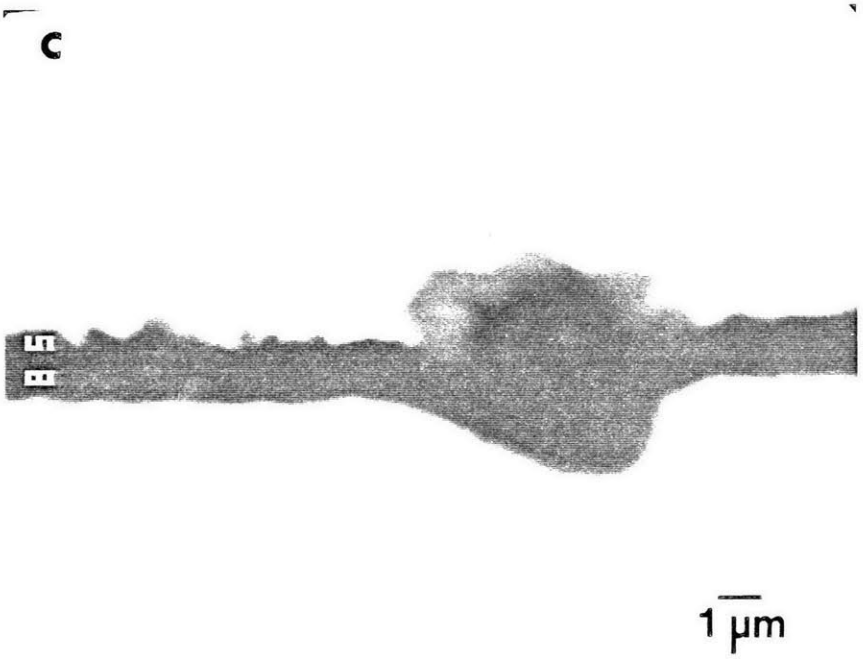

Figure 5.68 Cont.—(c) EPMA back scattered electron image of a cross-section through the scale.

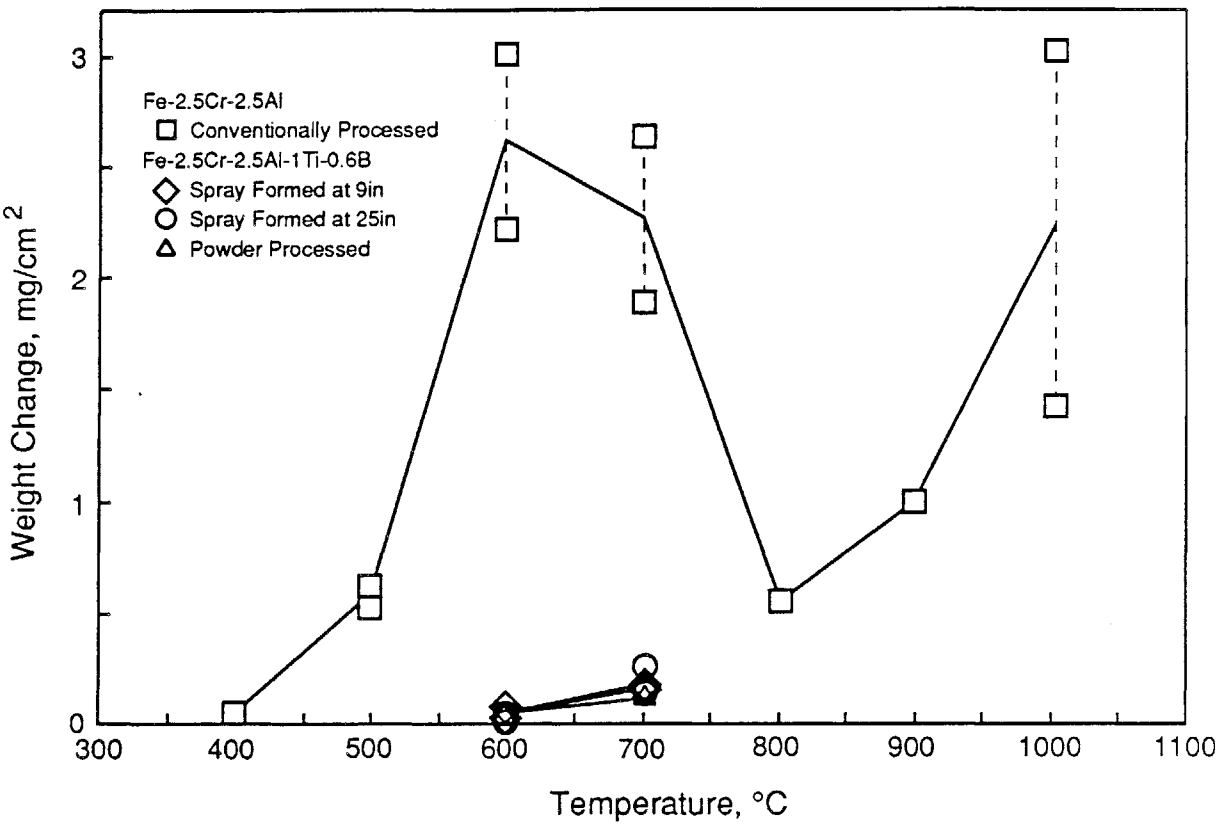

Figure 5.69—Weight gain of conventionally processed Fe-2.5Cr-2.5Al and rapidlly solidified Fe-2.5Cr-2.5Al-1Ti-0.6B alloys after 50h of oxidation after as a function of oxidation temperature.

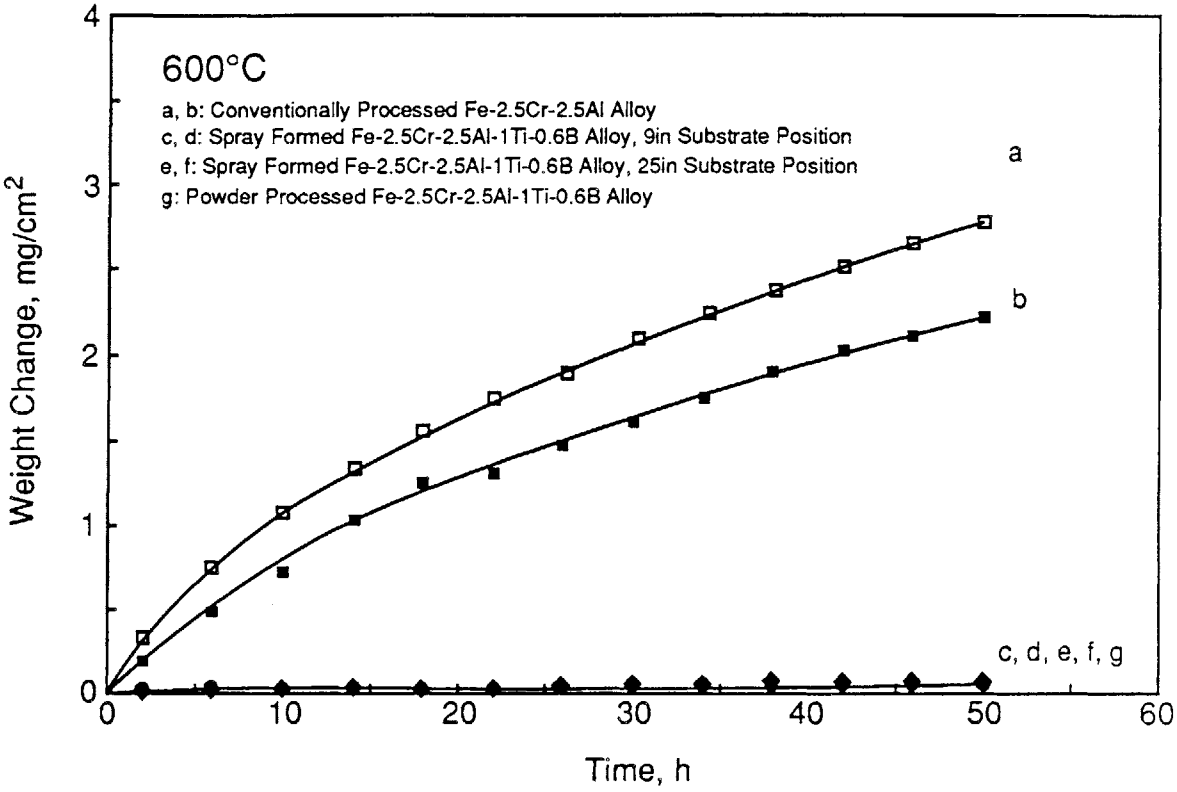

Figure 5.70—Weight change as a function of oxidation time for a conventionally processed Fe-2.5Cr-2.5Al alloy and three rapidly solidified Fe-2.5Cr-2.5Al-1Ti-0.6B alloys oxidized at 600°C.

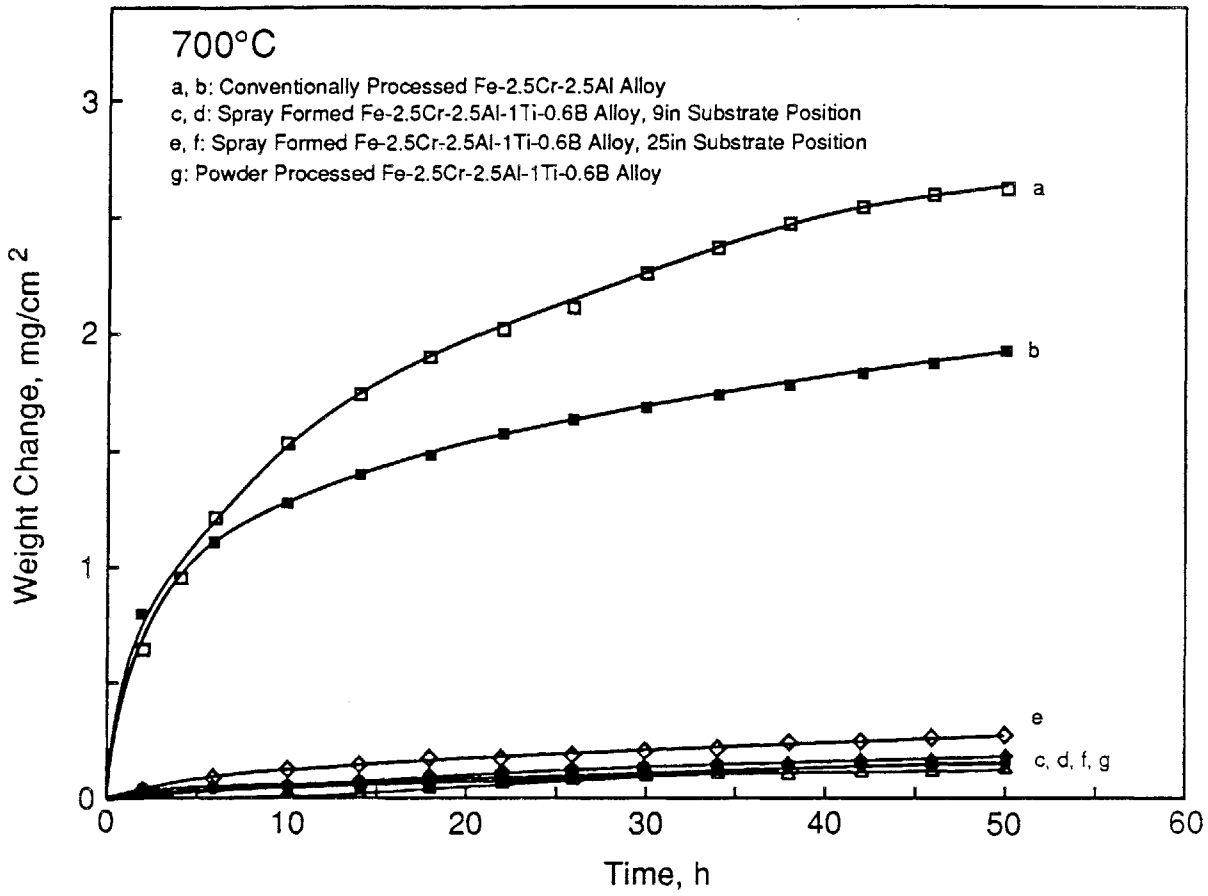

Figure 5.71—Weight change as a function of oxidation time for a conventionally processed Fe-2.5Cr-2.5Al alloy and three rapidly solidified Fe-2.5Cr-2.5Al-1Ti-0.6B alloys oxidized at 700°C.

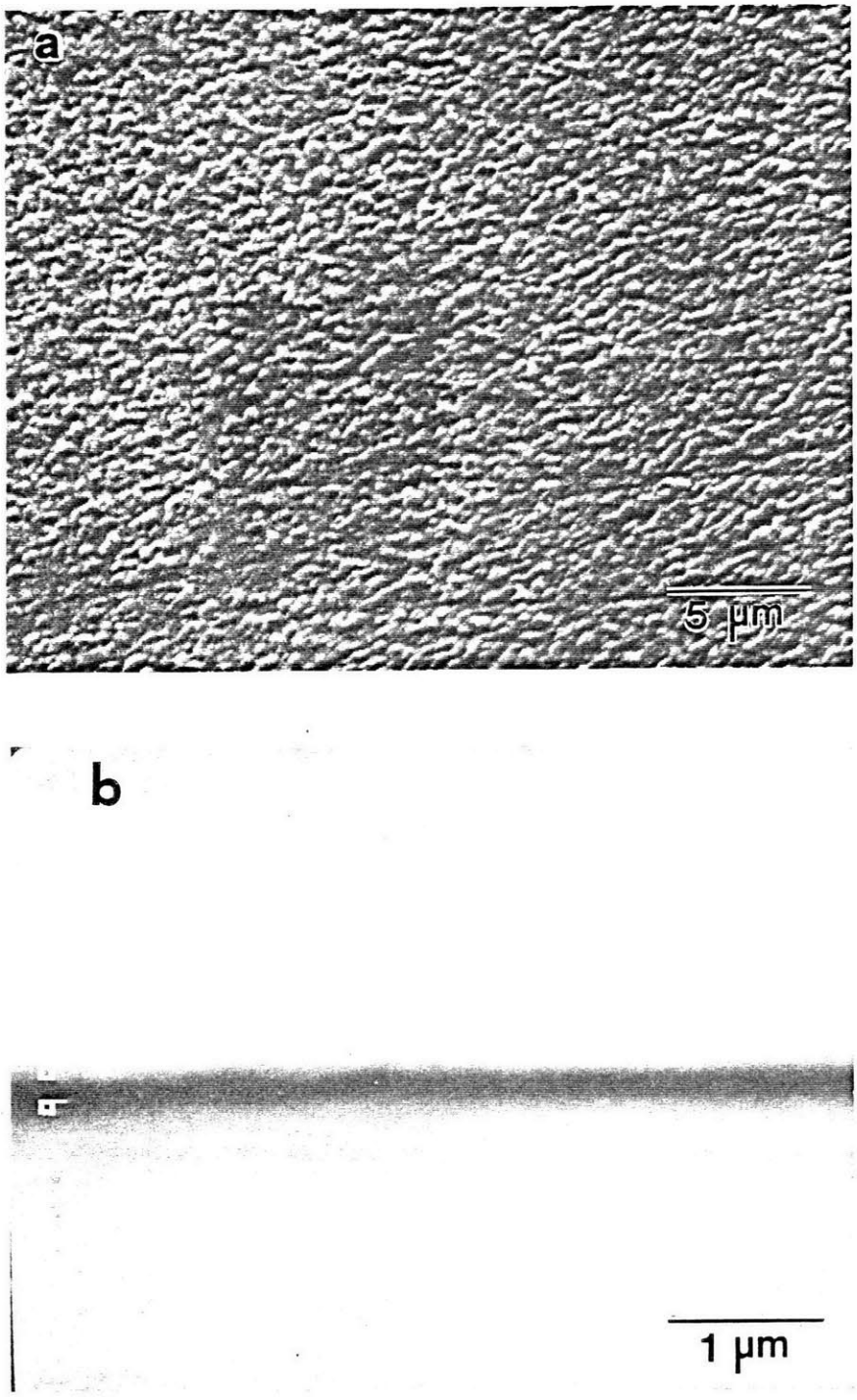

Figure 5.72—Scale formed on a conventionally processed Fe-2.5Cr-2.5Al alloy oxidized at 400°C for 50h: (a) SEM secondary electron image of scale surface and (b) EPMA back scattered electron image of scale cross-section.

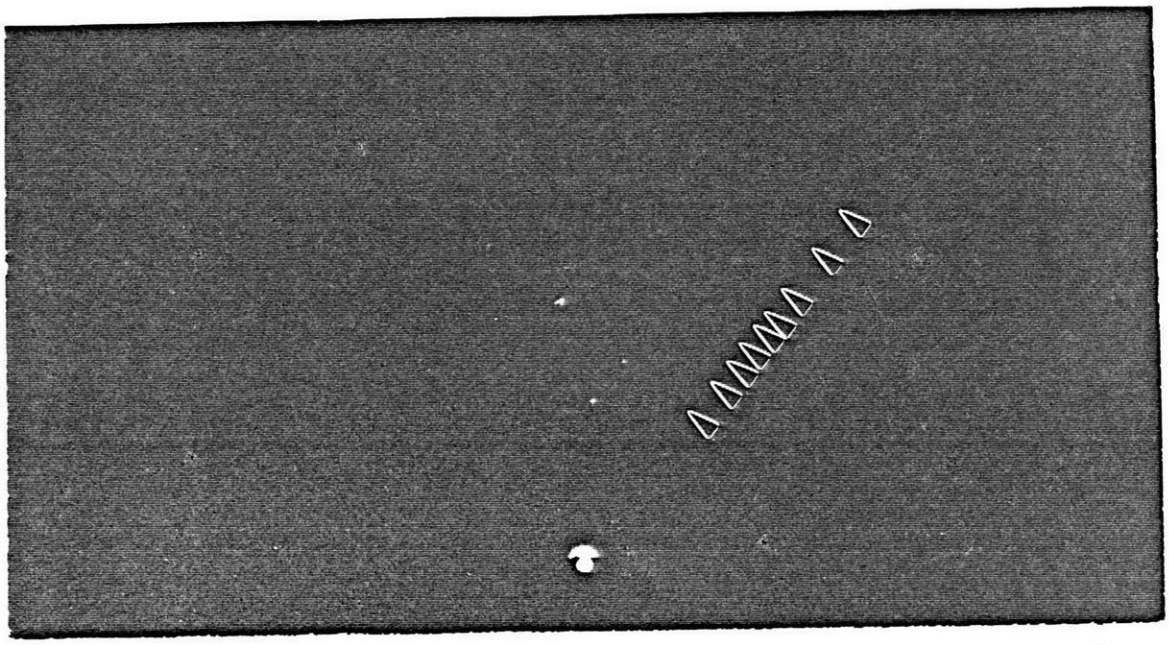

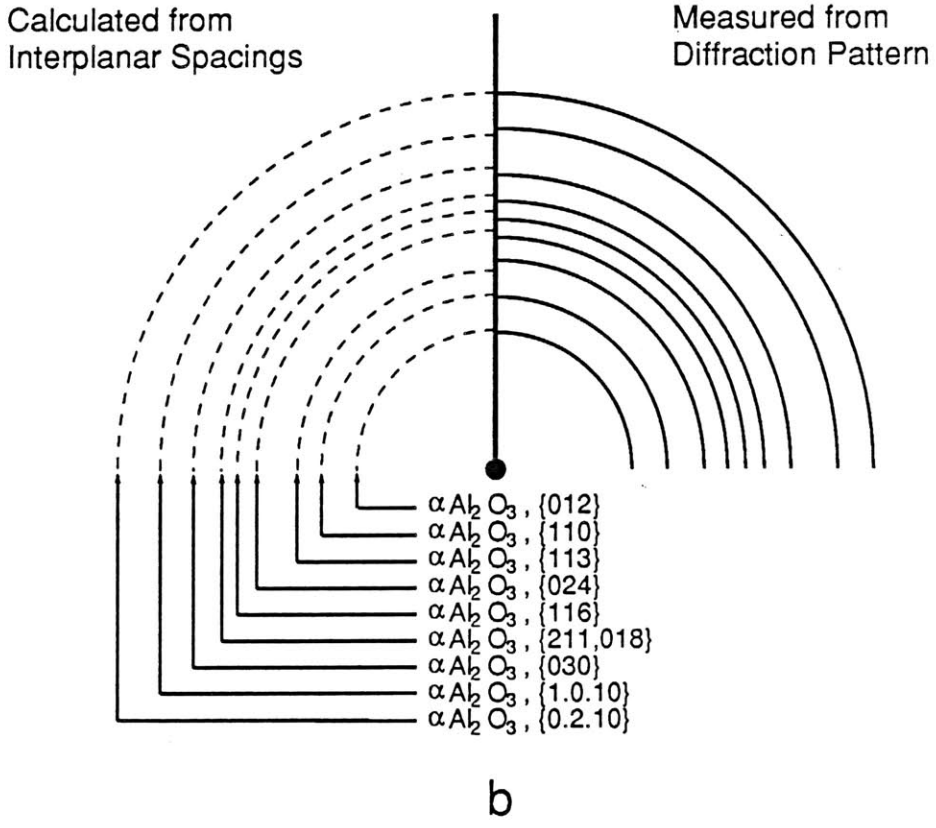

b

Figure 5.73—Reflected high energy electron diffraction pattern from the surface of a conventionally processed Fe-2.5Cr-2.5Al alloy that was oxidized at 400°C for 50h (a) and index of pattern (b).

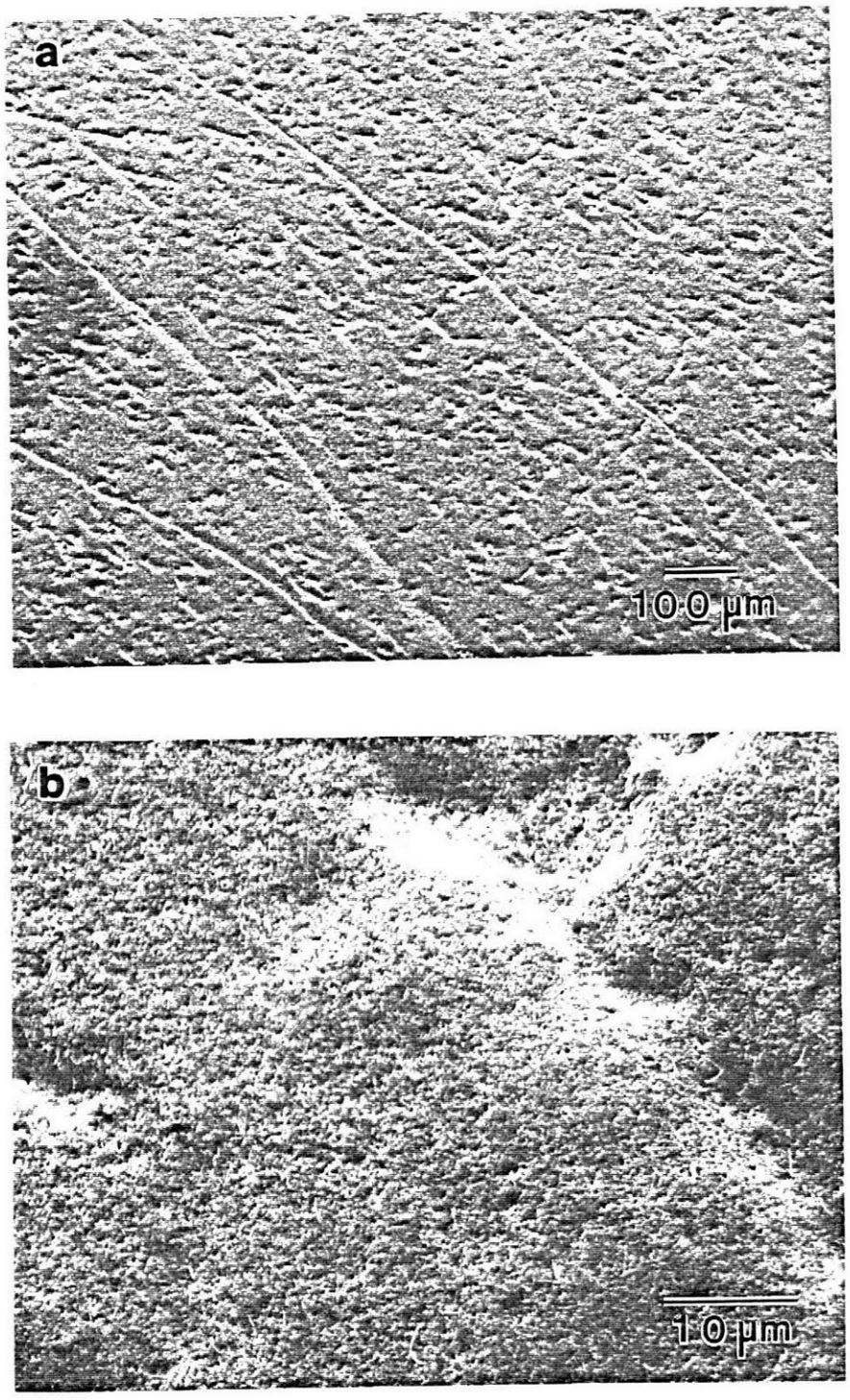

Figure 5.74—SEM secondary electron images of the scale formed on a conventionally processed Fe-2.5Cr-2.5Al alloy oxidized at 500°C for 50h: (a) low magnification and (b) high magnification.

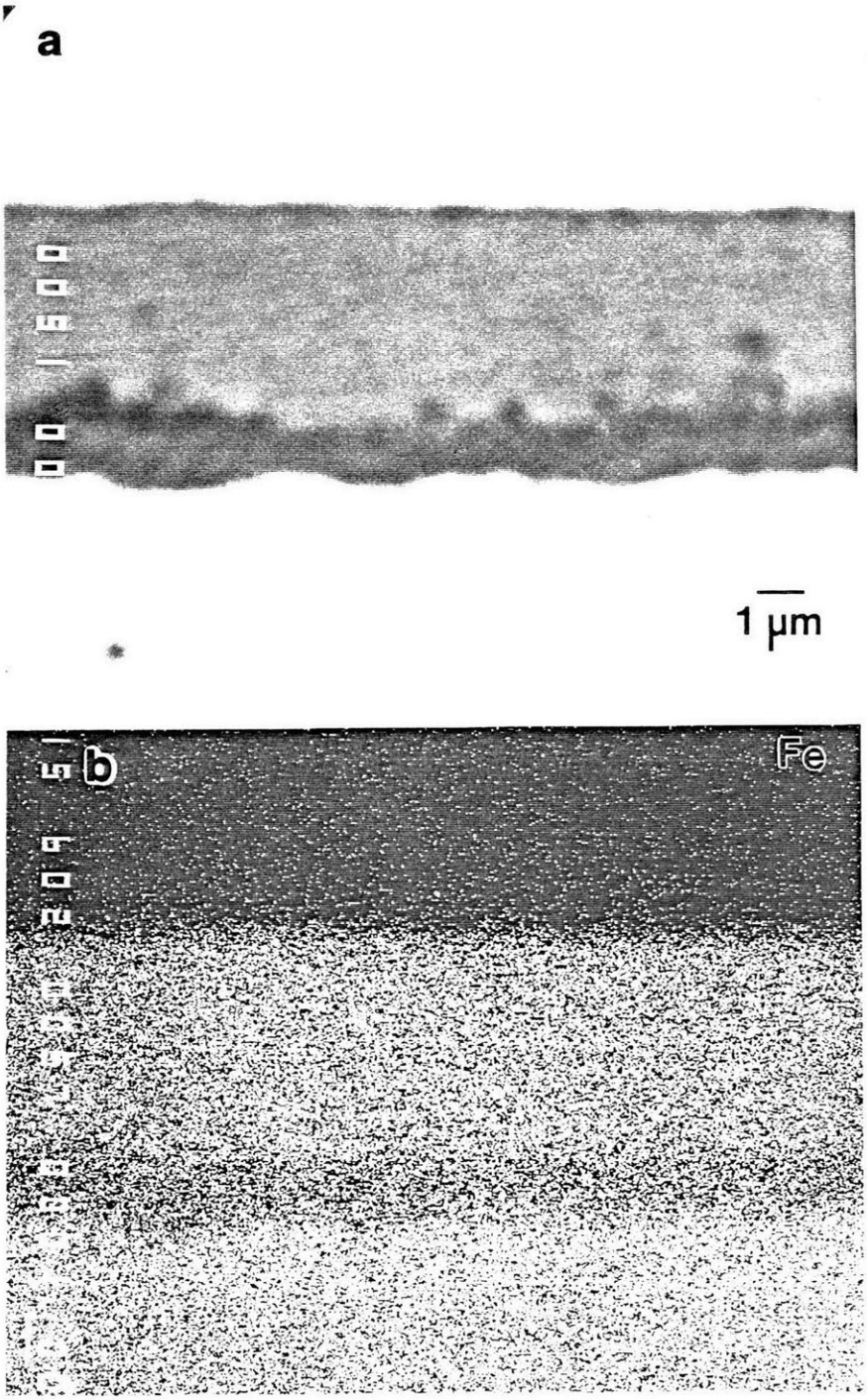

Figure 5.75—EPMA images of a cross-section through the scale shown in Figure 5.74: (a) back scattered electron image and (b) elemental X-ray intensity map for iron.

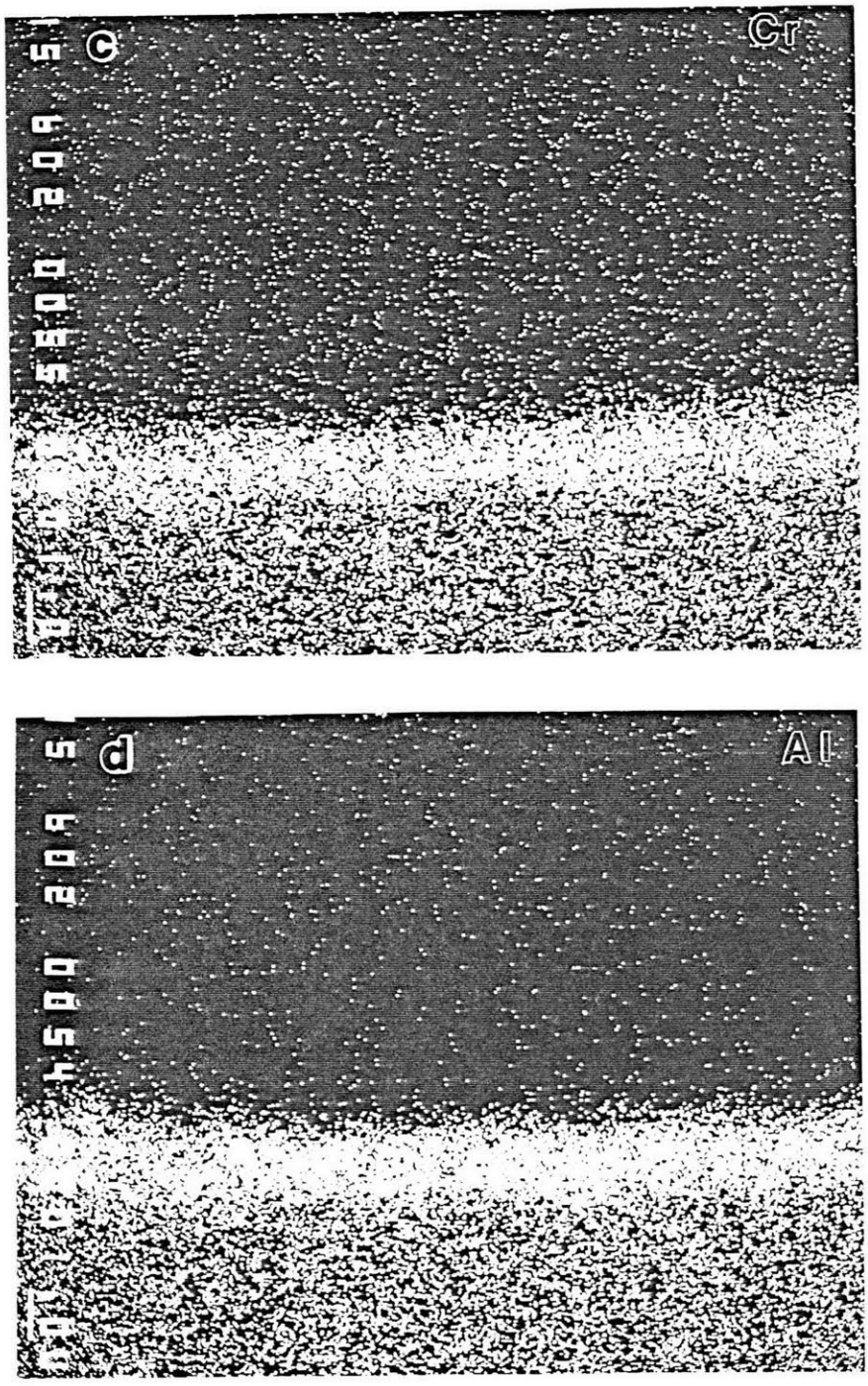

Figure 5.75 Cont.—Elemental X-ray intensity maps for (c) chromium and (d) aluminum.

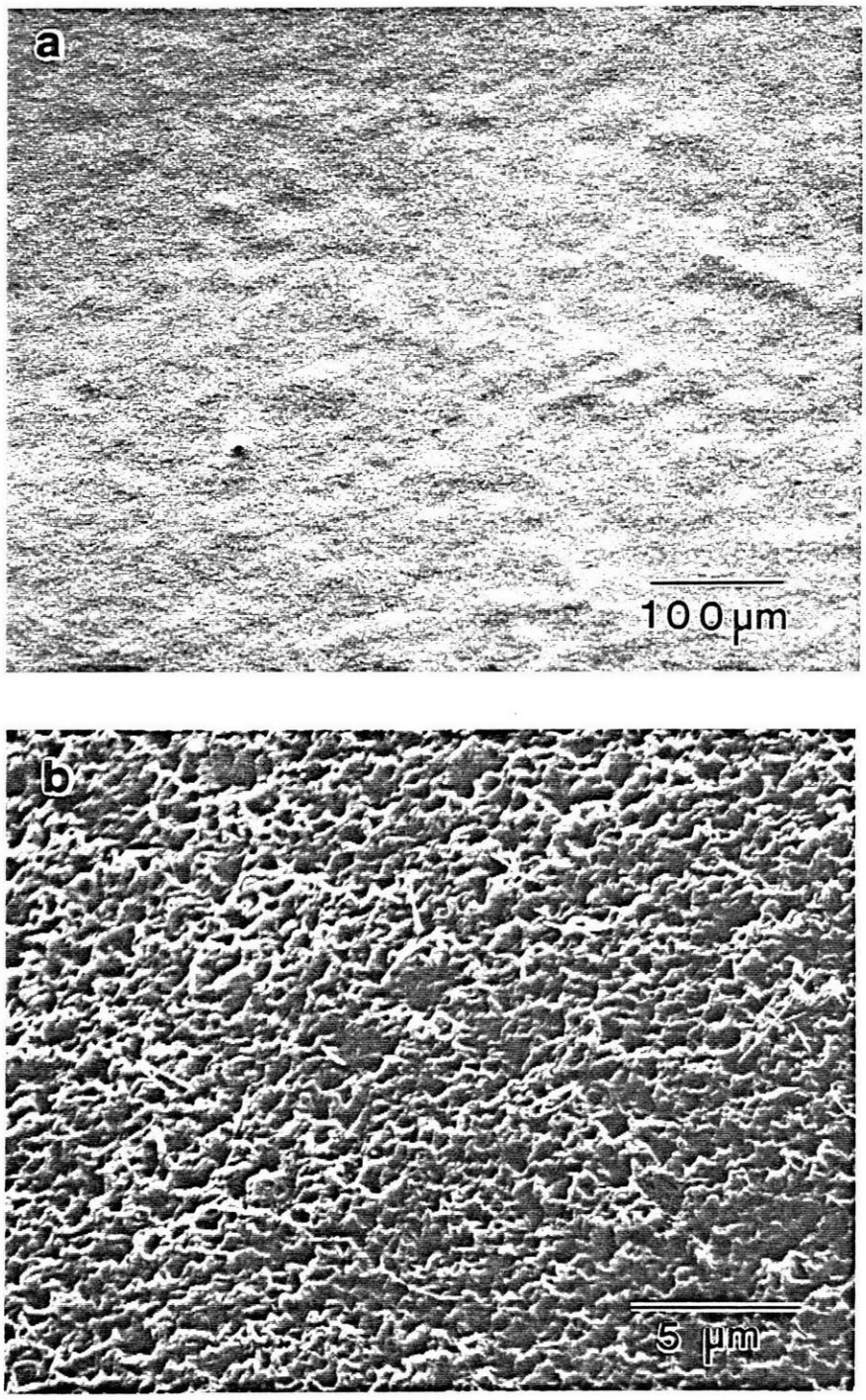

Figure 5.76—SEM secondary electron image of the scale formed on a conventionally processed Fe-2.5Cr-2.5Al alloy oxidized at 600°C for 50h: (a) low magnification and (b) high magnification.

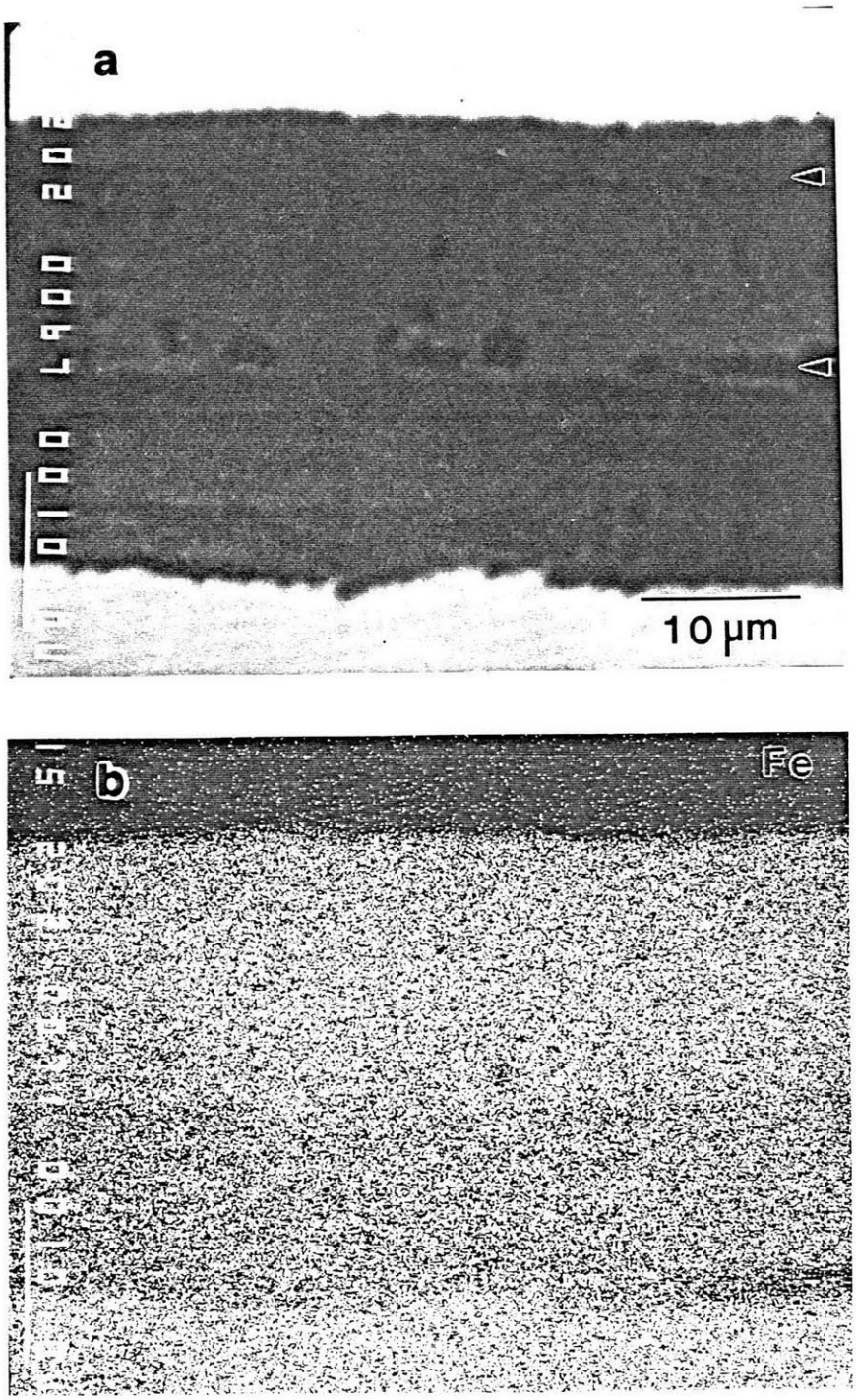

Figure 5.77—EPMA images of a cross-section through the scale shown in Figure 5.76: (a) back scattered electron image and (b) elemental X-ray intensity map for iron.

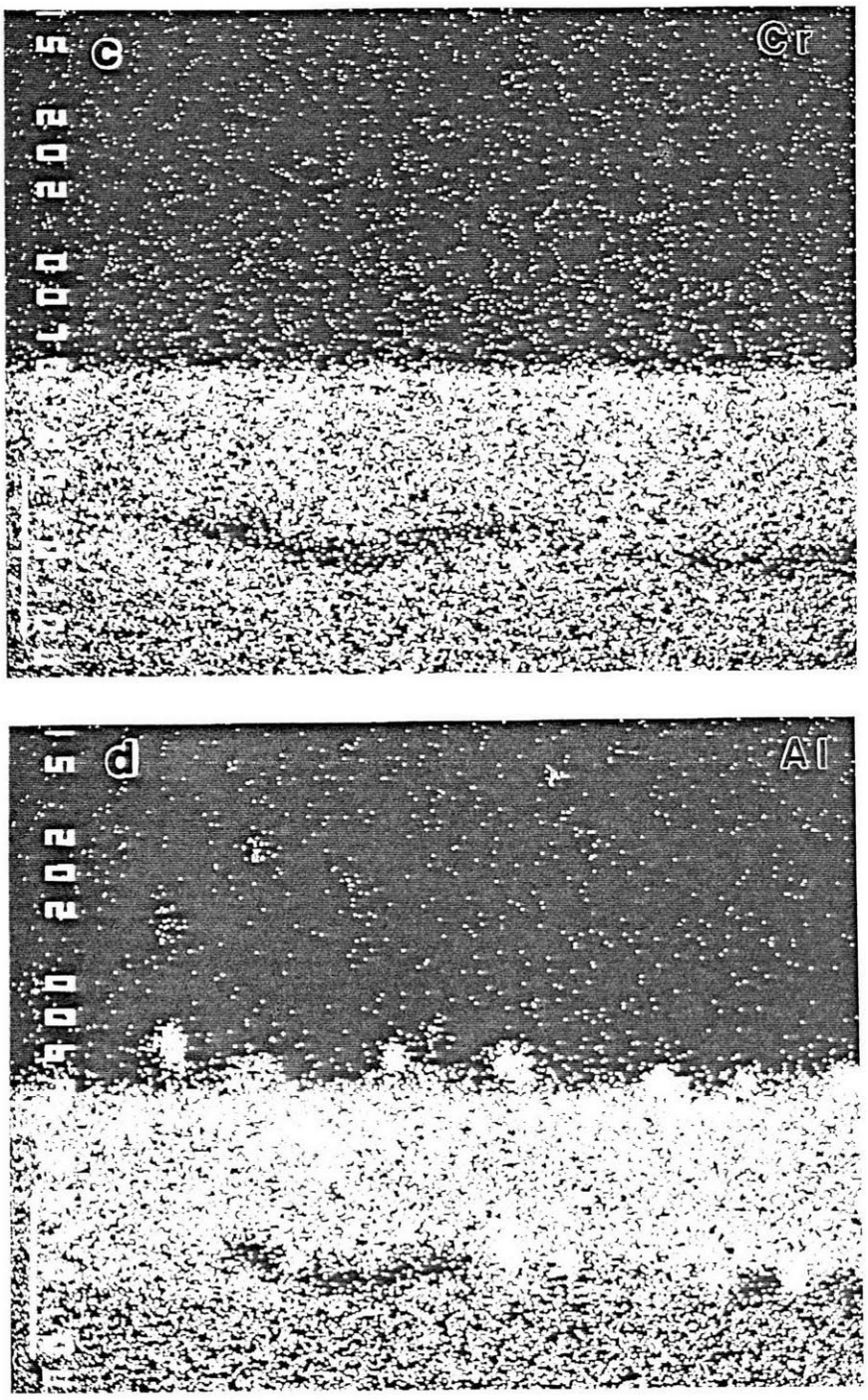

Figure 5.77 Cont.—Elemental X-ray intensity maps for (c) chromium and (d) aluminum.

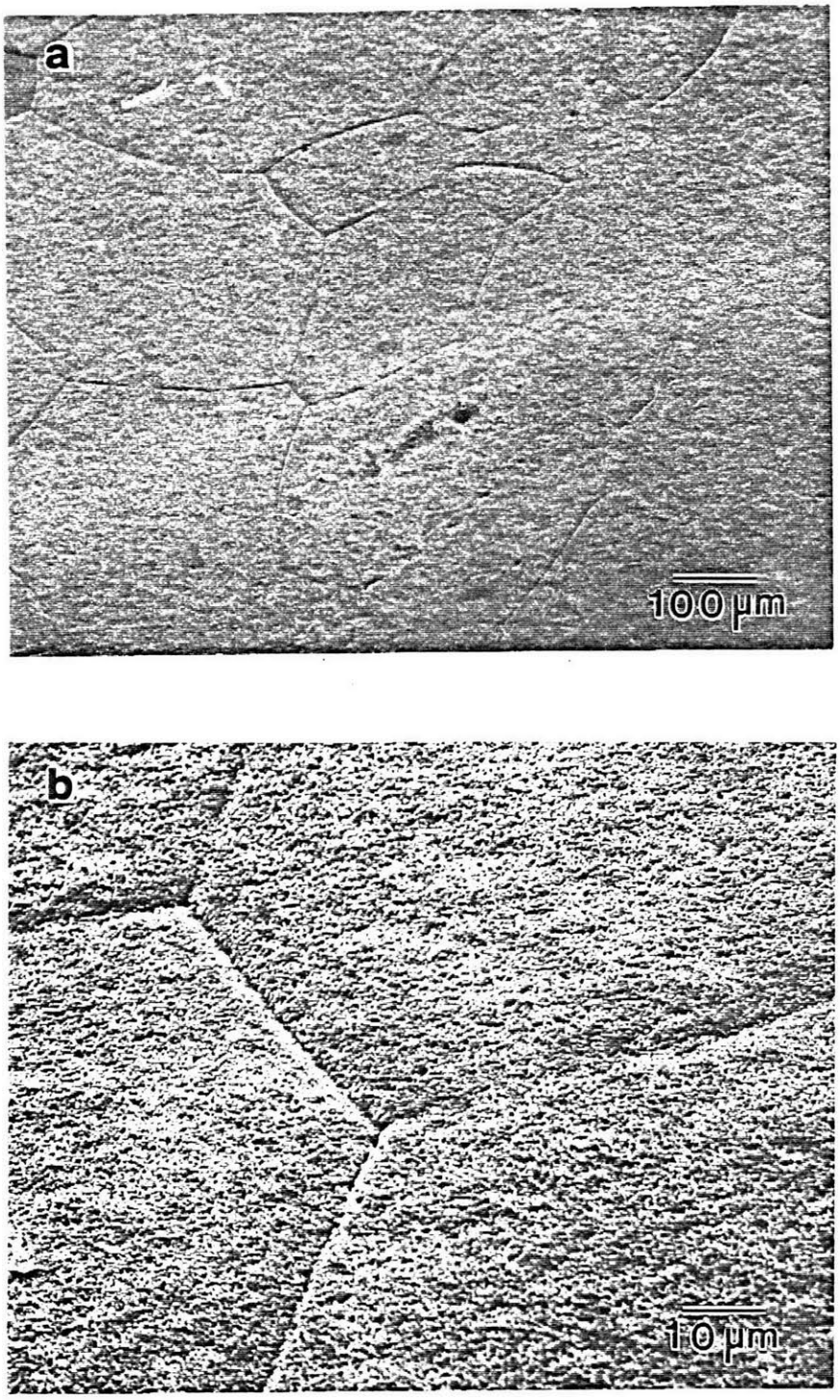

Figure 5.78—SEM secondary electron image of the scale formed on a conventionally processed Fe-2.5Cr-2.5Al alloy oxidized at 700°C for 50h: (a) low magnification and (b) high magnification.

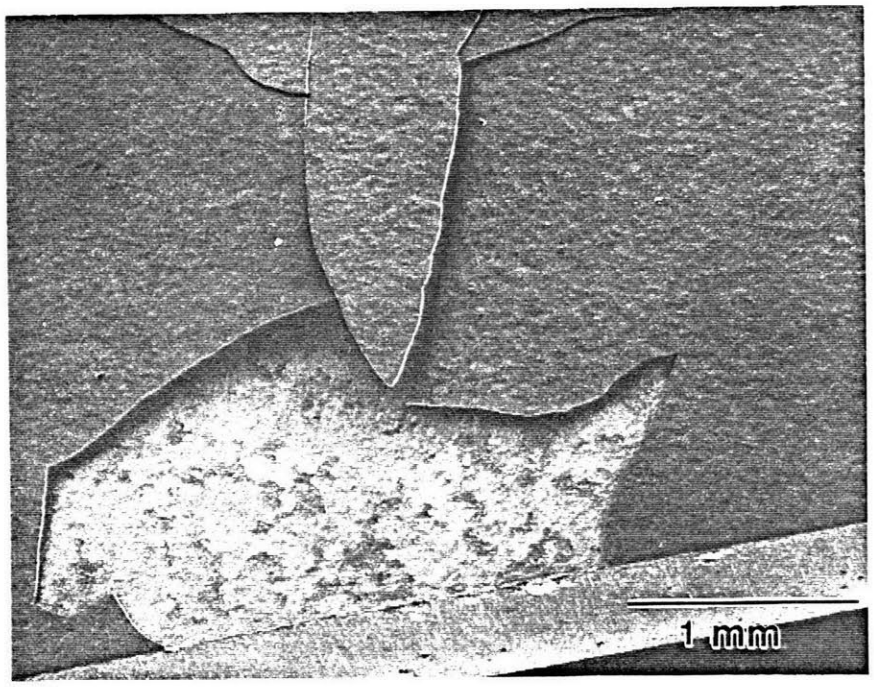

Figure 5.78 Cont.—(c) SEM secondary electron image of spalled scale on a conventionally processed Fe-2.5Cr-2.5Al alloy oxidized at 700°C for 50h.

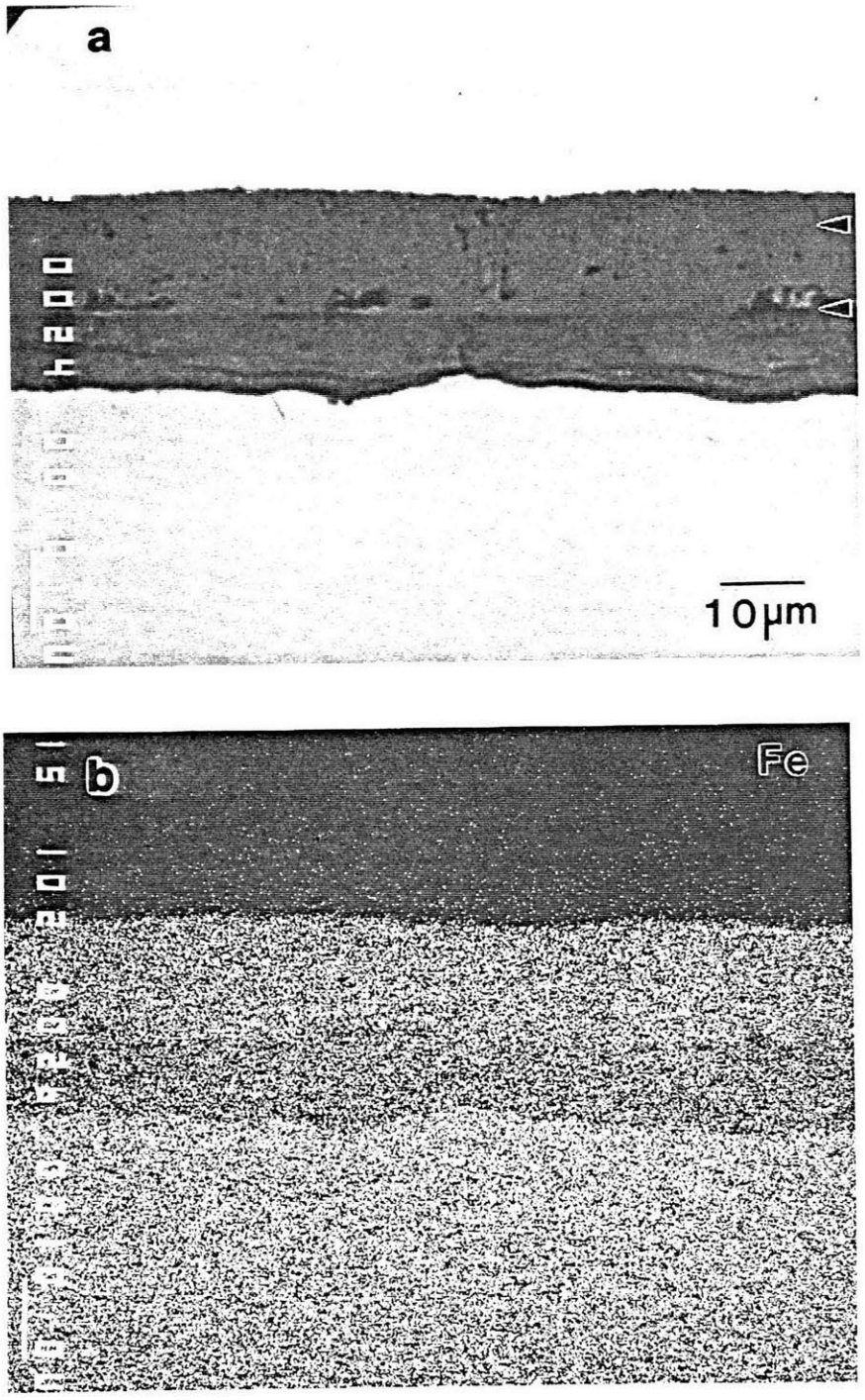

Figure 5.79—EPMA images of a sross-section through the scale shown in Figure 5.78: (a) back scattered electron image and (b) elemental X-ray intensity map for iron.

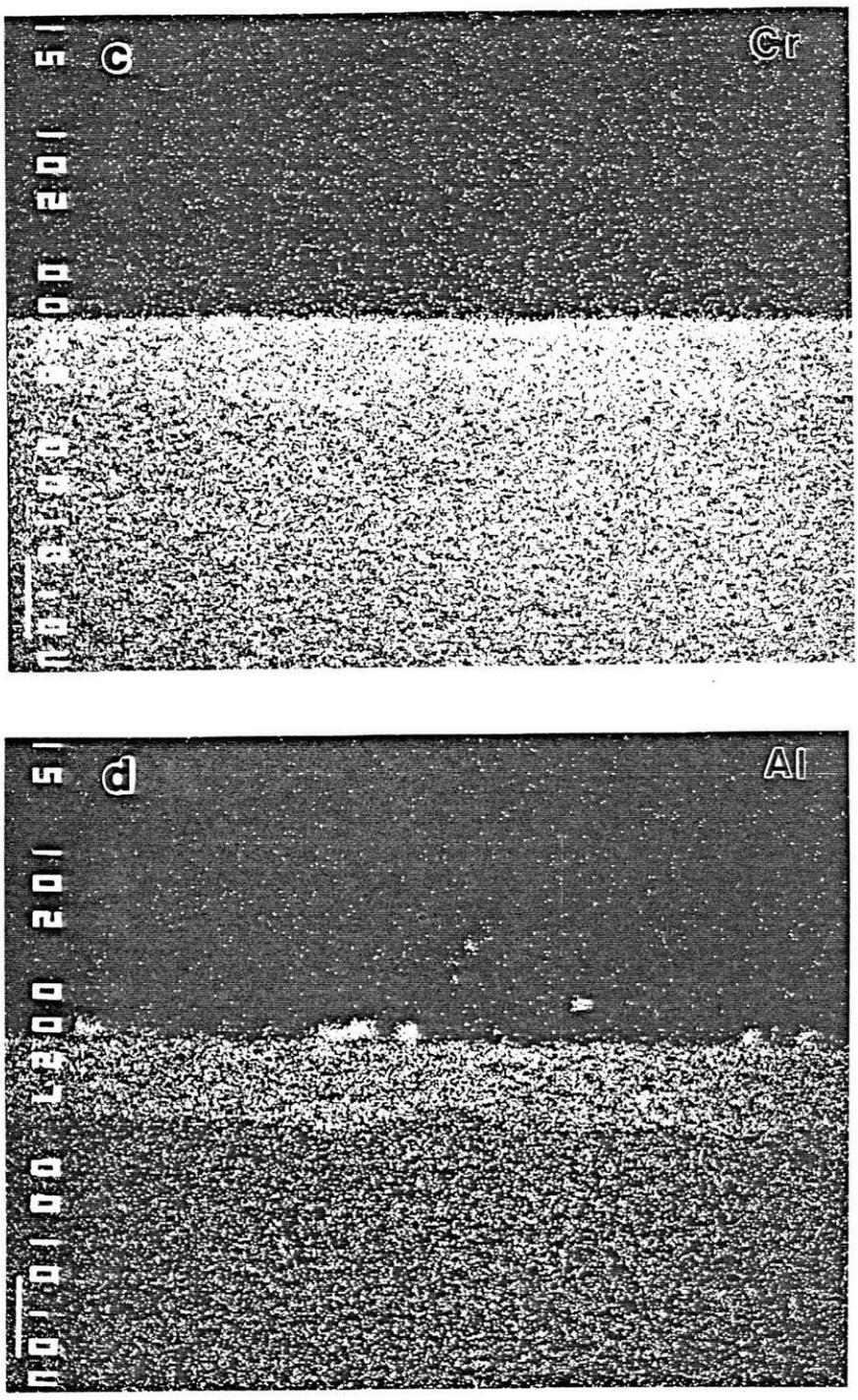

Figure 5.79 Cont.—Elemental X-ray intensity maps for (c) chromium and (d) aluminum.

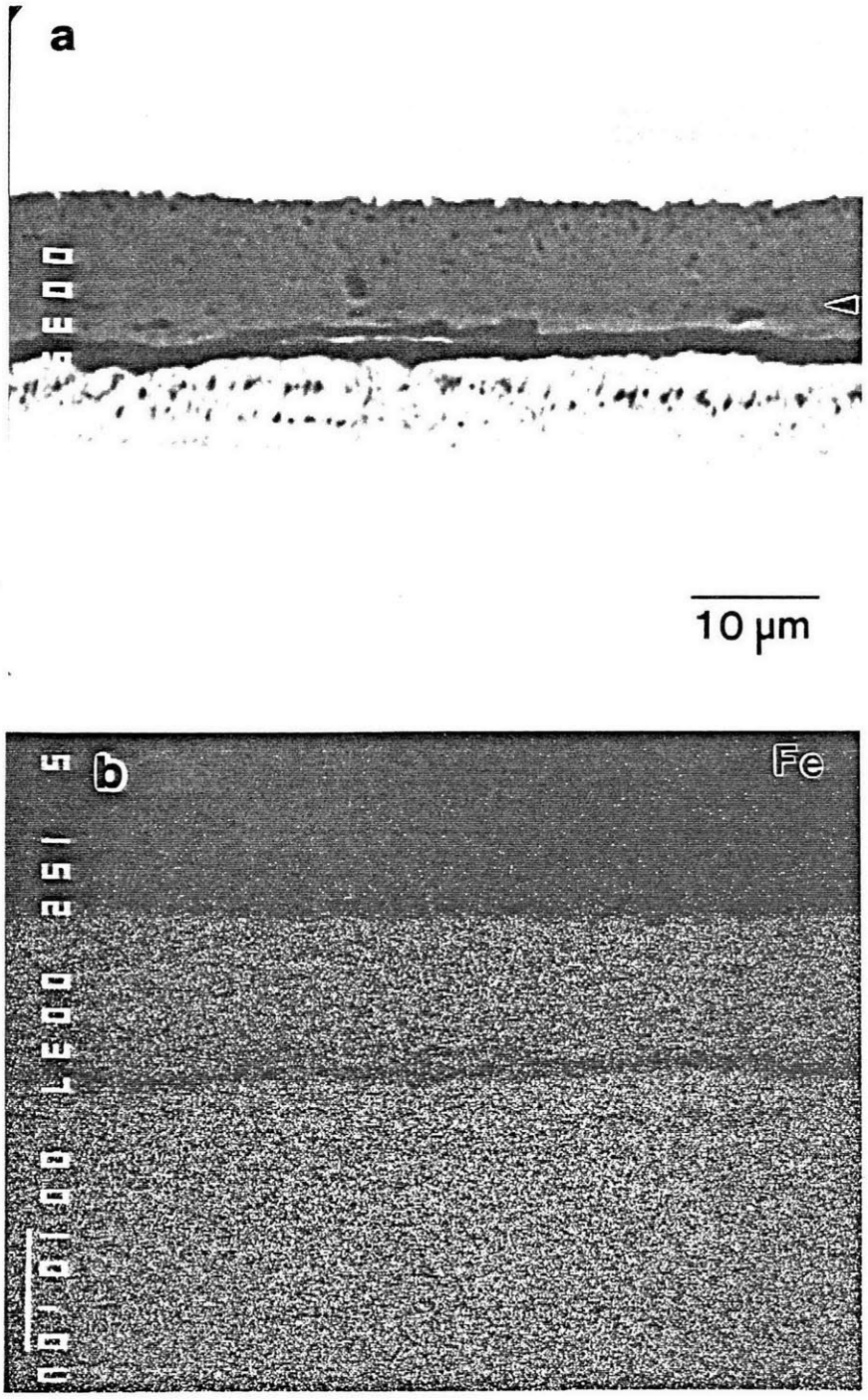

Figure 5.80—EPMA images of a cross-section through the scale shown in Figure 5.78: (a) back scattered electron image and (b) elemental X-ray intensity map for iron.

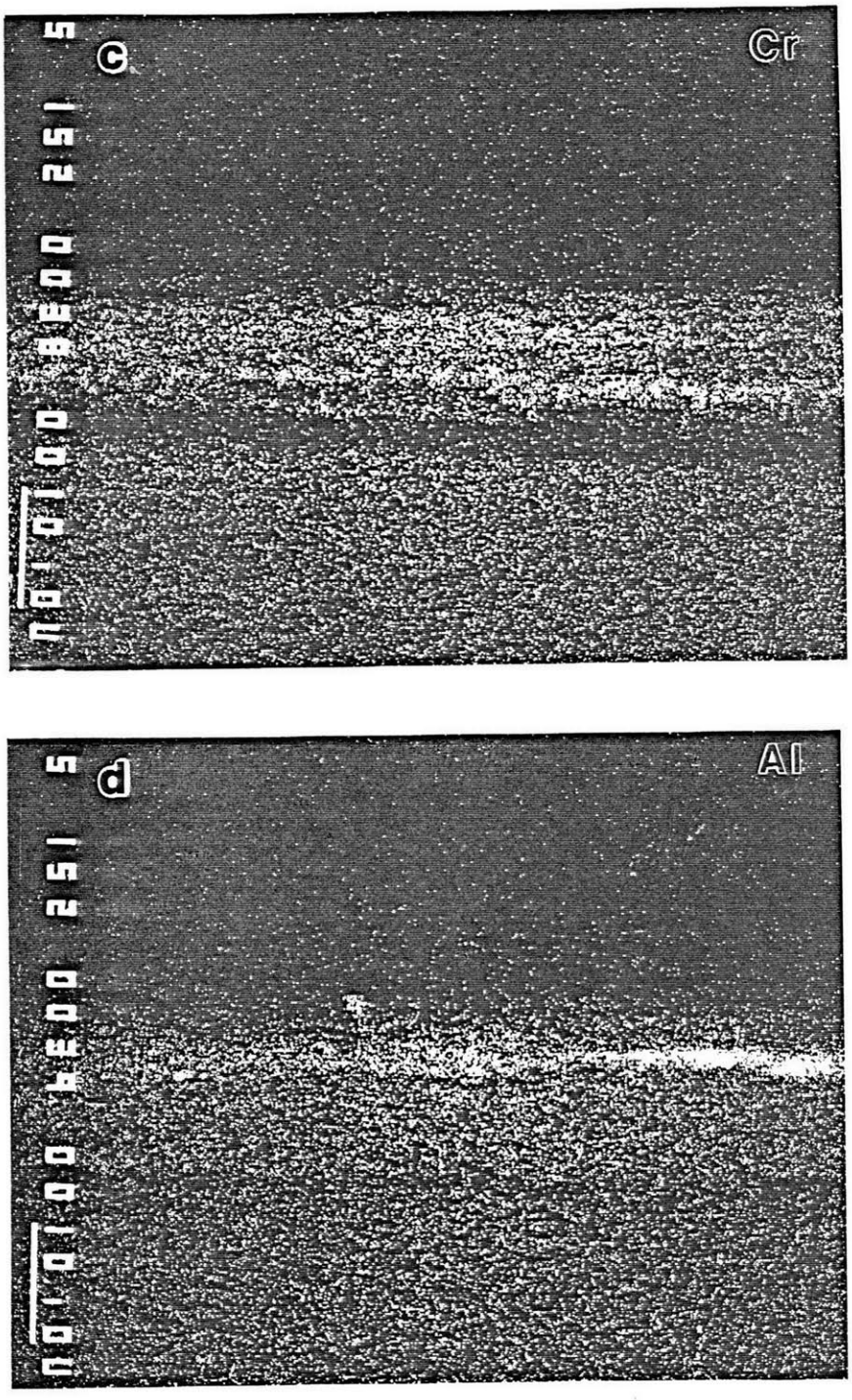

Figure 5.80 Cont.—Elemental X-ray intensity maps for (c) chromium and (d) aluminum.

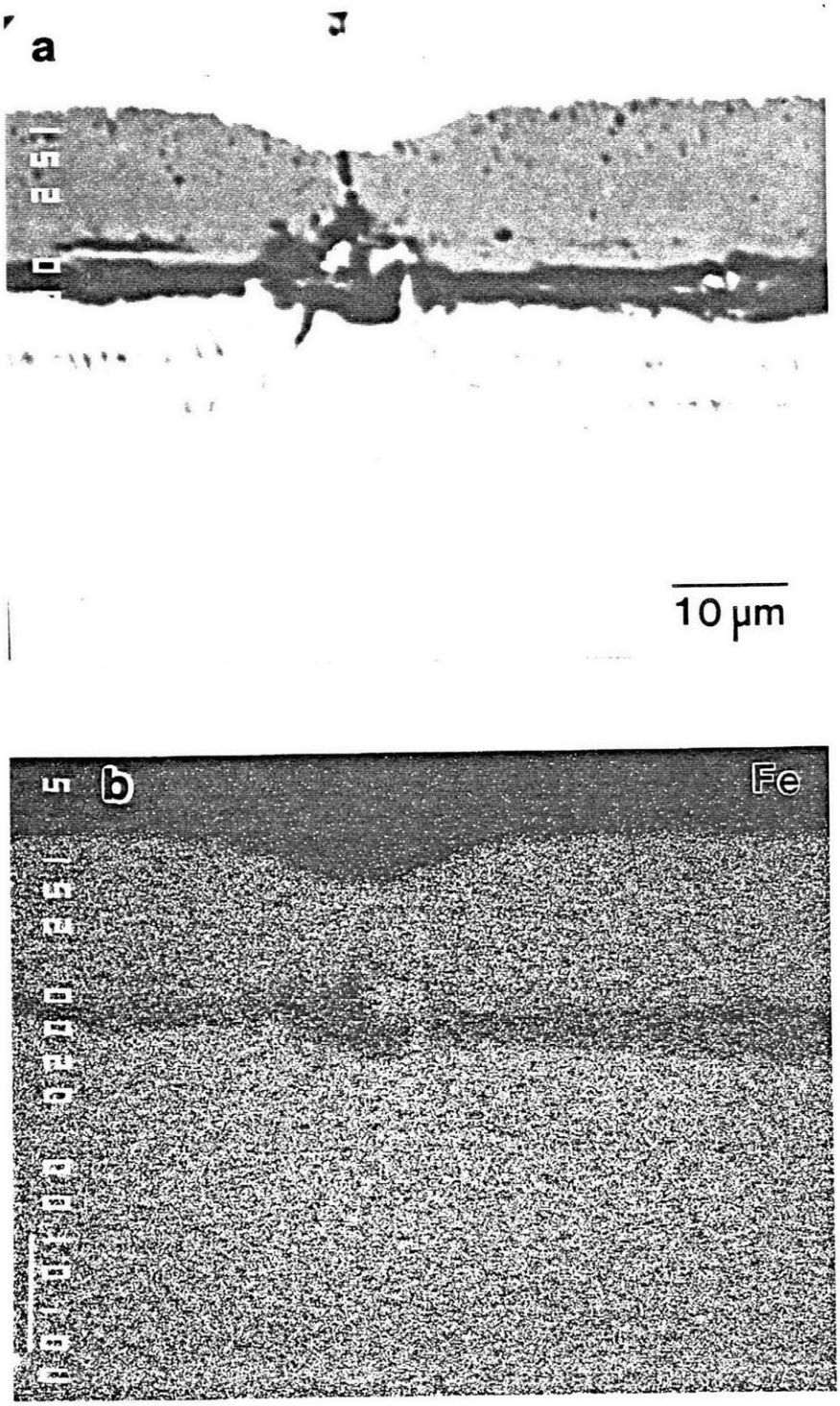

Figure 5.81—EPMA images of a cross-section through the scale shown in Figure 5.78: (a) back scattered electron image and (b) elemental X-ray intensity map for iron.

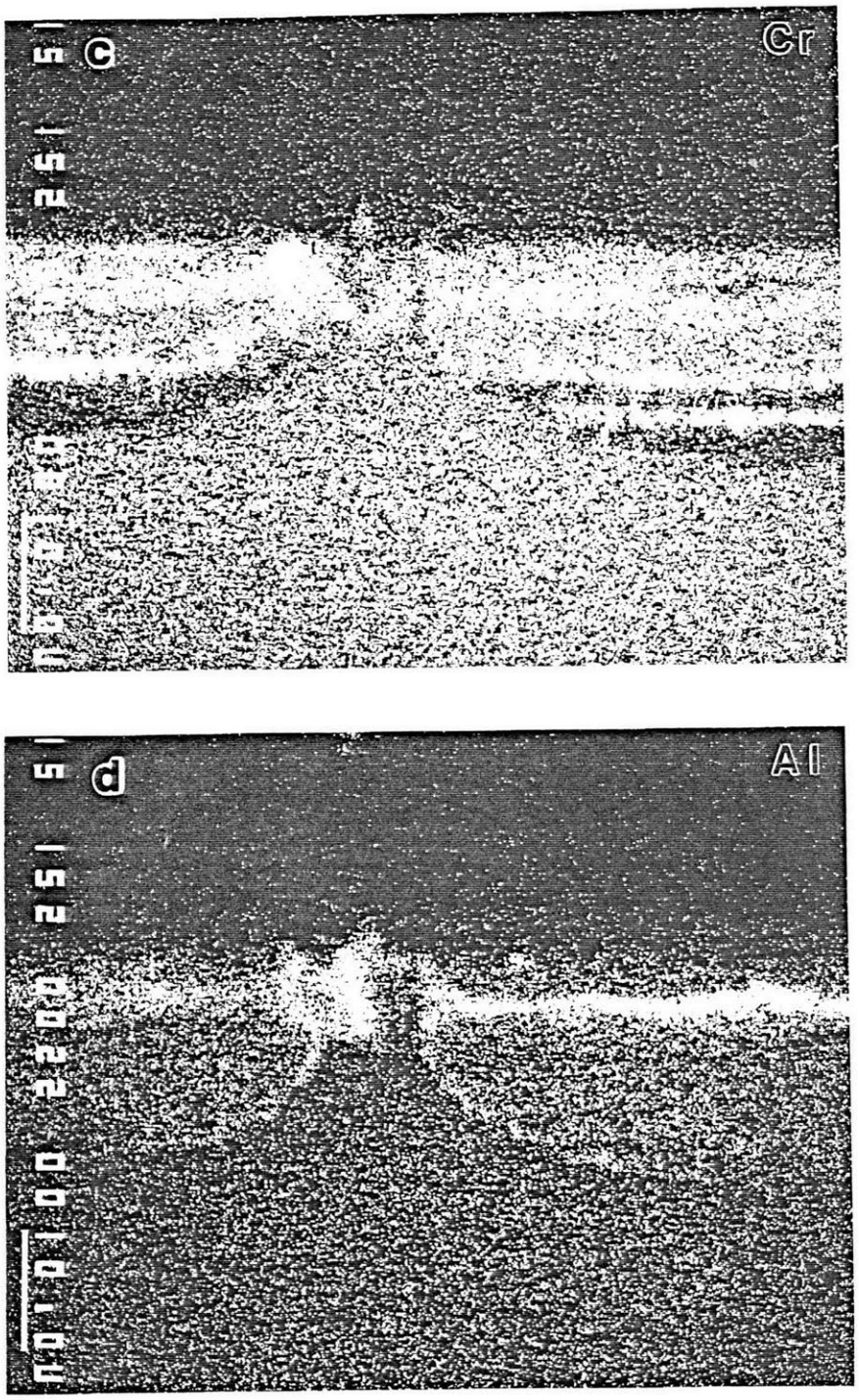

Figure 5.81 Cont.—Elemental X-ray intensity maps for (c) chromium and (d) aluminum.

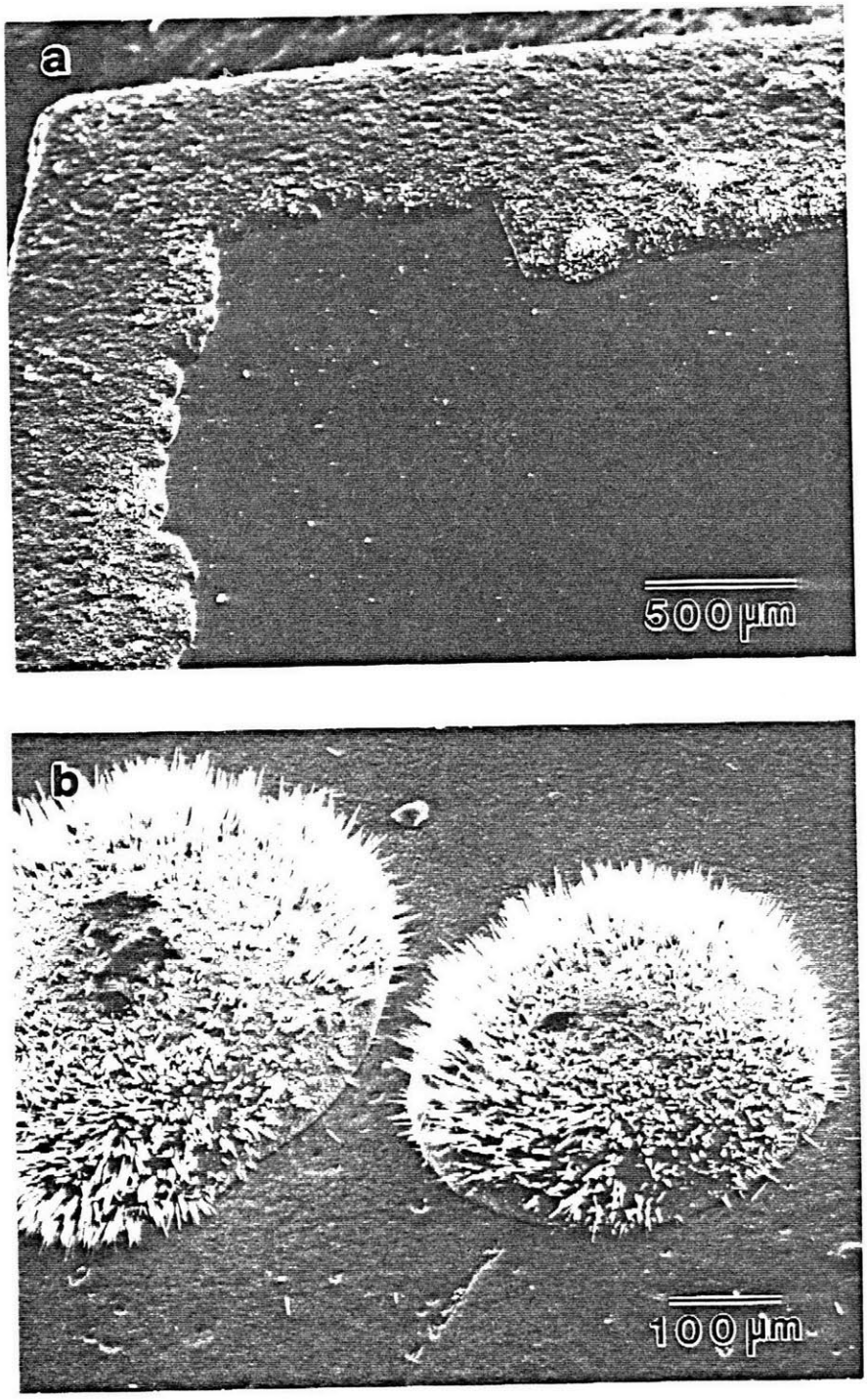

Figure 5.82—SEM secondary electron image of the scale formed on a conventionally processed Fe-2.5Cr-2.5Al alloy oxidized at 800°C for 50h: (a) low magnification and (b) high magnification.

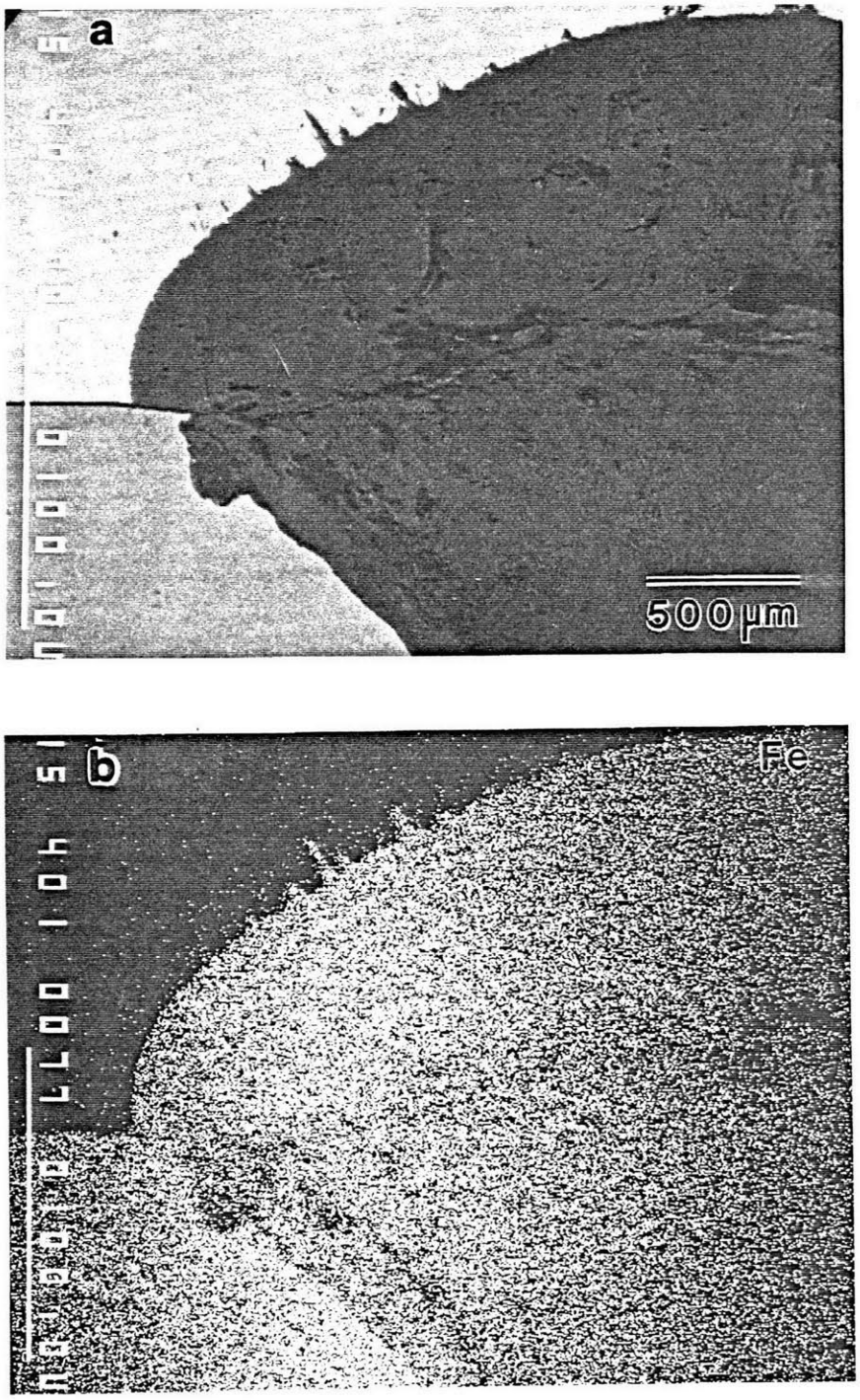

Figure 5.83—EPMA images of a nodule formed on the alloy shown in Figure 5.82: (a) back scattered electron image and (b) elemental X-ray intensity map for iron.

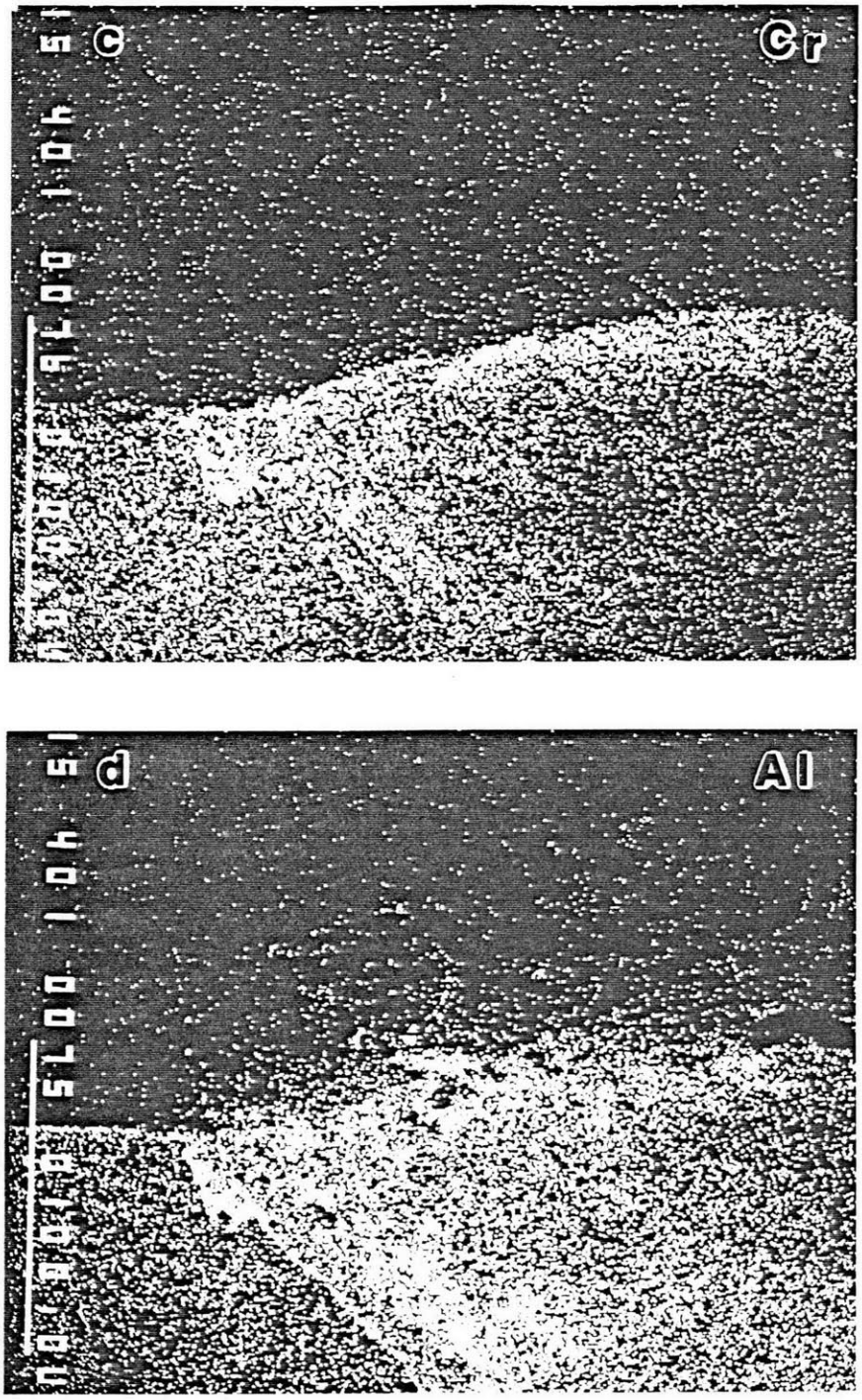

Figure 5.83 Cont.—Elemental X-ray intensity maps for (c) chromium and (d) aluminum.

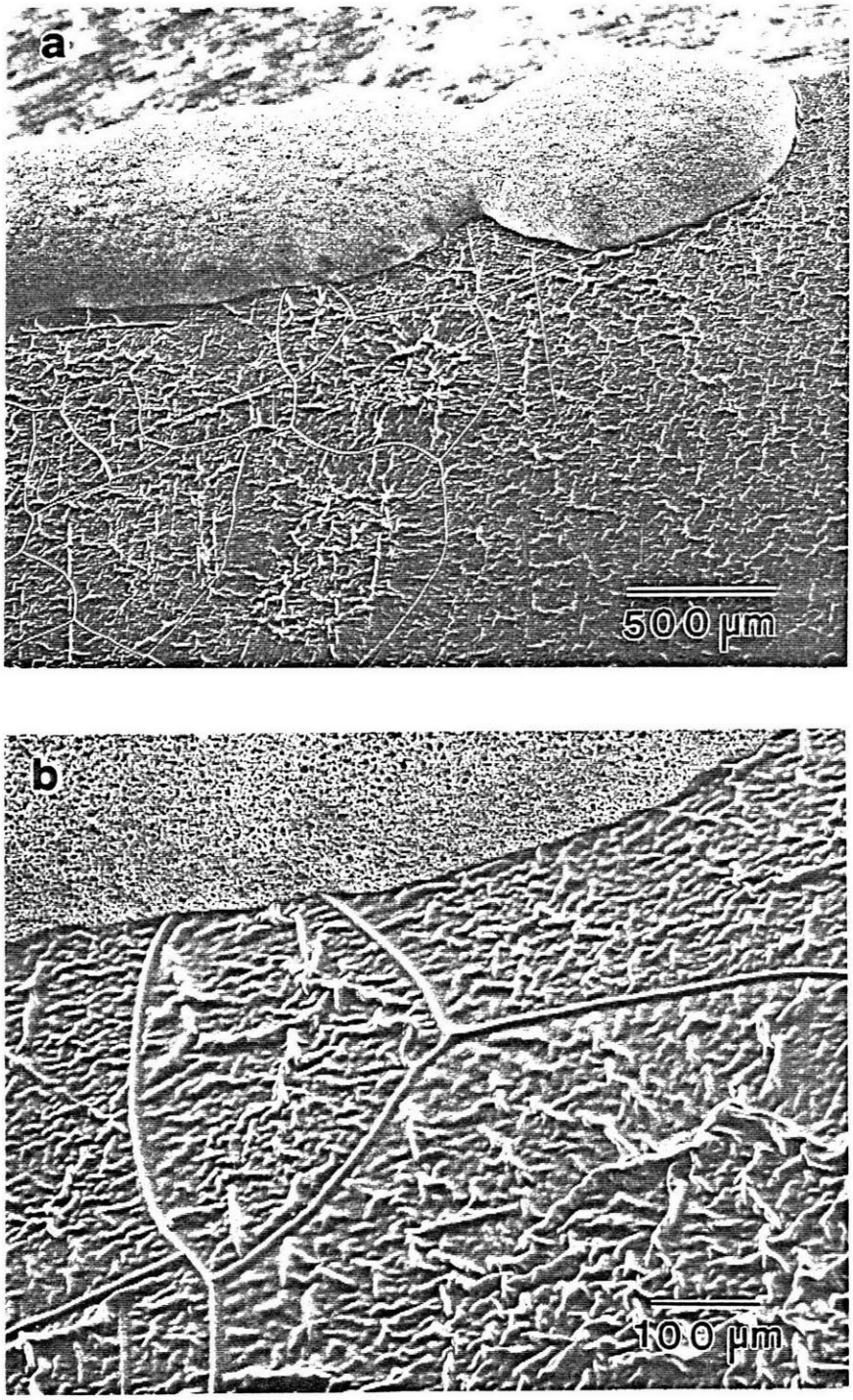

Figure 5.84—SEM secondary electron images of the scale formed on a conventionally processed Fe-2.5Cr-2.5Al alloy oxidized at 900°C for 50h: (a) low magnification and (b) high magnification.

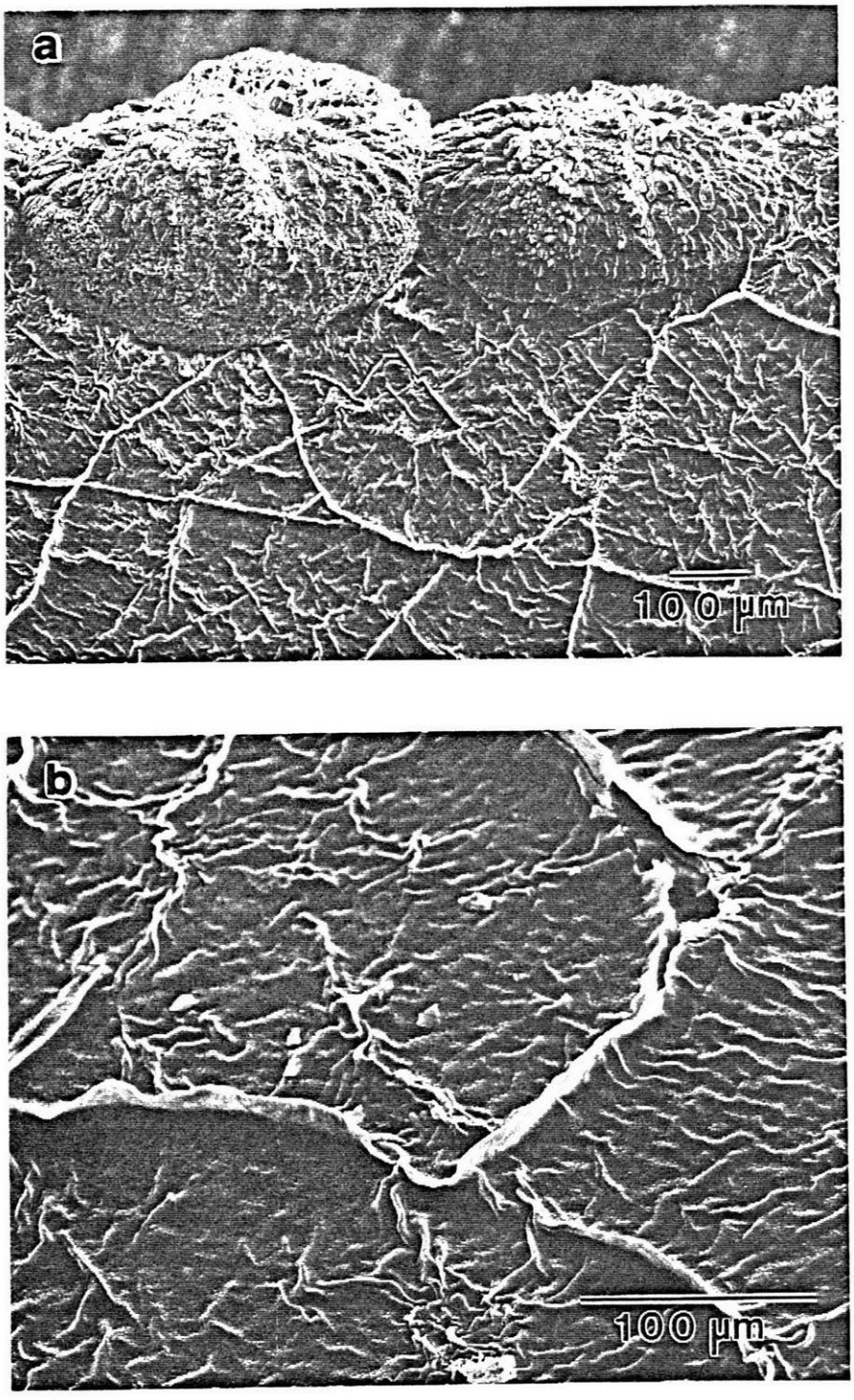

Figure 5.85—SEM secondary electron image of the scale formed on a conventionally processed Fe-2.5Cr-2.5Al alloy oxidized at 1000°C for 50h: (a) low magnification and (b) high magnification.

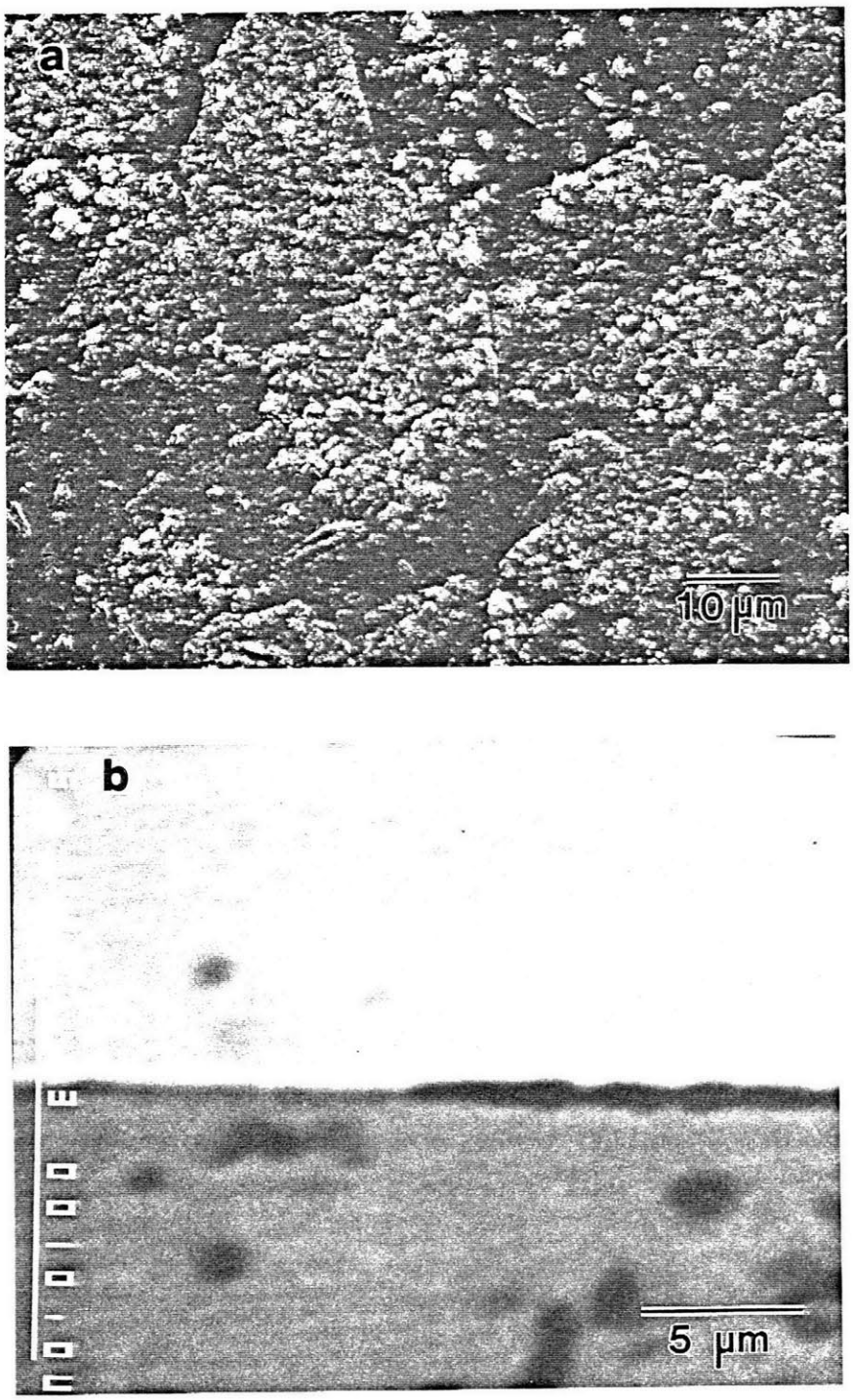

Figure 5.86—Scale formed on an Fe-2.5Cr-2.5Al-1Ti-0.6B alloy spray formed at a 0.23m (9in) substrate distance after oxidation at 600°C for 50h: (a) SEM secondary electron image of scale surface and (b) EPMA back scattered electron image of scale cross-section.

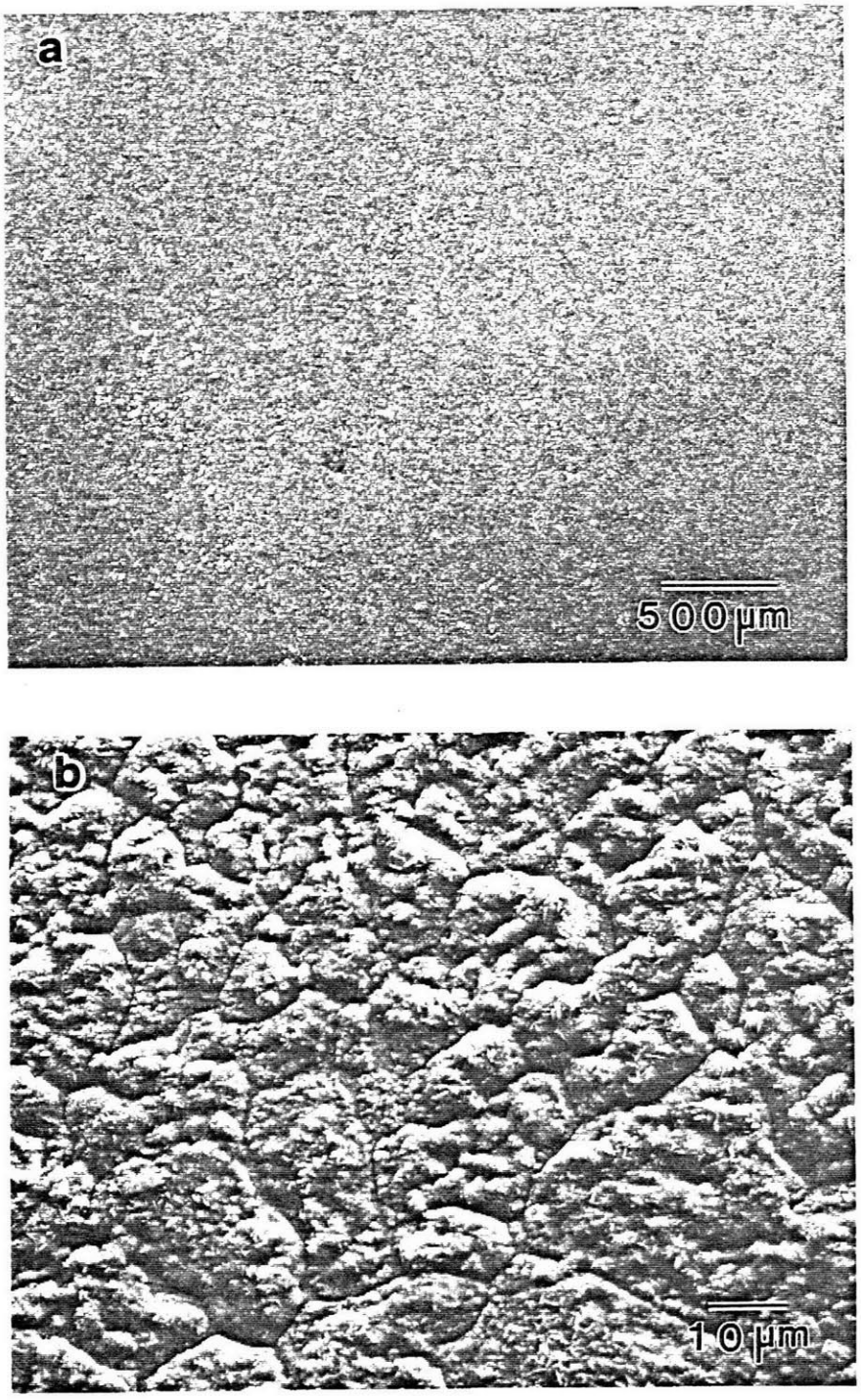

Figure 5.87—SEM secondary electron images of the scale formed on an Fe-2.5Cr-2.5Al-1Ti-0.6B alloy spray formed at a 0.23m (9in) substrate distance after oxidation at 700°C for 50h: (a) low magnification and (b) high magnification.

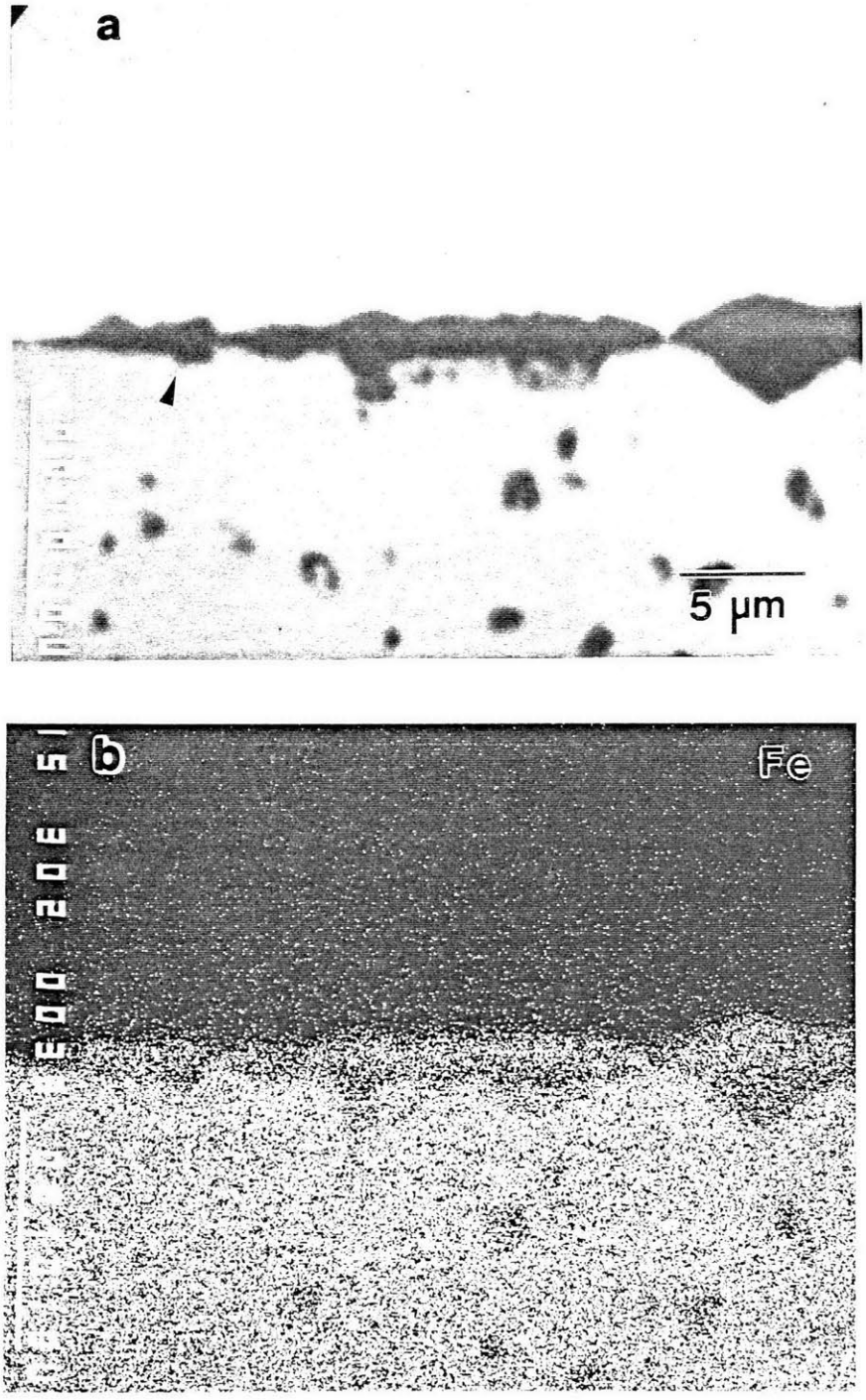

Figure 5.88—EPMA images of a cross-section through the scale shown in Figure 5.87: (a) back scattered electron image and (b) elemental X-ray intensity map for iron.

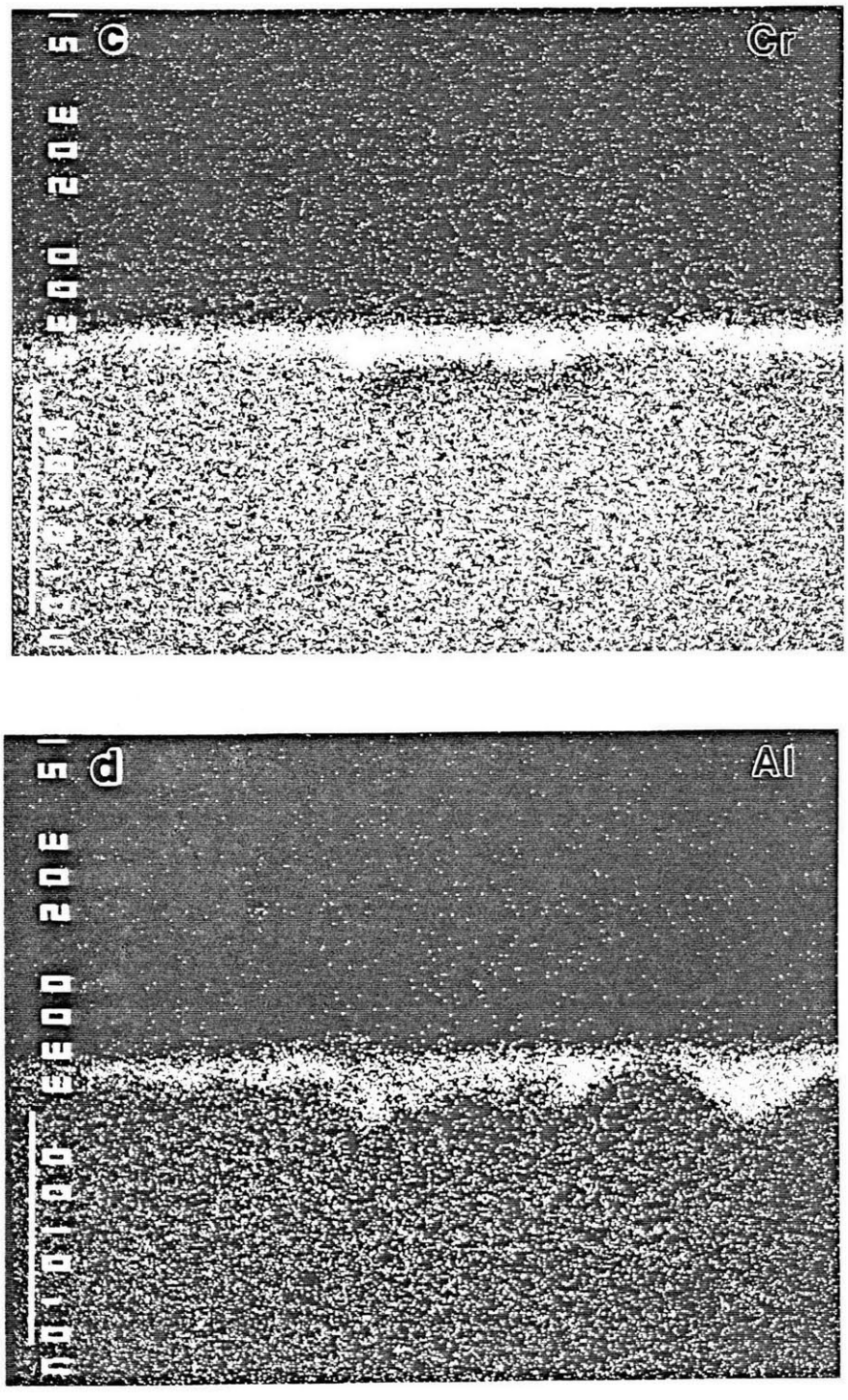

Figure 5.88 Cont.—Elemental X-ray intensity maps for (c) chromium and (d) aluminum.

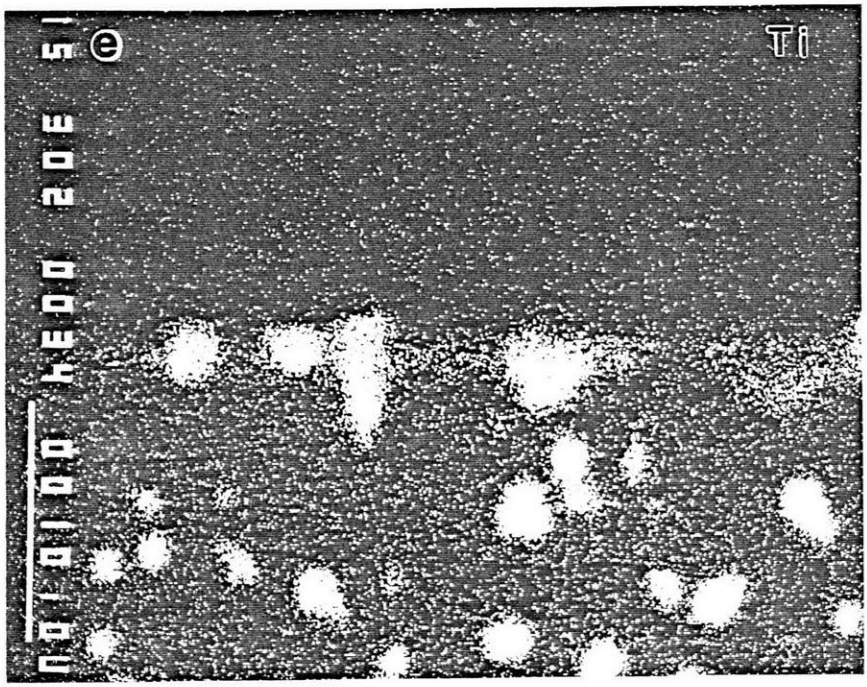

Figure 5.88 Cont.—(e) Elemental X-ray intensity map for titanium.

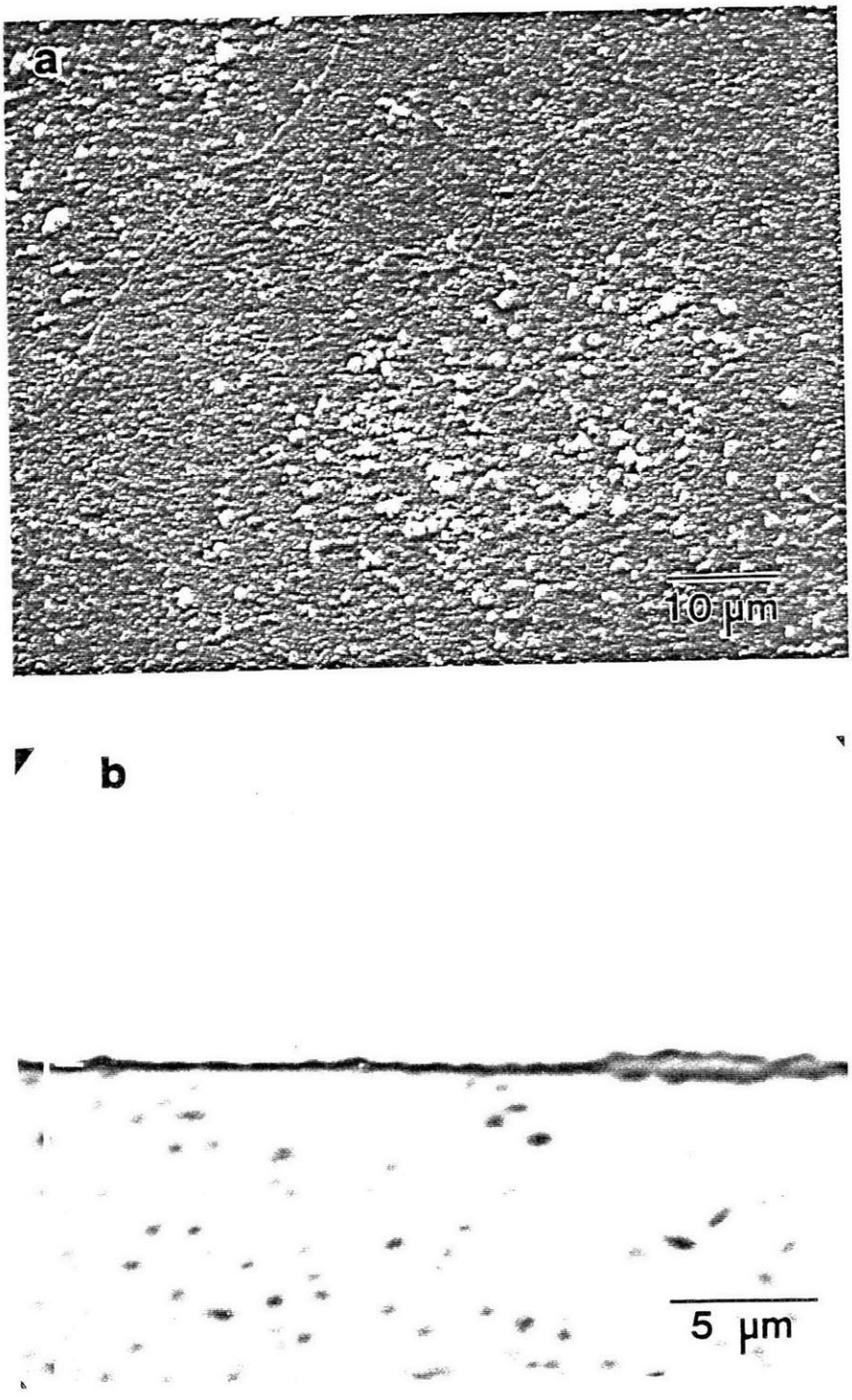

Figure 5.89—Scale formed on an Fe-2.5Cr-2.5Al-1Ti-0.6B alloy spray formed at a 0.64m (25in) substrate distance and oxidized at 600°C for 50h: (a) SEM secondary electron image of scale surface and (b) EMPA back scattered electron image of scale cross-section.

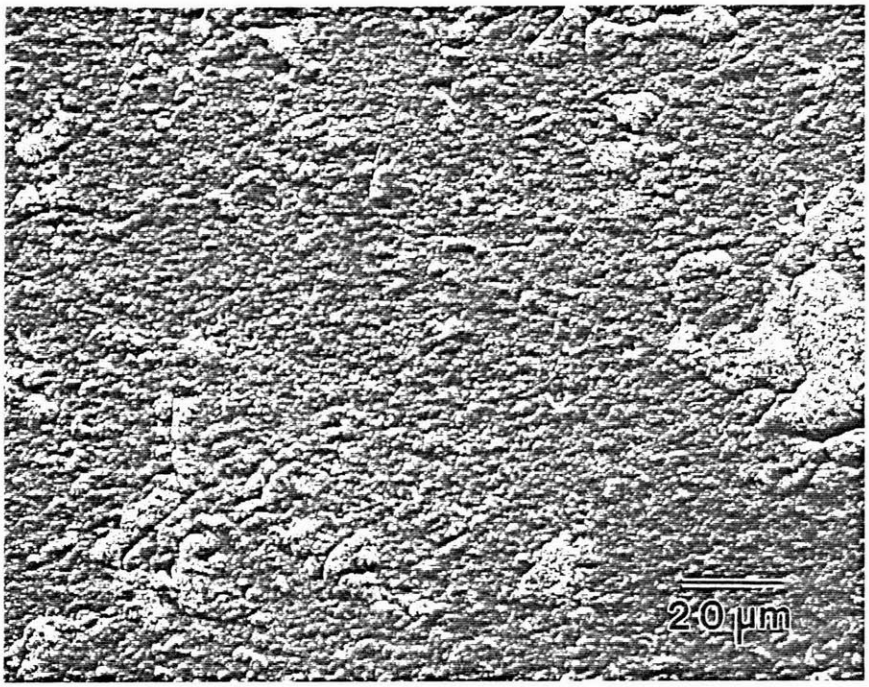

Figure 5.90—SEM secondary electron image of the oxide scale formed on an Fe-2.5Cr-2.5Al-1Ti-0.6B alloy spray formed at a 0.64m (25in) substrate position and oxidized at 700°C for 50h.

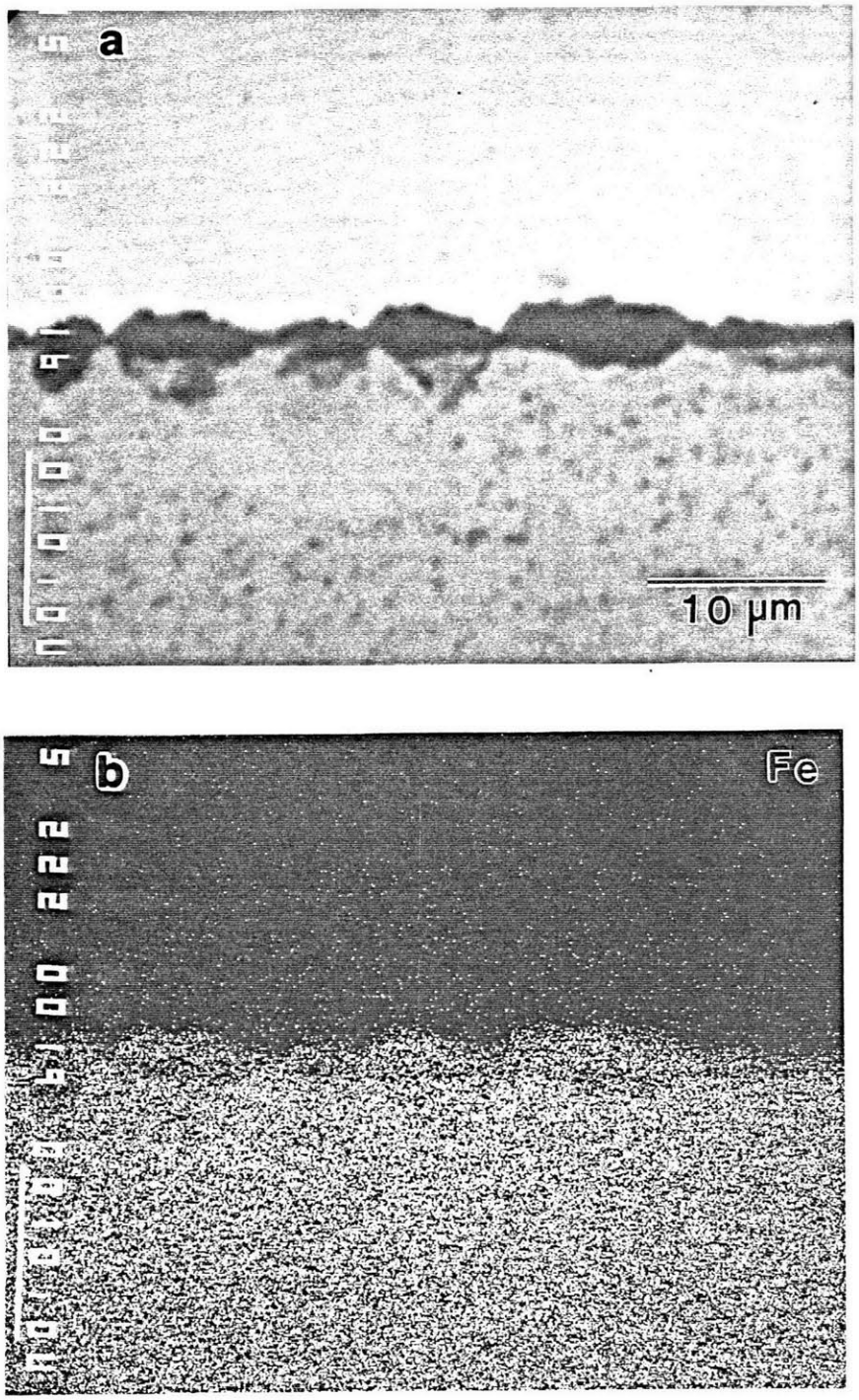

Figure 5.91—EPMA images of a cross-section through the scale shown in Figure 5.90: (a) back scattered electron image and (b) elemental X-ray intensity map for iron.

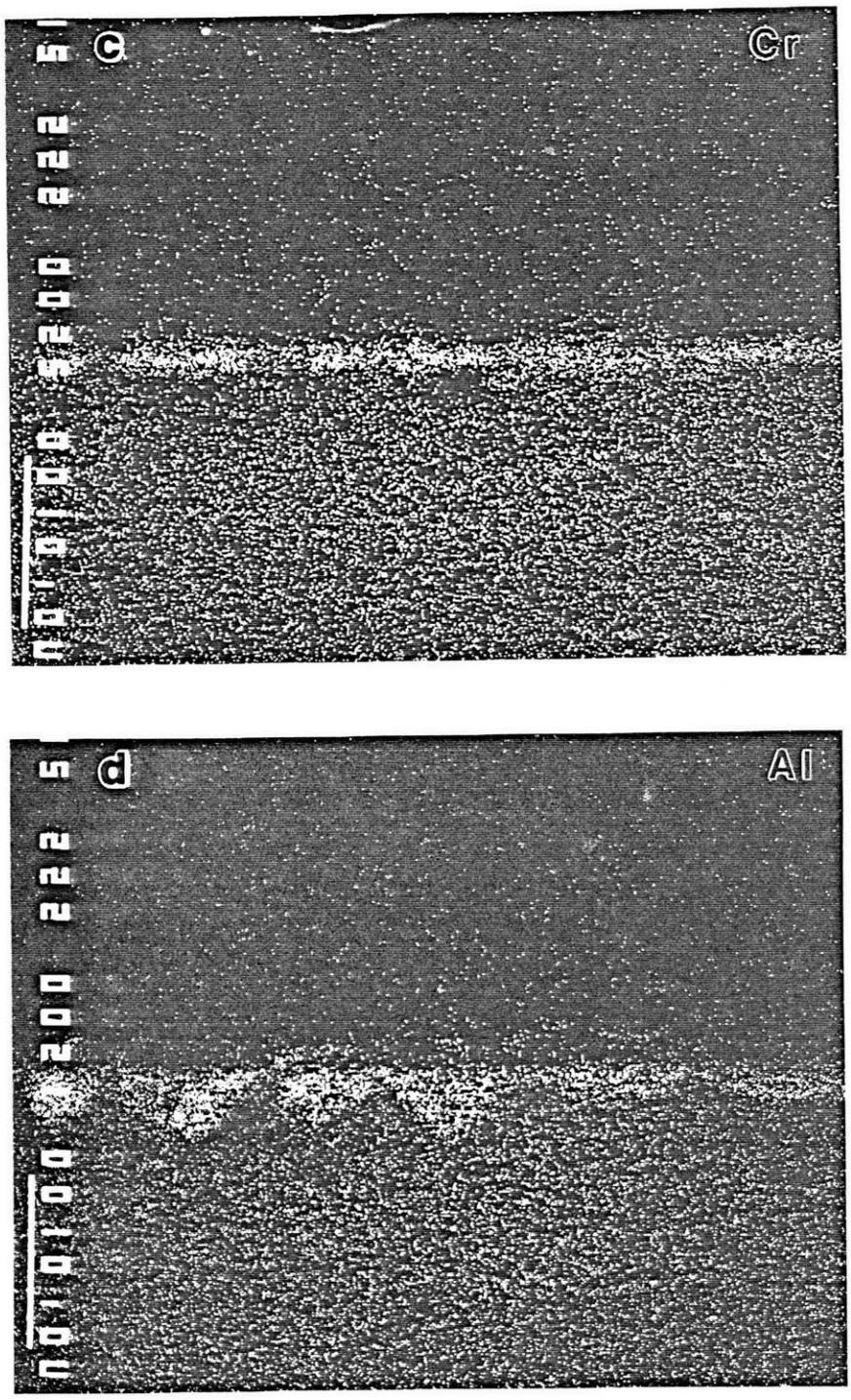

Figure 5.91 Cont.—Elemental X-ray intensity maps for (c) chromium and (d) aluminum.

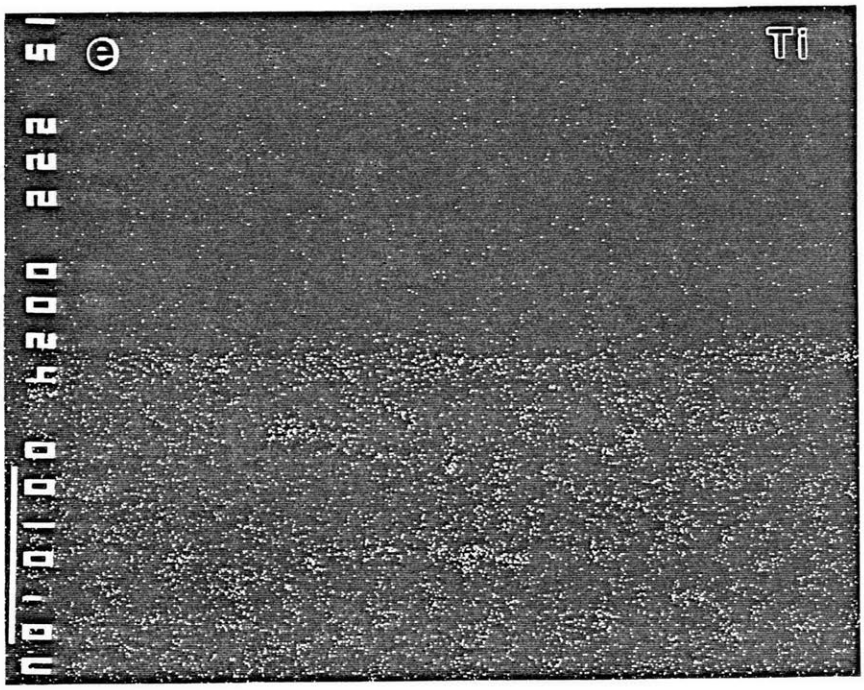

Figure 5.91 Cont.—(e) Elemental X-ray intensity map for titanium.

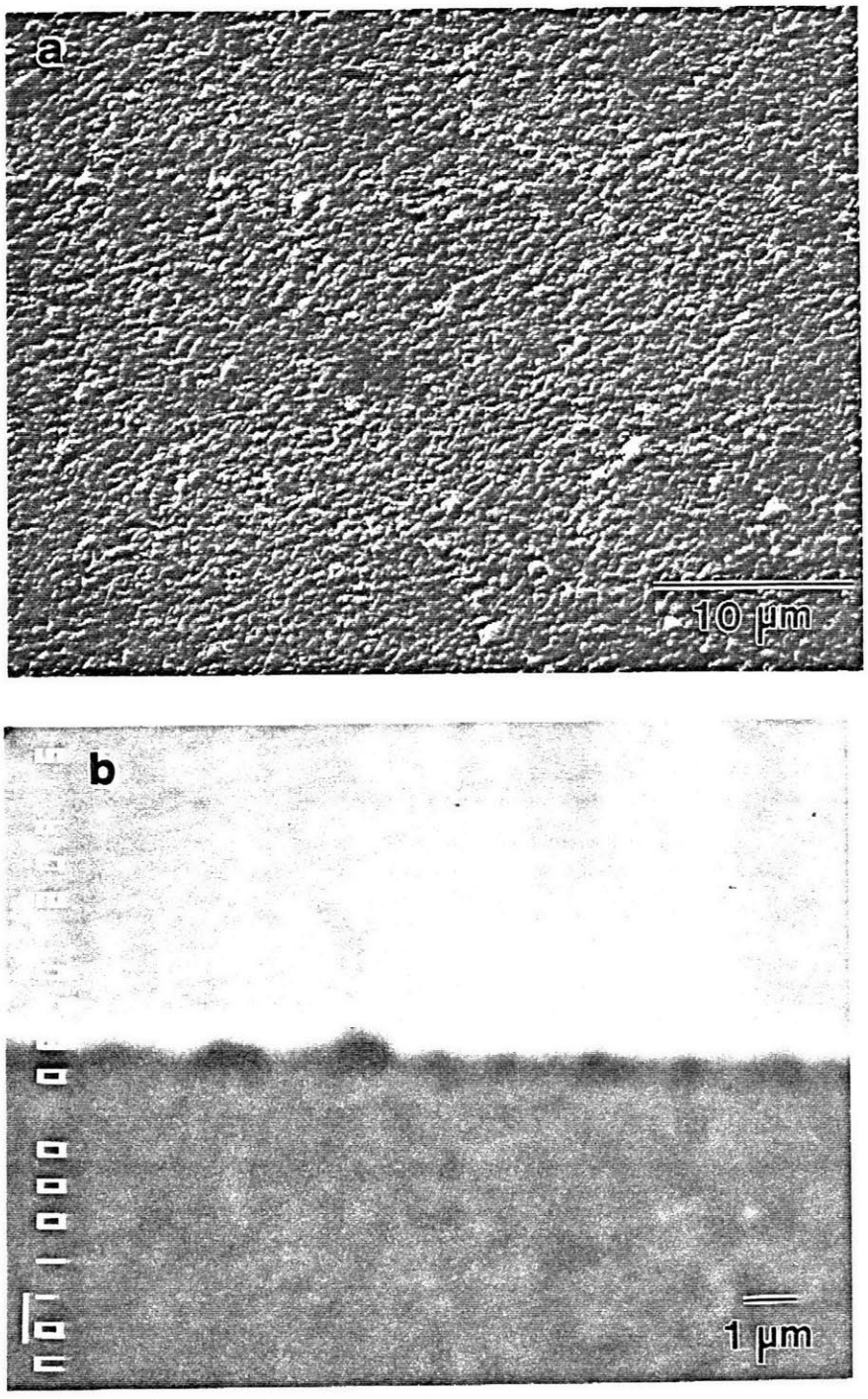

Figure 5.92—Scale formed on a powder processed Fe-2.5Cr-2.5Al-1Ti-0.6B alloy oxidized at 600°C for 50h: (a) SEM secondary electron image of scale surface and (b) EPMA back scattered image of scale cross-section.

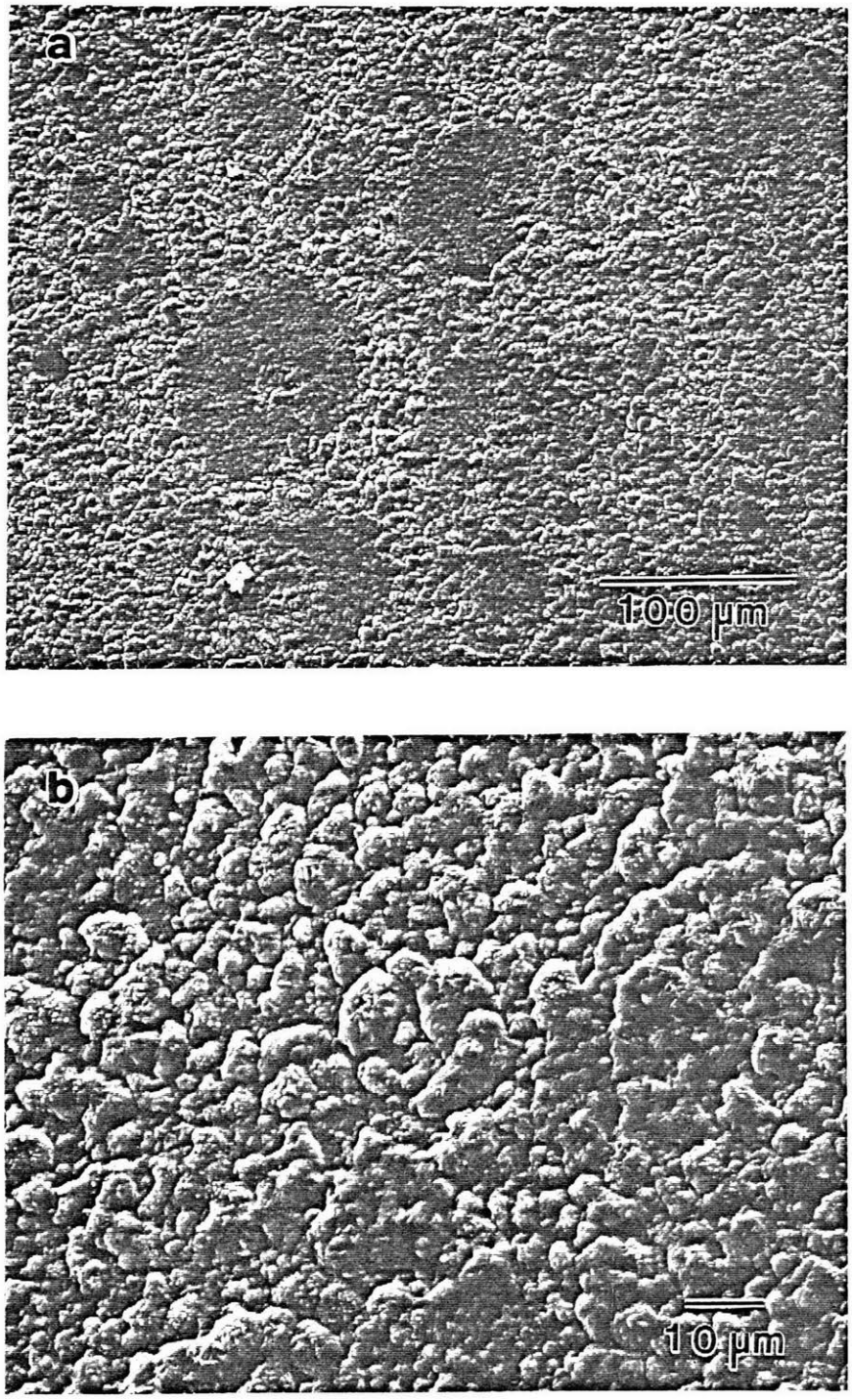

Figure 5.93—SEM secondary electron images of scale formed on a powder processed Fe-2.5Cr-2.5Al-1Ti-0.6B alloy oxidized at 700°C for 50h: (a) high magnification and (b) low magnification.

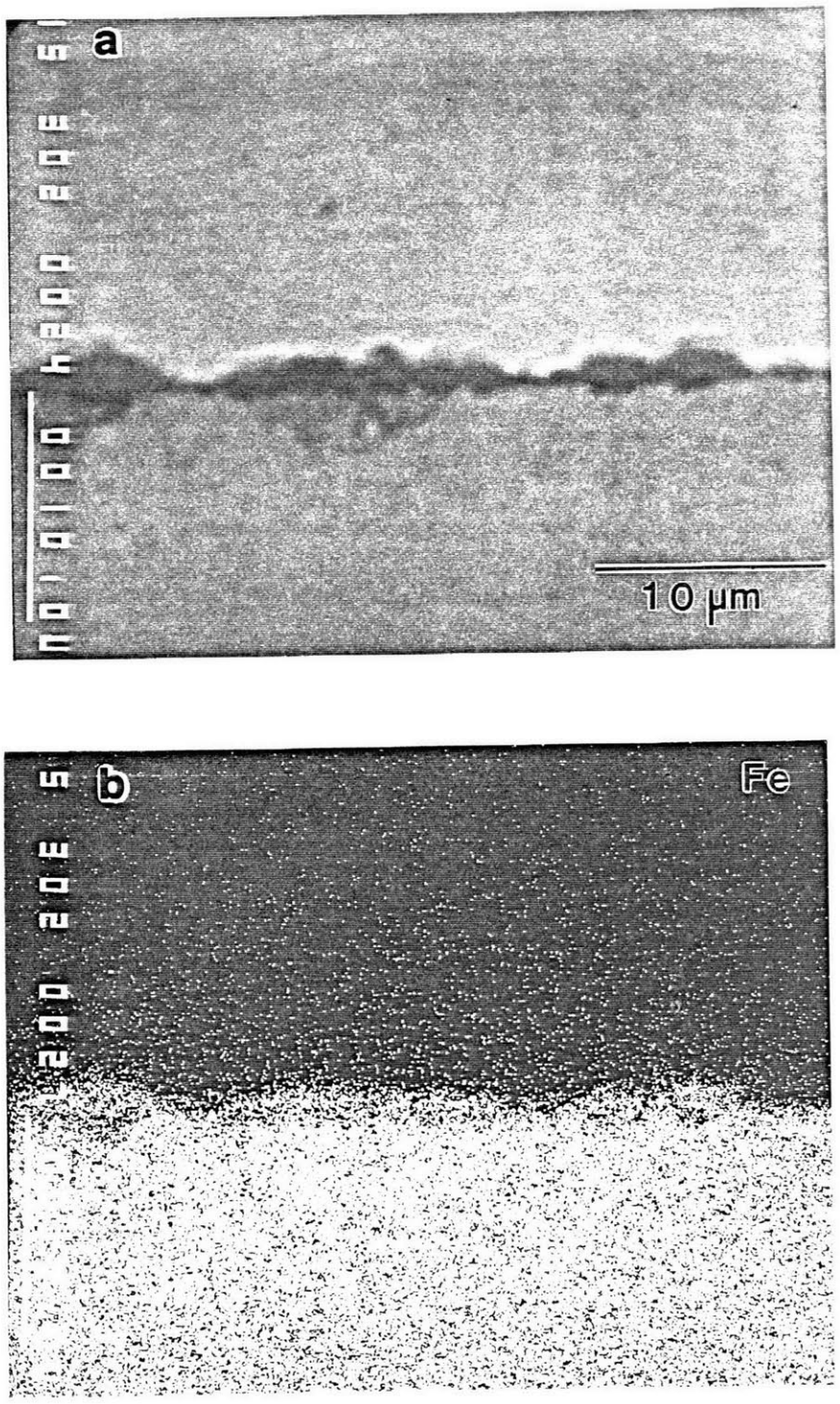

Figure 5.94—EPMA image of a cross-section through the scale shown in Figure 5.93: (a) back scattered electron image and (b) elemental X-ray intensity map for iron.

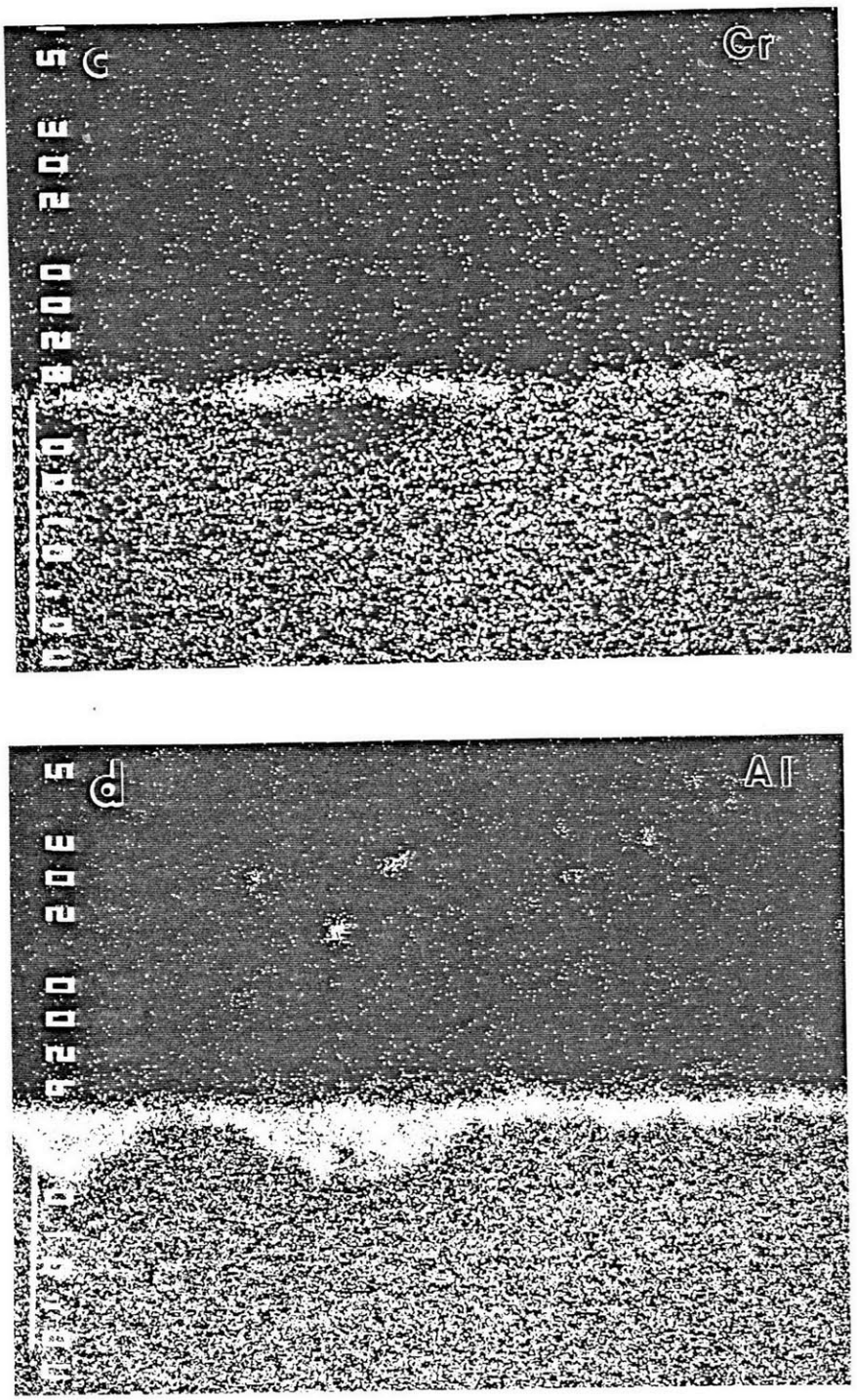

Figure 5.94 Cont.—Elemental X-ray intensity maps for (c) chromium and (d) aluminum.

Figure 5.94 Cont.—(e) Elemental X-ray intensity map for titanium.

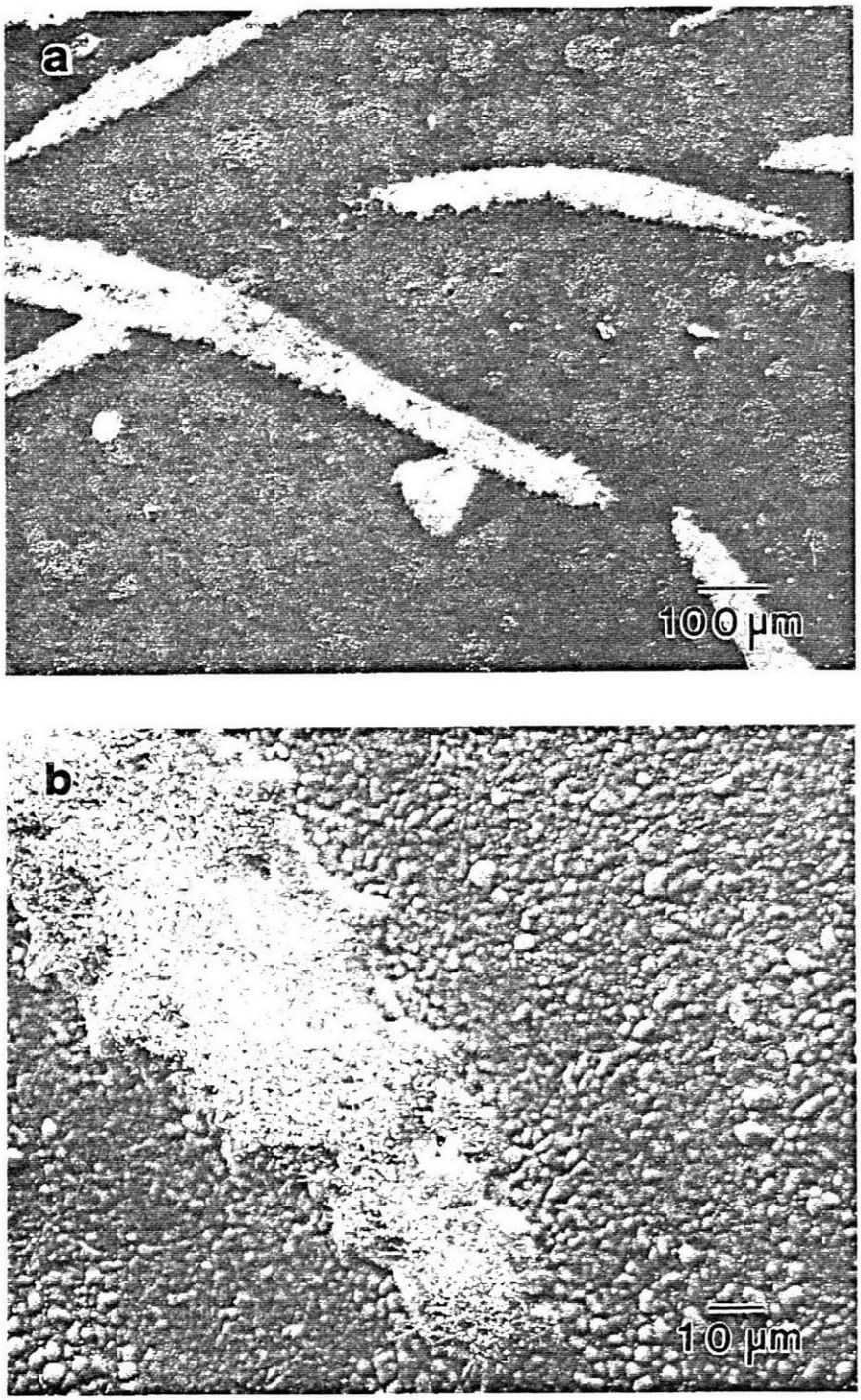

Figure 5.95—SEM secondary electron image of the scale formed on a powder processed Fe-2.5Cr-2.5Al-1Ti-0.6B alloy oxidized at 700°C for 50h. Field of view is in region where abnormal grain growth had occured during powder consolidation: (a) low magnification and (b) high magnification.

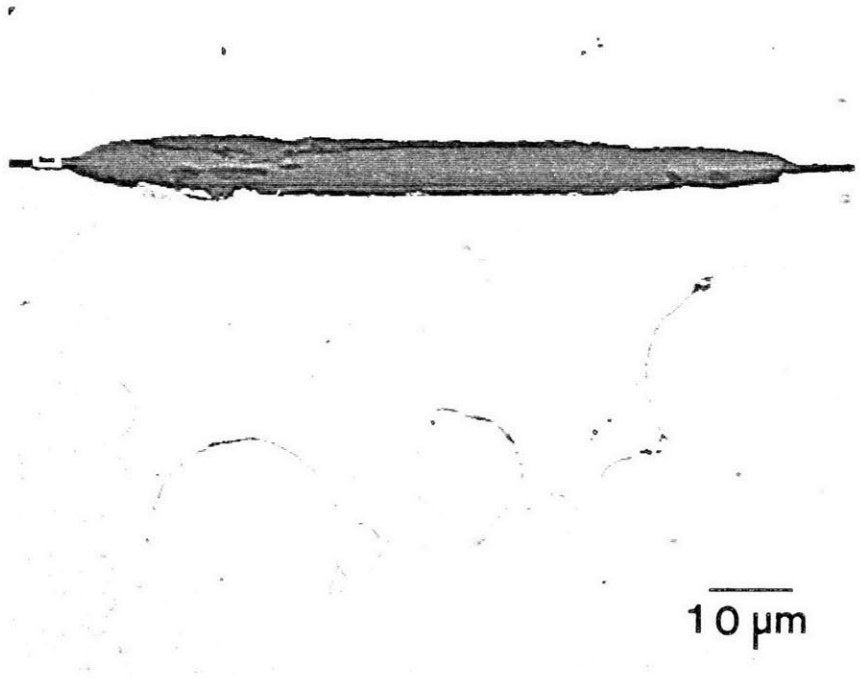

Figure 5.96—EPMA backscattered electron immage of a cross-section through scale shown in figure 5.95.

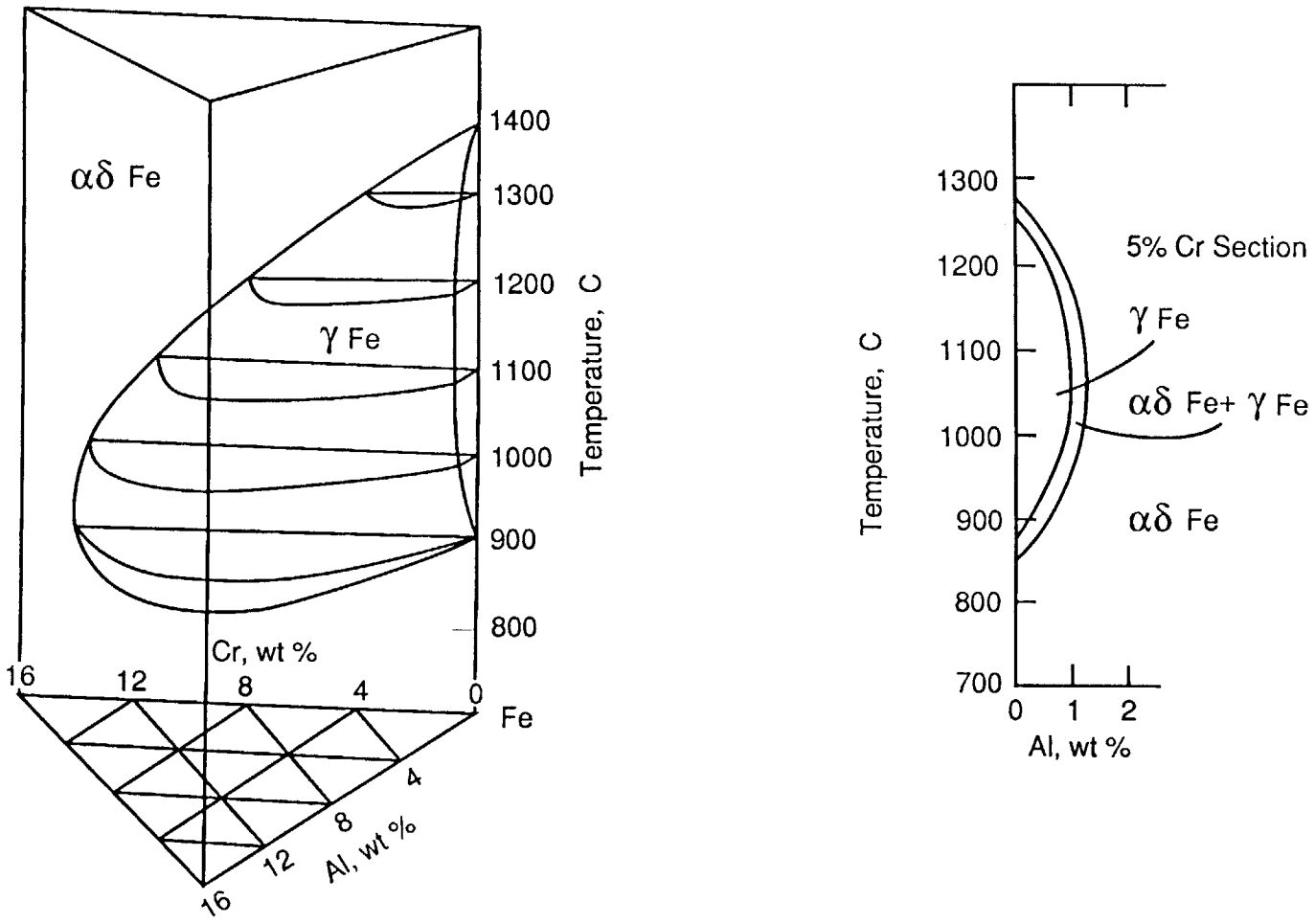

Figure 6.1—γ-loop in Fe-Cr-Al system.

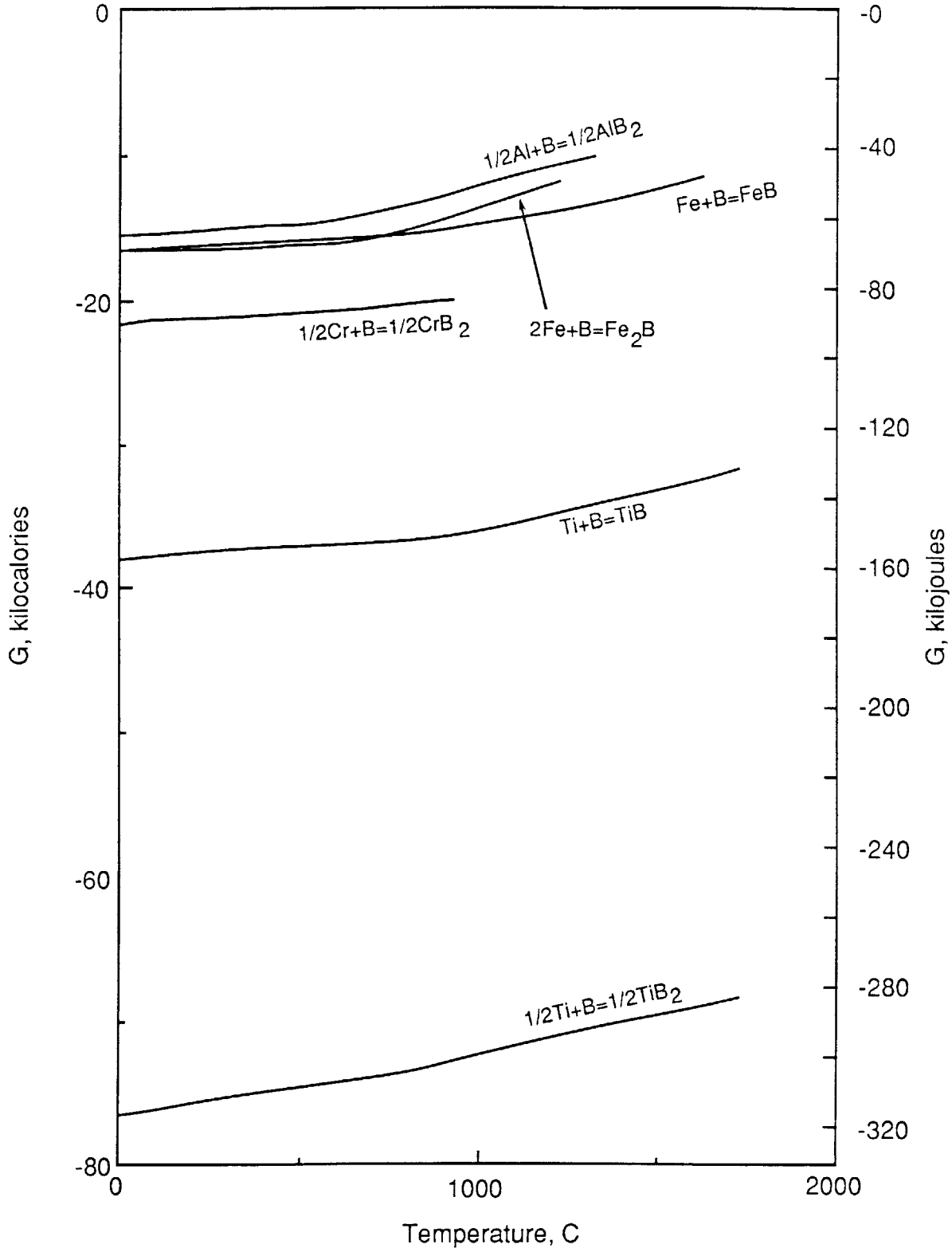

Figure 6.2—Standard free energies of formation of borides in the Fe-Cr-Al-Ti system.

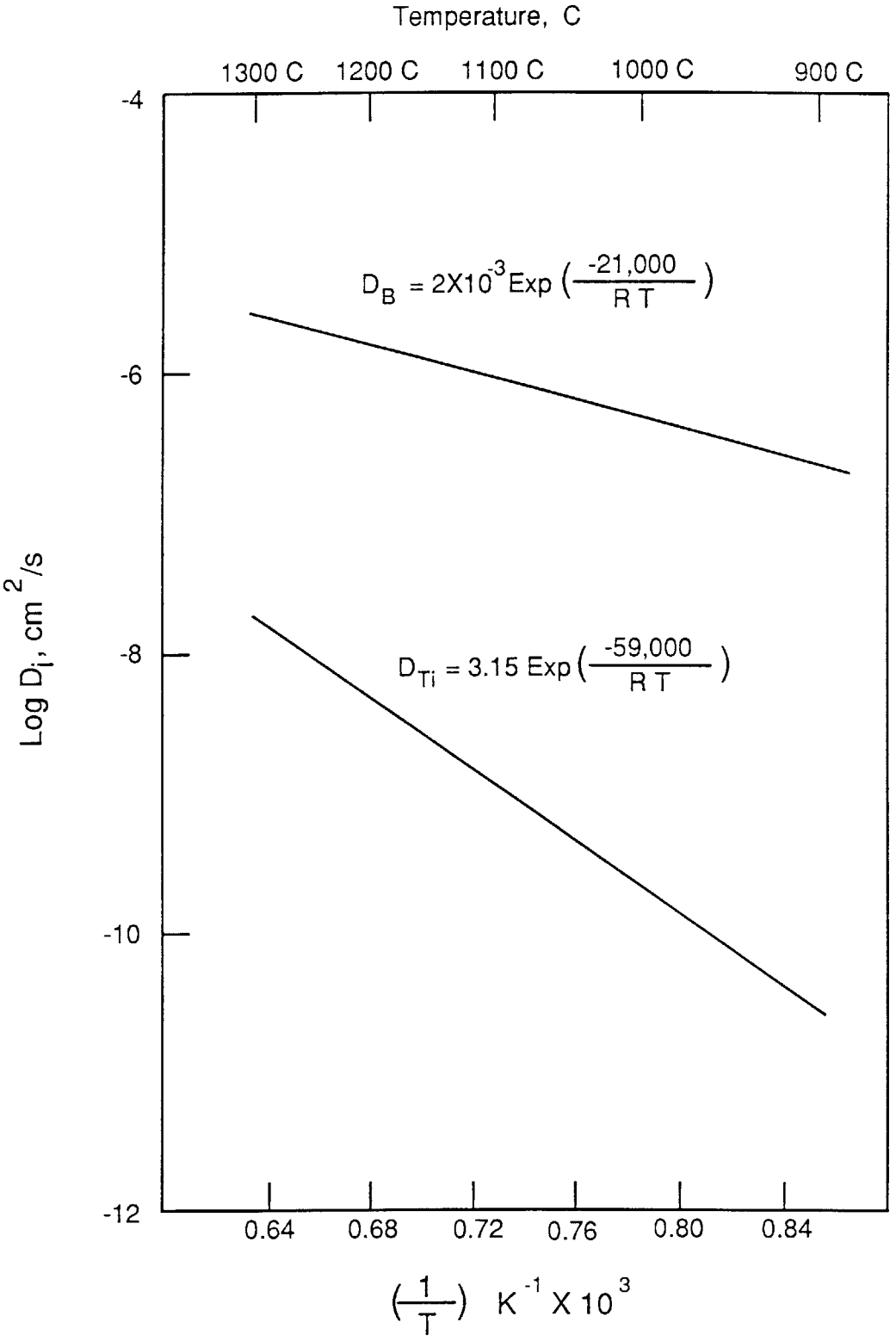

Figure 6.3—Diffusivity of titanium and boron in iron.

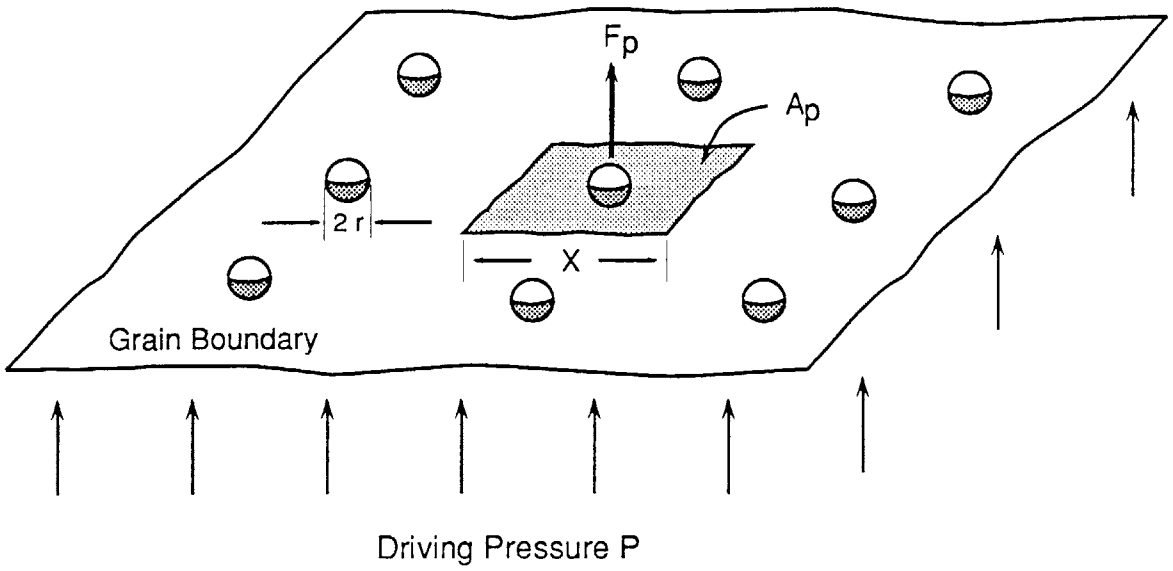

Figure 6.4—Grain boundary pinned by array of particles.

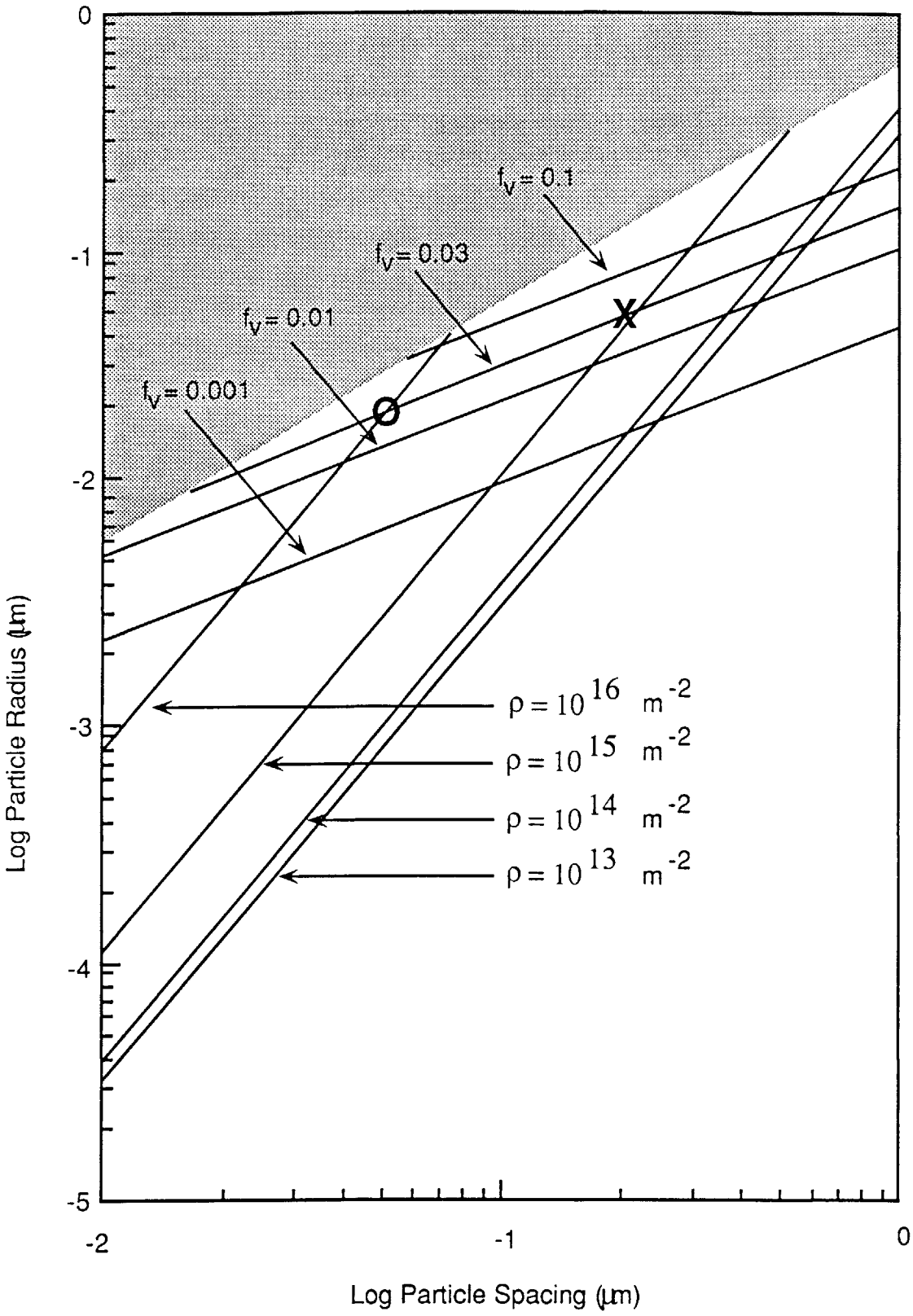

Figure 6.5—Combination of particle size and particle radius necessary to prevent grain growth for an alloy with a one micron grain size and particles situated only on the grain boundaries.

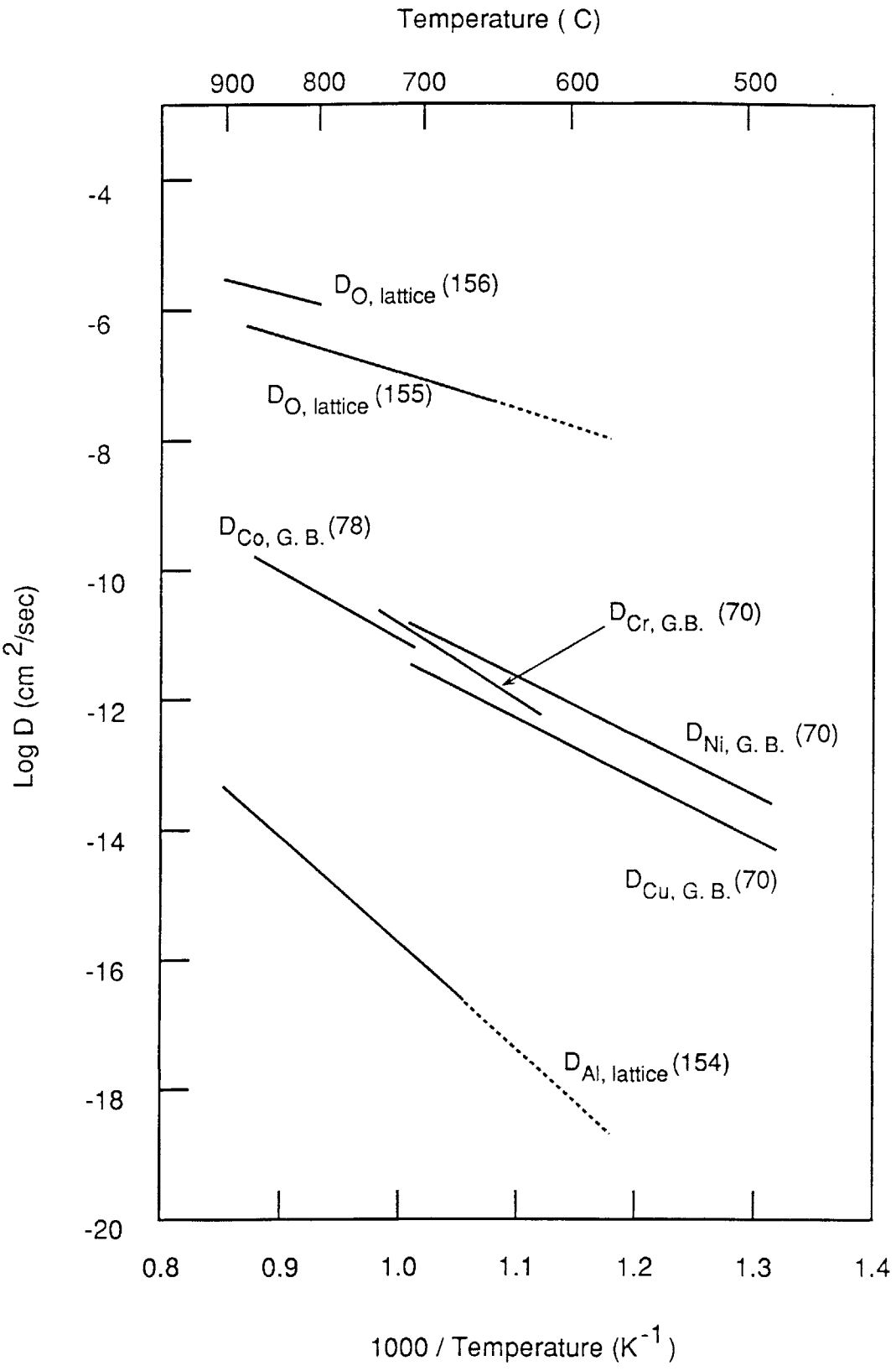

Figure 6.6—Diffusion coefficient of various elements in alfa iron.

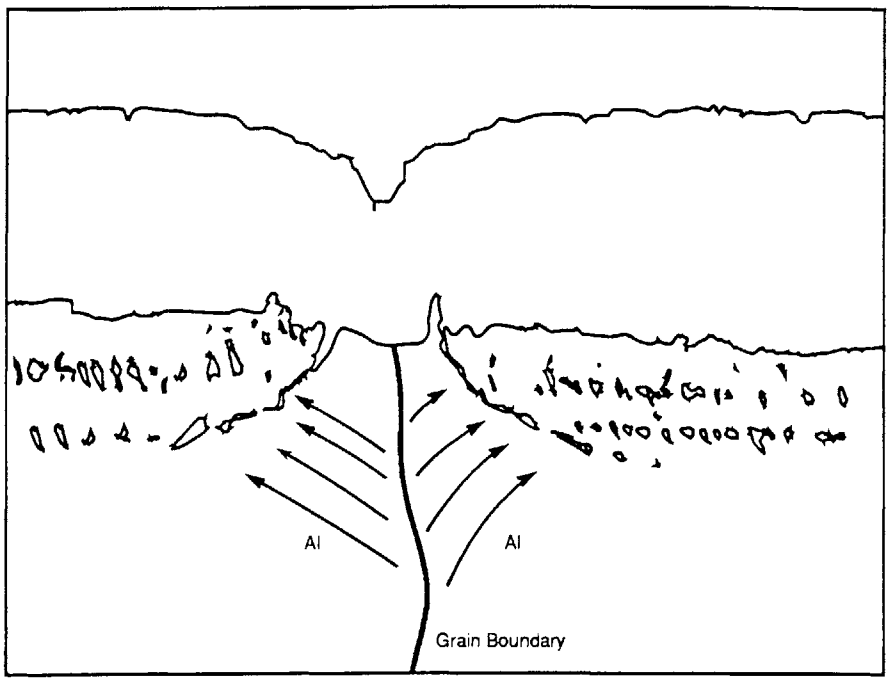

Figure 6.7–chematic diagram of inhanced aluminum difusion along an alloy grain boundary.

Table 6.1–Summary of Oxidation Products

Fe-4Cr-4Al ALLOY SERIES

Conventionally Processed Fe-4Cr-4Al Alloy

400°C : External α-Al_2O_3 layer.

500°C : External α-Al_2O_3 layer plus iron oxide patches over alloy grains.

600°C : External α-Al_2O_3 layer plus iron oxide patches over alloy grains.

700°C : External α-Al_2O_3 layer plus iron oxide nodules at specimen edges.

800°C : External α-Al_2O_3 layer.

900°C : External, convoluted α-Al_2O_3 layer.

1000°C : External, convoluted α-Al_2O_3 layer.

Conventionally Processed Fe-4Cr-4Al- 1Ti Alloy

900°C : External, convoluted α-Al_2O_3 layer plus titanium nodules.

1000°C : External, convoluted α-Al_2O_3 layer plus titanium nodules.

Radidly Solidified Fe-4Cr-4Al Alloy

400°C : External α-Al_2O_3 layer.

500°C : External α-Al_2O_3 layer.

600°C : External α-Al_2O_3 layer.

700°C : External α-Al_2O_3 layer.

800°C : External α-Al_2O_3 layer.

900°C : External α-Al_2O_3 layer.

1000°C : External α-Al_2O_3 layer.

Table 6.1 Cont.–Summary of Oxidation Products

Fe-2.5Cr-2.5Al ALLOY SERIES

Conventionally Processed Fe-2.5Cr-2.5Al Alloy

400°C : External α-Al_2O_3 layer.

500°C : Continuous, external $Fe(Cr, Al)_2O_4$, Fe_3O_4, and Fe_2O_3 layer.

600°C : Continuous, external $Fe(Cr, Al)_2O_4$, Fe_3O_4, and Fe_2O_3 layer.

700°C : Continuous, external Fe_3O_4, and Fe_2O_3 layer and internal $Fe(Cr, Al)_2O_4$ and α-Al_2O_3.

800°C : External a-Al_2O_3 layer plus iron oxide nodules at specimen edges.

900°C : External, convoluted α-Al_2O_3 layer plus iron oxide nodules.

1000°C : External, convoluted α-Al_2O_3 layer plus iron oxide nodules.

Rapidly Solidified Fe-2.5Cr-2.5Al-1Ti-0.6B Alloy (1μm and 10μm grain size)

600°C : External α-Al_2O_3.

700°C : External and internal α-Al_2O_3 plus complex iron oxides.

Table 6.2–Effective effective diffusion coefficient in cm^2/s.

Temp. / G.S.	600 C	700 C
1 μm	10^{-15}	10^{-14}
10 μm	10^{-16}	$1.1X10^{-15}$

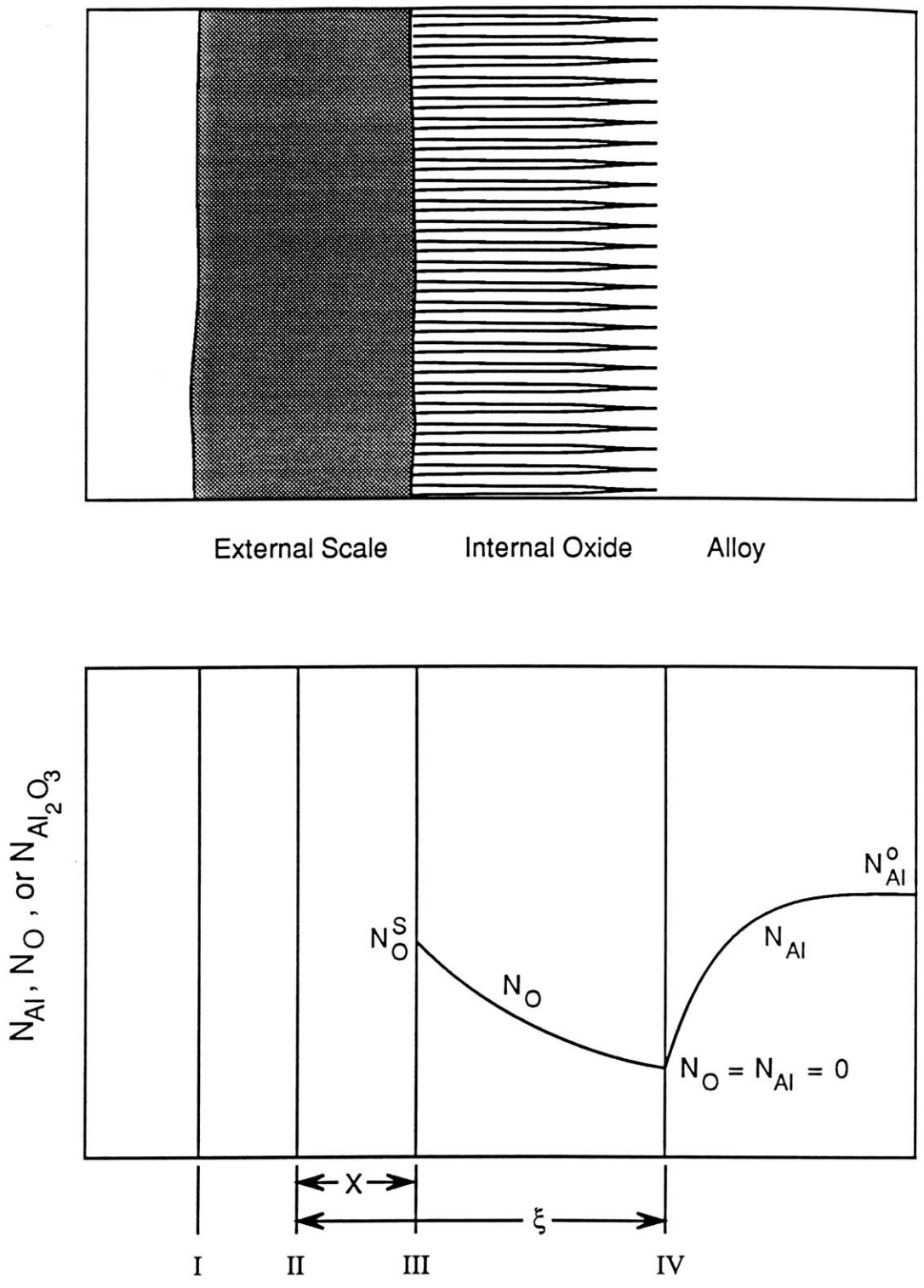

Figure 6.8—Schematic diagram of the oxide (a) and concentration profiles of oxygen and aluminum (b) for the oxidation of an Fe-2.5Cr-2.5Al alloy at 700 C. The plane at II indicates the original gas/metal interface.